

University of Warwick institutional repository: <http://go.warwick.ac.uk/wrap>

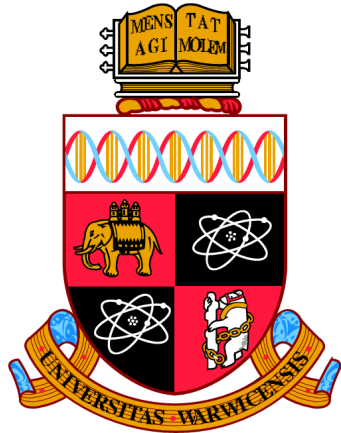
**A Thesis Submitted for the Degree of PhD at the University of Warwick**

<http://go.warwick.ac.uk/wrap/67618>

This thesis is made available online and is protected by original copyright.

Please scroll down to view the document itself.

Please refer to the repository record for this item for information to help you to cite it. Our policy information is available from the repository home page.



# Molecular Alignment Techniques for Polarised Spectroscopy

**Kasra Razmkhah**

A thesis submitted in partial fulfilment of requirements for the  
degree of Doctor of Philosophy in Chemistry

University of Warwick, Department of Chemistry  
September 2014

---



*For mum and dad*

تقدیم به پدر و مادر عزیزم به پاس عشق و محبت نامتناهیشان، حمایت بی دریغشان و  
از خودگذشتگی بی قید و شرطشان

*Kasra*







# Contents

<b>Contents</b>	i
<b>List of Illustrations</b>	vii
<b>List of Tables</b>	xvii
<b>Acknowledgements</b>	xxi
<b>Declaration</b>	xxiii
<b>Abbreviations</b>	xxv
<b>Summary</b>	xxvii
<b>Chapter One</b>	1
<b>Introduction</b>	
1.1 Linear dichroism	4
1.2 Raman spectroscopy	5
1.2.1 History and the development	7
1.2.2 Raman scattering theory	8
<b>Chapter Two</b>	
<b>Oxidized polyethylene films for orienting polar molecules for linear dichroism spectroscopy</b>	11
2.1 Introduction	13
2.2 Materials and methods	14
2.2.1 Sample preparation	14
2.2.2 Ultra-violet absorbance and linear dichroism spectroscopy	16
2.2.3 X-ray photoelectron spectroscopy	17
2.2.4 Contact angle measurements	18
2.2.5 XRD measurements	18
2.3 Results and discussion	19
2.3.1 PE <sup>OX</sup> oxidised films	19
2.3.2 UV-visible studies on the interactions of molecules deposited on stretched polyethylene film	23
2.3.3 Orienting small molecules on PE	29

2.3.3.1 Progesterone: a medium polarity molecules that orients in the same manner on PE and PE <sup>OX</sup>	29
2.3.3.2 Uniaxial orientation	31
2.3.3.3 DAPI	32
2.3.3.4 1-Prenecarboxaldehyde: different binding on PE and PE <sup>OX</sup>	34
2.4 Conclusions	37
<b>Chapter Three</b>	<b>39</b>
<b>Anthracene: Optical properties and dimerisation investigation</b>	
3.1 Introduction	41
3.2 Materials and methods	42
3.2.1 Linear dichroism and absorbance spectroscopy studies	42
3.2.2 Fluorimetry studies	42
3.2.3 Fluorescence detected linear dichroism studies	43
3.3 Results and discussion	44
3.3.1 Linear dichroism and absorbance spectroscopy studies	44
3.3.1.1 Monomeric anthracene	45
3.3.1.2 Oligomeric anthracene	48
3.3.2 Fluorimetry studies	52
3.3.3 Fluorescence detected linear dichroism studies	56
3.3.4 Computational modelling for possible dimers of anthracene	59
3.4 conclusions	62
<b>Chapter Four</b>	<b>65</b>
<b>Optical properties of xanthene based fluorescent dyes studied by stretched film linear dichroism</b>	
4.1 Introduction	67
4.2 Material and methods	68
4.2.1 PE <sup>OX</sup> film preparation	68
4.2.2 Linear dichroism and UV-visible absorbance spectroscopy studies	69
4.3 Results and discussion	70
4.3.1 Xanthene	71
4.3.2 9-Methyl-2,3,7-trihydroxy-6-fluorone	73

4.3.3 Pyronin Y and pyronin B	74
4.3.4 Fluorescein	77
4.3.5 Rhodamine 6G	78
4.4 Conclusions	79
<b>Chapter Five</b>	<b>81</b>
<b>Molecular dimerisation investigation using stretched polyethylene linear dichroism and fluorescence detected linear dichroism</b>	
5.1 Introduction	83
5.2 Materials and methods	85
5.2.1 UV-visible experiments	86
5.2.2 Fluorimetry experiments	86
5.2.3 Film preparation	86
5.2.4 Linear dichroism and fluorescence detected linear dichroism experiments	87
5.3 Results and discussion	88
5.3.1 4',6-diamidino-2-phenylindole	88
5.3.2 Naphthalene	91
5.3.3 Pyrene	96
5.3.4 Perylene	103
5.3.5 Olympicene	107
5.3.6 Computational modelling to study the possibility of dimerisation for polycyclic aromatic hydrocarbons	112
5.4 Conclusions	115
<b>Chapter Six</b>	<b>117</b>
<b>Polarised Raman spectroscopy application for aligned small biomolecules (Introducing Raman linear sum and difference spectroscopy)</b>	
6.1 Introduction	119
6.2 Materials and methods	119
6.2.1 Polarised Raman spectroscopy	120
6.3 Results and discussion	122
6.3.1 Polyethylene	122
6.3.2 Polytetrafluoroethylene	127

6.3.3 Progesterone	129
6.3.4 DAPI	131
6.3.5 1-Pyrenecarboxaldehyde	133
6.3.6 Anthracene	135
6.3.7 Thymine, thymidine and thymidine 5'-monophosphate	139
6.3.8 Cytosine, cytidine and cytidine 5'-monophosphate	143
6.3.9 Methyl-3-a-acetoxy-d-7,9(11)-choladienate	146
6.3.10 2,2':5',2"-terthiophene	148
6.3.11 1,10-phenanthroline	151
6.3.12 Fluorene and Fmoc chloride	154
6.4 Conclusions	156
<b>Chapter Seven</b>	<b>159</b>
<b>Studying the alignment of small biomolecules embedded in lipid vesicles</b>	
7.1 Introduction	161
7.2 Materials and methods	163
7.2.1 UV-visible LD	163
7.2.2 Polarised Raman spectroscopy of molecules on polyethylene	164
7.2.3 Lipid preparation	164
7.2.4 Polarised Raman spectroscopy of molecules embedded in lipid vesicles	165
7.2.5 Differential scanning calorimetry experiments of molecules embedded into lipid vesicles	165
7.3 Results and discussion	167
7.3.1 UV-visible LD experiments of the molecules aligned on PE and PE <sup>OX</sup>	167
7.3.1.1 Retinoids	167
7.3.1.2 Abietic acid	170
7.3.2 Polarised Raman spectroscopy of the molecules aligned on polyethylene	173
7.3.2.1 Retinoids	173
7.3.2.2 Abietic acid	175

7.3.3 Differential scanning calorimetry of the molecules embedded into lipid vesicles	176
7.3.4 Computational modelling studies on the docking position of guest molecules embedded in lipid bilayer	178
7.3.5 UV-visible LD experiments of retinal embedded into lipid vesicles deposited on PE <sup>OX</sup> and quartz	180
7.3.6 Polarised Raman spectroscopy of the molecules embedded into lipid vesicles	181
7.4 Conclusions	183
<b>Chapter Eight</b>	<b>185</b>
<b>Spectroscopic signatures of an fmoc–tetrapeptide, fmoc and fluorine</b>	
8.1 Introduction	187
8.2 Materials and methods	188
8.2.1 Ultra-violet absorbance, circular and linear dichroism spectroscopy	189
8.2.2 Fourier transform infrared and Raman spectroscopy	190
8.3 Results and discussion	191
8.3.1 UV-visible spectroscopic data	191
8.3.1.1 Absorbance	191
8.3.1.2 Circular dichroism	191
8.3.1.3 Linear dichroism	193
8.3.2 Vibrational data	195
8.3.2.1 FTIR	195
8.3.2.2 Raman spectroscopy	196
8.4 Conclusions	197
<b>Chapter Nine</b>	<b>199</b>
<b>Conclusions and the future work</b>	
9.1 Conclusions	201
9.2 Future work	204
9.2.1 Shear flow Raman linear dichroism	204
9.2.2 Linear dichroism and RLD of molecules imbedded inside lipid systems deposited on quartz	204

9.2.3 Cryo-linear dichroism and cryo-polarised Raman spectroscopy	205
9.2.4 Calculating the reduced fluorescence detected linear dichroism	205
<b>Bibliography</b>	207
<b>Appendices</b>	225

## List of Illustrations

<b>Fig. 1.1</b>	Schematic model for the effect of stretching on polymer chains and guest molecules imbedded between them. $\chi$ is the angle between the long axis of average molecules and the horizon.	5
<b>Fig. 1.2</b>	The schematic model for Sir C.V. Raman's early experiment on the change of the incident light colour after passing through a solution. The sun light used as the source of the light and the results were collected by visual observation.	8
<b>Fig. 1.3</b>	The schematic diagrams for a) Rayleigh, b) Stokes and c) anti-Stokes scatterings where $\Delta E_i$ and $\Delta E_s$ are respectively the energy of the incident and the scattered light, and $\nu_i$ and $\nu_s$ are the incident and scattered light frequency respectively. The frequency difference between the ground state and the first vibrational state is shown by $\nu_m$ . In the Rayleigh scattering the energy of the incident and the scattered (emitted) lights are equal, whilst they are different in the inelastic scatterings; the scattered light has lower energy levels than the incident light in the stokes scattering and has higher energy than the incident light in the anti-Stokes scattering.	10
<b>Fig. 2.1</b>	a) Mechanical film stretcher designed and built at the University of Warwick. b) Cylindrical film holder (originally designed for oriented circular dichroism measurements) where film is held between two quartz plates (1 mm thick) themselves sandwiched between Teflon rings and O-rings.	15
<b>Fig. 2.2</b>	a) Water drops on polyethylene films treated at the indicated power levels for the indicated times. b) The contact angle of PE films placed in the plasma asher at different power levels as a function of time.	20
<b>Fig. 2.3</b>	X-ray diffraction patterns of un-stretched and 2 $\times$ stretched PE films.	22
<b>Fig. 2.4</b>	a) The absorbance spectra of anthracene (40 $\mu$ L from a 0.5 mg/mL methanolic solution) deposited on a 1.8 $\times$ stretched PE <sup>OX</sup> film taken every 2 minutes from the first moments of sample loading for 2 hours. For presenting purposes only 10 spectra are shown (the time each spectrum is recorded is shown in the legend). The arrows show the ascending and descending trends in the peak intensity upon the time. b) and c) show the signal intensity trends upon the time of the measurement for the peaks at 254 and 248 nm (a) and 394, 378 and 268 nm (b).	24
<b>Fig. 2.5</b>	a) The UV-visible LD spectra of anthracene (the same conditions as absorbance experiment) deposited on a 1.8 $\times$ stretched PE <sup>OX</sup> film taken every 2 minutes from the first moments of sample loading for 2 hours. For presenting purposes only 10 spectra are shown (the time each spectrum is recorded is shown in the legend). The arrows show the ascending and descending trends in the peak intensity upon the time. b) and c) show the signal intensity trends upon the time of the measurement for the peaks at 254 and 248 nm (a) and 394 and 381 nm (b).	25
<b>Fig. 2.6</b>	a) The UV-visible LD spectra of anthracene deposited on a 1.8 $\times$ stretched PE <sup>OX</sup> film taken every 2 minutes from the first moments of sample loading for 2 hours. Liquid nitrogen was poured on the stretched polymer 8 and 62 minutes after the	26

experiment started. For presenting purposes only short wavelength region of the spectrum is shown for 10 spectra are shown (Spectra recorded between 4<sup>th</sup> and 12<sup>th</sup> minutes are shown on the left hand side and the ones recorded between 58<sup>th</sup> and 62nd minutes are shown on the right hand side). b) and c) show the signal intensity trends upon the time of the measurement for the peaks at 254 and 248 nm (a) and 381 nm (b). The jump at 28<sup>th</sup> minute in figure b could be due to a change in the ambient light.

a) The UV-visible LD spectra of anthracene deposited on a 1.8× stretched PE<sup>OX</sup> film taken every 2 minutes from the first moments of sample loading for 2 hours. The polyethylene was heat using a blow drier 6 and 60 minutes after the experiment started. For presenting purposes only short wavelength region of the spectrum is shown for 10 spectra are shown (Spectra recorded between 2<sup>nd</sup> and 10<sup>th</sup> minutes are shown on the left hand side and the ones recorded between 56<sup>th</sup> and 64<sup>th</sup> minutes are shown on the right hand side). b) and c) show the signal intensity trends upon the time of the measurement for the peaks at 254 and 248 nm (a) and 381 nm (b).

**Fig. 2.7** Spectra of progesterone (deposited from 0.65 mg/mL in chloroform for PE and methanol for PE<sup>OX</sup> and left to dry). LD on (a) PE, and (b) PE<sup>OX</sup> prestretched by factors ranging from 1 to 2.2×. (c) and (d) LD<sup>r</sup> for data from (a) and (b) respectively overlaid with absorbance and LD spectra for 1.8× stretch. 28

**Fig. 2.9** Left: LD of progesterone (~ 0.5 mg/mL) on 1.8× stretched a) PE and b) PE<sup>OX</sup> films as a factor of rotation angle,  $\chi$ , of the film. 0° is where the stretch direction is as close to horizontal as loading the film in a small circle enabled, right: LD at wavelength indicated as a function of  $\chi$ . Dashed line is the plot of  $\cos(2\chi)$ . 31

**Fig. 2.10** Spectra of DAPI on PE<sup>OX</sup> (deposited from 0.4 mg/mL in methanol and left to dry). (a) LD prestretched by factors ranging from 1 to 2.2×. (b) LD<sup>r</sup> for data from (a) overlaid with absorbance and LD spectra for 1.8× stretch. 33

**Fig. 2.11** LD of DAPI (deposited from 0.4 mg/mL in methanol) on PE<sup>OX</sup> stretched 1.8× as a function of film-rotation angle. a) wavelength scans, b) signal at 203, 229, 272 and 336 nm as a function of rotation angle  $\chi$  overlaid on a plot of  $\cos(2\chi)$ . 33

**Fig. 2.12** 4',6-Diamidino-2-phenylindole illustrating approximate transition polarizations consistent with this work and the PVA reference. 34

**Fig. 2.13** Left: LD spectra of 1-pyrenecarboxaldehyde (deposited from 0.4 mg/mL in chloroform for PE and methanol for PE<sup>OX</sup> and left to dry) on (a) PE, and (b) PE<sup>OX</sup> prestretched by factors ranging from 1 to 2.2×, right: The corresponding LD<sup>r</sup> spectra of the spectra on the left side overlaid with the LD and absorbance spectra when the film stretched for 1.8×. 35

**Fig. 2.14** Polarizations of PyCO transitions assuming the orientation direction of PE<sup>OX</sup> is as indicated by the thick solid line (the longest molecular axis with O lying flat on the film). The thick dashed line is then the orientation on PE. 36

**Fig. 2.15** LD of 1-pyrenecarboxaldehyde on (a) PE and (b) PE<sup>OX</sup> as a function of film-rotation angle. Left: wavelength scans, right: signal at 205, 233, 249, 276, 288, 364, 375 and 395 nm as a function of rotation angle  $\chi$  overlaid on a plot of  $\cos(2\chi)$ . Note: the film stretcher horizontal direction was not quite parallel to the PE stretch direction due to challenges of loading the film into the cylindrical holder. 37

<b>Fig. 3.1</b>	Schematic model of anthracene molecule showing the long and short axis of the molecule aligned with Z and Y axis of the molecule respectively.	41
<b>Fig. 3.2</b>	The schematic diagram for 90°-setup-fluorimetry experiment for samples deposited on stretched PE films. The stretcher is placed horizontally in the beam path the way that the film has an angle of 45° with respect to the excitation beam (green arrow) and the detector (presented as eye in the figure).	43
<b>Fig. 3.3</b>	The schematic diagrams for a) LD and b) FDLD experiments for samples aligned on stretched PE films. A longpass filter is placed in front of the detector to block the incident light, so only the emission fluorescence reaches the detector.	44
<b>Fig. 3.4</b>	LD of anthracene on a) PEOX and b) PE (from 0.15 and 0.4 mg/mL solutions respectively) as a function of film-rotation angle. Left: wavelength scans, right: signal at 246, 253, 324, 339, 353, 360 and 379 nm plotted as a function of rotation angle $\chi$ overlaid on a plot of $\cos(2\chi)$ . Note: the film stretcher horizontal direction was not quite parallel to the PE stretch direction due to challenges of loading the film into the cylindrical holder.	45
<b>Fig. 3.5</b>	Spectra of anthracene. (a) Absorbance of anthracene in solution (0.25 mg/mL cyclohexane) overlaid on absorbance spectra of 1.8× stretch films (PE) deposited from chloroform solutions of the concentrations indicated in the figure. (b) LD corresponding to (a) film spectra with solution absorbance overlaid normalised to have areas under the curves equal to one. (c) LD (deposited from 0.1 mg/mL solution in methanol, to ensure monomer, see text) on PEOX as a function of stretch factor (indicated – sample deposited after stretching). LD deposited from solutions in chloroform in (e) 1 mg/mL (g) 8 mg/mL as a function of stretch (sample added before stretching). (d), (f), and (h) LD' for data from respectively (c), (e), and (g) overlaid with absorbance and LD spectra for 1.8× stretch.	47
<b>Fig. 3.6</b>	The three proposed orientations of anthracene on PEOX films, (a) uniaxially oriented single molecules, (b) extended cross-hatched structure and (c) skewed dimers.	51
<b>Fig. 3.7</b>	Absorbance spectra of anthracene in methylcyclohexane solution with ascending concentrations from 0.05 to 2 mg/mL (listed in the legends). Except from the band at 253 nm in 2 mg/mL spectrum (due to the instrument cut-off), all bands' intensities follow the Beer Lambert Law.	52
<b>Fig. 3.8</b>	Fluorescence emission spectra of anthracene in methylcyclohexane solution with ascending concentrations from 0.05 to 2 mg/mL (listed in the legends). Each set of spectra was recorded using different excitation wavelength (indicated in top left hand corner). All spectra are shown scaled to have the area under the curve of the spectrum equal 1 to facilitate comparison of relative intensities.	53
<b>Fig. 3.9</b>	Fluorescence emission spectra of anthracene deposited on PE (1.8× stretched) from methylcyclohexane solution with concentrations of 0.1, 4 and 8 mg/mL (black, red and blue lines respectively). Each set of spectra was recorded using different excitation wavelength. All spectra are shown integrated to have the area under the curve of the spectrum equal 1.	55
<b>Fig. 3.10</b>	LD (left) and corresponding FDLD (right) spectra of anthracene deposited on 1.8× stretched PEOX from (a) 0.1, (b) 1 and (c) 4 mg/mL methanolic solution (drops of	57

chloroform were added to help dissolve 4 milligrams of anthracene in methanol). The black line in each diagram (indicated as 1 in the legend) represents the first aliquot of sample (40  $\mu$ L) on the film. Each number in the legend represents the number of aliquots (40  $\mu$ L) added on the film.

<b>Fig. 3.11</b>	LD (solid) and FDLD (dashed) spectra of monomeric anthracene (black, 0.1 mg/mL) and oligomeric (red and blue, 1 and 4 mg/mL respectively) on PE <sup>OX</sup> .	58
<b>Fig. 3.12</b>	The schematic models of the possible dimers of anthracene generated by the Molecular Dynamics approach.	60
<b>Fig. 3.13</b>	The schematic model of the most stable possible dimer of anthracene generated by the docking approach.	61
<b>Fig. 4.1</b>	a) Xanthene with z and y axes indicated by    and $\perp$ respectively, b) 9-methyl-2,3,7-trihydroxy-6-fluorone, c) pyronin Y, d) pyronin B, e) fluorescein, and f) rhodamine 6G.	67
<b>Fig. 4.2</b>	Spectra of xanthene on PE <sup>OX</sup> dropped from a 0.2 mg/mL solution onto an unstretched film and then stretched (stretch factor as indicated in inset).    and $\perp$ indicate transition polarization with respect to the xanthene long axis in Fig. 4.1. (a) LD, (b) LD' calculated as indicated in §2 (Eq. 2.1) overlaid with absorbance and LD spectra of $\times 2.4$ stretched PE <sup>OX</sup> . (c) absorbance, LD and LD' spectra of different concentration (0.2 and 1 mg/mL) on 2.4 $\times$ stretched PE <sup>OX</sup> (d) wavelength scans, (e) signal at 205, 251 and 292 nm as a function of rotation angle $\chi$ overlaid on a plot of $\cos(2\chi)$ .	72
<b>Fig. 4.3</b>	(a) LD spectra of 9-methyl-2,3,7-trihydroxy-6-fluorone on PE <sup>OX</sup> deposited from 0.01 and 0.2 mg/mL solution and stretched by a factor of $\times 2.4$ .    and $\perp$ indicate transition polarization with respect to the xanthene long axis in Fig. 2. (b) Absorbance and LD' spectra of the LD spectra in Fig. 3(a) overlaid with solution absorbance spectrum (S).	74
<b>Fig. 4.4</b>	(a) LD spectra of pyronin Y on PE <sup>OX</sup> deposited from solutions of concentrations indicated in the Figure.    and $\perp$ indicate transition polarization with respect to the xanthene long axis in Fig 4.1a (b) Absorbance and LD' spectra of samples with concentrations 0.01 and 0.2 mg/ml overlaid with solution absorbance spectrum (S) and the dimer/monomer difference spectrum.	76
<b>Fig. 4.5</b>	(a) LD spectra of pyronin B on PE <sup>OX</sup> deposited from solutions of concentrations indicated in the Figure.    and $\perp$ indicate transition polarization with respect to the xanthene long axis in Fig. 4.1. (b) Absorbance and LD' spectra of samples with concentrations 0.01 and 0.2 mg/ml overlaid with solution absorbance spectrum (S) and the dimer/monomer difference spectrum.	77
<b>Fig. 4.6</b>	(a) LD spectra of fluorescein on PE <sup>OX</sup> deposited from solutions of concentrations indicated in the Figure.    and $\perp$ indicate transition polarization with respect to the xanthene long axis in Fig. 2. (b) Absorbance and LD' spectra of samples with concentrations 0.01 and 0.2 mg/ml overlaid with solution absorbance spectrum (S) and the dimer/monomer difference spectrum.	78
<b>Fig. 4.7</b>	(a) LD spectra of rhodamine 6G on PE <sup>OX</sup> deposited from solutions of concentrations indicated in the Figure.    and $\perp$ indicate transition polarization with respect to the xanthene long axis in Fig. 4.1. (b) Absorbance and LD' spectra of samples with concentrations 0.01 and 0.2 mg/ml overlaid with solution absorbance spectrum (S) and the dimer/monomer difference spectrum.	79

<b>Fig. 4.8</b>	(a) H-aggregate geometry which is consistent with the data for MeOH 3-fluorone and pyronin Y at high concentrations. (b) Offset stacked geometry which is consistent with the data for pyronin B, fluorescein, and rhodamine 6G at high concentrations.	80
<b>Fig. 5.1</b>	The absorbance spectra of air recorded when 300 (black), 341 (red) and 400 nm (blue) longpass filters are inserted in front of the PEM (after subtraction of the corresponding spectra of air when the filter was not placed).	83
<b>Fig. 5.2</b>	The chemical structure of a) 4',6-diamidino-2-phenylidole, b) naphthalene, c) pyrene, d) perylene and e) olympicene.	85
<b>Fig. 5.3</b>	The absorbance, fluorescence emission (excitation wavelength: 342 nm) and excitation (emission wavelength: 455 nm) spectra of DAPI (0.1 mg/mL).	89
<b>Fig. 5.4</b>	LD (left) and corresponding FDLD (right) spectra of DAPI deposited on 1.8 $\times$ stretched PE <sup>OX</sup> from (a and b) 0.01 and (c and d) 0.1 mg/mL methanolic solutions. The black line in each diagram (indicated as 1 in the legend) represents the first aliquot of sample (40 $\mu$ mL) on the film. Each number in the legend represents the number of aliquots (40 $\mu$ mL) added on the film.	90
<b>Fig. 5.5</b>	LD (solid) and FDLD (dashed) spectra of DAPI deposited on PE <sup>OX</sup> (1.8 $\times$ stretched) from methanolic solutions with different concentrations: 0.01 (black) and 0.1 (red) mg/mL.	91
<b>Fig. 5.6</b>	The absorbance and fluorescence emission spectra of naphthalene (0.01 mg/mL).	92
<b>Fig. 5.7</b>	LD (left) and corresponding FDLD (right) spectra of naphthalene deposited on 1.8 $\times$ stretched PE <sup>OX</sup> from (a and b) 0.1, (c and d) 1, (e and f) 8 and (g and h) 15 mg/mL methanolic solutions. The black line in each diagram (indicated as 1 in the legend) represents the first scan in the total of 12 scans. Each number in the legend represents the number of the scan recorded from each sample.	94
<b>Fig. 5.8</b>	Schematic chemical structures for naphthalene's a) monomeric and three dimeric forms: b) eclipse, c) crossed and d) J-aggregate.	95
<b>Fig. 5.9</b>	LD (solid) and FDLD (dashed) spectra of naphtalene deposited on PE <sup>OX</sup> (1.8 $\times$ stretched) from methanolic solutions with different concentrations: 0.1 (black), 1 (red), 8 (blue) and 15 (magenta) mg/mL. The spectra shown in this figure are recorded by a single scan after depositing the sample on polyethylene film.	96
<b>Fig. 5.10</b>	The absorbance and fluorescence emission spectra of pyrene (0.05 mg/mL).	97
<b>Fig. 5.11</b>	LD (left) and corresponding FDLD (right, a 341 nm longpass filter was used) spectra of pyrene deposited on 1.8 $\times$ stretched PE <sup>OX</sup> from (a and b) 0.1 and (c and d) 1 and (e and f) 4 mg/mL methanolic solutions. The black line in each diagram (indicated as 1 in the legend) represents the first aliquot of sample (40 $\mu$ mL) on the film. Each number in the legend represents the number of aliquots (40 $\mu$ mL) added on the film.	98
<b>Fig. 5.12</b>	LD (solid) and FDLD (dashed, a 341 nm longpass filter was used) spectra of pyrene deposited on PE <sup>OX</sup> (1.8 $\times$ stretched) from methanolic solutions with different concentrations: 0.1 (black), 1 (red) and 4 (blue) mg/mL. The 1 and 4	100

mg/mL LD spectra are respectively 8 and 20 times, and all FDLD spectra 5 times reduced in intensity.	
<b>Fig. 5.13</b> LD (left) and corresponding FDLD (right, a 400 nm longpass filter was used) spectra of pyrene deposited on 1.8 $\times$ stretched PE <sup>OX</sup> from (a and b) 0.1 and (c and d) 1 and (e and f) 4 mg/mL methanolic solutions. The black line in each diagram (indicated as 1 in the legend) represents the first aliquot of sample (40 $\mu$ L) on the film. Each number in the legend represents the number of aliquots (40 $\mu$ L) added on the film.	101
<b>Fig. 5.14</b> LD (solid) and FDLD (dashed, a 400 nm longpass filter was used) spectra of pyrene deposited on PE <sup>OX</sup> (1.8 $\times$ stretched) from methanolic solutions with different concentrations: 0.1 (black), 1 (red) and 4 (blue) mg/mL. The 0.1 mg/mL LD spectrum is 5 times magnified and that of 4 mg/mL is 1.5 times reduced in intensity.	102
<b>Fig. 5.15</b> The FDLD spectra of pyrene using a 400 (black) and a 341 (red) nm longpass filters when the solution concentration is a) 0.1, b) 1 and c) 4 mg/mL. The spectra recorded using different longpass filters are obtained from different samples.	102
<b>Fig. 5.16</b> Absorbance (black), LD (red) and LD <sup>r</sup> (blue) spectra of perylene (from a 0.01 mg/mL methanolic solution) deposited on 1.8 $\times$ stretched PE <sup>OX</sup> .	104
<b>Fig. 5.17</b> The absorbance and fluorescence emission spectra of perylene (0.01 mg/mL).	105
<b>Fig. 5.18</b> LD (left) and corresponding FDLD (right) spectra of perylene deposited on 1.8 $\times$ stretched PE <sup>OX</sup> from (a and b) 0.01, (c and d) 0.1 and (e and f) 1 mg/mL methanolic solutions. The black line in each diagram (indicated as 1 in the legend) represents the first aliquot of sample (40 $\mu$ L) on the film. Each number in the legend represents the number of aliquots (40 $\mu$ L) added on the film.	106
<b>Fig. 5.19</b> LD (solid) and FDLD (dashed) spectra of perylene deposited on PE <sup>OX</sup> (1.8 $\times$ stretched) from methanolic solutions with different concentrations: 0.01 (black), 0.1 (red) and 1 (blue) mg/mL.	107
<b>Fig. 5.20</b> LD (solid line) and LD <sup>r</sup> (dashed) spectra of olympicene deposited from 0.01 (black), 0.1 (red and blue) mg/mL methanolic solutions on 1.8 $\times$ stretched PE <sup>OX</sup> . The blue spectra are recorded when two aliquots (each aliquot is 40 $\mu$ L) of the sample (0.1 mg/mL) was deposited on the film.	108
<b>Fig. 5.21</b> The absorbance and fluorescence emission spectra of olympicene (0.1 mg/mL).	109
<b>Fig. 5.22</b> LD (left) and corresponding FDLD (right) spectra of olympicene deposited on 1.8 $\times$ stretched PE <sup>OX</sup> from (a and b) 0.01, (c and d) 0.1 and (e and f) 1 mg/mL methanolic solutions. The black line in each diagram (indicated as 1 in the legend) represents the first aliquot of sample (40 $\mu$ L) on the film. Each number in the legend represents the number of aliquots (40 $\mu$ L) added on the film.	110
<b>Fig. 5.23</b> LD (solid) and FDLD (dashed) spectra of olympicene deposited on PE <sup>OX</sup> (1.8 $\times$ stretched) from methanolic solutions with different concentrations: 0.01 (black), 0.1 (red) and 1 (blue) mg/mL. The LD spectrum of 0.01 mg/mL sample has been magnified 5 times and the intensity of the spectrum related to 1 mg/mL sample is reduced 8 times for presenting purposes.	111

<b>Fig. 5.24</b>	The schematic models of the possible dimers of naphthalene generated by Molecular Dynamics and docking approach.	113
<b>Fig. 5.25</b>	The schematic models of the possible dimers of pyrene generated by Molecular Dynamics and docking approach.	113
<b>Fig. 5.26</b>	The schematic models of the possible dimers of perylene generated by Molecular Dynamics and docking approach.	114
<b>Fig. 5.27</b>	The schematic models of the possible dimers of olympicene generated by Molecular Dynamics and docking approach.	115
<b>Fig. 6.1</b>	The custom-made BioTools Chiral Raman 2-X Spectrometer with its schematic instrumentation map.	121
<b>Fig. 6.2</b>	The schematic model for in and out of plane bending vibrations for CH <sub>2</sub> .	124
<b>Fig. 6.3</b>	Spectra of PE <sup>OX</sup> . a) RLS and b) RLD spectra recorded for different stretching factors, from unstretched (solid black) to 2.2× (dashed red). Each spectrum was recorded using the BioTools instrument with 60 mW laser power for 10 minutes.	125
<b>Fig. 6.4</b>	Raman spectra of PTFE film when it is unstretched (black), stretched with 1.2× (red) and 1.6× (blue) stretching factor. RLS spectra (a) before and (b) after normalising by the area beneath the spectra. (c) RLD spectra.	127
<b>Fig. 6.5</b>	LD spectra of anthracene (40 µL) deposited on a) PE and b) PTFE (cut from thread seal tape) from a 0.1 mg/mL chloroform solution.	129
<b>Fig. 6.6</b>	RLS (black) and RLD (red) spectra of progesterone deposited on PE film overlaid with the Raman spectrum of progesterone in powder phase (cyan, the spectrum intensity diminished 11 times). Peaks labelled by an asterisk are present in both the progesterone powder spectrum and PE. Progesterone's Raman spectrum below 1000 cm <sup>-1</sup> (not shown here), like other steroids, is full of C–H bending vibrations which makes the interpretation of each peak exceedingly difficult. The powder spectrum is recorded using the Renishaw inVia instrument and the spectra of the sample deposited on PE are recorded by the BioTools spectrometer.	130
<b>Fig. 6.7</b>	Raman spectrum of DAPI in powder phase (cyan) overlaid with RLS (black) and RLD (red) spectra of the molecule deposited on PE <sup>OX</sup> . The labelled peaks by asterisks are from the PE substrate. The polyethylene negative C–H band in the spectrum works like an internal standard to confirm the aligning orientation of DAPI on PE chains.	133
<b>Fig. 6.8</b>	RLS (black) and RLD (red) spectra of 1PyCO on PE. The labelled peaks with asterisks correspond to polyethylene's C–H stretching vibrations. The spectra recorded by the RenishawinVia spectrometer.	135
<b>Fig. 6.9</b>	Calculated RLS spectra (with arbitrary, but consistent, intensity scale), and calculated RLD spectra (with arbitrary, but consistent, intensity scale) for anthracene oriented with the anthracene long axis at 0°, 45°, and 90° to the orientation direction.	136
<b>Fig. 6.10</b>	Different RLD spectra of anthracene deposited on PE film recorded using the BioTools spectrometer. Each spectrum is recorded by either moving the film around or preparing a new sample by depositing the molecules on a new PE film.	137

The PE spectrum has been subtracted from each anthracene spectrum. The spectra are displaced to present the change in the peak directions more clearly.	
<b>Fig. 6.11</b> Schematic structure of anthracene with its vibration directions along its long (red) and short axis (blue).	139
<b>Fig. 6.12</b> Molecular structures of a) thymine, b) thymidine and c) thymidine 5'-monophosphate with their longest axes shown in red.	140
<b>Fig. 6.13</b> The RLS (black) and RLD (red) spectra of a) thymine, b) thymidine and c) thymidine 5'-monophosphate deposited on 1.8 $\times$ stretched PE <sup>OX</sup> . The peaks labelled by asterisks are from polyethylene vibrations.	141
<b>Fig. 6.14</b> Molecular structures of a) cytosine, b) cytidine and c) cytidine 5'-monophosphate with their longest axes shown in red.	143
<b>Fig. 6.15</b> The RLS (black) and RLD (red) spectra of a) cytosine, b) cytidine and c) cytosine 5'-monophosphate deposited on 1.8 $\times$ stretched PE <sup>OX</sup> . The peaks labelled by asterisks are from polyethylene vibrations.	144
<b>Fig. 6.16</b> The schematic structure for methyl 3a-acetoxy-d 7,9(11)-choladienate with the RLS (black) and RLD (black) spectra of the molecule deposited on a 1.8 $\times$ stretched PE <sup>OX</sup> . The peaks labelled with asterisks are from polyethylene vibrations. The red line on the structure presents the molecule's long axis. (However, there are free rotations along chain C–C bonds.)	146
<b>Fig. 6.17</b> The absorbance, LD and LD <sup>r</sup> spectra of 2,2':5',2"-terthiophene deposited from a 0.3 mg/mL methanolic solution onto 1.8 $\times$ stretched PE <sup>OX</sup> overlaid with the schematic chemical structure of the molecule with its transition moment directions labelled on it with red arrows.	149
<b>Fig. 6.18</b> The RLS (black) and RLD (red) spectra of 2,2':5',2"-terthiophene deposited on 1.8 $\times$ stretched PE <sup>OX</sup> . The peaks labelled by asterisks are from polyethylene vibrations.	150
<b>Fig. 6.19</b> The absorbance, LD and LD <sup>r</sup> spectra of 1,10-phenanthroline deposited on 1.8 $\times$ stretched PE <sup>OX</sup> overlaid with the schematic chemical structure of the molecule with its transition moment direction labelled on it with red arrow.	152
<b>Fig. 6.20</b> The RLS (black) and RLD (red) spectra of 1,10-phenanthroline deposited on 1.8 $\times$ stretched PE <sup>OX</sup> . The peaks labelled by asterisks are from polyethylene vibrations.	153
<b>Fig. 6.21</b> The schematic chemical structures of a) fluorene and b) fmoc chloride.	154
<b>Fig. 6.22</b> The RLS spectra of fluorene (black) and fmoc chloride (red) with their corresponding RLD spectra (blue and purple respectively). The peaks labelled by asterisks are from polyethylene vibrations.	155
<b>Fig. 7.1</b> Three general ways a guest molecule interacts with lipid vesicles: a) inserting between the phospholipid molecules, b) lying on the surface of the vesicle and c) being captive inside the vesicle.	161
<b>Fig. 7.2</b> Chemical structures of a) DPPC, b) retinol, c) retinal and d) abietic acid.	162
<b>Fig. 7.3</b> LD spectra of retinol (0.4 mg/mL, 35–40 $\mu$ L) deposited on a) PE <sup>OX</sup> and c) PE stretched to different lengths (from unstretched to the stretching factor of 2.2 $\times$ ). b) and d) LD <sup>r</sup> spectra respectively correspond to a) and c) overlaid with absorbance and LD spectra of the sample deposited on 1.8 $\times$ stretched films. e)	168

	and g) LD spectra by the factor of rotation when the film ( $\text{PE}^{\text{OX}}$ and PE respectively) is stretched $1.8\times$ . f) and h) signals from e) and g) respectively at 370 nm as a function of rotation angle $\chi$ overlaid on a plot of $\cos(2\chi)$ .	
<b>Fig. 7.4</b>	LD spectra of retinal (0.4 mg/mL, 35–40 $\mu\text{L}$ ) deposited on a) $\text{PE}^{\text{OX}}$ and c) PE stretched to different lengths (from unstretched to the stretching factor of $2.2\times$ ). b) and d) $\text{LD}'$ spectra respectively corresponding to a) and c) overlaid with absorbance and LD spectra of the sample deposited on $1.8\times$ stretched films. e) and g) LD spectra by the factor of rotation when the film ( $\text{PE}^{\text{OX}}$ and PE respectively) is stretched $1.8\times$ . f) and h) signals from e) and g) respectively at 370 nm as a function of rotation angle $\chi$ overlaid on a plot of $\cos(2\chi)$ .	169
<b>Fig. 7.5</b>	LD spectra of abietic acid (0.4 mg/mL, 35–40 $\mu\text{L}$ ) deposited on a) $\text{PE}^{\text{OX}}$ and c) PE stretched to different lengths (from unstretched to the stretching factor of $2.2\times$ ). b) and d) $\text{LD}'$ spectra respectively correspond to a) and c) overlaid with absorbance and LD spectra of the sample deposited on $1.8\times$ stretched films. e) and g) LD spectra by the factor of rotation when the film ( $\text{PE}^{\text{OX}}$ and PE respectively) is stretched $1.8\times$ (the polyethylene baseline of spectra in the figure g is not subtracted and only manually corrected using OriginLab software's baseline subtraction tool). f) and h) 370 nm signals from e) and g) respectively overlaid on a plot of $\cos(2\chi)$ .	171
<b>Fig. 7.6</b>	RLS (black) and RLD (red) spectra of a) retinol and b) retinal (on polyethylene film) overlaid with their powder spectra (cyan, the spectrum intensity diminished for presenting purposes). Peaks labelled by an asterisk are from polyethylene vibrations.	174
<b>Fig. 7.7</b>	The RLS and RLD spectra (black and red solid lines respectively) of abietic acid deposited on polyethylene film overlaid with the unpolarised powder spectrum (cyan). The long frequency region of the spectrum is magnified 10 times.	175
<b>Fig. 7.8</b>	DSC thermograms illustrating the effect of retinals and abietic acid on gel→liquid/crystalline transitions of DPPC.	177
<b>Fig. 7.9</b>	Simulated models for interactions between retinol, retinal and abietic acid with DPPC molecules in a bilayer system (top) with their corresponding zoomed in ball-and-stick models (bottom).	179
<b>Fig. 7.10</b>	LD spectra of retinal deposited on a) $\text{PE}^{\text{OX}}$ (then stretched from $1.4\times$ to $2.0\times$ stretching factor) and b) quartz plate when the plate's surface was placed perpendicular to the direction of beam light (black line) and when it was a bit tilted (red line).	181
<b>Fig. 7.11</b>	RLS and RLD spectra of DPPC vesicles (magenta and blue dashed lines respectively) and DPPC vesicles containing guest molecules: (a) retinol, b) retinal and c) abietic acid (with 1:4 lipid to retinoid molar ratio) dried on $\text{PE}^{\text{OX}}$ (black and red solid lines respectively). d) The RLS spectra of retinoids (powder: thin solid line, deposited on $\text{PE}^{\text{OX}}$ : thick solid line, and embedded into DPPC vesicles deposited on $\text{PE}^{\text{OX}}$ : dashed line). The $1500\text{--}1850\text{ cm}^{-1}$ region of the spectra is selected to present as the rest is dominated by polyethylene peaks. The intensity for DPPC spectra (dashed magenta and blue) has been normalised in this diagram.	182
<b>Fig. 8.1</b>	Molecular structures of a) fluorene, b) Fmoc-Cl, and c) Fmoc-GRDS with probable fluorene orientation axes in stretched polyethylene films as deduced from reduced linear dichroism spectra.	188

<b>Fig. 8.2</b>	a) Absorbance spectra (0.1 mg/mL in 1 mm pathlength cuvettes) of fluorene and Fmoc-Cl in methanol, Fmoc-Cl on PE film (dried sample) GRDS and Fmoc-GRDS in water. b) CD spectra of GRDS, Fmoc-GRDS(RT) and Fmoc-GRDS(FT) (0.1 mg/mL, 1 mm path length), GRDS, Fmoc-GRDS(RT) spectra are smoothed (30 points with 3 polynomial order).	192
<b>Fig. 8.3</b>	a) Polyethylene stretched film absorbance, LD, and LD' spectra of fluorene, b) polyethylene stretched film absorbance, LD, and LD' spectra of Fmoc-Cl and LD of Fmoc-GRDS, c) solution absorbance (0.5 mm pathlength), couette flow LD, scattering corrected LD (a = 92000 and k = 3) and LD' of Fmoc-GRDS(FT).	193
<b>Fig. 8.4</b>	ATR FTIR spectra of fluorene and Fmoc (0.5 mg/mL) in methanol, GRDS (100 mg/mL) and Fmoc-GRDS (0.1 mg/mL respectively, sonicated or for 10 minutes at 55–60°C) in water.	196
<b>Fig. 8.5</b>	a) Raman spectra of fluorene and Fmoc powders (with 785 nm laser, 30 scans). b) Raman spectra (collected with samples placed on a quartz plate) of Fmoc powder (Fmoc (785 nm laser, 30 scans), Fmoc-GRDS(FT) (100 mg/mL, 785 nm laser, 100 scans), Fmoc-GRDS powder (633 nm laser, 100 scans) and GRDS powder (633 nm laser, 100 scans).	197

## List of Tables

<b>Table 2.1</b>	Carbon 1s orbital XPS data for PE and PE <sup>OX</sup> . 30° denotes 30° angle of beam incidence. 90° denotes perpendicular incidence (so maximum penetration).	21
<b>Table 2.2</b>	Angles between DAPI transition moments and the orientation axis in the PVA data of Kubista et al. and the PE <sup>OX</sup> data of this work. PE <sup>OX</sup> LD <sup>r</sup> data are for 1.8×stretch. The directions illustrated in Fig. 2.12 are consistent with both data sets.	34
<b>Table 2.3</b>	LD <sup>r</sup> data for 1-pyrenecarboxaldehyde on PE and PE <sup>OX</sup> at 1.8×stretch, literature transition polarizations for pyrene, and PyCO transition moment polarizations ( $\pm 3^\circ$ ) with respect to the PE <sup>OX</sup> z as illustrated in Fig. 2.9 (+ denotes anticlockwise rotation as illustrated).	37
<b>Table 3.1</b>	Approximate effective polarizations (error is of the order of 5%) of the vibronic components of the 379 nm B <sub>2u</sub> vibronic progression of anthracene, and the fractions of short axis and long axis electronic contributions to the total determined from 1.8× stretch data in Fig. 3.4b assuming the 254 nm band is long axis polarised. Calculations are performed on the centre of each band from low energy half height to high energy half height. The fraction of the a <sub>g</sub> progression is fraction of intensity that is due to the short axis polarized component assuming the same oscillator strength for the two components.	48
<b>Table 3.2</b>	Different component spectra identified in the anthracene film LD spectra of Fig. 4.3. ‘Large’ indicates where the long wavelength region has enhanced intensity relative to the 250 nm region. Vibronic progressions are indicated where they are apparent. Sh denotes shoulder.	49
<b>Table 3.3</b>	The calculated angles between long axis and short axis of dimer units presented in the Fig. 3.10 and 3.11.	62
<b>Table 5.1</b>	Longpass filter cut-offs used to record FDLD spectra of each sample.	87
<b>Table 5.2</b>	The absorption and emission wavelengths of DAPI from the literature compared with the data we recorded in our laboratory.	89
<b>Table 5.3</b>	The angles between the long axis and the short axis of each dimer units. To estimate the angles we assumed the long axis horizontal and then calculated the angles between two dimer units. The numbers in front of each configuration in the table below refer to the models in the Fig. 5.24–27.	112
<b>Table 6.1</b>	List of samples and spectrometers used to produce the RLD spectra.	121
<b>Table 6.2</b>	The Raman band frequency and RLD direction (Fig. 6.3) with the assignment of PE Raman peaks. Abbreviation: sym: symmetrical, asym: asymmetrical.	123
<b>Table 6.3</b>	The Raman band frequency and RLD direction (Fig. 6.4c), with the assignment, of PTFE Raman peaks. Abbreviation: sym: symmetrical, asym: asymmetrical.	127
<b>Table 6.4</b>	The band frequency, RLD direction (Fig. 6.6), and assignments of progesterone Raman peaks. The frequencies labelled in red are present in	131

	both progesterone (powder and sample deposited on PE film) and polyethylene. Abbreviation: str: stretching, bend: bending.	
<b>Table 6.5</b>	The Raman band frequency and RLD direction (Fig. 6.7) with the assignment of DAPI Raman peaks. The band at 2879 cm <sup>-1</sup> labelled with red is present in polyethylene. Abbreviation: str: stretching.	132
<b>Table 6.6</b>	1-PyCO Raman band frequencies with their RLD directions (Fig.6.8). The frequencies labelled with red are arise from PE film C–H stretching vibrations.	134
<b>Table 6.7</b>	Anthracene Raman frequencies in powder phase and dried on PE film compared with literature along with the assignment for each vibration.	136
<b>Table 6.8</b>	Anthracene's RLD peak directions for calculated and recorded spectra for each peak. The first three rows correspond the RLD peak directions of calculated anthracene spectra when the molecule is aligned 0 (bold black), 45 (bold red) and 90 (bold blue) degrees in respect to the orienting direction. The rest are related to the RLD spectra shown in Fig. 6.10. The bold spectra are the ones with similar RLD directions to the calculated spectra.	138
<b>Table 6.9</b>	The RLS peak wavenumbers, their corresponding RLD signs (Fig. 6.13) and assignments for thymine, thymidine and thymine 5'-monophosphate. The frequencies labelled by red are related to vibrations from polyethylene. Abbreviations: str (stretching), bend (bending), def (deformation), sym (symmetrical) and asym (asymmetrical).	142
<b>Table 6.10</b>	The RLS peak wavenumbers, their corresponding RLD signs (Fig. 6.15) and assignments for cytosine, cytidine and cytidine 5'-monophosphate. The frequencies labelled by red are related to vibrations from polyethylene. Abbreviations: str (stretching), bend (bending).	145
<b>Table 6.11</b>	The RLS wavenumber peaks with their corresponding RLD signal signs (Fig. 6.16) and assignments for methyl 3a-acetoxy-d 7,9(11)-choladienate. Abbreviations: str: stretching, def: deformation, sym: symmetrical, asymm: asymmetrical.	147
<b>Table 6.12</b>	The RLS wavenumber peaks with their corresponding RLD signal signs (Fig. 6.18) and assignments for 2,2':5',2''- terthiophene. Abbreviations: str: stretching, def: deformation, sym: symmetrical, asymm: asymmetrical.	151
<b>Table 6.13</b>	The RLS wavenumber peaks with their corresponding RLD signal signs (Fig. 6.20) and assignments for 1,10-phenanthroline. Abbreviations: str: stretching, def: deformation, sym: symmetrical, asymm: asymmetrical.	153
<b>Table 6.14</b>	The RLS wavenumber peaks with their corresponding RLD signal (Fig. 6.22) signs and Assignments for fluorene and Fmoc chloride. Abbreviations: str: stretching, bend: bending, def: deformation, asymm: asymmetrical.	155
<b>Table 7.1</b>	The S value of retinol and retinal deposited on PE and PE <sup>OX</sup> (determined by assuming the transition moment of the molecule is parallel to the stretching direction (a=0)).	168
<b>Table 7.2</b>	The band frequency, RLD direction, and assignments of retinol and retinal's Raman peaks. The frequencies labelled in red are polyethylene vibrations. Abbreviation: str: stretching, bend: bending, UT: unmethylated trans mode.	174
<b>Table 7.3</b>	The band frequency, RLD direction, and assignments of abietic acid's Raman peaks. The frequencies labelled in red are polyethylene vibrations. PE:	176

polyethylene, Abbreviation: str: stretching, bend: bending, scissors: scissoring vibrations.

<b>Table 7.4</b>	Transition temperatures (T <sub>c</sub> ) of pure DPPC and DPPC/retinoids and DPPC/abietic acid (0.1 molar fraction).	177
<b>Table 7.5</b>	The calculated affinity energies of retinol, retinal and abietic acid with DPPC molecules obtained from Autodock Vina program package.	180



## Acknowledgements

It is a great pleasure to thank everyone who has helped me during my PhD project at the University of Warwick. First and foremost, I would like to express my sincere gratitude to my supervisor, Prof. Alison Rodger. Without her help, guidance, patience, enthusiasm and encouragement, this study would not have been possible. It has been an honour to be her student and a privilege to work under her supervision. Her time and effort is deeply appreciated.

I am grateful for the help received from Dr. Patrycja Kowalska during the preliminary stages of this work. I would like to thank Dr. Nikola Chmel, who has been always available to help me throughout my research, and my colleagues in the Biophysical Chemistry lab: Don Praveen Amarasinghe, Claire Broughton, Glen Dorrington, Vince Hall, Joe Jones, Daniela Patrícia Lobo, Caroline Montgomery, Vidya Muthukumar, Steve Norton, Meropi Sklepari and Alan Wemyss. I especially want to thank Alan for his help in developing the fluorescence detected linear dichroism theory. I want to thank the project students who I had the privilege to assist during their MSc, MChem and MOAC projects, for helping me in collecting data: Yi Zou, Amie Roberts, Haydn Little, Don Praveen Amarasinghe, Xuning Wang, Sharon Molineux and Scott Clarke.

I am also very grateful to Dr. Shirin Jamshidi, for providing me with computational modelling data used to support the experimental results of this work, Dr. Marc Walker, for running the X-ray photoelectron spectroscopy experiments, Dr. Richard Walton for his help with X-ray diffraction experiments, Dr. Christopher Kay for his help with NMR experiments, and Anish Mistry for synthesising the olympicene compound for our LD and FDLD experiments.

I would like to take this opportunity to thank everyone who has helped and collaborated with me in writing papers published during this project: Prof. Alison Rodger, Prof.

Laurence A. Nafie, Prof. James R. Cheeseman, Dr. Patrycja Kowalska, Dr. Nikola Chmel,  
Dr. Matthew Gibson, Dr. Tim Daffron, Haydn Little and Yi Zou,

I want to thank the University of Warwick, for letting me using the equipment at the City Advanced Materials 2 and Materials and Analytical Sciences (MAS) facilities, and BioTools for building the custom-made polarised Raman spectrometer we designed.

I would like to acknowledge all my past and present friends and colleagues who supported me throughout this work. I thank Yi Zou, Bushra Qamar, Dr. Huilin Li, Dr. Jason Nurse, Anish Mistry, Rozbeh Bonyadi, Yeganeh Bonyadi, Siavash Esfahani, Ling Pei Ooi, Salisa Yuktan, Alaina Emmanuel, Polina Dimitriou and Amanda Vuong.

I am deeply grateful to my parents and my brother and my sister-in-law for their unconditional love and support through all these years. I also want to thank my long-time friend Zahra Tajik and all my friends back home; especially Mahyar Emami Moghadam and Farzaneh Basiri.

## Declaration

This thesis is submitted to the University of Warwick in support of my application for the degree of Doctor of Philosophy. It has been composed by myself and has not been submitted in any previous application for any degree.

The work presented (including data generated and data analysis) was carried out by the author in the Department of Chemistry at the University of Warwick between November 2010 and September 2014. This work is all my own except where acknowledged at the start of individual chapters and within the text.

The content has not previously been published, except as detailed in the publications listed below:

1. Razmkhah, K., et al., *Oxidized polyethylene films for orienting polar molecules for linear dichroism spectroscopy*. Analyst, 2014. **139**(6): p. 1372-1382.
2. Razmkhah, K., et al., *Optical properties of xanthene based fluorescent dyes studied by stretched-film linear dichroism*. RSC Adv., 2014. **4**: p. 37510-37515.
3. Zou, Y., et al., *Spectroscopic signatures of an Fmoc-tetrapeptide, Fmoc and fluorene*. RSC Advances, 2013. **3**(27): p. 10854-10858.



## Abbreviations

§	Chapter
$\mu$	Micro, $10^{-6}$
$\Delta H$	Enthalpy difference
$\nu$	Frequency
A	Absorbance
Asym	Asymmetrical
Bend	Bending
CCD	Charge-coupled device
CD	Circular dichroism
$\text{CHCl}_3$	Chloroform
Choladienate	methyl 3alpha-acetoxy-delta 7,9(11)-choladienate
$\text{cm}^{-1}$	Wavenumber
CMP	Cytidine 5'-monophosphae
DAPI	4',6-diamidino-2-phenylindole
Def	Deformation
DNA	Deoxyribonucleic acid
DSC	Differential scanning calorimetry
DPPC	Dipalmitoylphosphatidylcholine
Fig	Figure
FDLD	Fluorescence detected linear dichroism
Fmoc	Fluorenylmethyloxycarbonyl
FT	Fibre-forming temperature
FTIR	Fourier transform infra-red
GRDS	Glycine-arginine-aspartic acid-serine
LD	Linear dichroism
$\text{LD}^r$	Reduced linear dicroism
LMV	Large multilamellar vesicles
MeOH	Methanol
mW	Mili Watts
nm	Nanometer, $10^{-9}$

NMR	Nuclear magnetic resonance
PE	Polyethylene
PE <sup>OX</sup>	Oxidised polyethylene
PTFE	Polytetrafluoroethylene
PNA	Peptide nucleic acid
PVA	Polyvinylalcohol
PyCO	1-Pyrenecarboxaldehyde
RLS	Raman linear sum
RLD	Raman linear difference
RT	Room temperature
s	Second
S	Solution
Str	Stretching
Sym	Symmetrical
T <sub>c</sub>	Crystallisation temperature
TMP	Thymidine 5'-monophosphate
UT	Unmethylated trans mode
XPS	X-ray photoelectron spectroscopy
XRD	X-ray diffraction

## Summary

The alignment of the bonds in a molecule or the orientations that individual molecules take with respect to each other in a macromolecular structure is of significant importance to understanding the molecular mechanics and the nature of their interactions with their environment. There are a variety of different techniques available to investigate this matter.<sup>1,2</sup> In comparison with other widely used techniques such as crystallography and fibre diffraction, linear dichroism (LD) is simpler to apply, less time-consuming and also gives useful information about the transition polarisations.<sup>3–5</sup> In the preliminary stages of this work, we tried to optimise the technique in order to collect data of higher quality than had been previously possible for a wide range of different types of molecules with different characteristics. We invented a new method of orienting polar and slightly-polar molecules by changing the surface of polyethylene (PE) films to have oxygen groups on them, making PE<sup>OX</sup>. Then we tried to combine the improved orientation and LD spectroscopy techniques with fluorimetry to make fluorescence detected linear dichroism (FDLD) to increase the sensitivity and selectivity of our experiments. As all UV-visible spectroscopy techniques, including LD and FDLD, are limited by the small number of UV-active functional groups (chromophores) in molecules, we then turned to vibrational spectroscopy techniques. In particular, we have worked on a new type of polarised Raman spectroscopy - Raman Linear Difference (RLD) spectroscopy. The first RLD spectra had been published in 2011.<sup>6</sup> In this work, we used our new PE<sup>OX</sup> films and the new Raman spectroscopic technique to study the alignment of molecules in the vibrational realm. After recording high resolution polarised vibrational data for a set of small molecules using a Raman microscopy system, we designed a new polarised Raman spectrometer which was built in the final stages of this project. We evaluated the newly built instrument by repeating polarised Raman experiments we had performed on the microscope system and found that the results were a significant improvement.







# **Chapter One**

## Introduction



To know the orientation that molecules take with respect to the environment they are in could open new insights onto biomechanical aspects of different biological phenomena such as interactions of drugs with DNA molecules, orientation of protein channels inside cell lipid membrane or of steroid receptors on cancer cell walls. It could also provide useful information for synthetic chemists, polymer chemists and nanotechnology engineers. X-ray crystallography, NMR experiments and spectroscopic techniques are widely used techniques to get information about the structure of molecules, the orientation of their components and their alignment with respect to other molecules in the system. Usually, X-ray crystallography requires complicated and time consuming sample preparation procedures, and NMR is limited to the size of the molecule under the study and requires professional expertise to interpret the resulting data. By way of contrast, spectroscopic techniques such as UV-visible linear dichroism, polarised infrared and polarised Raman spectroscopy require minimum sample preparation and time, providing useful information about the structure and orientation of molecules. UV-visible linear dichroism is limited by the number of distinct transitions in a molecule making polarised vibrational spectroscopy techniques with many more transitions advantageous.

The aim of this work was to develop polarised vibrational spectroscopy to obtain useful information on the orientation parameters of molecules. Raman spectroscopy has advantages over the infrared absorption spectroscopy, in the case of biological samples, which led us to develop a new polarised Raman scattering technique. In the first stages of this work we focused on optimising the sample preparation procedure to record polarised spectroscopic data. Thus, we were able to record spectra of a higher resolution than had been previously possible for a wide range of small molecules. Using UV-visible linear dichroism we compared data collected using our newly optimised technique with ones

obtained using the conventional way and data which had been reported in the literature. Besides UV-visible linear dichroism, we applied our technique to record fluorescence detected linear dichroism in order to investigate the dimerisation of a set of polycyclic aromatic hydrocarbons. Finally, using this technique with polarised Raman spectroscopy theory we had previously developed, we were able to record vibrational data on the orientation of different bonds in a set of different molecules. We also tried using the technique to study the alignment of small biomolecules imbedded into lipid bilayer systems.

As the linear dichroism and polarised Raman spectroscopy are the two main techniques developed and optimised during this work, below is a brief introduction on the techniques.

### **1.1 Linear dichroism <sup>7-9</sup>**

Linear dichroism is a UV-visible spectroscopy technique used to study the level of orientation for an aligned system. The chromophores in molecules which are intrinsically aligned or compelled to be oriented (by an external force) in one direction, absorb the linearly polarised light differently when it is polarised parallel ( $\parallel$ ) and perpendicular ( $\perp$ ) to the alignment axis. An LD spectrometer measures this small difference as is shown in Eq. 1.1:

$$LD = A_{\parallel} - A_{\perp} \quad \text{Eq. 1.1}$$

A chromophore within an aligned molecule absorbs more light when its orientation axis is oriented parallel to the polarisation of light, and hence produce a positive LD signal. In

contrast, a chromophore will absorb less light when its orientation axis is arranged perpendicular to the light polarisation, and hence producing a negative LD signal.

As discussed above, in order to have an LD signal, a molecule has to be either intrinsically oriented or is oriented during an experiment. Depending on the polarity, size and other characteristics of the molecule under the study, there are different orienting techniques.<sup>10</sup>

The shear flow force is widely used for aligning long and thin molecules such as DNA and fibre proteins.<sup>11,12</sup> The sample is placed between two concentric cylinders, one stationary and one spinning, so the induced shear flow aligns the long molecules with their long axis horizontal. Another widely used orienting technique is to use stretched polymer films for small molecules such as steroids<sup>13</sup>, polycyclic aromatics<sup>14</sup> and nucleotides<sup>15</sup>. In this technique the molecules adsorbed onto polymers surface layers and, as Fig. 1.1 shows, stretching the film, aligns the molecules imbedded between polymer's chains.<sup>8</sup>

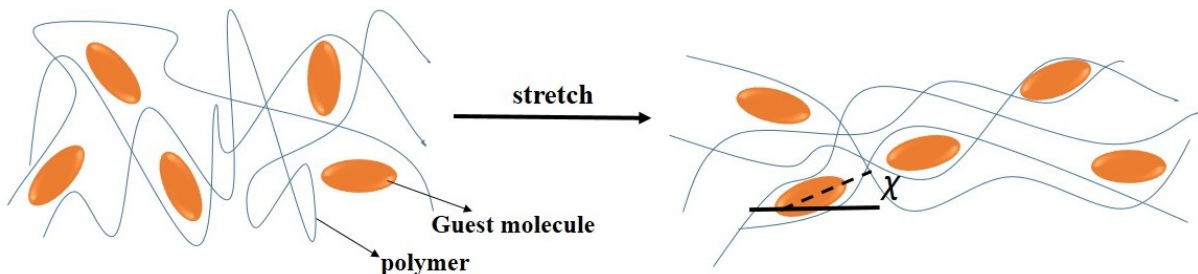


**Fig. 1.1** Schematic model for the effect of stretching on polymer chains and guest molecules imbedded between them.  $\chi$  is the angle between the long axis of average molecules and the horizon.

## 1.2 Raman spectroscopy

Vibrational spectroscopic techniques such as infra-red and Raman spectroscopy are widely used in chemistry and physics to characterise the structural features of molecules. Many

applications have been developed in art and archeology<sup>16</sup>, electronics<sup>17</sup>, and material science<sup>18</sup>. Despite providing similar vibrational information, Raman spectroscopy has some advantages over the IR spectroscopy. Apart from belonging to two different type of spectroscopy (absorbance and scattering), a key element making two techniques different is the dissimilar *selection rules* each technique follows. Thus a vibration is IR-active only if the electric field of an electromagnetic beam changes the charge distribution along the bond or in other words changes the electric dipole moment of the bond. The greater the change in the dipole moment during a vibration, the more intensive the peak in the IR spectrum. The dipole moment changes when the charge times the distance in the molecule changes. Thus symmetrical vibrations in bonds involving similar elements (such as C=C or symmetric stretches of carbon dioxide) are not IR-active as the change in their charge times distance is constant. In contrast, for a vibration to be Raman-active, it should change the shape of the electron cloud or in another words it should change the polarisability of the bond. In molecules with a centre of inversion vibrations are either Raman or IR active. In molecules of lower symmetry most vibrations are apparent in both spectra but with different intensities. A particularly useful fact for biomolecules is that the Raman scattering of H<sub>2</sub>O is small, so it does not hide the signals due to solutes. By way of contrast H<sub>2</sub>O IR-active vibrations have intense signals. These differences make Raman spectroscopy more beneficial than the IR spectroscopy when the sample under the study is in an aqueous solution or contains water (e.g. biological samples). Usually the IR spectra of such molecules contain a broad peak around 3200 cm<sup>-1</sup>, corresponding to water's O–H stretching vibrations, which obscure the C–H, N–H and O–H stretching vibrations of the sample. More importantly, water has IR absorbance intensity in the amide regions (~1650 cm<sup>-1</sup>) of the spectrum whereas Raman does not. Another advantage of Raman spectrometers over conventional IR machines is their larger frequency range from the very

near IR to the very far IR ( $7\text{--}3850\text{ cm}^{-1}$ ). IR spectrometers are more limited particularly in aqueous solution.

### 1.2.1 History and the development

Raman spectroscopy was first explained by the Indian physicist Sir C.V. Raman, when he observed light scattering through liquid and solid samples. These discoveries led to him later being awarded a Nobel Prize in 1930.<sup>19</sup> Raman developed Lord Rayleigh's explanation of the sky's colour. Formerly, Rayleigh had reported that the blue colour of the mid-day sky is due to the scattering of the blue wavelengths of the sun light by the air molecules more than red.<sup>20</sup> However, he explained that the blue colour of the sea is caused by the reflection of the sky colour. Raman and his collaborators' experiments on an Alpine glacier proved that the blue colour of the sea is also due to the light scattering.

Raman and his collaborator, K.S. Krishnan, isolated the violet light of the solar spectrum by placing a violet filter between the sun and a beaker containing different solutions (Fig. 1.2). The observed scattered light was violet in colour as was expected from the Rayleigh's law. However, after passing the scattered light through a green filter (to remove everything except green light), a weak green light was observed. This was due to the inelastic scattering of the violet incident light after hitting the solution in the beaker. This experiment was repeated for 60 different samples and the results were published in The Nature magazine in 1928.<sup>21</sup> In the following years Raman replaced sun by the mercury lamps as the source of the incident light<sup>22</sup> and used a quartz spectrograph<sup>23</sup> which allowed him to photograph the scattered light spectrum and measure its wavelengths.

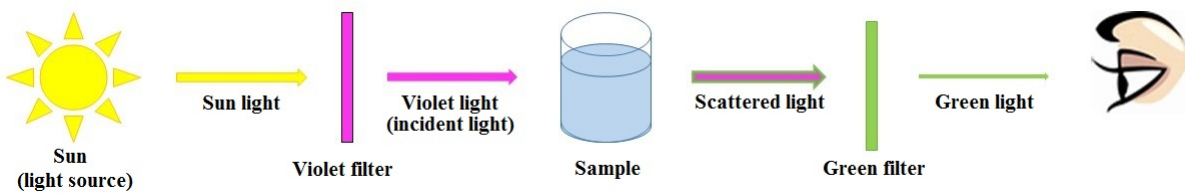


**Fig. 1.2** The schematic model for Sir C.V. Raman's early experiment on the change of the incident light colour after passing through a solution. The sun light used as the source of the light and the results were collected by visual observation.

The first commercial Raman spectrometer became available in 1953.<sup>24</sup> Since then gradual improvements have taken place in the instrumentation of the Raman spectrometer. This happened for:

- 1) the illumination source<sup>25–28</sup>, from the mercury lamps<sup>22</sup> to microwave powered lamps<sup>29</sup> and then lasers<sup>30</sup> and microchip lasers such as Nd-LSB<sup>31</sup>,
- 2) the detection system, from photographic plates to cooled cascade type RCA IP21 detector<sup>32</sup> and then photomultipliers<sup>33–35</sup> and CCD cameras (charge-coupled device), and
- 3) the optics by adding monochromators and holographic grating to reduce the stray light interference.

All the improvement and developments in Raman instrumentation made recent machines faster, more accurate, simpler and cheaper than the machine built in 1953.<sup>36</sup>

### 1.2.2 Raman scattering theory<sup>37–40</sup>

A molecular Raman vibration occurs when the energy of an electromagnetic photon changes the shape of the electron cloud around a bond. The photon's energy transfers the

bond electrons to higher ‘virtual’ (*i.e.* ill-defined due to Heisenberg’s uncertainty principle) vibrational states. The electrons remain in this so-called “excited” state for a very short period of time (about  $10^{-13}$  to  $10^{-14}$  s) so have a large energy uncertainty. Upon emitting a photon, the molecule returns (usually) to the ground electronic state, sometimes to a different vibrational level from which it started. Almost all the scattered photons have the same energy as the incident light thus returning to the starting state. Such elastic scattering is called Rayleigh scattering (Fig. 1.3a). Another type of scattering in which the energy of the scattered light is different from that of the incident light, is called Raman scattering. The Stokes and anti-Stokes are two types of this inelastic scattering. A Stokes scattering ( $10^{-6}$  the intensity of Rayleigh scattering) happens when the molecule emits a photon with smaller energy than the incident light, thus ending up in a vibrational level higher than the ground state (Fig. 1.3b). The anti-Stokes phenomenon happens even less than the Stokes scattering. It occurs when for some reason, such as high temperature, the molecule begins in a higher vibrational level than ground state. The light emitted in this situation may possess a shorter wavelength (higher energy) than the incident light (Fig. 1.3c).

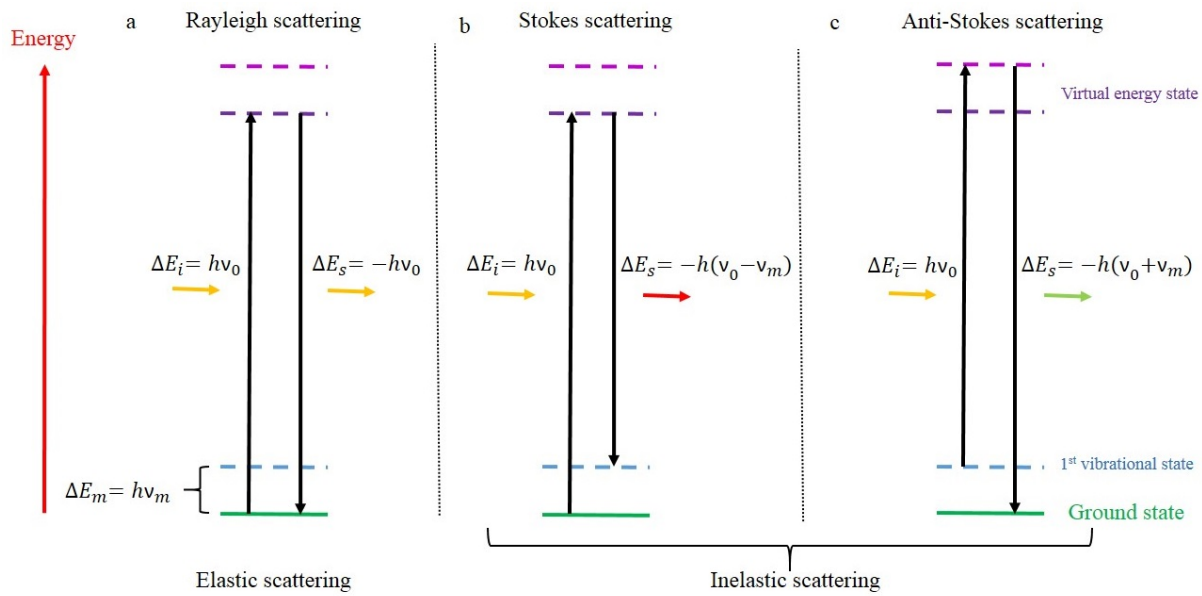


**Fig. 1.3** The schematic diagrams for a) Rayleigh, b) Stokes and c) anti-Stokes scatterings where  $\Delta E_i$  and  $\Delta E_s$  are respectively the energy of the incident and the scattered light, and  $\nu_i$  and  $\nu_s$  are the incident and scattered light frequency respectively. The frequency difference between the ground state and the first vibrational state is shown by  $\nu_m$ . In the Rayleigh scattering the energy of the incident and the scattered (emitted) lights are equal, whilst they are different in the inelastic scatterings; the scattered light has lower energy levels than the incident light in the Stokes scattering and has higher energy than the incident light in the anti-Stokes scattering.

As shown in the Fig. 1.3 the frequency difference between the ground and the first vibrational states is equal to the energy difference between the incident and the scattering lights. By blocking the wavelengths with the same frequency as the incident light with a notch filter, only the inelastic scattered light reaches the detector. The Raman machine's detector measures the difference between the incident and scattered light energies and calculates it as the Raman shift frequency ( $\text{cm}^{-1}$ ). Each molecular vibration has a different energy, due to its components and the environment, so its Raman shift ( $\nu_m$ ) is different. The computer connected to the Raman spectrometer registers each vibration as a peak with distinct Raman shift and Raman intensity.

# **Chapter Two**

## **Oxidized polyethylene films for orienting polar molecules for linear dichroism spectroscopy**

### **Acknowledgement**

XPS data were collected at the Science City Photoemission Facility, University of Warwick and contact angle measurements were performed using the Science City Advanced Materials 2 Facility. The equipment used was obtained through Birmingham Science City: Innovative Uses for Advanced Materials in the Modern World with support from Advantage West Midlands (AWM) and part funded by the European Regional Development Fund (ERDF). I would like to thank Dr. Richard Walton for his help with X-ray diffraction experiments, Dr. Marc Walker for his help with X-ray photoelastic spectroscopy experiment, and Dr. Christopher Kay and Dr. Nikola Chmel for their help with NMR data collection and analysis.



## 2.1 Introduction

As it is discussed in §1, stretched polymers, in particular polyethylene films (PE), have been used to orient small planar molecules for decades. Thulstrup et al. in 1970<sup>41</sup> concluded that it was generally agreed that most of the solute was dissolved in the amorphous parts of a PE sheet. Despite this, Wirtz et al.<sup>42</sup> concluded in 2011 that the oriented chromophores are bound to PE crystals (though with a distribution about the stretch direction) and are oriented when the crystallites to which they are bound orient. They also deduced that the crystallites become oriented along the stretching direction of a film, because the large local strain destroys the lamellae (thin extended sheets of crystallites that are typically tens of nanometers thick and tens of micrometers long) and subsequently recrystallization occurs. Thus they concluded that stretching does not cause a gradual increase in alignment of a molecule but causes the crystallite to which it is bound to orient or, at higher stretch ratios, a phase change that leads to more crystallites. We do know that molecules are likely to orient on PE with their long axes parallel to the stretching direction.<sup>43</sup> However, PE films do not orient polar or hydrophilic molecules. To solve the problem a change in the substrate to polyvinylalcohol (PVA) films is usually recommended in literature<sup>44</sup>. However, these films take days to prepare and usually involve the analyte being integrated into the polymerising film.<sup>45</sup> This makes the kind of experiments discussed below, where we vary concentration of parent solution and degree of stretch, extremely time consuming. PVA films are also very brittle and hard to stretch reproducibly.<sup>46</sup>

In this work we report the development and application of oxidised polyethylene films ( $\text{PE}^{\text{OX}}$ ) to determine transition polarizations of polar molecules with the same versatility and ease of use that is possible with PE.

## 2.2 Materials and methods

All chemicals were purchased from Sigma-Aldrich and used without further purification.

Solvents used in the measurements were 18.2 MΩ-cm water (Millipore Direct-QTM), chloroform (spectrophotometric grade, Sigma-Aldrich), methanol (Laboratory grade, Fisher Chemicals) and methyl cyclohexane (spectrophotometric grade, Sigma-Aldrich).

The PE films to be used as sample matrices were cut from Glad® Snap Lock® bags, and stretched so that the direction of stretch is parallel to the observable faint lines in the film. Stock solutions of each analyte were prepared in chloroform (for PE) or methanol (for PE<sup>OX</sup>).

### 2.2.1 Sample preparation

For most experiments, a piece of PE or PE<sup>OX</sup> film (of size  $2.5 \times 4 \text{ cm}^2$ ) was placed between two jaws of the mechanical stretcher designed for this purpose (Fig. 2.1a). The film was then stretched from 2.5 centimetres to different lengths. The analyte was sometimes added before and sometimes after stretching the film (see details in 2.3 Results and discussion). Baselines were collected on stretched films where a small volume of solvent had been dropped on and left to dry. Samples (30–40 mL in solution with the same solvent as the baseline) were placed on the stretched film, then left to evaporate creating a dried layer. The stretched film and its holder were usually placed horizontally into the spectrometer so that the light beam was incident on the analyte with the stretch direction was horizontal (in our instrument the direction of the parallel polarized light).

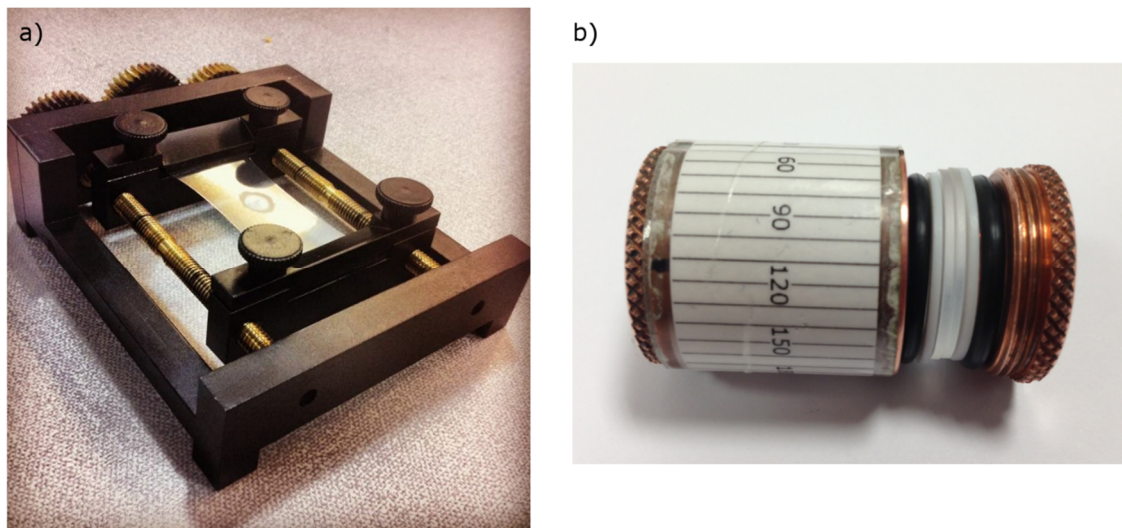


**Fig. 2.1** a) Mechanical film stretcher designed and built at the University of Warwick. b) Cylindrical film holder (originally designed for oriented circular dichroism measurements)<sup>47</sup> where film is held between two quartz plates (1 mm thick) themselves sandwiched between Teflon rings and O-rings.

In order to check for the presence of higher order structures e.g. formation of dimers or sample crystallisation on the surface of the film, several samples were routinely prepared using serial dilutions of the stock solution. In the absence of higher order structures, shapes of the obtained LD spectra are independent of concentration.

In some experiments the film was mounted in a cylindrical holder (Fig. 2.1b) and rotated to different orientations. For film-rotation LD experiments, the film was first stretched in the film stretcher, the sample added and then the film transferred (ensuring it remained stretched) to the cylindrical film holder shown in Fig. 2.1b. To secure the sample within the cylindrical film holder, the two quartz plates were placed on either side of the PE film and clamped to maintain the tension on film. The film was cut to remove excess PE film. The sandwiched film was then placed in the holder and fixed in place by a screw fitting which, when screwed fully into the holder, maintained the tension on the film.

## 2.2.2 Ultra-violet absorbance and linear dichroism spectroscopy

Ultra-violet absorbance and LD spectra on films oriented with the stretch direction parallel to the horizontally polarized light were measured using a Jasco J-815 circular dichroism spectropolarimeter adapted for LD spectroscopy by collecting LD in one data channel and A in another. In general, baselines were collected on the films before the addition of the sample. The data acquisition and baseline subtraction were performed using the J-815 Spectra Manager software version 2.07.02. The spectra of samples (and baselines) were measured as a function of different stretching lengths of polyethylene. If a single film was measured at different stretch factors, baselines were measured on three independent films treated in as close to identical fashion as was possible. All measurements for film-rotation LD were performed using a Bio-Logic MOS-450 spectrometer.

Reduced LD ( $LD^r$ ), the LD divided by the isotropic absorbance, is independent of concentration and path length (sample thickness, which can change upon stretching). The usefulness of the  $LD^r$  depends on both spectra being measured on exactly the same molecules. This requires both the film not to be moved and there not to be any unoriented molecules in the light beam whose absorbance is measured but which do not contribute to the LD. In the simple case of uniaxial orientation with the horizontal polarization of the instrument along the film stretch direction<sup>46</sup>

$$LD^r = \frac{LD}{A} = \frac{3}{2} S(3\langle \cos^2 \alpha \rangle - 1) \quad \text{Eq. 2.1}$$

where  $\alpha$  is the angle between the molecular orientation direction, z, and the polarization of the transition of interest,  $\langle \rangle$  denotes average over the population of molecules present, and  $S$  is the orientation parameter (0 for unoriented samples, 1 for perfectly oriented samples).

### 2.2.3 X-ray photoelectron spectroscopy

The X-ray photoelectron spectroscopy (XPS) data<sup>48</sup> were collected at the Science City Photoemission Facility, University of Warwick by Dr. Marc Walker. The samples investigated in this study were mounted on Omicron sample plates using electrically conductive carbon tape and loaded in to the fast-entry chamber. Once a pressure of less than  $1 \times 10^{-7}$  mbar had been achieved (approx. 1 hour), the samples were transferred to a 12-stage storage carousel, located between the preparation and main analysis chambers, for storage at pressures of less than  $2 \times 10^{-10}$  mbar. XPS measurements were conducted in the main analysis chamber (base pressure  $2 \times 10^{-11}$  mbar), with the sample being illuminated using an XM1000 monochromatic Al-K $\alpha$  X-ray source (Omicron Nanotechnology). The measurements were conducted at room temperature and at a take-off angle of 90° (more penetration depth) and 30° (closer to the surface). The photoelectrons were detected using a Sphera electron analyser (Omicron Nanotechnology), with the core levels recorded using a pass energy of 10 eV (resolution approx. 0.47 eV). Due to the insulating nature of the samples, a CN10 charge neutralizer (Omicron Nanotechnology) had to be used in order to prevent surface charging, whereby a low energy (typically 1.5 eV) beam of electrons was directed on to the sample during XPS data acquisition. The data were analysed using the CasaXPS package, using Shirley backgrounds and mixed Gaussian–Lorentzian (Voigt) line shapes. All binding energies were calibrated to the C 1s peak at 284.6 eV. The energy is calibrated weekly using the Fermi edge of a polycrystalline Ag sample is accurate to ( $\pm$ )0.02 eV. Compositional analysis of Au, Cu and Ag samples was used to give a transmission function for the analyser resulting in an accuracy of around 1%. The uncertainty in composition analysis of the system was estimated using a polycrystalline silver. We scanned four peaks and in

an ideal world they would give equal composition. In reality it is  $\pm 1\%$ , however, doing this test (known as the transmission function) allowed us to be as accurate as we could be. In terms of energy position, we will have used the charge neutraliser and then energy-referenced the data afterwards. These energies are accurate to  $\pm 0.1$  eV provided we picked a valid reference value. In any case, it is not only the absolute position, however, also the separation of components in, say, the C 1s region which we used for peak assignment.

#### **2.2.4 Contact angle measurements**

Contact angle measurements were performed using a Krüss DSA (droplet shape analyser) 100 (Krüss Instruments, Germany) on a 10 mL droplet of water dispensed onto polyethylene substrate. The Tangent-1 fitting measurement was used to yield the left and right three phase contact angles of the droplet.

#### **2.2.5 XRD measurements**

X-ray diffraction (XRD) experiments were performed on Siemens D500 diffractometer with the CuK $\alpha$  ( $\lambda$  1.5428 Å) radiation source, step  $0.02^\circ$  and step interval 20 s.

## 2.3 Results and discussion

As explained in §1 Linear dichroism, LD, is a differential absorption spectroscopy technique from which one can extract transition moment polarizations if the sample orientation is known or chromophore orientation information if transition moments have been assigned. The main work of this chapter relates to a new polymer surface for LD, PE<sup>OX</sup>. The results below describe how PE<sup>OX</sup> was produced and characterised thus enabling us to collect data on previously intractable samples.

### 2.3.1 PE<sup>OX</sup> oxidised films

Tissington, et al.<sup>49</sup>, showed that by using oxygen plasma treatment it is possible to form active oxygen-containing groups on the surface of the polyethylene film. In this work pieces of PE film ( $2.5 \times 4$  cm) were placed in a Plasma Asher and treated with two different powers (50 and 100 W) and four different timings (10, 30, 60 and 120 seconds). As Fig. 2.2 shows, the hydrophilicity of the surface increases with the duration of the treatment. However, the lower power showed higher final levels of hydrophilicity as deduced from the water contact angle (Fig. 2.2). This could be caused by the degradation of the PE fibres at high plasma power.<sup>50</sup> For our spectroscopy experiments we therefore chose to prepare films using 50 W and 1 minute and denote the treated films as PE<sup>OX</sup>.

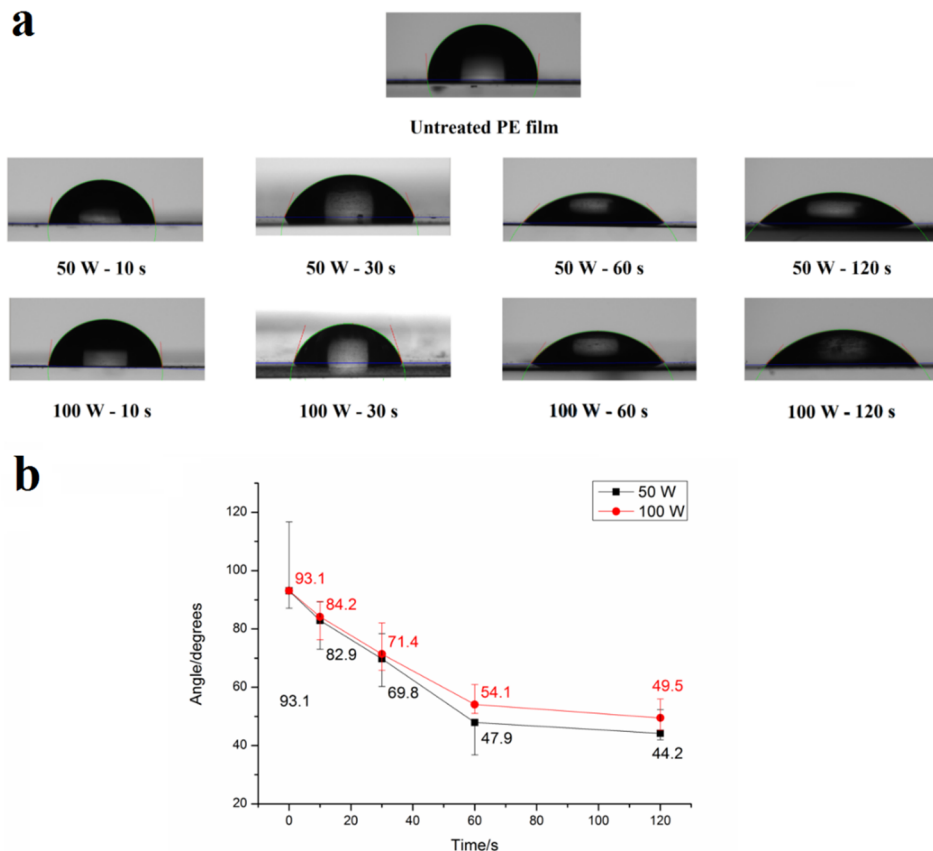


**Fig. 2.2** a) Water drops on polyethylene films treated at the indicated power levels for the indicated times. b) The contact angle of PE films placed in the plasma ashler at different power levels as a function of time.

To investigate the type and percentage of different oxygen based functional groups added on the PE films we performed x-ray photoelectron spectroscopy (XPS) experiments (performed and analysed by Dr. Marc Walker) on the treated PE films in different conditions explained above. The collected data for oxygen functional groups on PE and PE<sup>OX</sup> are summarised in Table 2.1. The 30° data are indicative of surface groups as the beam penetrates less than in the 90° configuration. The treated samples show a slight enhancement over time in carbonyls relative to OH, consistent with oxidation proceeding from alcohol, to aldehyde, to carboxylic acid. The difference as a function of angle of incidence suggests that the surface is slightly enriched with carbonyls (relative to OH) compared to the depth of the film.

**Table 2.1** Carbon 1s orbital XPS data for PE and PE<sup>OX</sup>. 30° denotes 30° angle of beam incidence. 90° denotes perpendicular incidence (so maximum penetration).

<b>Peak Energy</b>	<b>Assignment</b>	% of counts in region				
		<b>PE 90°</b>	<b>PE<sup>OX</sup> 50 W, 30 s 30°</b>	<b>PE<sup>OX</sup> 50 W, 30 s 90°</b>	<b>PE<sup>OX</sup> 50 W, 60 s 30°</b>	<b>PE<sup>OX</sup> 50 W, 60 s 90°</b>
284.6	C-C, C-H	54.70%	51.56%	49.46%	51.22%	48.44%
284.99	PET loss peak 1	27.35%	25.78%	24.73%	25.61%	24.22%
285.38	PET loss peak 2	5.47%	5.16%	4.95%	5.12%	4.84%
285.77	PET loss peak 3	0.88%	0.83%	0.79%	0.82%	0.78%
285.93	C-OH	3.57%	1.13%	8.10%	0.60%	8.55%
287.06	H-O-C-O-H [?]	0.00%	5.84%	3.46%	6.64%	4.02%
288.02	C=O	7.53%	4.39%	3.16%	3.97%	3.14%
289.31	COOH	0.51%	5.31%	5.35%	6.01%	6.02%
	Total O%	11.5%	16.5%	20.0%	17.0%	20.5%

The X-ray diffraction studies performed by Dr. Chmel seem to support the conclusion that stretching increases the crystallinity of PE.<sup>51</sup> The XRD pattern of non-stretched PE (prestretched by the manufacturer during production) and 2.0× stretched (using the LD stretcher) film are shown in Fig. 2.3. The two reflections at 22° and 24° are characteristic of the typical orthorhombic *Pnam* crystalline phase of PE.<sup>52</sup> The intensity of these reflections, however, suggests that they are not the prevalent phase in the unstretched film. The intense reflections at 14° and 17° dominate the diffractogram. There is an excellent agreement between these and other less intense reflections and the monoclinic *Cc* phase of polyisopropylene (PP),<sup>53</sup> suggesting that the film used is in fact a ethylene/propylene copolymer—with the propylene component being highly crystalline. This is further supported by the NMR analysis<sup>51</sup>, done by Dr. Chmel, which suggests that 1.5% of the film by weight is PP. There are also several less intense reflections of varying sharpness present in the diffractogram, suggesting presence of at least one more crystalline or semicrystalline phase in the sample. There are significant changes in the diffractogram after stretching 2.0×. The relative intensities of the reflections characteristic of the orthorhombic crystallites are much stronger than for an unstretched film, suggesting that

the crystallites of this structure are now prevalent in the film. The relative intensities of the  $22^\circ$  and  $24^\circ$  reflections (orthorhombic PE) have also changed after stretching suggesting a change in preferred orientation of the crystallites in the film. Other differences include appearance of new reflections at  $19^\circ$  and  $36^\circ$  as well as disappearance of a low intensity sharp reflection at  $12^\circ$ , which suggests profound changes in the relative amounts and orientations of different crystal phases present throughout the film. Using the Scherrer equation it was possible to estimate the size of the crystallites in the polymer.<sup>54</sup> The estimated values for PP crystallites do not change after stretching, while the average size of the PE crystallites decreases with stretching, which is consistent with creation of new (smaller) crystallites in the polymer.

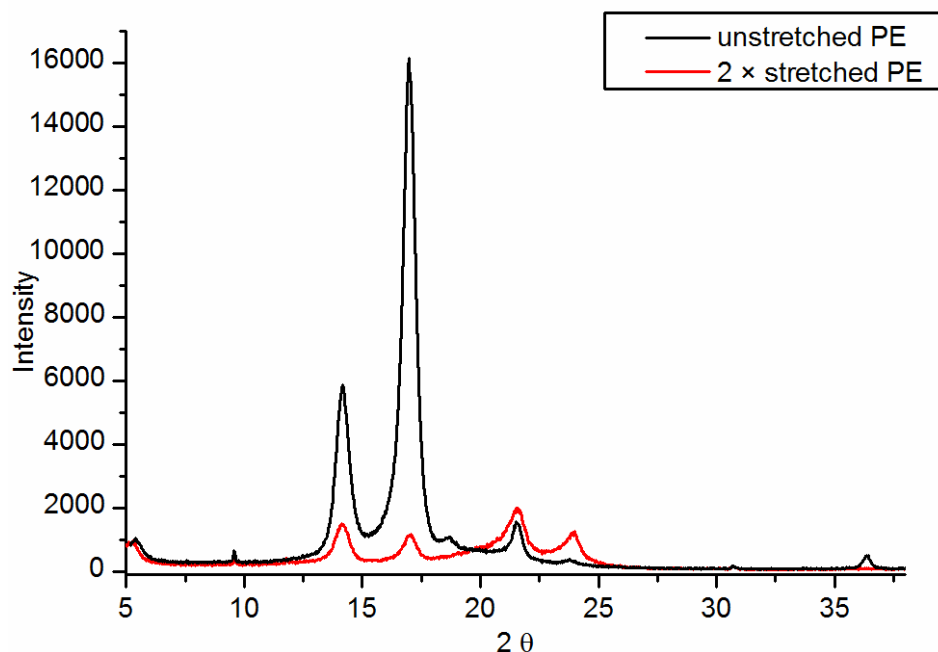


**Fig. 2.3** X-ray diffraction patterns of un-stretched and 2 $\times$  stretched PE films. The uncertainty in measurement was kept below  $0.015^\circ$ .

### 2.3.2 UV-visible studies on the interactions of molecules deposited on stretched polyethylene film

As explained before molecules adsorbed on the surface of polyethylene interact with the crystalline phase of the polymer. Thus aligning the crystalline phase, induced by stretching, would lead to orient the guest molecules. To understand the interactions between the molecules, polyethylene and the light, we performed a series of stretched polyethylene UV-visible spectrometry and LD experiments (using a BioLogic MOS-450). In this experiment we chose small planar molecule of anthracene, which will be studied in more detail in §3 as our probe molecule.

Fig. 2.4 shows the absorbance spectra for anthracene deposited on a  $1.8\times$  stretched oxidised polyethylene film recorded every 2 minutes for 2 hours after the sample was loaded on the film. The intensity of almost all peaks (Fig. 2.4b and c) increased significantly over time in the first 30 minutes after the sample was loaded. The intensity then increased in a much slower manner for 30 minutes and finally stopped after an hour from the beginning of the measurement. This enhancement is due to the slow evaporation of the solvent (methanol) and the increase of the sample concentration on the PE<sup>OX</sup> film. However, continuous exposure to the incident light of the machine triggered photolysis which led to the slow decrease in the intensity of all peaks (shown by dashed arrows in the Fig. 2.4a).

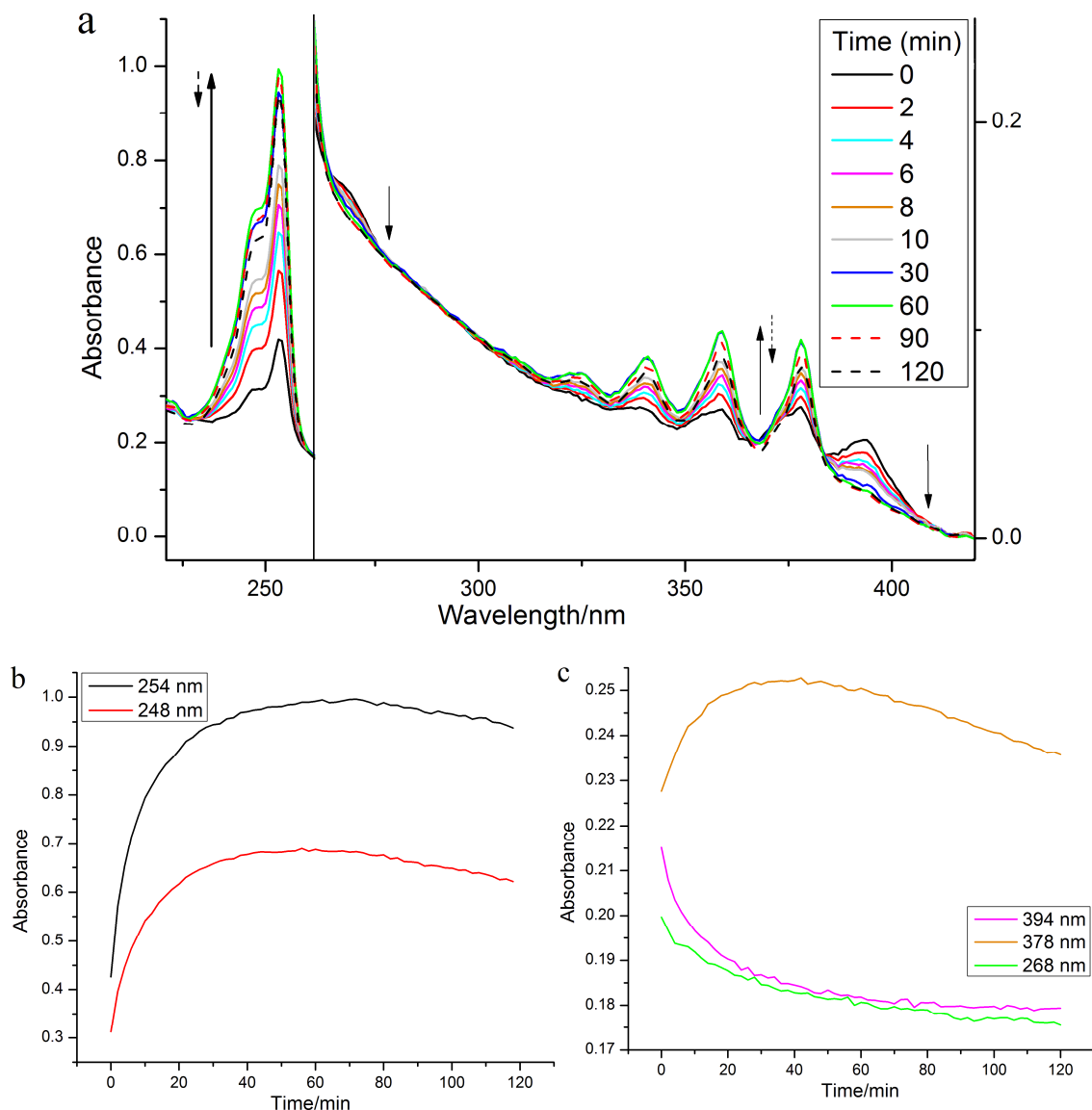
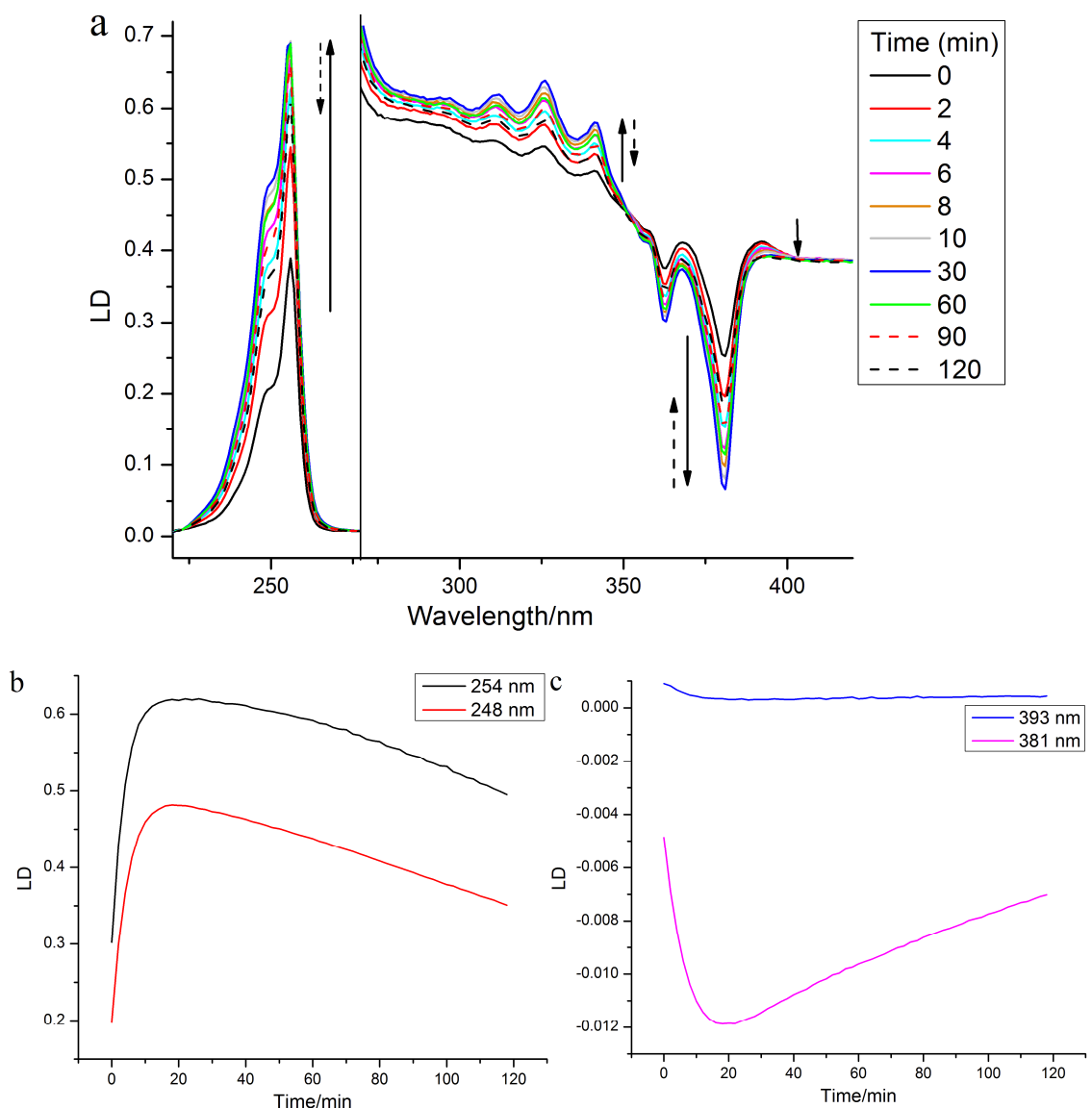


**Fig. 2.4** a) The absorbance spectra of anthracene (40  $\mu\text{L}$  from a 0.5 mg/mL methanolic solution) deposited on a 1.8 $\times$  stretched PE<sup>OX</sup> film taken every 2 minutes (time for recording one spectrum) from the first moments of sample loading for 2 hours. For presenting purposes only 10 spectra are shown (the time each spectrum is recorded is shown in the legend). The arrows show the ascending and descending trends in the peak intensity upon the time. b) and c) show the signal intensity trends upon the time of the measurement for the peaks at 254 and 248 nm (a) and 394, 378 and 268 nm (b).

Fig. 2.4 a and c show a decrease in the intensity trend for the bands at 394 and 268 nm upon time from the beginning of the experiment. These bands, which will be more studied and discussed later in §3 are arising from non-monomeric structures formed on the surface of PE<sup>OX</sup> due to the high concentration of the solution. As attraction forces between such

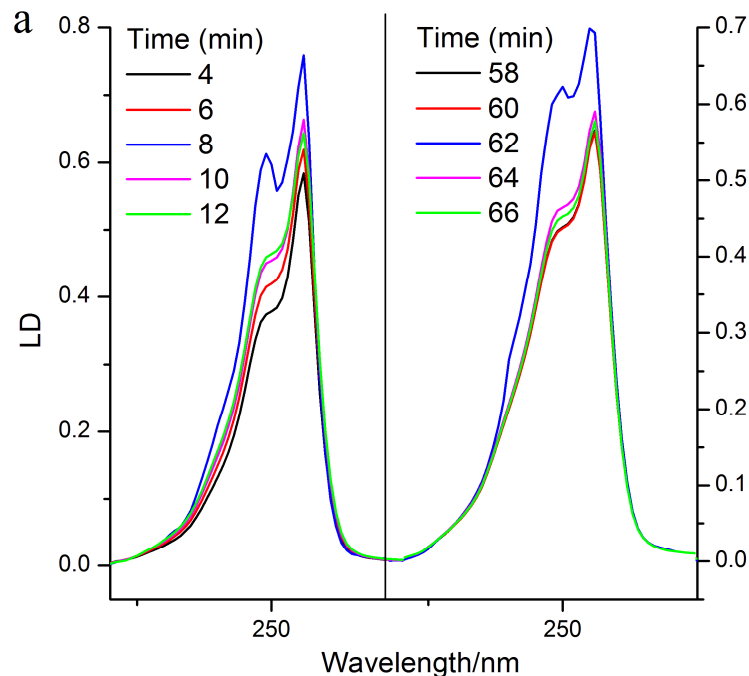
dimeric units are far weaker than molecular bindings, they undergo the photodecomposition faster than the monomeric molecules.

Linear dichroism experiments (Fig. 2.5) showed similar result to the absorbance spectroscopy: the intensity of peaks increased the first quarter of the experiment, which could be due to both enhancement in concentration and alignment of the sample, then decreased with a higher rate than absorbance signals.



**Fig. 2.5** a) The UV-visible LD spectra of anthracene (the same conditions as absorbance experiment) deposited on a 1.8 $\times$  stretched PE<sup>OX</sup> film taken every 2 minutes from the first moments of sample loading for 2 hours. For presenting purposes only 10 spectra are shown (the time each spectrum is recorded is shown in the legend). The arrows show the ascending and descending trends in the peak intensity upon the time. b) and c) show the signal intensity trends upon the time of the measurement for the peaks at 254 and 248 nm (a) and 394 and 381 nm (b).

To investigate the role of PE crystalline phase in orienting guest molecules, we performed a temperature dependent stretched polymer LD. According to J. Cowie and J. McEwen's differential scanning calorimetry data<sup>55</sup> polyethylene's glass transition temperature is –78 °C (however, depending on the density and crystallinity of the polymer it could vary to –125 °C).<sup>56</sup> Liquid nitrogen (boiling point: –196.15 °C) was used in order to decrease the temperature lower than PE's glass transition temperature. As was expected decreasing the temperature and consequently increasing the amount crystalline phase, led to an abrupt and significant enhancement in the intensity of anthracene LD peaks (Fig. 2.6).



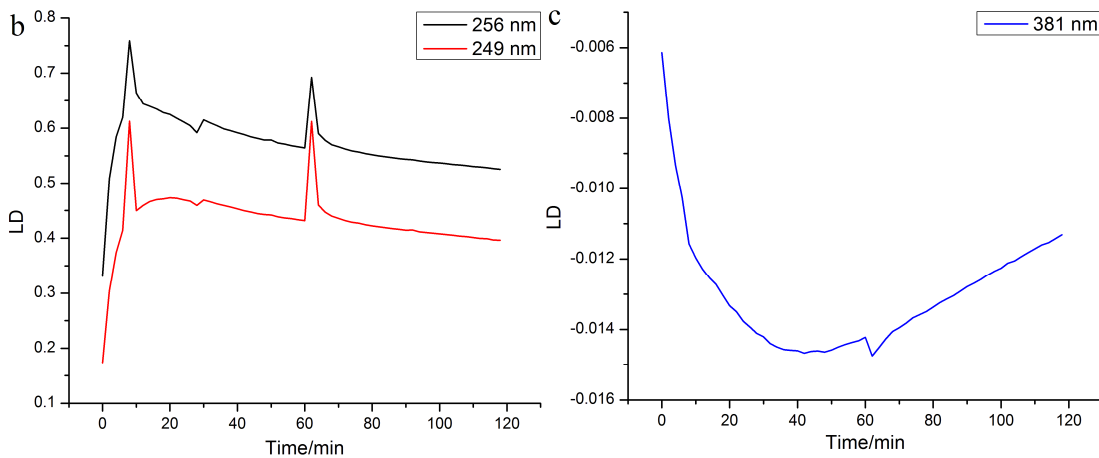


**Fig. 2.6** a) The UV-visible LD spectra of anthracene deposited on a 1.8 $\times$  stretched PE<sup>OX</sup> film taken every 2 minutes from the first moments of sample loading for 2 hours. Liquid nitrogen was poured on the stretched polymer 8 and 62 minutes after the experiment started. For presenting purposes only short wavelength region of the spectrum is shown for 10 spectra are shown (Spectra recorded between 4<sup>th</sup> and 12<sup>th</sup> minutes are shown on the left hand side and the ones recorded between 58<sup>th</sup> and 62<sup>nd</sup> minutes are shown on the right hand side). b) and c) show the signal intensity trends upon the time of the measurement for the peaks at 254 and 248 nm (a) and 381 nm (b). The jump at 28<sup>th</sup> minute in figure b could be due to a change in the ambient light.

Besides the temporary enhancement in the alignment of anthracene on PE<sup>OX</sup>, freezing the polymer helped to partly eliminate vibrational transitions in anthracene. This could be observed in Fig. 2.6a (6<sup>th</sup> and 62<sup>nd</sup> minutes, blue spectrum) where the LD peaks are become sharper and there is a slight separation between the band at 256 and its shoulder at 249 nm.

Results achieved from freezing the polyethylene encourages us to repeat the experiment and study the behaviour of the polymer when it is heated. Polyethylene is a thermoplastic polymer with high melting point (85–145 °C) so by using an industrial blow drier (generating 45°C heat) we tried to increase its amorphous phase without melting it. Fig. 2.7 shows the effect of heat on anthracene's LD spectrum. The intensity of the LD peaks decreased significantly when we heat the polymer and it returned to its natural trend quickly after the heat was removed. The LD spectra recorded when the heat was being

applied show slightly broader peaks than the rest, which could be due to a slight increase in the number of vibrational transitions occurring because of the heat.

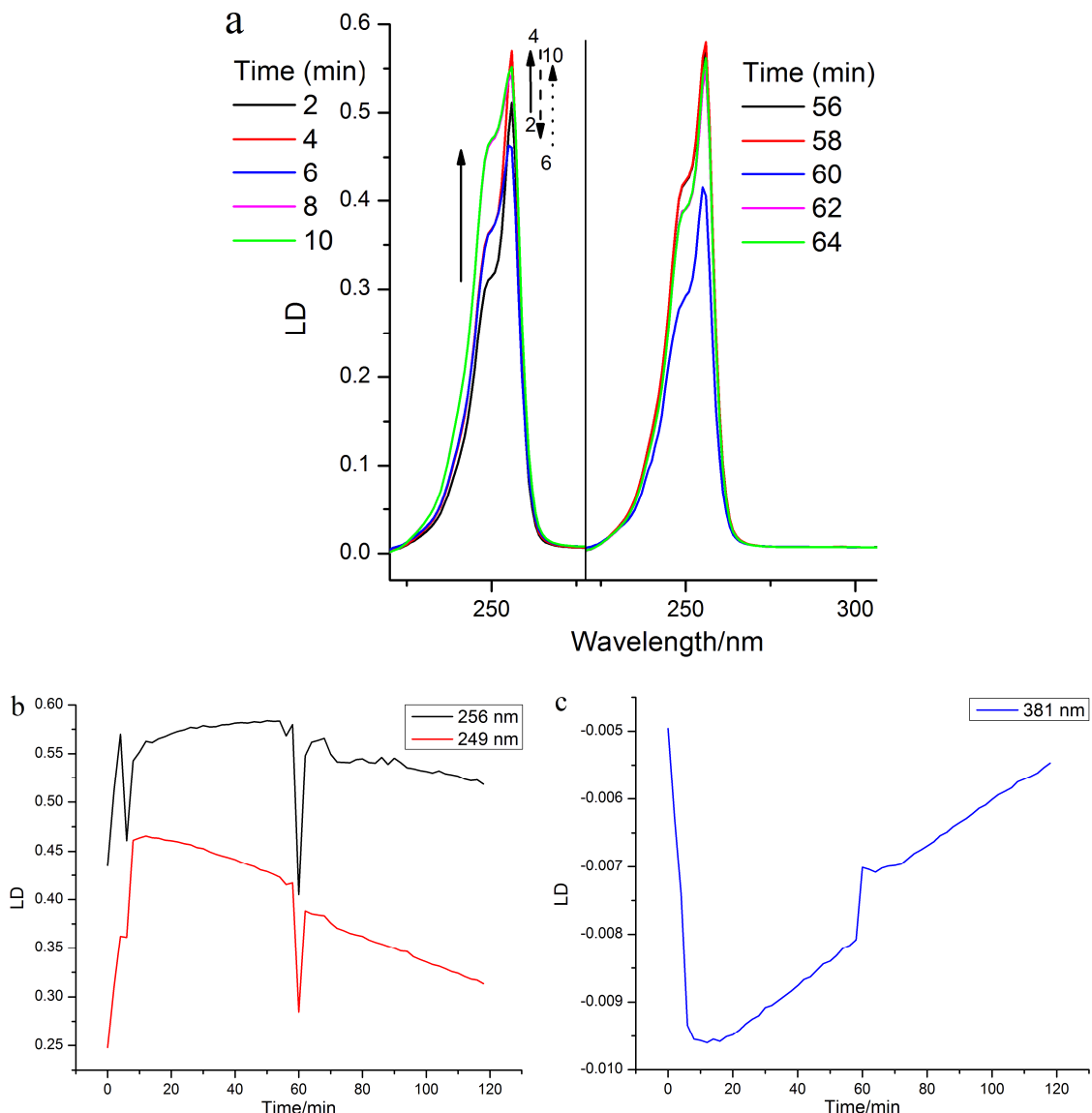


**Fig. 2.7** a) The UV-visible LD spectra of anthracene deposited on a 1.8 $\times$  stretched PE<sup>OX</sup> film taken every 2 minutes from the first moments of sample loading for 2 hours. The polyethylene was heat using a blow drier 6 and 60 minutes after the experiment started. For presenting purposes only short wavelength region of the spectrum is shown for 10 spectra are shown (Spectra recorded between 2<sup>nd</sup> and 10<sup>th</sup> minutes are shown on the left hand side and the ones recorded between 56<sup>th</sup> and 64<sup>th</sup> minutes are shown on the right hand side). b) and c) show the signal intensity trends upon the time of the measurement for the peaks at 254 and 248 nm (a) and 381 nm (b).

These experiments helped us to understand more about polyethylene's morphology, the effect of solvent and temperature on absorbance and LD spectroscopy of molecules deposited on PE.

### 2.3.3 Orienting small molecules on PE

#### 2.3.3.1 Progesterone: a medium polarity molecule that orients in the same manner on PE and PE<sup>OX</sup>

Fig. 2.8 shows the LD spectra on both PE and PE<sup>OX</sup> films of a medium polarity molecule, progesterone, with a single  $\pi-\pi^*$  transition in the accessible region of the spectrum. The progesterone spreads somewhat more uniformly on PE<sup>OX</sup> when dissolved in methanol than on PE when dissolved in chloroform which seems to have resulted in slightly better (in terms of LD<sup>r</sup>) spectra and higher orientation factor S. The LD<sup>r</sup> traces are fairly flat as expected for a single transition. If we assume that (i) the molecular orientation is uniaxial (see below for more discussion of this); (ii) the long axis is the z-axis, and (iii) the transition is polarized along the carbonyl bond, then using Eq. 2.1, S ~ 0.12 for 1.8× stretch PE and 0.13 for 1.8× stretch PE<sup>OX</sup> (with error less than %5). We can therefore conclude that PE<sup>OX</sup> orients progesterone in much the same way as PE but with marginally higher efficiency and uniformity.

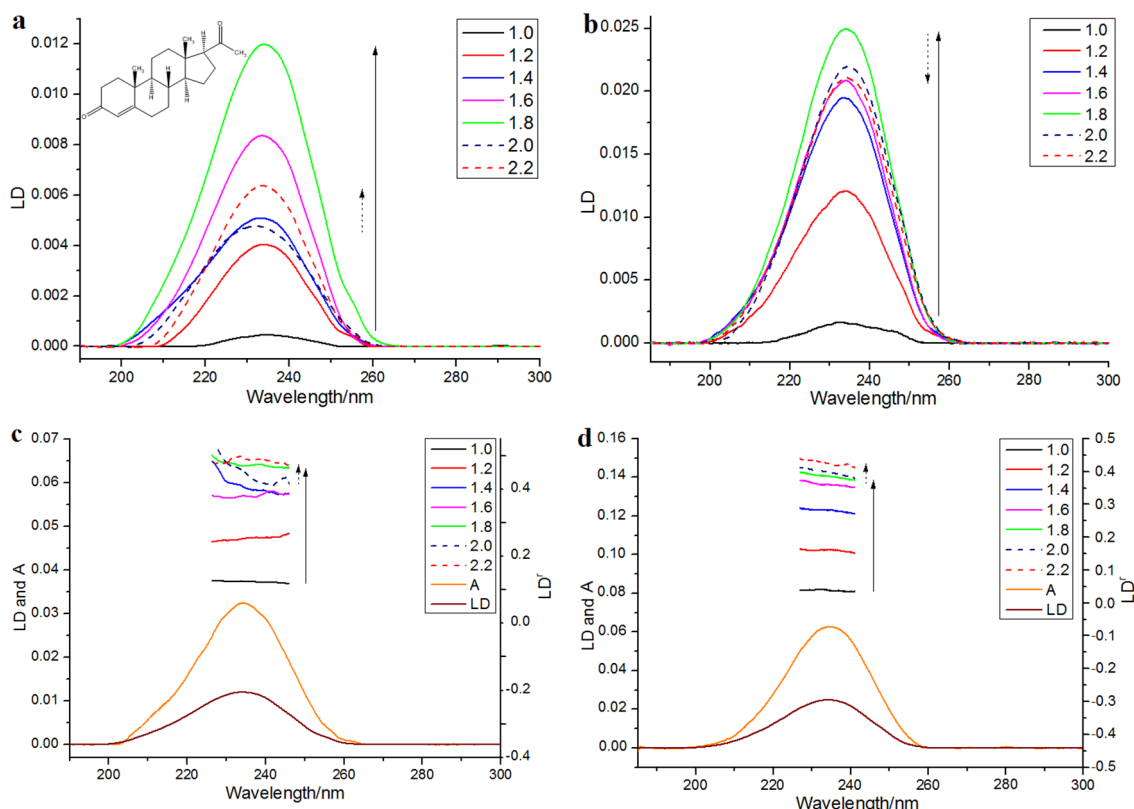


**Fig. 2.8** Spectra of progesterone (deposited from 0.65 mg/mL in chloroform for PE and methanol for PE<sup>OX</sup> and left to dry). LD on (a) PE, and (b) PE<sup>OX</sup> prestretched by factors ranging from 1 to 2.2×. (c) and (d) LD' for data from (a) and (b) respectively overlaid with absorbance and LD spectra for 1.8× stretch.

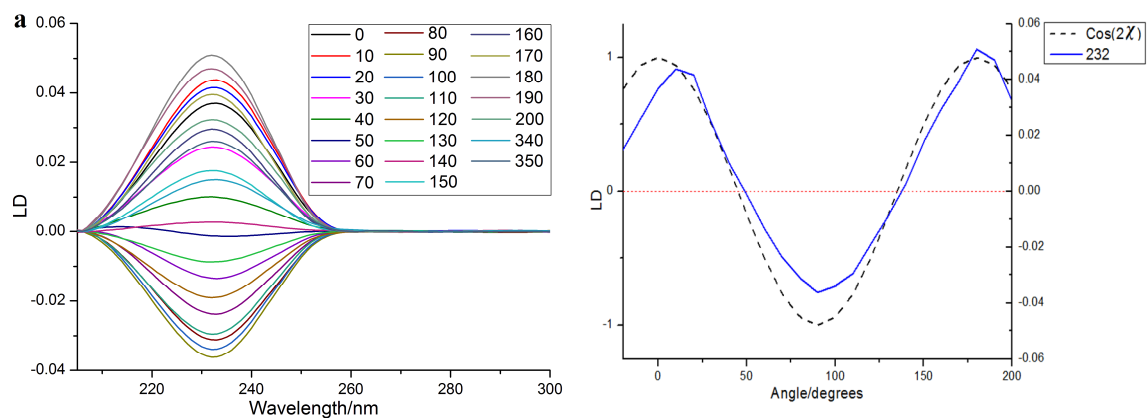
We wished to optimise the sample orientation in the films and also to check whether degree of stretching affected the spectroscopy. The progesterone spectra suggest that the maximum LD is obtained with a stretch factor of ~ 1.8 and a maximum LD' with factor of ~ 2.0 when the sample was added to a stretched film. This ran counter to our expectation that more stretching would always correspond to more orientation. For progesterone, and for the other analytes discussed below, the variation in LD' maximum proved to be due mainly to variations in the absorbance; molecules unoriented on the film absorb light but may not contribute to the LD. The film thickness did not change significantly with stretching, though the changes in the spectra do show changes in the binding of the analytes to the PE.

### 2.3.3.2 Uniaxial orientation

The analysis of LD is facilitated if we can use Eq. 2.2, which holds for uniaxially oriented samples. We have concluded<sup>51</sup> that a sample is uniaxially oriented if its LD signal depends on the rotation about the  $X$ -axis (direction of propagation of light) according to

$$\begin{aligned} LD^r &= \frac{LD}{A_{iso}} = \frac{A_z - A_Y}{A_{iso}} \\ &= \frac{3}{2}(3\langle \cos^2 \theta \rangle - 1)(3\langle \cos^2 \alpha \rangle - 1)\cos(2\chi) \\ &= \frac{3}{2}(3\langle \cos^2 \alpha \rangle - 1)\cos(2\chi) \end{aligned} \quad \text{Eq.2.2}$$

where  $\chi$  is the angle between  $Z$  (the stretch direction of the film) and the horizontal direction,  $\theta$  is the angle between  $z$  (the molecular orientation axis) and  $Z$ , and  $A_{iso}$  is the isotropic absorbance. If there are multiple populations of molecules or less symmetric orientation mechanisms, then a different function of  $\chi$ ,  $\alpha$ , and  $\theta$  is observed. Thus, we can use plots of  $LD$  as a function of  $\chi$  to determine whether a molecule is uniaxially oriented (Fig. 2.9).



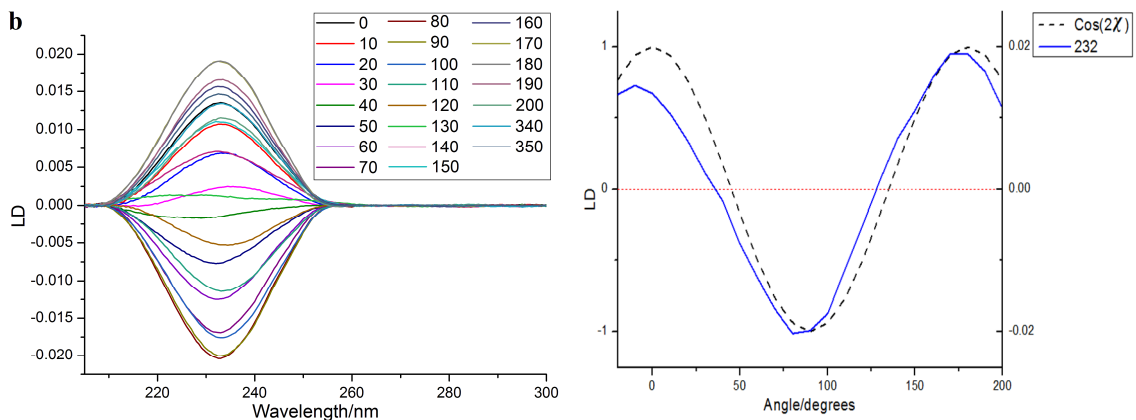


**Fig. 2.9** Left: LD of progesterone ( $\sim 0.5$  mg/mL) on  $1.8\times$  stretched a) PE and b)  $\text{PE}^{\text{OX}}$  films as a factor of rotation angle,  $\chi$ , of the film.  $0^\circ$  is where the stretch direction is as close to horizontal as loading the film in a small circle enabled, right: LD at wavelength indicated as a function of  $\chi$ . Dashed line is the plot of  $\cos(2\chi)$ .

An overlay of the LD of progesterone as a function of film-rotation angle,  $\chi$ , is shown in Fig. 2.9 along with a plot of signals at the LD maxima as a function of  $\chi$ . The  $\cos(2\chi)$  dependence of the signals means that either the molecule behaves as a uniaxial rod or the film ensures uniaxial orientation or a combination of the two. Within experimental error of loading the sample and noting none of the spectra are baseline corrected, each molecule and film studied in this work behave consistently with a uniaxial orientation mechanism.

### 2.3.3.3 DAPI

DAPI (4,6-diamidino-2-phenylindole) is a good test case for  $\text{PE}^{\text{OX}}$  as DAPI fails to orient on PE and there is literature PVA film data available for comparison.<sup>57</sup> Fig. 2.10 shows the variable stretch LD spectra of DAPI on  $\text{PE}^{\text{OX}}$ . Our data go to lower wavelength than the PVA spectrum but in other respects are similar. The broad band at approximately 350 nm actually consists of two transitions, one at 330 nm and another at 380 nm. Analysis of their DAPI PVA data led Kubista et al. to conclude that  $S \sim 0.66$  and that the 380 nm transition

was the most oriented and was polarized close to the indole-phenyl bond.<sup>57</sup> They assigned polarizations to the other transitions but were not able to determine whether they were  $+d^\circ$  or  $-d^\circ$  from  $z$ . Comparison of their data with our PE<sup>OX</sup> data (Fig. 2.10) gives us a way to determine this since the relative magnitudes of peaks on PVA and PE<sup>OX</sup> differ, indicating a slightly different orientation.

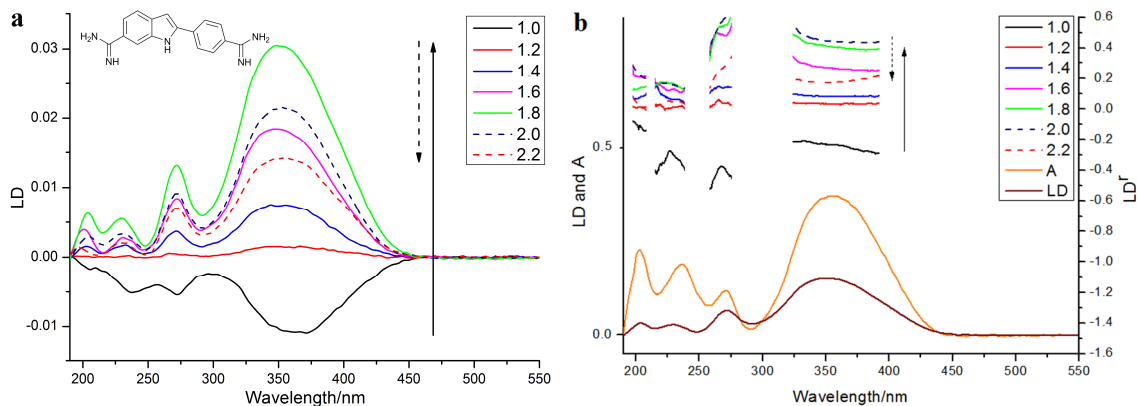


**Fig. 2.10** Spectra of DAPI on PE<sup>OX</sup> (deposited from 0.4 mg/mL in methanol and left to dry). (a) LD prestretched by factors ranging from 1 to 2.2×. (b) LD' for data from (a) overlaid with absorbance and LD spectra for 1.8× stretch.

Like progesterone, DAPI's LD signal on 1.8× stretched PE<sup>OX</sup> follows  $\cos(2\chi)$ , showing the molecule behaves uniaxially on PE<sup>OX</sup> (Fig. 2.11).

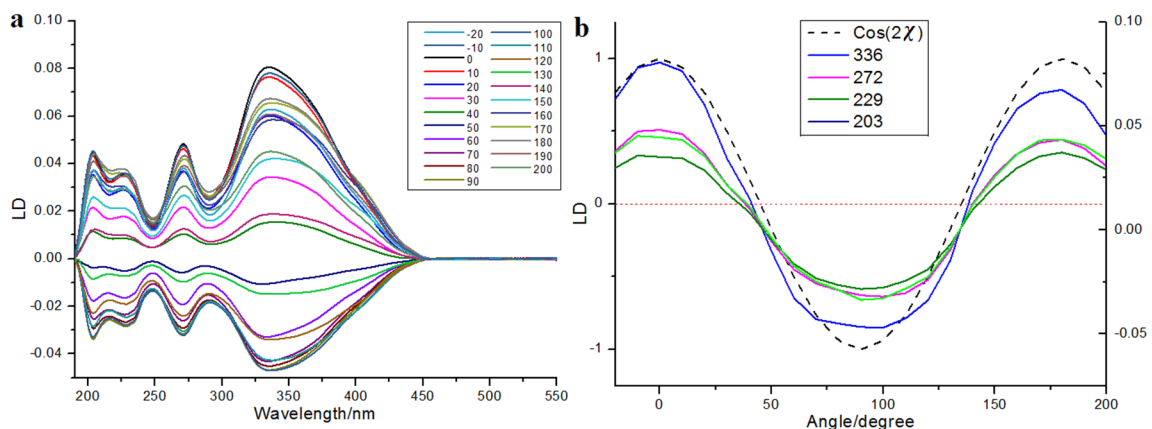


**Fig. 2.11** LD of DAPI (deposited from 0.4 mg/mL in methanol) on PE<sup>OX</sup> stretched 1.8× as a function of film-rotation angle. a) wavelength scans, b) signal at 203, 229, 272 and 336 nm as a function of rotation angle  $\chi$  overlaid on a plot of  $\cos(2\chi)$ .

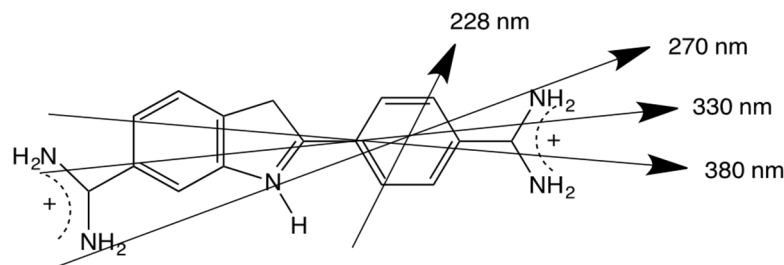


**Fig. 2.12** 4',6-Diamidino-2-phenylindole illustrating approximate transition polarizations consistent with this work and the PVA reference.<sup>57</sup>

The 270 nm transition on  $\text{PE}^{\text{OX}}$  (Table 2.2) has the largest value of  $\text{LD}^r$ , so we assume it is along z ( $\alpha=0$ ). It then follows that for the  $1.8\times$  stretch  $\text{PE}^{\text{OX}}$  experiment,  $S \sim 0.18$ . The directions of z and the other transition moments can then be deduced from  $\text{LD}^r$  data and are given in Table 2.2 where the PVA results are also summarized. Transition moment polarizations consistent with both data sets are illustrated in Fig. 2.12. Overall, the quality of the DAPI– $\text{PE}^{\text{OX}}$  spectra suggest  $\text{PE}^{\text{OX}}$  can replace PVA for polar molecules making a much simpler quicker experiment.

**Table 2.2** Angles between DAPI transition moments and the orientation axis in the PVA data of Kubista et al.<sup>57</sup> and the  $\text{PE}^{\text{OX}}$  data of this work.  $\text{PE}^{\text{OX}}$   $\text{LD}^r$  data are for  $1.8\times$  stretch. The directions illustrated in Fig. 2.12 are consistent with both data sets. The uncertainty for angle measurements was less than %5.

Wavelength	PVA angle	$\text{PE}^{\text{OX}}$ angle	$\text{LD}^r$ on $\text{PE}^{\text{OX}}$
380 nm	0–5°	26°	0.39
330 nm	15–17°	17°	0.48
270 nm	12–19°	0°	0.55
228 nm	>50°	45°	0.14

### 2.3.3.4 1-Pyrenecarboxaldehyde: different binding to PE and $\text{PE}^{\text{OX}}$

1-Pyrenecarboxaldehyde (PyCO, Fig. 2.13) provides an interesting illustration of how PE and  $\text{PE}^{\text{OX}}$  may, in some cases, be used to provide complementary data that can be used in

a manner similar to that done for DAPI and PE<sup>OX</sup> above since PyCO turns out to orient slightly differently on the two films. The aldehyde group of PyCO is polar and the pyrene is very non-polar. LD data for the pyrene chromophore on films and in liposomes are available in the literature<sup>43,58,59</sup> (see Table 2.3). The absorbance spectroscopy of PyCO (Fig. 2.13) is similar to that of pyrene but shifted to longer wavelengths with additional features including the 234 nm peak. PyCO has C<sub>s</sub> symmetry (pyrene is D<sub>2h</sub>), so its π–π\* transitions are constrained to be in the plane but not necessarily along either the long axis or the short axis of the pyrene chromophore.

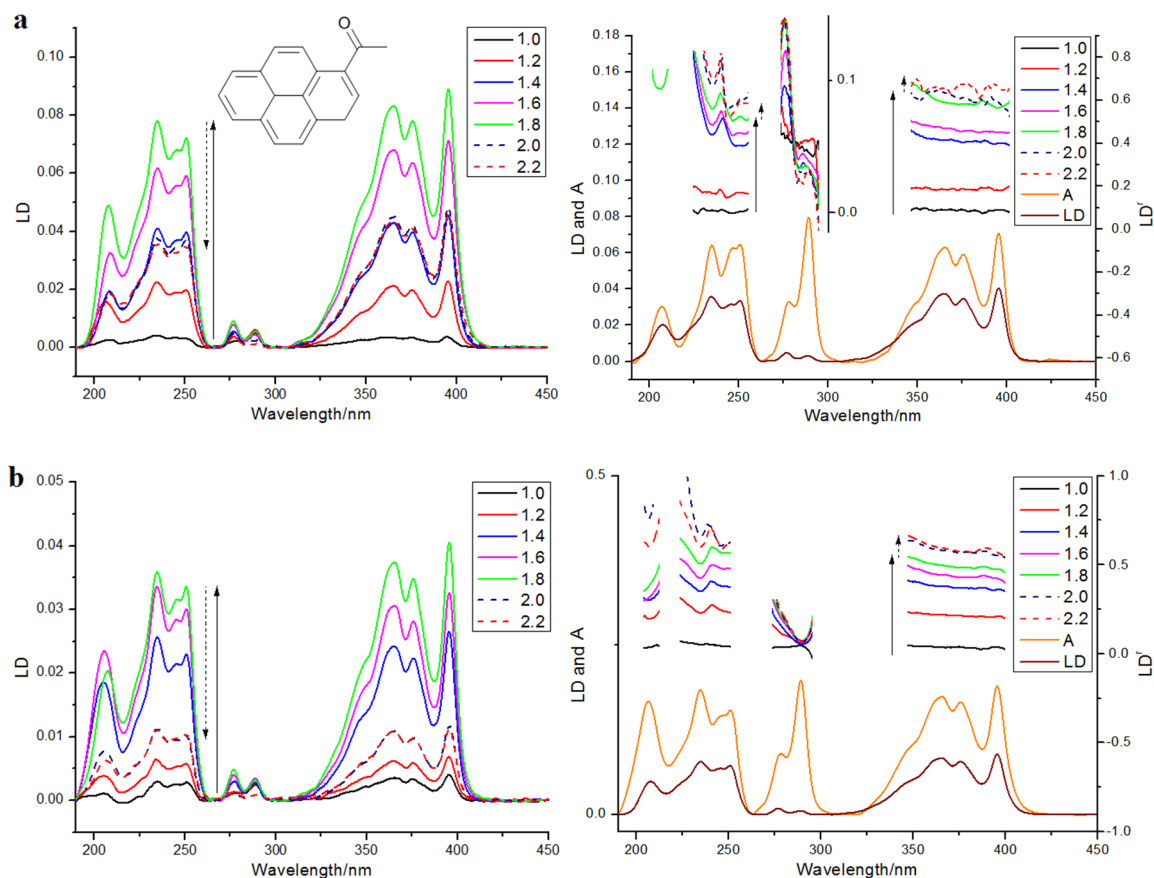


**Fig. 2.13** Left: LD spectra of 1-pyrenecarboxaldehyde (deposited from 0.4 mg/mL in chloroform for PE and methanol for PE<sup>OX</sup> and left to dry) on (a) PE, and (b) PE<sup>OX</sup> prestretched by factors ranging from 1 to 2.2×, right: The corresponding LD' spectra of the spectra on the left side overlaid with the LD and absorbance spectra when the film stretched for 1.8×.

The LD and LD<sup>r</sup> spectra (Fig. 2.13) indicate spectral ranges of single polarizations as summarised in Table 2.3. With PE<sup>OX</sup>, the 207 nm transition is closest to Z (though its LD<sup>r</sup> value does depend on how the baseline correction is done), then the 350–400 nm band, whereas with PE, 246–253 nm has the largest LD<sup>r</sup>, so is closest to Z. In pyrene these transitions are all long-axis polarized. We speculate that the two films orient PyCO differently because the carbonyl interacts with the more polar PE<sup>OX</sup> surface but not with PE. The solid arrow in Fig. 2.14 is thus a reasonable estimate of z for PE<sup>OX</sup> with (the lower limit of) S = 0.21. An iterative trial and error process led us to conclude that S was the same for both films (knowing PyCO behaves uniaxially on both films, Fig. 2.15); there was 6° difference between their molecular orientation axes (the orientation axis on PE is illustrated by the dashed line in Fig. 2.13 and by the solid arrow on PE<sup>OX</sup>); and the transition polarizations are approximately as illustrated in Fig. 2.14 and summarized in Table 2.3. The 207 nm, 380 nm and 234 nm transitions are thus close to the pyrene long axis, whereas the others, particularly the former pyrene short axis polarized transitions, are significantly perturbed from their pyrene values.

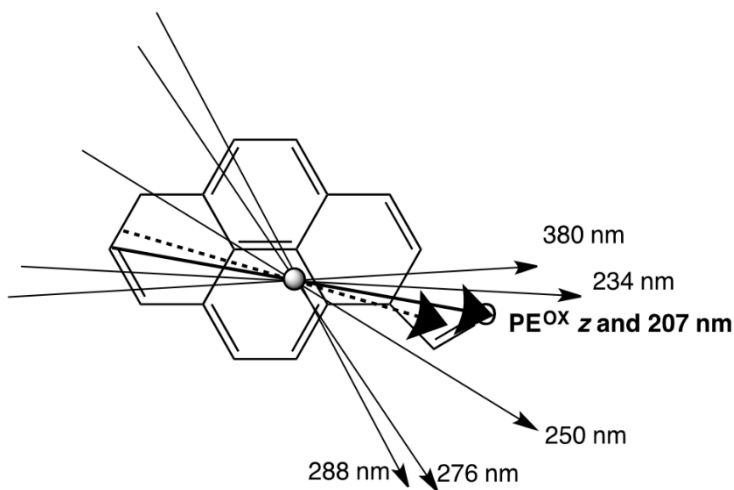


**Fig. 2.14** Polarizations of PyCO transitions assuming the orientation direction of PE<sup>OX</sup> is as indicated by the thick solid line (the longest molecular axis with O lying flat on the film). The thick dashed line is then the orientation on PE.

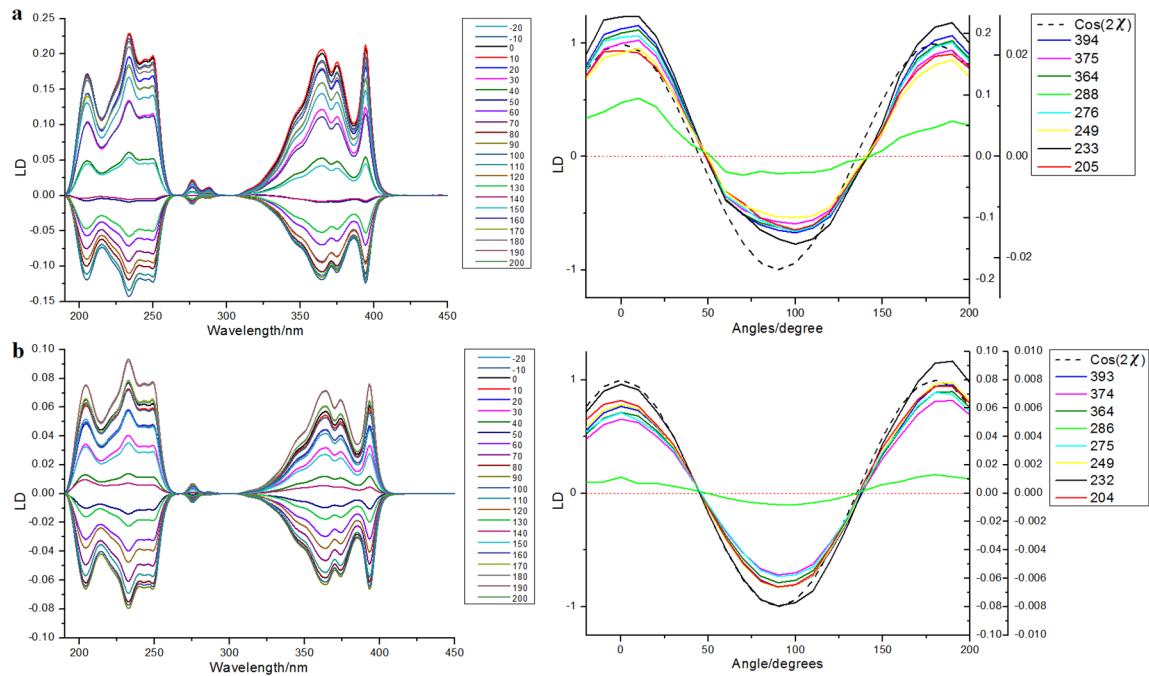


**Fig. 2.15** LD of 1-pyrenecarboxaldehyde on (a) PE and (b) PE<sup>OX</sup> as a function of film-rotation angle. Left: wavelength scans, right: signal at 205, 233, 249, 276, 288, 364, 375 and 395 nm as a function of rotation angle  $\chi$  overlaid on a plot of  $\cos(2\chi)$ . Note: the film stretcher horizontal direction was not quite parallel to the PE stretch direction due to challenges of loading the film into the cylindrical holder.

**Table 2.3** LD<sup>r</sup> data for 1-pyrenecarboxaldehyde on PE and PE<sup>OX</sup> at 1.8× stretch, literature transition polarizations for pyrene, and PyCO transition moment polarizations ( $\pm 3^\circ$ ) with respect to the PE<sup>OX</sup> z as illustrated in Fig. 2.14(+ denotes anticlockwise rotation as illustrated). The uncertainty for angle measurements was less than %5.

Wavelength	LD <sup>r</sup> on PE	LD <sup>r</sup> on PE <sup>OX</sup>	Pyrene assignment <sup>60</sup>	PyCO assignment
207 nm	0.39	0.64		$\sim 0^\circ$
234 nm	0.53	0.62		$+9^\circ$
246–253 nm	0.57	0.51	220–240 nm: Long	$-21^\circ$
276 nm	0.28	0.13	260 nm: Long	$-46^\circ$
288 nm	0.077	0.038	270–280 nm: Short	$+53^\circ$
350–400 nm	0.51	0.56	300–340 nm: Long	$-16^\circ$

## 2.4 Conclusions

In this work we have shown that we can change the surface properties of polyethylene (PE) by oxygen plasma treatment enough to enable even the most polar of small molecules to

be oriented on its oxidised surface ( $\text{PE}^{\text{OX}}$ ). Overall, the quality of the DAPI  $\text{PE}^{\text{OX}}$  spectra suggest  $\text{PE}^{\text{OX}}$  can replace polyvinyl alcohol for polar molecules making a much simpler and quicker experiment. In general we found that the sample deposition was more uniform with the  $\text{PE}^{\text{OX}}$  surfaces making it usually the preferred substrate. The orientation of our films increased with stretch factor due to changes in crystallinity and crystallite orientation in the PE substrate (which also includes crystalline polypropylene). For some molecules (e.g. 1-pyrenecarboxaldehyde) we found the different interactions between analyte and the two films enabled us to assign transition moments of low symmetry molecules. Easy transition moment assignment follows if the molecules orient uniaxially on the polymer film. We have shown that a simple matrix rotation experiment can be used to determine whether or not the orientation may be assumed to be uniaxial.

# **Chapter Three**

## **Anthracene: Optical properties and dimerisation investigation**

### **Acknowledgement**

I wish to thank Prof. Alison Rodger for providing me the exciton coupling calculations I used in this chapter. I would like to thank Alan Wemyss for helping me in optimising the fluorescence detected linear dichroism technique used in this chapter. I also want to thank Don Praveen Amarasinghe for the absorbance data collected for this chapter as a part of his MOAC mini project. I wish to acknowledge Dr. Shirin Jamshidi for providing the computational modelling data for this chapter.



### 3.1 Introduction

Anthracene is a well-studied molecule with extensive literature on its spectroscopy in solution, crystal and on films. However, we found in preliminary studies that despite this work, there were still many mysteries regarding anthracene's behaviour, particularly on films. Much of the challenge proved to relate to anthracene's propensity to dimerise or oligomerise on films.

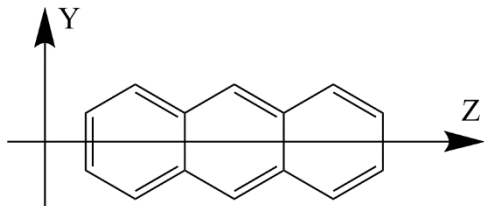


**Fig. 3.1** Schematic model of anthracene molecule showing the long and short axis of the molecule aligned with Z and Y axis of the molecule respectively.

As the starting point for our analyses below, we accept the work of Friedrich et al.<sup>61</sup>, namely that the long wavelength band for anthracene is the  $^1\text{L}_\text{a}$  band of  $\text{B}_{2\text{u}}$  symmetry (i.e. y-polarized in an axis system where z is the anthracene long axis and y is its in-plane short axis, Fig. 3.1) with the origin at about 379 nm (depending on the solvent). This transition has clear vibronic progressions in solution and on film (Fig. 3.3a). We can see totally symmetric ( $\text{a}_{1\text{g}}$ ) vibrational progressions due to a  $\sim 1420 \text{ cm}^{-1}$  stretching vibration and a  $399 \text{ cm}^{-1}$  skeletal bending vibration (which is apparent as a high energy shoulder at  $\sim 372 \text{ nm}$  in our spectra). Overlaid on these is a  $1480 \text{ cm}^{-1}$ <sup>62</sup> or  $1630 \text{ cm}^{-1}$  or perhaps  $1481 \text{ cm}^{-1}$ <sup>61</sup>  $\text{b}_{3\text{g}}$  progression that mixes in intensity from the  $250 \text{ nm}$   $^1\text{B}_\text{b}$  long axis polarized band resulting in intensity of  $\text{B}_{1\text{u}}$  symmetry. The electronic polarization of this progression is therefore along z.

## 3.2 Materials and methods

Anthracene was purchased from Sigma and used without further purification. Solvents used in the measurements were 18.2 MΩ-cm water (Millipore Direct-QTM), chloroform (spectrophotometric grade, Sigma-Aldrich), methanol (Laboratory grade, Fisher Chemicals) and methyl cyclohexane (spectrophotometric grade, Sigma-Aldrich).

The PE films to be used as sample matrices were prepared as explained in §1.

### 3.2.1 Linear Dichroism and absorbance spectroscopy studies

The LD and absorbance spectra of anthracene were recorded as reported in §1.

### 3.2.2 Fluorimetry studies

The fluorescence emission spectra of anthracene in methylcyclohexane solution (0.05–2 mg/mL, using a 0.5 centimeter-pathlength-cell) and deposited on PE film were recorded using a FP-6500 Jasco spectrofluorometer when the detector was aligned 90° to the incident light (Fig. 3.2). Each time, the excitation wavelength was set on a peak wavelength of the anthracene absorbance spectrum when a bandpass of 3 nm for both monochromators (excitation and emission) was set.

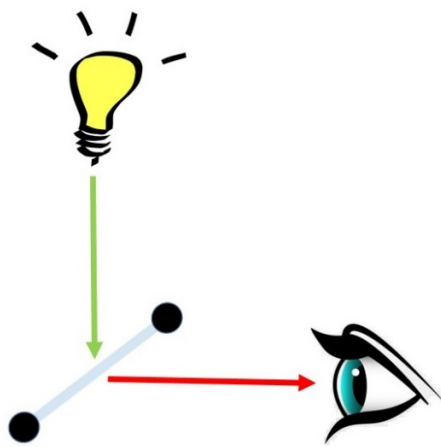


**Fig. 3.2** The schematic diagram for 90°-setup-fluorimetry experiment for samples deposited on stretched PE films. The stretcher is placed horizontally in the beam path the way that the film has an angle of 45° with respect to the excitation beam (green arrow) and the detector (presented as eye in the figure).

### 3.2.3 Fluorescence detected linear dichroism studies

The FDLD spectra of anthracene (with different concentrations) deposited on  $1.8 \times$  stretched PE<sup>OX</sup> film were recorded in  $0^\circ$  geometry using a BioLogic MOS-450 spectrophotometer when a 4 nm bandpass for the excitation monochromator was set (Fig. 3.3). The FDLD experiments were performed with the same conditions used for collecting LD spectra inserting a long-pass-filter (400 nm) in front of the photomultiplier tube. The PE<sup>OX</sup> films' spectra were used as the background in each case. Each time an aliquot ( $\sim 40\mu\text{L}$ ) of the sample was deposited on PE<sup>OX</sup>, the LD and FDLD spectra of it were recorded by averaging 2 and 3 spectra respectively. All spectra were recorded using a 0.5 nm/s scanning speed. Sample aliquots were added until a change in the shape of spectra noticed.

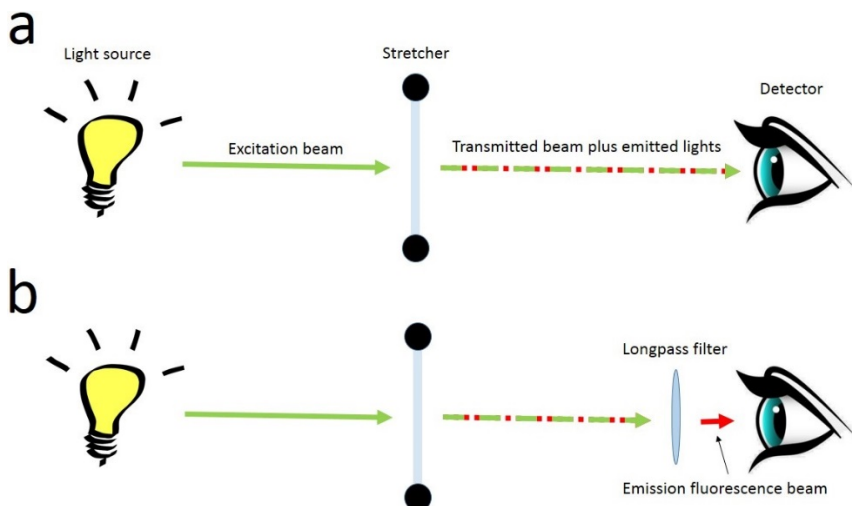


**Fig. 3.3** The schematic diagrams for a) LD and b) FDLD experiments for samples aligned on stretched PE films. A longpass filter is placed in front of the detector to block the incident light, so only the emission fluorescence reaches the detector.

### 3.3 Results and discussion

#### 3.3.1 Linear dichroism and absorbance spectroscopy studies

Despite being a non-polar molecule, anthracene orients well (see below) on both PE and PE<sup>OX</sup> films. The PE<sup>OX</sup> data are usually slightly better as the sample spreads more uniformly on the film. LD film rotation experiments show that the monomeric anthracene orientation is always uniaxial in our experiments (Fig. 3.4a), whilst anthracene's oligomeric structures do not behave entirely the same way (Fig. 3.4b). (§1)

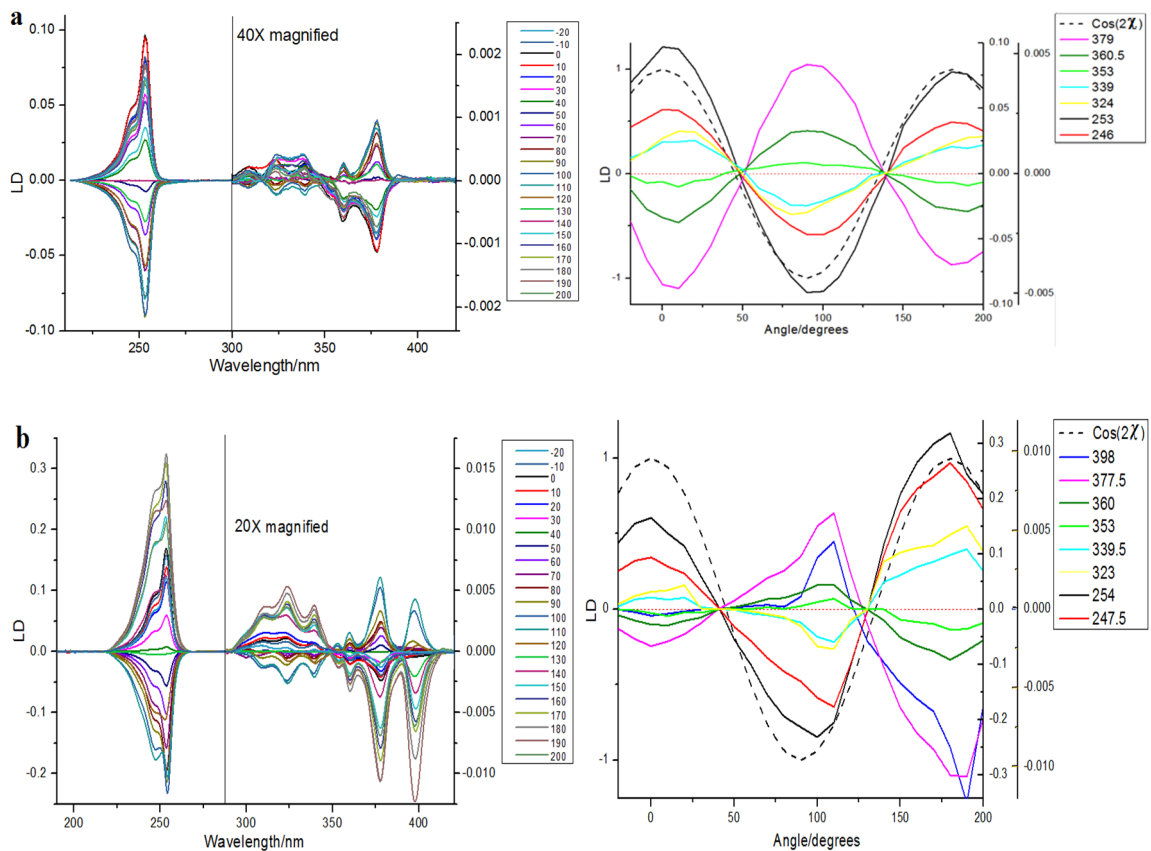


**Fig. 3.4** LD of anthracene on a) PE<sup>OX</sup> and b) PE (from 0.15 and 0.4 mg/mL solutions respectively) as a function of film-rotation angle. Left: wavelength scans, right: signal at 246, 253, 324, 339, 353, 360 and 379 nm plotted as a function of rotation angle  $\chi$  overlaid on a plot of  $\cos(2\chi)$ . Note: the film stretcher horizontal direction was not quite parallel to the PE stretch direction due to challenges of loading the film into the cylindrical holder.

### 3.3.1.1 Monomeric anthracene

By depositing anthracene from a dilute solution of CHCl<sub>3</sub> (0.1 mg/mL) onto PE we are able to ensure a fairly pure monomer spectrum as shown by a comparison of the film and solution (methylcyclohexane) absorption spectra (Fig. 3.5a) where the solution has a slight blue shift relative to the 0.1 mg/mL film spectrum. The monomer spectra as a function of stretch factor are shown in Fig. 3.5c and d. The longest wavelength band (the 0–0 vibronic band of the <sup>1</sup>L<sub>a</sub> band) in solution absorbance, film absorbance and film LD occurs at ~378

nm and the main vibronic components occur at  $\sim 1400 \text{ cm}^{-1}$  intervals. The third vibronic band has a positive LD signal indicating that the contribution of the 254 nm band is becoming dominant. If we assume that the strongly positive LD from 245–258 nm is long axis polarized with a  $\alpha = 0^\circ$ , then from Eq. 2  $S \sim 0.23$  for the  $1.8\times$  stretch (PE or  $\text{PE}^{\text{OX}}$ ). It then follows that the vibronic components of the 377 nm band have average angles as indicated in Table 3.1 with gradually increasing contribution from the long axis polarized electronic transition. The fact that the 378 nm (fundamental band)  $\alpha$  is not  $90^\circ$  reflects the fact that we do have some oligomeric species present (see below).

We begin our analysis with the 0.1 mg/mL sample which is very similar in spectra shape to the solution spectrum. We therefore conclude that what we are detecting in its absorbance and LD spectra is predominantly the monomer.

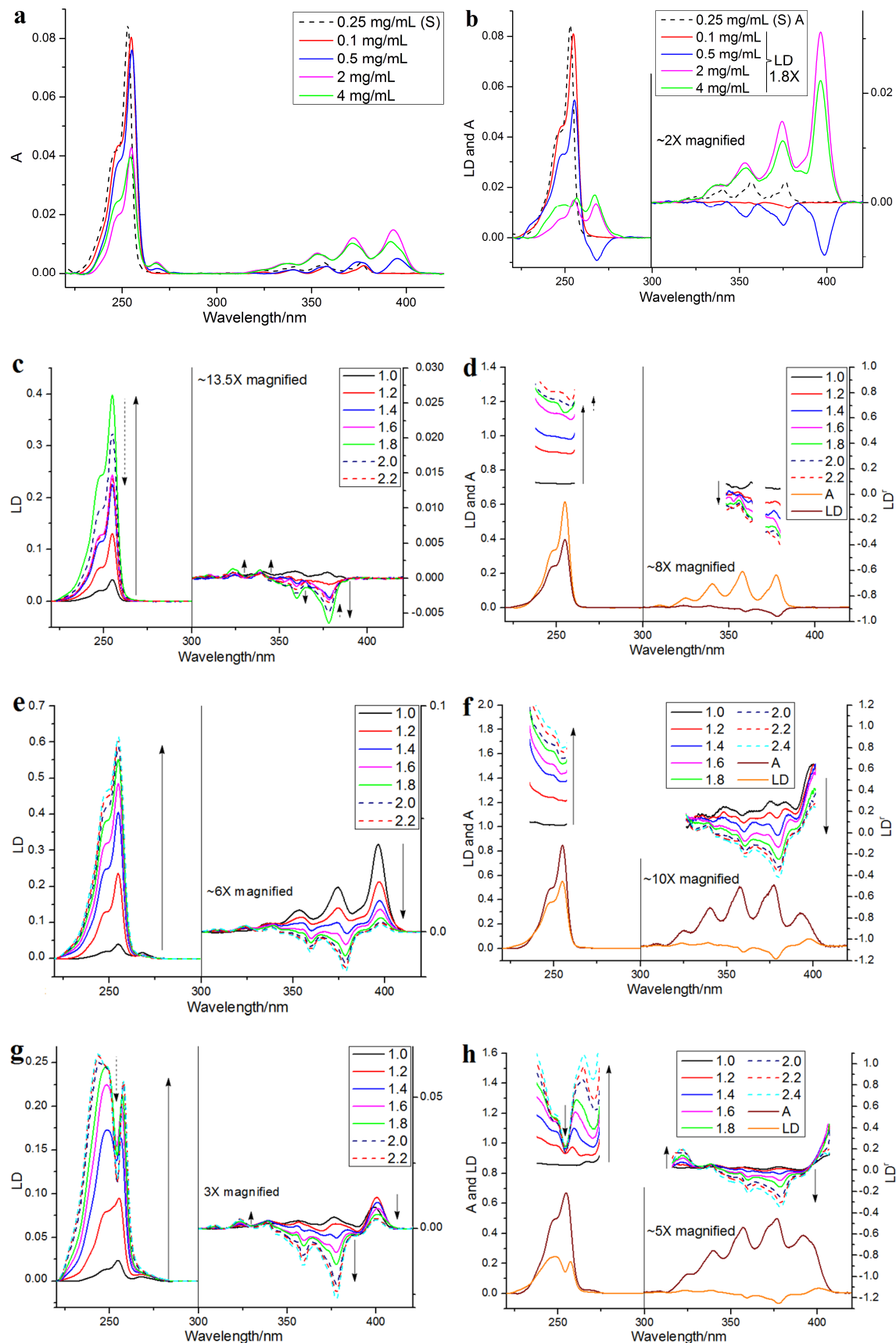


**Fig. 3.5** Spectra of anthracene. (a) Absorbance of anthracene in solution (0.25 mg/mL cyclohexane) overlaid on absorbance spectra of 1.8 $\times$  stretch films (PE) deposited from chloroform

solutions of the concentrations indicated in the figure. (b) LD corresponding to (a) film spectra with solution absorbance overlaid normalised to have areas under the curves equal to one. (c) LD (deposited from 0.1 mg/mL solution in methanol, to ensure monomer, see text) on PE<sup>OX</sup> as a function of stretch factor (indicated – sample deposited after stretching). LD deposited from solutions in chloroform in (e) 1 mg/mL (g) 8 mg/mL as a function of stretch (sample added before stretching). (d), (f), and (h) LD' for data from respectively (c), (e), and (g) overlaid with absorbance and LD spectra for 1.8× stretch.

**Table 3.1** Approximate effective polarizations (error is of the order of 5%) of the vibronic components of the 379 nm B<sub>2u</sub> vibronic progression of anthracene, and the fractions of short axis and long axis electronic contributions to the total determined from 1.8× stretch data in Fig. 3.4b assuming the 254 nm band is long axis polarised. Calculations are performed on the centre of each band from low energy half height to high energy half height. The fraction of the a<sub>g</sub> progression is fraction of intensity that is due to the short axis polarized component assuming the same oscillator strength for the two components.

Wavelength maximum assuming 1400 cm <sup>-1</sup> progression	Wavelength maximum of LD	LD sign	$\alpha_{\text{effective}}$	Fraction of a <sub>g</sub> progression (assuming only monomer present)
378 nm	378 nm	—	75°–90°	0.93–1.0
360 nm	360 nm	—	62°	0.78
342 nm	339 nm	+	47°	0.59
327 nm	323.5 nm	+	34°	0.45
313 nm	309 nm	+	31°	0.36

### 3.3.1.2 Oligomeric anthracene

A further complication is the possibility of anthracene forming dimers (or other higher order structures).<sup>63</sup> Chandross et al. identified two dimer forms with different spectroscopy: a so-called sandwich dimer which required a cryogenic glass to stabilize it and a stable dimer (or higher order structure) which they concluded had ~55° between the short axes and not more than 5° between the long axes. They were unable to study the 254 nm band of their stable dimer of anthracene as they found that the transition was shifted

beyond their range of observation.<sup>63</sup> Consistent with these structures, the crystal structure<sup>64</sup> has two distinct anthracene pairs, one parallel and slightly displaced and one skewed with angles of 54° between the short axes and 14° between the long axes. However, we found we could not interpret our film data in terms only of these structures.

If we prepare anthracene films from higher concentration solutions we observe absorbance and LD signals in the region of 400 nm and see intensity at ~268 nm and changes in the 245 nm region. What is observed depends on the way the experiment is done, whether the films are pre-stretched or stretched after the sample is added and also on the concentration of the solution that is added. Some examples are given in Fig. 3.5a, b, e–h showing the effect of exciton coupling<sup>65</sup> between anthracene units with intensity appearing at either high energy or low energy or both.

**Table 3.2** Different component spectra identified in the anthracene film LD spectra of Fig. 4.5. ‘Large’ indicates where the long wavelength region has enhanced intensity relative to the 250 nm region. Vibronic progressions are indicated where they are apparent. Sh denotes shoulder.

Spectrum in which component is most apparent	LD at ~230 nm	LD at ~254 nm	LD at ~268 nm	LD at 379 nm	LD at ~400 nm	Geometry consistent with LD
Monomer	0	+ve	0	–ve from 379 nm 14000 cm <sup>-1</sup>	0	Fig. 3.6a
0.5 mg/mL Fig. 3.5b	+ve (sh)	(?)	–ve	from 399 nm, 16000 cm <sup>-1</sup> (large)	–ve (large)	Fig. 3.6c
1 mg/mL Fig. 3.5e unstretched	0	(?)	+ve	+ve, from 396 nm, 14800 cm <sup>-1</sup> (large)		Fig. 3.6c
1 mg/mL Fig. 3.5e stretched	0	+	+ve (small)	–ve	+ve (small)	Fig. 3.6a and c
8 mg/mL Fig. 3.5g stretched	0	–ve	0	–ve (large), from 378 nm, ~14000 cm <sup>-1</sup>	0	Fig. 3.6b

Most of our concentrated films showed positive LD signals for the longest wavelength signal at 397 nm (the maximum of the stable dimer of Chandross et al.<sup>63</sup>) and at 266–267 nm. Some showed negative signals at both 399 nm and at 268 nm. There are at least 4 different component spectra apparent in our spectra, all overlaid on each other and the monomer. The monomer is dominant at low concentration (see above) and becomes dominant at high stretch with medium concentration stock solutions (1 mg/mL), reflecting the increased crystallinity of the PE with stretch making more monomer binding sites available. The high concentration (8 mg/mL) spectra seems to be an overlay of the 1 mg/mL unstretched spectrum with one that has negative LD occurring at the monomer transition energies for both the long and short axis polarized transitions. There is also a spectrum that has positive signals at energies lower than the monomer transitions (396 nm plus vibronic progression and 268 nm), but which matching higher energy exciton component is small or zero. Another spectrum with negative LD at 399 nm and 268 nm and positive (shoulder) at 230 nm is observed in a 0.5 mg/mL film. The features of these spectra are summarized in Table 3.2. The monomer, as discussed above, is uniaxially oriented with its long axis along the stretch direction giving positive 250 nm LD and negative 379 nm LD. The complex spectral features discussed above are the result of higher order anthracene structures adopting other orientations on the film and exciton coupling to give signals at higher and lower energies usually with one positive and one negative in sign. To have completely negative LD at the monomer transitions (8 mg/mL, last line of Table 3.2), the anthracenes must be oriented with their planes perpendicular to the stretch direction. If the anthracenes have parallel molecular planes, but the nearest neighbour long axes are twisted by 90° with respect to one another then there is zero exciton energy shift. An extended cross-hatched structure as illustrated in Fig. 3.6b is consistent with this and is expected to be stable on the stretched film. We postulate this is

what is happening in the 8 mg/mL film. The geometries giving rise to the 1 mg/mL unstretched and 0.5 mg/mL spectra are harder to identify uniquely. Possible arrangements include the following. A geometry similar to that of the skew pair in the crystal structure<sup>64</sup> gives rise to almost no intensity for the out-of-phase couplings for both long and short-axis anthracene transitions and (if the long axes are along the stretch direction) positive LD for the in-phase coupling. A geometry where one layer of anthracenes are aligned in a head-to-tail along the stretch direction (as are the monomers) and a second layer is tilted as in the crystal (14.4° between long axes and 54° between short axes) but displaced enough to ensure  $V < 0$  as illustrated in Fig. 3.6c accounts for the 1 mg/mL unstretched spectrum. The 0.5 mg/mL spectrum is consistent with a geometry where the first layer is the same as this but the second layer has the molecules parallel to the first and rotated about X axis by  $2\gamma - 60^\circ$  (Fig. 3.6c). This geometry has  $V > 0$  (All exciton coupling energy shifts are calculated by Prof. A. Rodger), both in-phase and out-of-phase short wavelength transitions positive, and long-wavelength in-phase positive but out-of-phase negative.

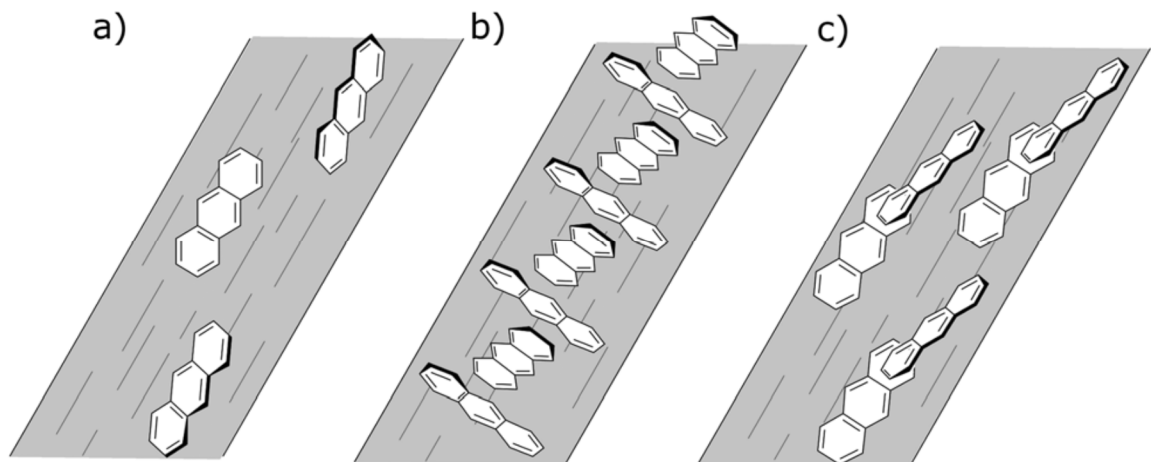


**Fig. 3.6** The three proposed orientations of anthracene on PE<sup>OX</sup> films, (a) uniaxially oriented single molecules, (b) extended cross-hatched structure and (c) skewed dimers.

### 3.3.2 Fluorimetry studies

There is some evidence in the literature of spectroscopic signatures of anthracene oligomers forming in solution.<sup>63</sup> Although we were interested in films, we first repeated the literature type of experiment. To investigate the presence of anthracene's dimers or other higher order structures in solution a series of UV/Vis absorbance spectra of anthracene dissolved in methylcyclohexane for a variety of concentrations was collected (Fig. 3.7). However, there is no significant sign of dimerisation upon increasing the concentration except for a gradual intensity increase for the very weak band at 265 nm.

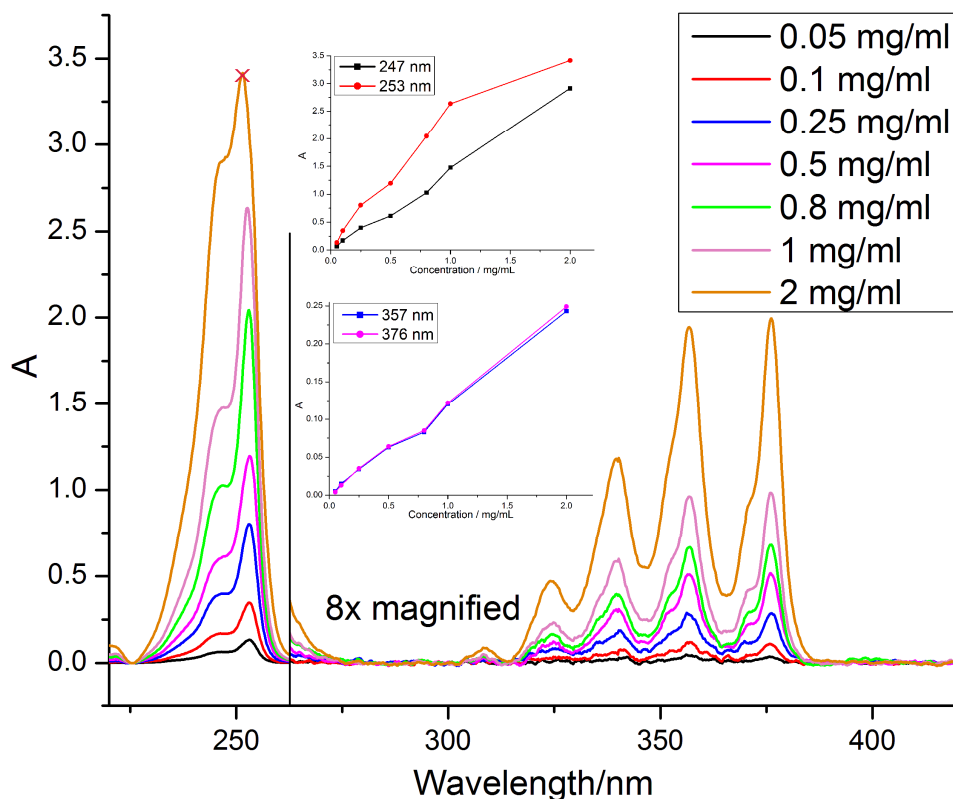


**Fig. 3.7** Absorbance spectra of anthracene in methylcyclohexane solution (room temperature) with ascending concentrations from 0.05 to 2 mg/mL (listed in the legends). Except from the band at 253 nm in 2 mg/mL spectrum (due to the instrument cut-off), all bands' intensities follow the Beer Lambert law.

Studies by Lacy and Lyons<sup>66</sup>, Ferguson<sup>67</sup> and Chandross<sup>63</sup> between 1964 and 1966 showed the feasibility of observing the presence of anthracene's excimer and excited state stable dimers in solution using fluorimetry. However, they did not provide a clear spectral interpretation, peak assignment or information about the concentration dependency of dimerisation. Our fluorescence emission spectra of anthracene solutions with different concentrations (Fig. 3.8) showed changes in relative intensities of fluorescence peaks when the concentration increases that is not in accord with the Beer Lambert law suggesting the presence of different interactions.

The resulting fluorescence spectrum consists of four bands at 380.4, 399.6, 423.2 and 448.2 nm. Corresponding to the absorbance bands at 378, 360 and 339 nm, we were able to assign the peaks at 380.4, 399.6 and 423.2 to 0–0, 0–1 and 0–2 energy levels respectively (the mirror image rule).<sup>68</sup>

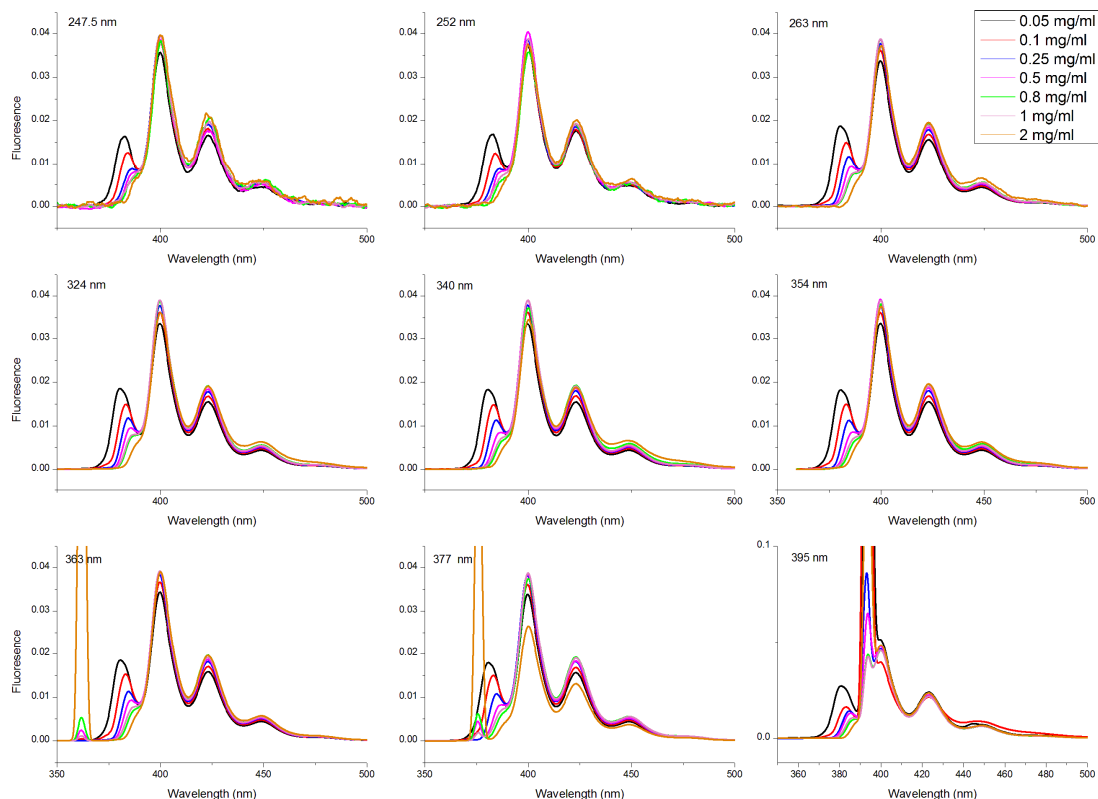
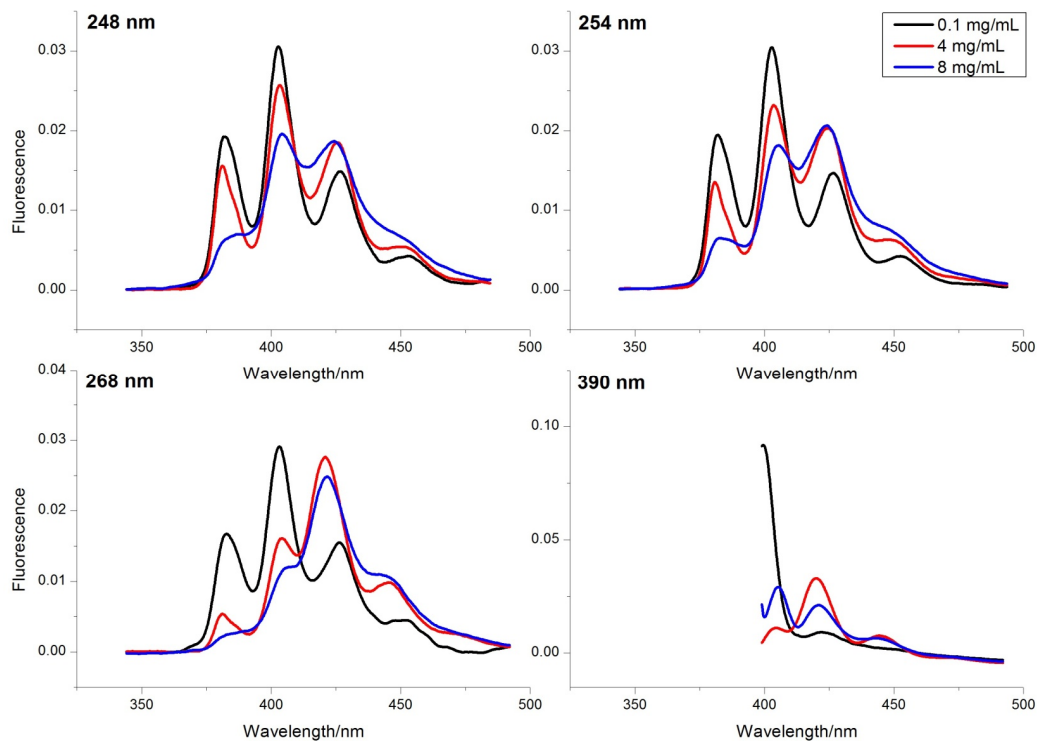


**Fig. 3.8** Fluorescence emission spectra of anthracene in methylcyclohexane solution with ascending concentrations from 0.05 to 2 mg/mL (listed in the legends). Each set of spectra was recorded using different excitation wavelength (indicated in top left hand corner). All spectra are shown scaled to have the area under the curve of the spectrum equal 1 to facilitate comparison of relative intensities.

As shown in Fig. 3.8 upon increasing the anthracene concentration, the fluorescence band at 382 nm reduces in intensity and slightly red shifts to become a shoulder for the band at 399.6 nm whilst the rest of the bands grow slightly in intensity. Ferguson<sup>67</sup> found that the changes in the amount of excited state stable dimer and the excimer could be observed by changes in the intensity of the band at 399.6 nm. Also changes in the intensity of bands at 423.2 and 448.2 nm could be due to the change in amount of the stable aggregate fractions in a sample. As the spectra in the Fig. 3.8 are integrated to have area equal to 1 we can conclude that the bands for the dimers influence grow in intensity when concentration increases.

As Ware and Cunningham<sup>69</sup> reported, anthracene as a "complex molecule" exhibits no resonance fluorescence, so the shape of the emission spectrum must not change when the excitation wavelength is set between 240 and 365 nm. However, our results show when the concentration is constant changing the excitation wavelength causes a relative intensity change for emission peaks. This could be further evidence for the presence of dimers. In low concentrations (mostly monomeric) the band at 380.4 nm has its highest intensity when the excitation wavelength is set at anthracene's short axis polarised wavelengths. In concentrations above 1 mg/mL it fluoresces more when the excitation wavelength is set on 247.5 and 252 nm. The other three bands have their highest and lowest intensities respectively when the excitation wavelength is set on 252 and 377 nm. This is due to the less long axis polarised transition moment mixing into the 380.4 nm band.<sup>61</sup>

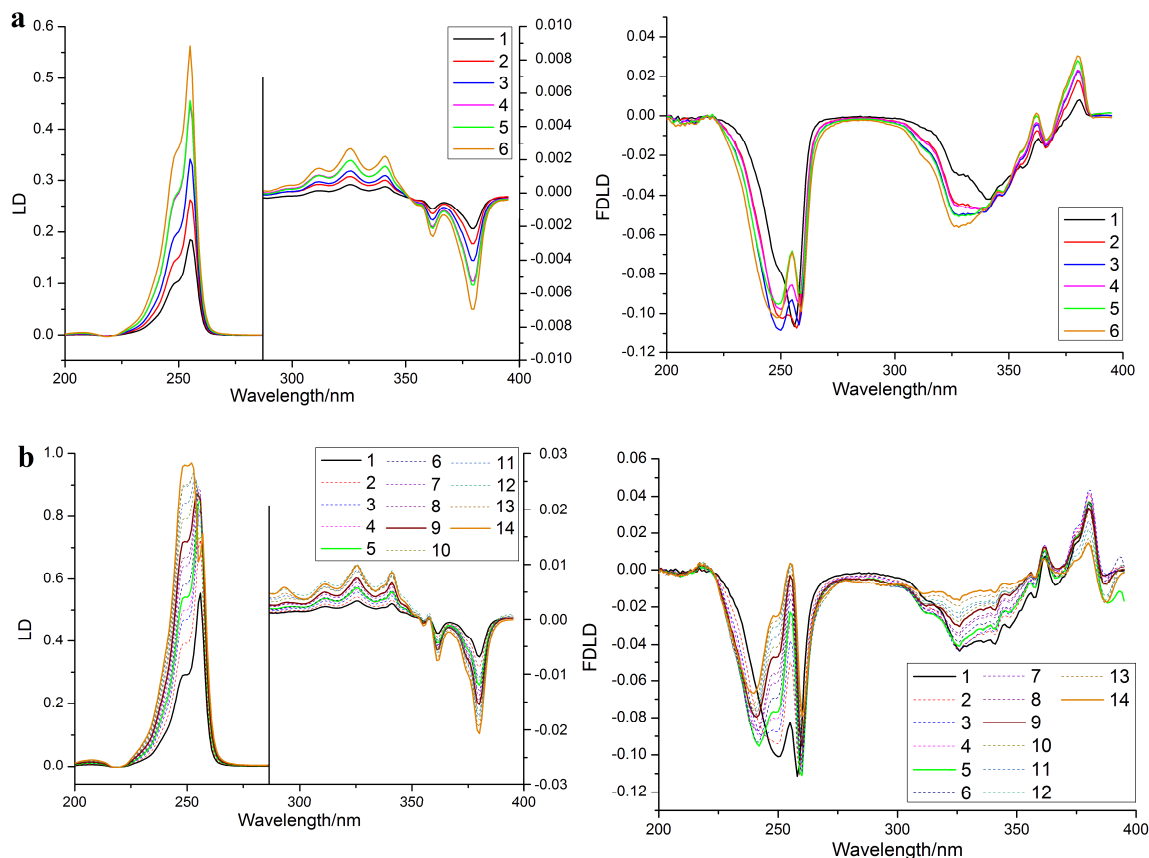
Repeating the analogous experiment on the dried anthracene on PE (a slight red shift of ~3 nm is observed), gave similar results to the solution experiment for the bands at 382, 426.2 and 453.8 nm (Fig. 3.9). However, the band at around 402 nm decreases in intensity when the concentration of the depositing solution was increased. As Ferguson notes, the excimer only forms in solution. Thus the peaks at 426.2 and 453.8 nm are more likely to be dominated by the excited states of stable dimers and aggregates.<sup>67</sup>



**Fig. 3.9** Fluorescence emission spectra of anthracene deposited on PE (1.8 $\times$  stretched) from methylcyclohexane solution with concentrations of 0.1, 4 and 8 mg/mL (black, red and blue lines respectively). Each set of spectra was recorded using different excitation wavelength. All spectra are shown integrated to have the area under the curve of the spectrum equal 1.

### 3.3.3 Fluorescence detected linear dichroism studies

Anthracene's fluorescent nature and our fluorimetry results motivated us to design a new fluorescence detected linear dichroism (FDLD) experiment to investigate the dimerisation of this molecule. Thus, for the first time, we set up a stretched PE<sup>OX</sup> FDLD experiment by depositing anthracene from different MeOH solutions onto PE<sup>OX</sup> films and recorded FDLD spectra in 0°-mode (the detector was placed in front of the incident light – Fig. 3.3) using a Bio-Logic MOS-450 spectrometer with a 400 nm long pass filter to avoid the unabsorbed incident light reaching the detector. Fig. 3.10 shows LD and FDLD spectra of a series of loads from anthracene solutions with different concentrations deposited on 1.8× stretched PE<sup>OX</sup>. Fig. 3.11 shows an overlay of selected spectra. Using different type of spectroscopy (absorbance versus fluorimetry) the signals in LD and FDLD show different sign.



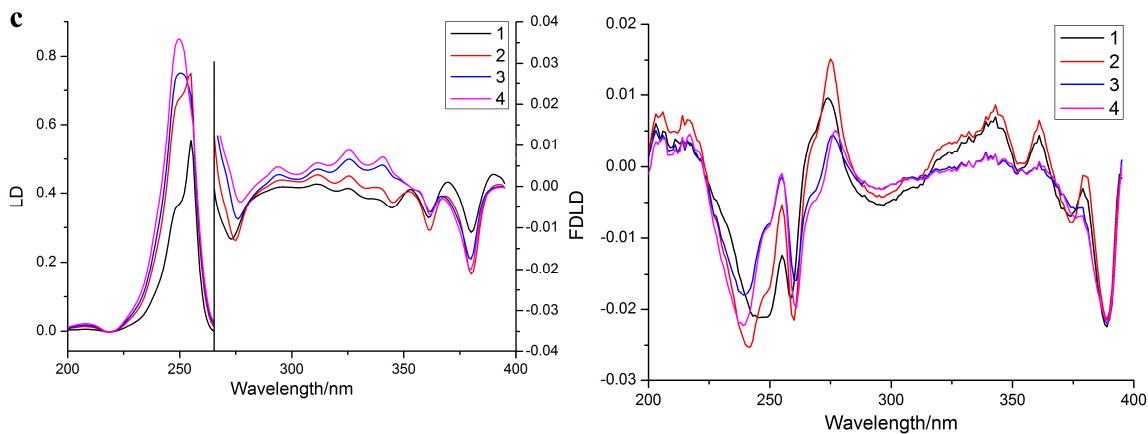


**Fig. 3.10** LD (left) and corresponding FDLD (right) spectra of anthracene deposited on 1.8x stretched PE<sup>OX</sup> from (a) 0.1, (b) 1 and (c) 4 mg/mL methanolic solution (drops of chloroform were added to help dissolve 4 milligrams of anthracene in methanol). The black line in each diagram (indicated as 1 in the legend) represents the first aliquot of sample (40 µL) on the film. Each number in the legend represents the number of aliquots (40 µL) added on the film.

Due to FDLD's higher sensitivity in comparison to LD, we were able to detect the formation of dimers and oligomers upon adding layers of molecules with greater sensitivity than was previously possible (Fig. 3.10). The first aliquot (40 µL) from a 0.1 mg/mL solution resulted the most monomeric spectrum judging from both LD and FDLD spectra. Adding more aliquots of sample did not cause significant shape change but only an increase in the intensity of LD bands. However, the FDLD spectra underwent an inversion in sign for the band at 255 nm and an increase in the intensity for the bands at 248 and 326 nm (3.8a). Loads from higher concentration (1 mg/mL) again did not show the presence of dimers in the LD spectra except for the final (14<sup>th</sup>) addition where a positive signal at 255 nm was apparent together with an increase in the intensity for the band at 248 nm. However, from the first aliquot, the FDLD spectrum showed a positive contribution to the signal at 255 nm overlaid on the broad negative band which increased in intensity upon adding more layers of molecules. Depositing more layers of anthracene molecules caused a change in the direction of the FDLD band at 248 nm, and appearance of the negative band at 387 nm (Fig. 3.10b). When the sample is deposited from 4 mg/mL solution a weak

negative LD band at 272 nm appeared which then red shifted to 276 nm when more sample was added. Also the band at 255 nm was obscured by the band at 250 nm. The short wavelength region of FDLD spectrum consists of a strong negative band at 240 nm, inverted long axis band at 255 nm with its shoulder at 249 nm, and a strong positive band at 275 with a shoulder at 266 nm. A strong negative band at 389 nm appears in the long wavelength region of spectrum (Fig. 3.10c).

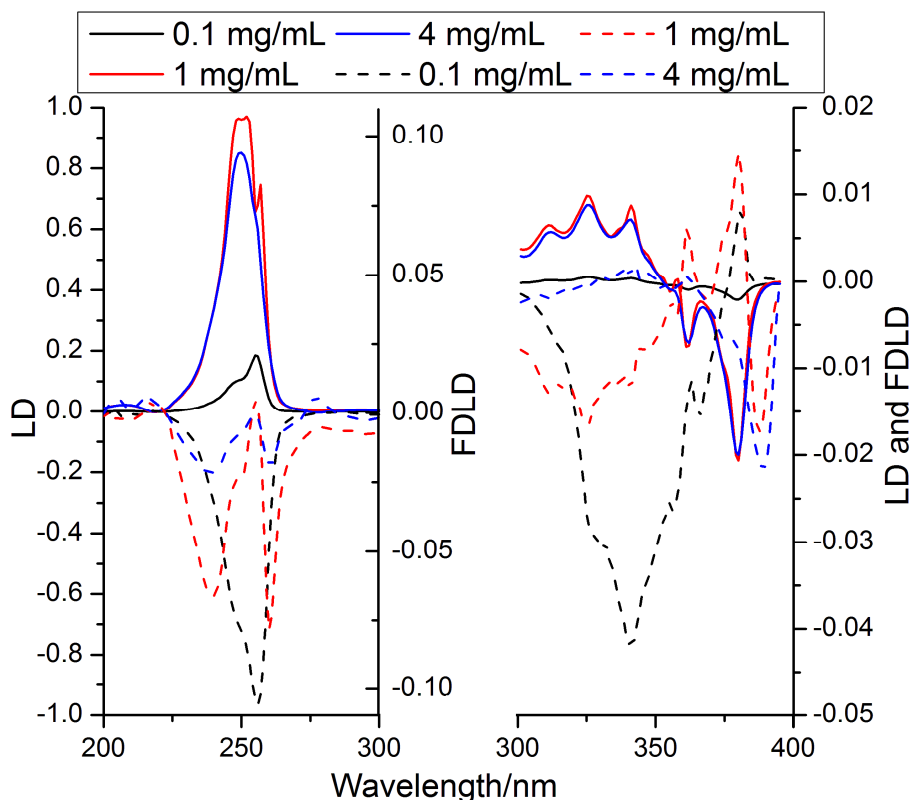


**Fig. 3.11** LD (solid) and FDLD (dashed) spectra of monomeric anthracene (black, 0.1 mg/mL) and oligomeric (red and blue, 1 and 4 mg/mL respectively) on PE<sup>OX</sup>.

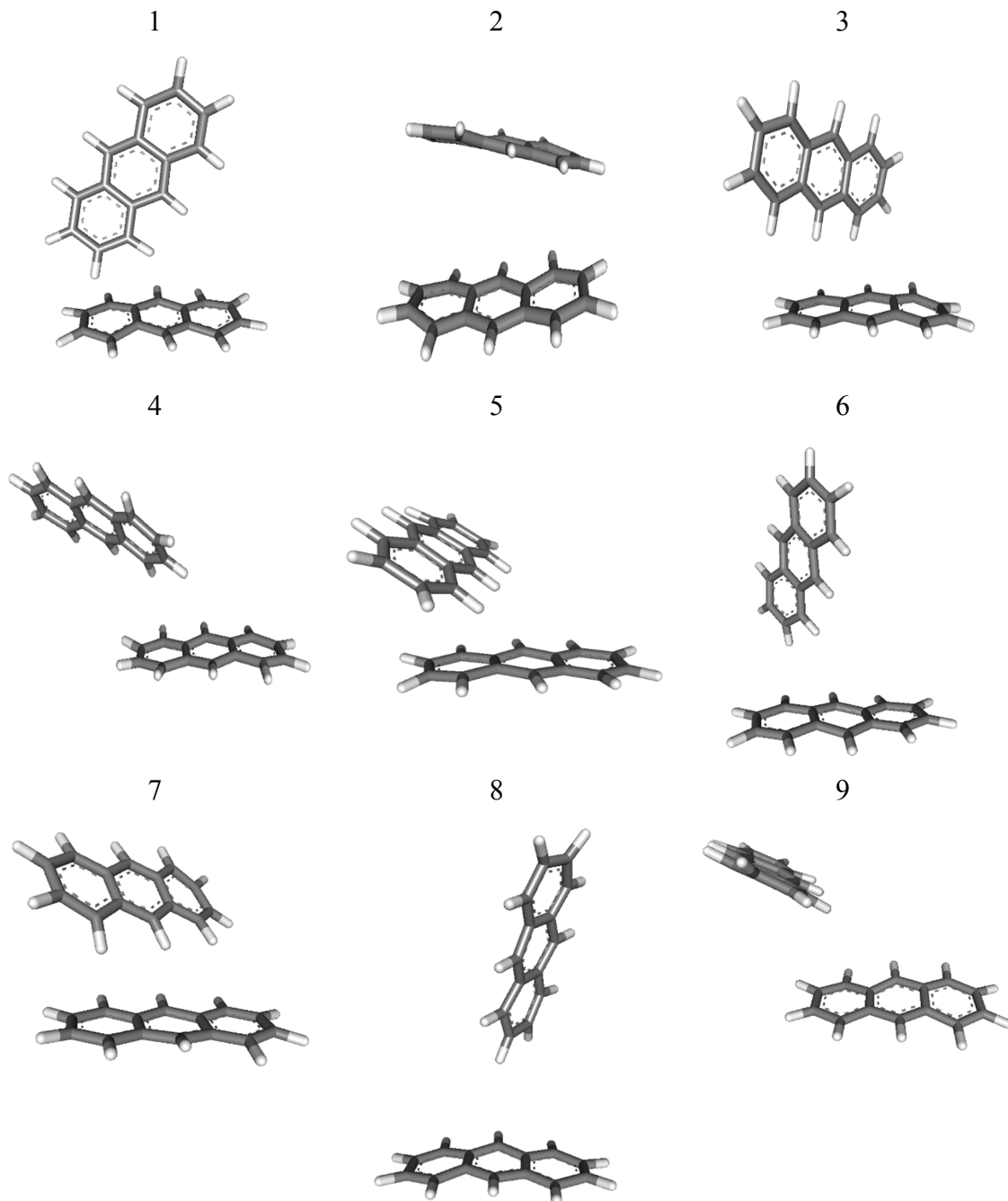
Fig. 3.11 shows the formation of different oligomeric anthracene structures upon increasing the concentration. FDLD spectra show more sensitivity and selectivity to the different types of dimeric structures. As discussed in §3.1 the monomeric anthracene molecules (0.1 mg/mL) orient with their long axis parallel to the stretching direction. Increasing the concentration leads to an intensity increase at  $\sim 240$  nm, an inversion in the

sign of the bands at 248 and 255 nm, and a band appearance at 388 nm in the FDLD spectrum (1 mg/mL). This corresponds to the dimer illustrated in Fig. 3.6b. When the concentration is 4 mg/mL, an extra positive band at 275 nm with a shoulder at 266 nm appears which is similar to the monomer long axis with 20 nm red shift. On the long wavelength of the FDLD spectrum the monomeric bands lose intensity and a strong dimeric band at 388 nm appears. This feature might have arisen from the formation of H-aggregates of anthracene with parallel planes with long axis rotated 90° to the stretching direction.

### 3.3.4 Computational modelling for possible dimers of anthracene (all computational simulations done for this chapter are performed by Dr. Shirin Jamshidi)

To evaluate the validity of our experimental data on dimerisation of anthracene, we compared them with the computational models generated using two different approaches of Molecular Dynamics (MD, AMBER program package)<sup>70,71</sup> and docking (Autodock Vina)<sup>72</sup>. In the MD approach, 15 molecules of anthracene were considered in contact with each other and methanol molecules in an octahedral box (399900.120 Å<sup>3</sup>). We deliberately chose the size of the box to be spacious enough so the molecules would move freely. Thus the possible dimeric configurations simulated by the software are only due to the favourable interactions between anthracene molecules and not because of the lack of space between them. The shape of the box was defined to be octahedral and not cubic to avoid molecules getting trapped in the corners of it. Anthracene molecules' movement in the box was simulated for 2 nanoseconds and 1000 frames were generated and the configurations suspected to be dimeric were selected. These configurations are shown in Fig. 3.12. The

angles between long axis and short axis of dimer unites of were calculated for each species (Table 3.3).



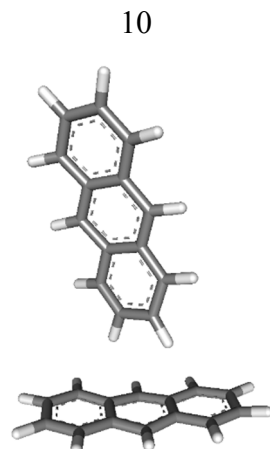


**Fig. 3.12** The schematic models of the possible dimers of anthracene generated by the Molecular Dynamics approach.

Using the docking approach we were able to calculate the energy level ( $-5.8$  kcal/mol) of the most stable possible dimer for anthracene with less than  $10^\circ$  difference between its unit's long axis and short axis (Fig. 3.13). This geometry is similar to one of the crystal structures proposed by Mathieson et al.<sup>64</sup>

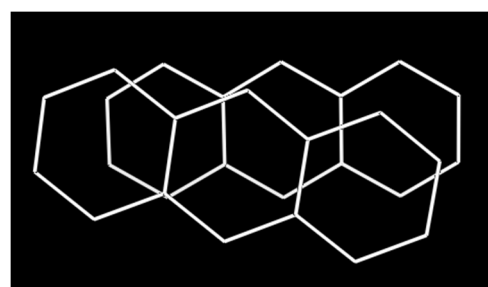


**Fig. 3.13** The schematic model of the most stable possible dimer of anthracene generated by the docking approach.

**Table 3.3** The calculated angles between long axis and short axis of dimer units presented in the Fig. 3.12 and 3.13.

Approach used	Figure	Longitudinal torsion (degrees)	Transverse torsion (degrees)
MD	3.12 - 1	8.25	72.75
	3.12 - 2	26.35	21.60
	3.12 - 3	35.77	77.95
	3.12 - 4	36.16	40.12
	3.12 - 5	41.56	81.12
	3.12 - 6	48.78	57.2
	3.12 - 7	48.95	13.41
	3.12 - 8	58.72	17.98
	3.12 - 9	69.85	40.99
	3.12 - 10	88.18	50.57
Docking	3.13	9.91	9.67

As shown in Table 3.3 computational simulations we have done suggest that there are more possible dimeric structures for anthracene than are reported in the literature. Such models could justify some of our experimental results on possible geometries for anthracene's higher order structures explained in this chapter. For example the models in Fig. 3.12-2 and Fig. 3.13 have similar configurations as H-aggregate dimer, and the model in Fig. 3.12-10 is close to the crossed-dimer configuration.

### 3.4 Conclusions

Our work on anthracene deposited on stretched film samples shows the importance of knowing what is being studied. For anthracene, the analyte must be deposited from quite low concentration solutions (<0.25 mg/mL) to ensure monomers dominate the spectroscopy. Films prepared from high concentration stock solutions of anthracene showed a variety of different higher order structures with corresponding variations in spectra resulting from different exciton couplings. The LD sign patterns can be readily

used to eliminate possible oligomer geometries, however, the overlay of spectra for different structures usually makes it challenging to definitively identify structures. Calculating the oligomeric exciton coupling effects on the absorbance and LD spectra of anthracene helped us identifying some dimeric conformations (Fig. 3.6 and Table 3.2). Our fluorescent spectroscopy experiments on solution samples with different concentrations and dried sample on PE films resulted in more information about different dimeric structures presenting in solution and dried films of anthracene. The FDLD data of anthracene on stretched PE, which was done for the first time, added a higher sensitivity and selectivity to our LD studies which is utilised more in §5 of this work. The FDLD experiments revealed that a slight change in the concentration of the sample deposited on PE films could lead to dimerisation. This had not been detectable before, using LD experiments. Computational simulations assisted us in justifying some of our experimental data interpretations on the possible geometries anthracene dimeric structures might have.



## **Chapter Four**

Optical properties of xanthene based fluorescent dyes studied by stretched film linear dichroism

### **Acknowledgement**

I would like to express my appreciation to Prof. Timothy R. Dafforn and Haydn Little from the University of Birmingham for their help.



## 4.1 Introduction

So-called xanthene dyes are commonly used to label proteins in order to probe their location and activity using fluorescence spectroscopy and microscopy. However, fundamental properties such as the polarizations of transitions for many of the dyes have not been available. In this chapter we report the use of oxidised polyethylene ( $\text{PE}^{\text{OX}}$ ) stretched film linear dichroism to determine the transition polarizations of xanthene, 9-methyl-2,3,7-trihydroxy-6-fluorone, pyronin Y, pyronin B, fluorescein, and rhodamine 6G (Fig. 4.1). The effect of the formation of higher order structures is also discussed when they occur.

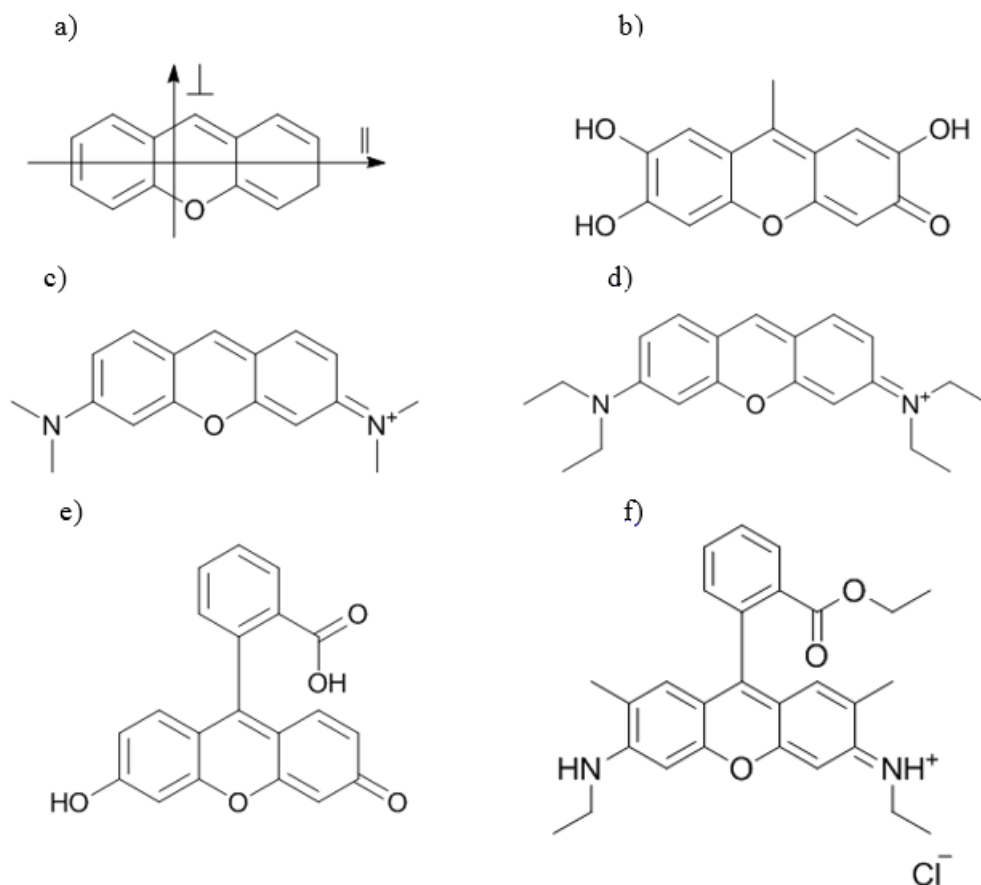


**Fig. 4.1** a) Xanthene with z and y axes indicated by || and ⊥ respectively, b) 9-methyl-2,3,7-trihydroxy-6-fluorone, c) pyronin Y, d) pyronin B, e) fluorescein, and f) rhodamine 6G.

## 4.2 Material and methods

Xanthene and 9-methyl-2,3,7-trihydroxy-6-fluorone were obtained from Aldrich and MP Biomedicals respectively, the other dyes were purchased from Sigma and used as received. Methanol and chloroform were obtained from respectively VWR Chemicals and Fisher Scientific. The polyethylene film was obtained from Glad® Snap Lock® plastic bags. The film was treated, as reported in §2, using an Emitech K1050X Plasma Asher with parameters: O<sub>2</sub> at 10 mmHg, 50 W RF power level, 1 minute ashing time to increase the hydrophilicity of the surface.<sup>51</sup>

### 4.2.1 PE<sup>OX</sup> film preparation

Polyethylene films (4 cm × 2.5 cm) were cut from Glad® Snap Lock® plastic bags. PE<sup>OX</sup> pieces were then prepared by treating the films in a Emitech K1050X Plasma Asher connected to an oxygen gas supply for 1 min at 50 W power setting. Then they were clamped between the jaws of a home built film<sup>2</sup> stretcher with the initial distance between the jaws being 2.5 cm. It has been shown in general that it does not matter whether the sample is added to PE films before or after stretching,<sup>51</sup> though different stretching amounts do affect the PE crystallite alignment and population which does affect the spectrum observed.<sup>2</sup> However, when a dye is prone to assembling into higher order structures, different films prepared in nominally the same way can give rise to different spectra, so repeat experiments are required.

#### 4.2.2 Linear dichroism and UV-visible absorbance spectroscopy studies

The protocol used in this work to collect single LD and absorbance spectra was first to stretch the film, then add an aliquot of solvent (methanol:chloroform = 70:30), measure the baseline and then add the sample and measure the sample LD and absorbance. When degree of film stretch was a variable a baseline film and a sample film were stretched in the same way and measured for each stretch factor. Data were collected using either a Jasco (Japan) J-720 (adapted to use a 150 W Xe lamp) or a Jasco J-815 spectropolarimeter both adapted for LD spectroscopy. The baseline spectra were subtracted from the sample spectra. Unfortunately, this methodology did not completely account for differences in scattering between the sample and baseline films, particularly in the absorbance spectra. This resulted in low wavelength LD<sup>r</sup> signals being attenuated. To calculate LD<sup>r</sup> spectra we therefore subtracted an additional baseline by zeroing spectra in linear steps at clear minima in the spectra using OriginPro 8.5.1 (OriginLab Corporation, US).

Solution absorbance spectra were obtained using a Jasco V-660 spectrophotometer with 0.1 mg/ml of sample dissolved in spectroscopic grade methanol. Quartz cuvettes were used with a path length of 0.01 cm. A background spectrum was measured for the solvent in the cuvette and subtracted from the sample spectrum.

Stock solutions of each dye were prepared by dissolving dye in analytical grade methanol and chloroform (70:30). An aliquot of 30 µl was dispensed onto each side of the PE<sup>OX</sup> film of desired stretch ratio (thus doubling the amount of dye while reducing the propensity to oligomerise) and the solvent was allowed to evaporate

over 3 minutes in the dark under a fume hood to maintain a controlled environment and to avoid degradation of the dye. 0.2 mg/mL and  $1.8 \times$  stretched PE<sup>OX</sup> films were used for the LD by the factor of rotation experiments. Other experiments were at concentrations noted in the figure captions.

### 4.3 Results and discussion

Although many of the highly fluorescing xanthene dyes often used as labels for proteins have a single aromatic ring conjugated to a xanthene motif (Fig. 4.1), most of their spectroscopy is due to the planar xanthene motif. We therefore began our work with the simpler structures of xanthene, 9-methyl-2,3,7-trihydroxy-fluorone (to represent the main chromophore of fluorescein), and pyronin Y and B (to represent the main chromophore of the rhodamine dyes). The key challenge in this work was the measurement of reproducible data. The dyes are prone to assembling into a range of dimer and higher order structures or aggregates, similar to the situation observed for anthracene in §3. These effects were particularly a problem given the evaporation method used to produce the film sample for spectroscopy. Further, absorbance detects all species on the film, whereas LD detects only the oriented molecules making measurement of LD<sup>r</sup> challenging. To address these issues we increased the relative populations of monomers by loading less dye (though the intensities are concomitantly reduced) using more dilute stock solutions of dye. Conversely, where a population of higher order structures was required high concentration samples were loaded from higher concentration stock solutions. The degree of stretch of the film also affects the populations, with high stretch factors

favouring monomers, presumably due to the increase in oriented crystallites in the film<sup>9</sup> (§2 and 3). The molecules studied in this work are all of sufficiently high symmetry that we can assume the transitions are polarized either along the long axis of the xanthene motif or perpendicular to it. The three-ring structures when bound to the films as isolated monomers are expected to align with their long axis along the PE<sup>OX</sup> stretch directions.<sup>51</sup> The situations for the more complex structures (fluorescein and rhodamines) and for oligomeric structures is less obvious and are discussed below.

### 4.3.1 Xanthene

Xanthene is a semi-planar molecule with group symmetry C<sub>2v</sub> mostly used as a fungicide and also is nominally the parent compound for all the fluorescein and rhodamine dyes. Spectra for xanthene are shown in Fig. 4.2. There is little or no spectral shape change as a function of stretch just a gradual increase in orientation. Also the increase in concentration does not change the spectrum shape. It is clear from these data and Eq. 1.1 (§1) that xanthene behaves uniaxially on PE<sup>OX</sup> and also that the weak transition from 280–300 nm is short axis (⊥) polarized (negative LD with LD<sup>r</sup> half the magnitude of the other bands) and the other two accessible transitions are long axis (||) polarized.

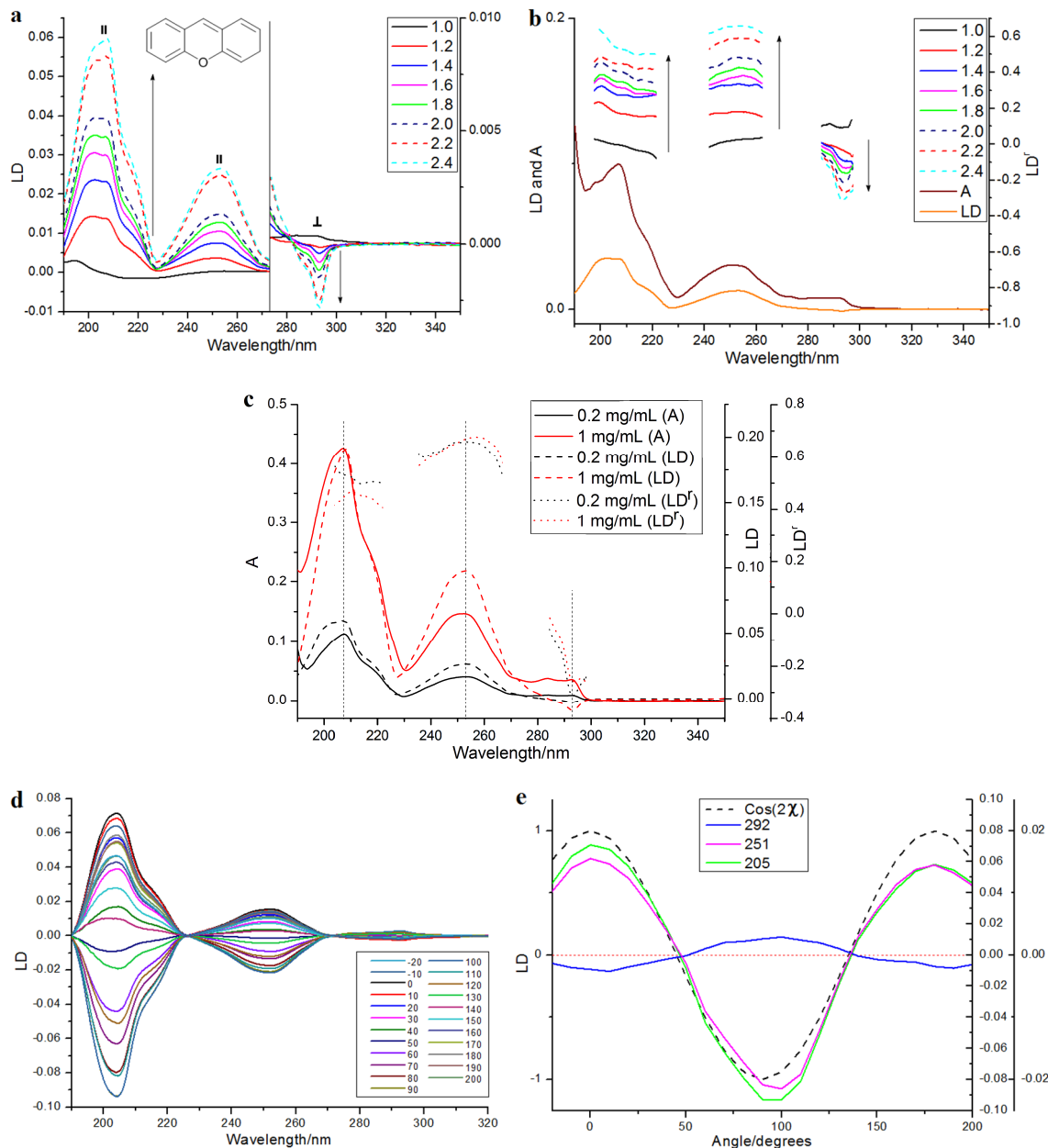


**Fig. 4.2** Spectra of xanthene on PE<sup>OX</sup> dropped from a 0.2 mg/mL solution onto an unstretched film and then stretched (stretch factor as indicated in inset). || and ⊥ indicate transition polarization with respect to the xanthene long axis in Fig. 4.1. (a) LD, (b) LD' calculated as indicated in §2 (Eq. 2.1) overlaid with absorbance and LD spectra of ×2.4 stretched PE<sup>OX</sup>. (c) absorbance, LD and LD' spectra of different concentration (0.2 and 1 mg/mL) on 2.4× stretched PE<sup>OX</sup> (d) wavelength scans, (e) signal at 205, 251 and 292 nm as a function of rotation angle  $\chi$  overlaid on a plot of  $\cos(2\chi)$ .

### 4.3.2 9-Methyl-2,3,7-trihydroxy-6-fluorone

The fluorone chromophore of fluorescein is midway between 9-methyl-2,3,7-trihydroxy-6-fluorone ( $\text{MeOH}_3\text{-fluorone}$ ) and xanthene so we also analysed the spectra for  $\text{MeOH}_3\text{-fluorone}$ . It is a  $\mathbf{C}_s$  symmetry molecule as illustrated in Fig. 4.1, though can be treated as approximately  $\mathbf{D}_{2h}$ . We found it challenging to obtain a monomeric LD spectrum with reasonable signal to noise ratio for this molecule. The small LD signals also meant that scattering affected the baselines noticeably, particularly at lower wavelengths. Fig. 4.3a shows the overlay of two LD spectra collected on  $2.4\times$  stretched films prepared from 0.01 and 0.2 mg/mL stock solutions. Fig. 4.3b shows the overlay of corresponding absorbance and  $\text{LD}^r$  spectra with a solution spectrum. The 0.01 mg/mL spectrum with positive LD maxima at 450 nm and 245 nm and negative maximum at 280 nm (see right hand axis of Fig. 4.3b) compares in position with the vibronically resolved solution phase spectrum, so we assume both are monomeric. The 450 nm and 245 nm transitions are therefore long-axis polarized ( $\parallel$ ) and 280 nm short-axis polarized ( $\perp$ ).

The 0.2 mg/mL spectrum in Fig. 3a is shifted to shorter wavelength than the 0.01 mg/mL one with additional positive LD intensity at 400 nm. In addition a broad negative LD is apparent from 290–350 nm. We attribute the extra features to dimers or higher order assemblies of the  $\text{MeOH}_3\text{-fluorone}$ . Given there is little or no extra intensity on the long wavelength side of the 450 nm band, a geometry similar to that of the so-called H-aggregate, where the monomers are stacked vertically with their long axes parallel to one another (Fig. 8) is most likely. The 400 nm dimer signal has positive LD indicating alignment along the stretch direction, thus the dimer

retains the monomer orientation. The lower wavelength regions are more complicated to interpret due largely to smaller signals and higher scattering. The 320 nm region is almost certainly short-axis polarized ( $\perp$ ), whereas the 245 nm region is long axis polarized ( $\parallel$ ). It should be noted that the 0.2 mg/mL absorbance spectrum has evidence of structures not apparent in the LD with significant intensity above 550 nm which is presumably due to assemblies that do not orient because they are far from the polymer film.

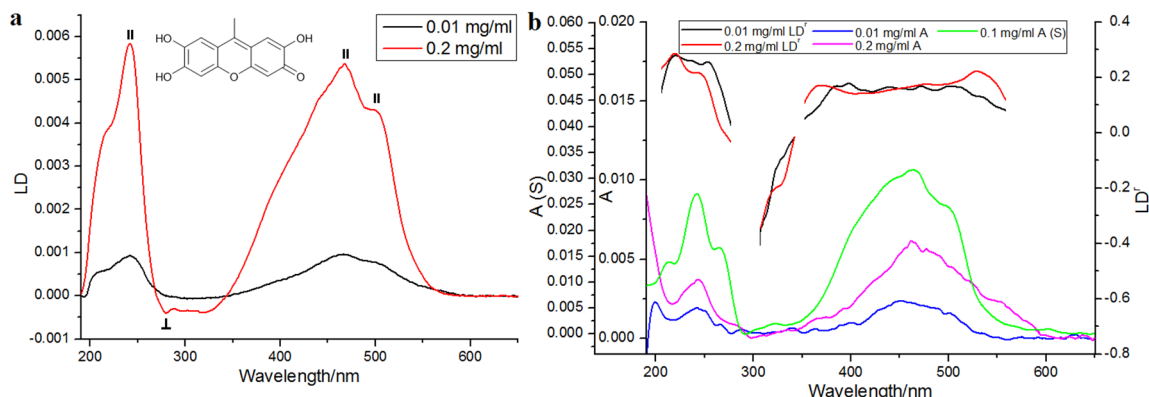


**Fig. 4.3** (a) LD spectra of 9-methyl-2,3,7-trihydroxy-6-fluorone on PE<sup>OX</sup> deposited from 0.01 and 0.2 mg/mL solution and stretched by a factor of  $\times 2.4$ .  $\parallel$  and  $\perp$  indicate transition polarization with respect to the xanthene long axis in Fig. 2. (b) Absorbance and LD' spectra of the LD spectra in Fig. 3(a) overlaid with solution absorbance spectrum (S).

#### 4.3.3 Pyronin Y and pyronin B

Pyronin Y and B are similar C<sub>2v</sub> molecules (Fig. 4.1c, d) chosen for this work because of their relationship to the xanthene motif part of the rhodamine dyes. As with other dyes, the pyronins are prone to dimerisation and oligomerisation and we

had to use a low stock solution concentration to be able to observe the monomer spectrum.

According to Jaconsen et al.,<sup>73</sup> the pyronin Y long wavelength monomer maximum is at 547 nm with a 511 nm H-aggregate (Fig. 4.8a, parallel vertical stack arrangement, presumably with the substituents on alternating sides) peak.<sup>74</sup> As shown in Fig. 4.4, the film LD from the most dilute pyronin Y solution has a larger positive LD component at 551 nm and a smaller one at 515 nm. When the stock solution concentration is increased and dimer or oligomers dominate the spectrum, a single positive LD band at 501 nm dominates (it is at ~509 nm in the absorbance) with intensity at both higher and lower energy relative to the monomer. Small negative LD signals also emerge at 350 nm and 300 nm for the oligomers. These peaks may be present in the monomer spectrum, but would be below the limit of detection in the monomer spectrum if present due to the concentration needed to ensure monomers dominate. Dimers/oligomers also have positive LD at 254 nm. Overall we can conclude that the transitions are long axis polarized above 400 nm, short axis polarized between 300 and 400 nm, and predominantly long axis polarised below 300 nm, though of mixed polarisation below 250 nm. These conclusions are consistent with the polyvinyl alcohol film polarized absorbance and the Pariser-Pople calculations of Okubo et al.<sup>75</sup>

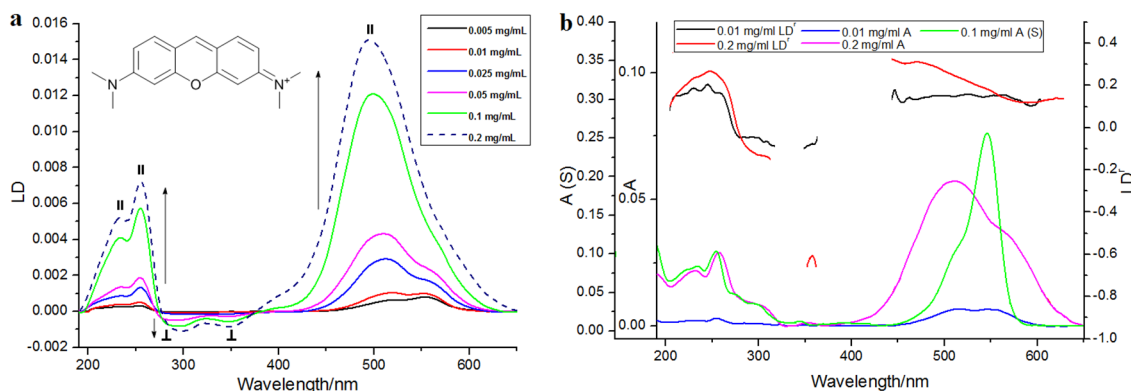


**Fig. 4.4** (a) LD spectra of pyronin Y on PE<sup>OX</sup> deposited from solutions of concentrations indicated in the Figure. || and ⊥ indicate transition polarization with respect to the xanthene long axis in Fig. 4.1a (b) Absorbance and LD' spectra of samples with concentrations 0.01 and 0.2 mg/ml overlaid with solution absorbance spectrum (S) and the dimer/monomer difference spectrum.

The wavelength maximum for pyronin B monomer is deemed to be at 552 nm and for the H-aggregates at 520 nm.<sup>74</sup> The pyronin B LD spectra of Fig. 4.5 show comparatively little shape change with increasing concentration until 0.1 mg/mL at which point negative high-energy and positive low energy intensities become apparent. The detectable monomer absorbance signals all have positive LD so are long axis polarized. The LD thus makes it more obvious than does the absorbance that the bulky substituents of pyronin B make more complicated structure(s) than was assumed for the simple H-aggregate of pyronin Y above. Assuming that the pyronin B dimer is formed by associating a second monomer with one already aligned on the film, a geometry giving rise to an in-phase positive component at longer wavelength and an out-of-phase negative component at shorter wavelength component<sup>51</sup> is to stack the pyronins as in a brick wall thus somewhere between an H- and J-aggregate as illustrated in Fig. 4.8. This geometry makes room for the bulky substituents and allows for effective  $\pi$ - $\pi$  interactions.

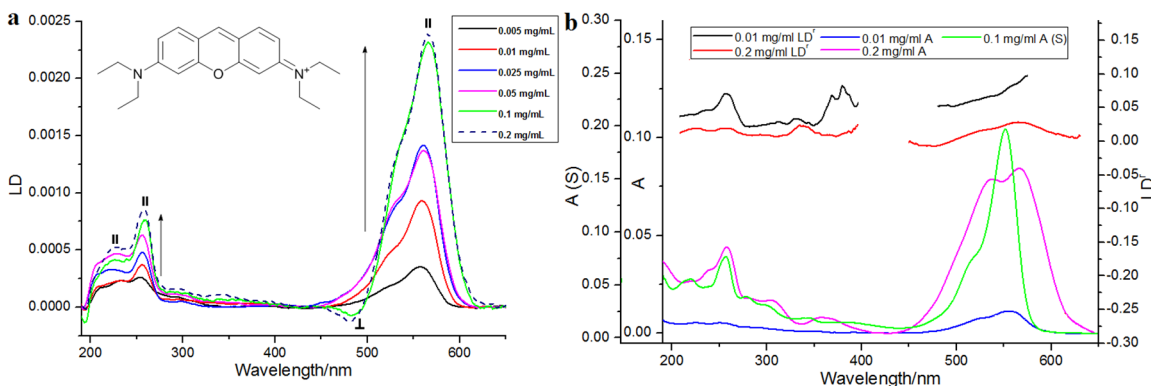


**Fig. 4.5** (a) LD spectra of pyronin B on  $\text{PE}^{\text{Ox}}$  deposited from solutions of concentrations indicated in the Figure. || and  $\perp$  indicate transition polarization with respect to the xanthene long axis in Fig. 4.1. (b) Absorbance and  $\text{LD}'$  spectra of samples with concentrations 0.01 and 0.2 mg/ml overlaid with solution absorbance spectrum (S) and the dimer/monomer difference spectrum.

#### 4.3.4 Fluorescein

Film LD spectra for fluorescein are given in Fig. 4.6. The low concentration sample (0.01 mg/mL) has positive LD at 497 nm and 465 nm, perhaps a very small negative LD at 322 nm, positive LD at 277 nm, and positive LD at 230 nm in accord with literature positions for monomer absorbances.<sup>76,77</sup> Thus, as with fluorone, we conclude that: the longest wavelength band is polarized along the long axis (||) of the xanthene chromophore; there is probably a short axis polarized ( $\perp$ ) transition at 322 nm; and the next bands are long axis polarized. At even slightly higher concentrations, the film LD spectrum becomes much more complicated with evidence of a small negative LD at 560 nm, positive LD at 516 nm, and negative LD at 453 nm with probably another component between these two. The lower wavelength region also changes. The number of new bands suggests a variety of oligomeric structures are formed on the film. The fluorescein oligomeric spectra

resemble those of pyronin B suggesting that fluorescein can also stack on the PE film in the brick-like structure of Fig. 8b.

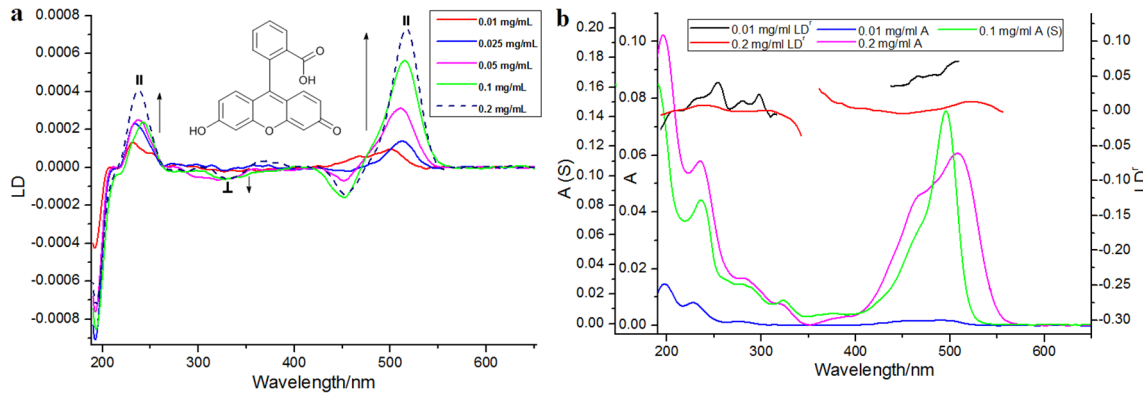


**Fig. 4.6** (a) LD spectra of fluorescein on PE<sup>OX</sup> deposited from solutions of concentrations indicated in the Figure. || and ⊥ indicate transition polarization with respect to the xanthene long axis in Fig. 2. (b) Absorbance and LD' spectra of samples with concentrations 0.01 and 0.2 mg/ml overlaid with solution absorbance spectrum (S) and the dimer/monomer difference spectrum.

#### 4.3.5 Rhodamine 6G

Fig. 4.7 shows the film LD and absorbance spectra of rhodamine 6G as a function of concentration of stock solution. At low concentration there is a larger positive LD peak at 535 nm and smaller positive peaks at 350, 290, 248, and 229 nm indicating these are all polarized along the long axis (||) of the xanthene chromophores. Comparison with solution absorbance data<sup>87</sup> with the film spectra indicates that this spectrum is monomeric rhodamine 6G. The high concentration samples behave similarly to the fluorescein, though have a greater propensity to stack.

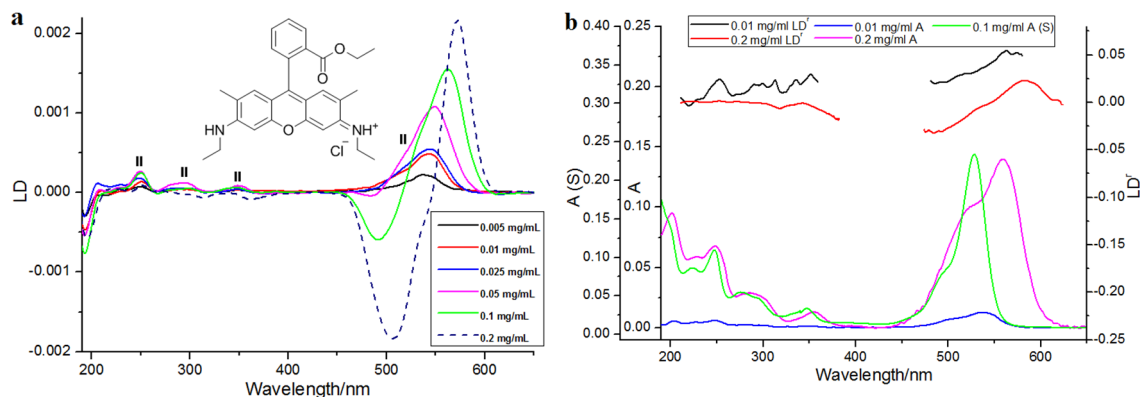


**Fig. 4.7** (a) LD spectra of rhodamine 6G on PE<sup>OX</sup> deposited from solutions of concentrations indicated in the Figure. || and ⊥ indicate transition polarization with respect to the xanthene long axis in Fig. 4.1. (b) Absorbance and LD' spectra of samples with concentrations 0.01 and 0.2 mg/ml overlaid with solution absorbance spectrum (S) and the dimer/monomer difference spectrum.

#### 4.4 Conclusions

We have undertaken careful studies of xanthene dyes on oxidised polyethylene film in order to be able to assign the polarizations of the component transitions. By depositing samples from 0.01 mg/mL solutions we were able to measure monomer stretched film spectra. Although xanthene is nominally the parent compound of these dyes, its spectroscopy differs significantly from the others. It has a small negative (short axis polarized, ⊥) LD band at ~290 nm and its higher energy transitions are long axis (||) polarised. The extra conjugation introduced into the xanthene moiety of fluorones, pyronins, fluoresceins and rhodamines results in an intense long axis polarized transition in the region of 500 nm. They also have long axis (||) polarized transitions from about 280 nm downwards in wavelength. There are suggestions of a weak short axis (⊥) polarized transition in the region of 320–350 nm in each case.

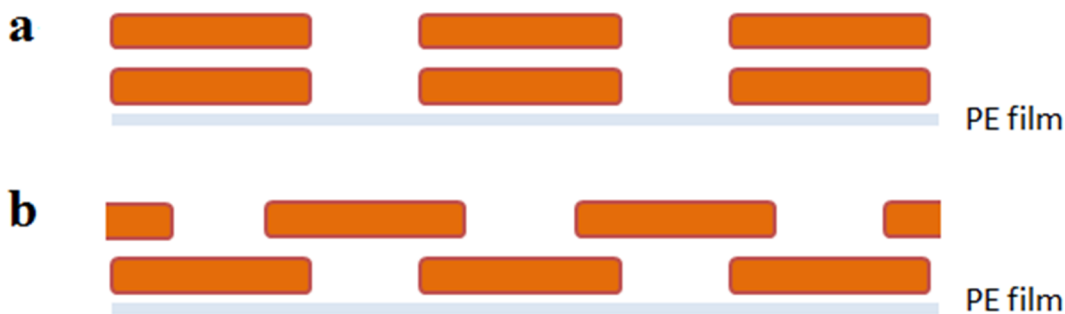


**Fig. 4.8** (a) H-aggregate geometry which is consistent with the data for MeOH<sub>3</sub>-fluorone and pyronin Y at high concentrations. (b) Offset stacked geometry which is consistent with the data for pyronin B, fluorescein, and rhodamine 6G at high concentrations.

Upon depositing the dyes from high concentration solutions, with the exception of xanthene itself, the spectra changed shape showing intensity on either the high energy side or on both high and low energy sides of the lowest energy transition indicating exciton coupling of the dyes (as explained in §3). 9-Methyl-2,3,7-trihydroxy-6-flourone and pyronin Y spectra are suggestive of them forming H-aggregates (parallel vertical stacks, Fig. 4.8a) aligned along the film stretch direction. This is consistent with the literature for pyronin Y. Pyronin B has also been suggested to form H-aggregates in solution, however, on the films we observed both high and low energy exciton components whose high energy term was negative in sign. A geometry that gives this sign pattern is an offset H-aggregate like a portion of a brick wall aligned along the film stretch direction (Fig. 4.8b). We postulate this is the geometry adopted in the pyronin B dimers/oligomers. Fluorescein and rhodamine 6G both follow the pyronin B spectroscopy so may also be adopting a brick-like stacking, presumably driven by the need to avoid the extra substituents overlapping.

# **Chapter Five**

Molecular dimerisation investigation using  
stretched polyethylene linear dichroism and  
fluorescence detected linear dichroism

## **Acknowledgement**

I would like to thank Professor Alison Rodger and Alan Wemyss for helping me with the FDLD theory development.



## 5.1 Introduction

Fluorescence detected circular dichroism (FDCC) was first introduced by Douglas Turner and Ignacio Tinoco in 1974.<sup>79</sup> They measured the difference in fluorescence intensity when the incident light was left and right circularly polarised to obtain the CD spectrum of single chromophore in a micromolecule when the chromophore was fluorescent. They developed the method by assuming that the excitation spectrum of the fluorescent chromophore is similar to its absorbance spectrum. The FDCC spectra can be collected by any CD spectrometer in the same way as was done by Turner and Tinoco, by moving the photomultiplier tube to 90°, with the difference that in the new spectrometers the Pockels cells, which are voltage-controlled waveplates, are replaced by photoelastic modulators (PEM). In order to record a FDCC spectrum a longpass filter with a selected wavelength is inserted in front of the photomultiplier tube, so by blocking the excitation light, only the fluorescence reaches the detector (Fig. 5.1).

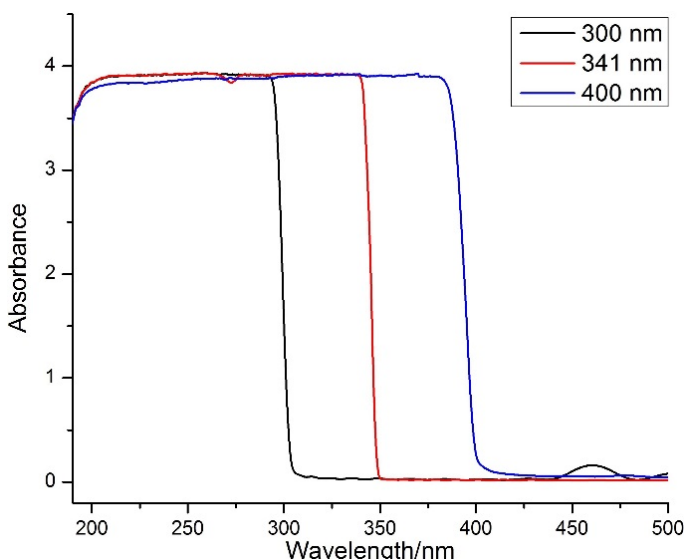


**Fig. 5.1** The absorbance spectra of air recorded when 300 (black), 341 (red) and 400 nm (blue) longpass filters are inserted in front of the PEM (after subtraction of the corresponding spectra of air when the filter was not placed).

A similar experiment can be performed in linear dichroism mode if a spectropolarimeter is adapted for LD spectroscopy. Fluorescence detected LD (FDLD) has some potential advantages over conventional LD experiments, if a fluorophore is being studied, as it is expected to require lower concentrations and be more sensitive to the changes in the structure and alignment of the molecules under study.<sup>80</sup> The other advantage is the selectivity of the technique, so if the absorption wavelength of the fluorescent chromophore is coincident with that of other chromophores in the system, their LD signal can be studied independently. Morimatsu et al. utilised FDLD to analyse the structure of RecA–DNA complex filaments.<sup>81</sup> This helped them to achieve information about the alignment of ethidium bromide residues of RecA–DNA–ethidium bromide complex, whereas LD measurements provides only the sum of the signals related to the complex obscured by the signal from DNA at ~258 nm.

Our results in §3 showed that FDLD is more sensitive to the change in the alignment and dimerisation of anthracene molecules than LD experiments. In this chapter we studied the FDLD of a group of molecules, including 4',6-diamidino-2-phenylindole (DAPI, a fluorescent stain usually used to bind to the minor groove of A–T rich sequences of DNA<sup>57,82</sup>) and four polycyclic aromatic hydrocarbons (naphthalene, pyrene, perylene and olympicene) depicted in the Fig. 5.2. In particular we considered the role of their degree of alignment and the potential complications caused by their dimerisation.

## Detected Linear Dichroism

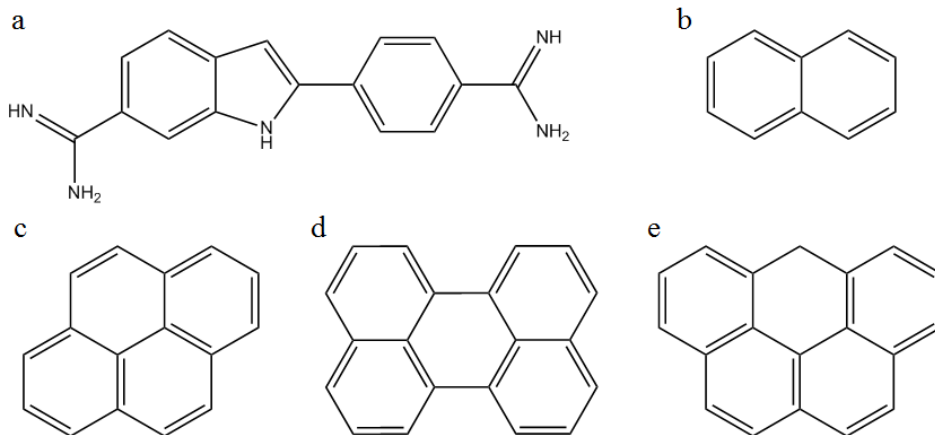


**Fig. 5.2** The chemical structure of a) 4',6-diamidino-2-phenylidole, b) naphthalene, c) pyrene, d) perylene and e) olympicene.

## 5.2 Materials and methods

DAPI, naphthalene and perylene were purchased from Sigma and pyrene was obtained from Janssen Chimica. Olympicene was synthesised by A. Mistry at the University of Warwick.<sup>83</sup> All chemicals were used without further purification. Methanol (Laboratory grade, Fisher Chemicals) was used as the solvent. Different concentrations of each molecule were prepared by dissolving the solid in methanol.

The longpass cut-off filters used in this work were of the “step-function” series bought from Semrock.

### 5.2.1 UV-visible experiments

The UV-visible spectra of the methanolic solutions (0.05–0.1 mg/mL) of each sample were recorded using a 0.1 cm pathlength cell and a Jasco V-660 UV-visible spectrophotometer. Methanol's spectrum was used as the background.

### 5.2.2 Fluorimetry experiments

The emission fluorescence spectra of the methanolic solutions (0.01–0.1 mg/mL) of each sample were recorded using a 0.5 centimeter-pathlength-cell and a Jasco FP-6500 spectrofluorometer. A bandpass of 3 nm for both monochromators (excitation and emission) was set. The excitation wavelength for each sample was set on the most intense peak of its UV absorbance spectrum.

The UV-visible and emission fluorescence spectra of samples helped us to choose the most suitable long-pass-filter for each sample (Table 5.1) so to block the excitation wavelength and only record the emission spectra.

### 5.2.3 Film preparation

The PE<sup>OX</sup> films were prepared as described in §2.

### 5.2.4 Linear dichroism and fluorescence detected linear dichroism experiments

The LD and FDLD spectra of samples (with different concentrations) deposited on 1.8× stretched PE<sup>OX</sup> film were recorded in 0° geometry using a BioLogic MOS-450 spectrophotometer as explained in §3. Sufficient signal:noise ratio was achieved with a 4 nm bandpass for both excitation and emission monochromators. The FDLD experiments were performed with the same conditions used for collecting LD spectra but also inserting a long-pass-filter (Table 5.1) in front of the photomultiplier tube. The PE<sup>OX</sup> films' spectra were used as the background in each case. Each time an aliquot (~40 µL) of the sample (apart from naphthalene) was deposited on PE<sup>OX</sup>, the LD and FDLD spectra of it were recorded by averaging 2 and 3 spectra respectively. All spectra were recorded using a 0.5 nm/s scanning speed. Sample aliquots were added until a change in the shape of the spectrum was noticed. In the case of naphthalene, 14 single accumulation spectra were collected for the sample deposited from different concentrations on PE<sup>OX</sup> and then the spectra were compared with each other and those of different concentrations as discussed below.

**Table 5.1** Longpass filter cut-offs used to record FDLD spectra of each sample.

Sample	Longpass filter used / nm		
	300	341	400
<b>DAPI</b>			×
<b>Naphthalene</b>	×		
<b>Pyrene</b>		×	×
<b>Perylene</b>			×
<b>Olympicene</b>		×	

### 5.3 Results and discussion

The absorbance and emission fluorescence spectra of DAPI and different polycyclic aromatic hydrocarbons were recorded in order to choose the right longpass filter to block the absorbance wavelengths and allow fluorescence wavelength reaching the detector to record the FDLD spectra. More aliquots of each solution were added to induce dimerisation of the molecules deposited on the stretched PE<sup>OX</sup>.

#### 5.3.1 4',6-diamidino-2-phenylindole

The absorbance and fluorescence spectra of DAPI are shown in the Fig. 5.3. Table 5.2 shows the wavelengths for DAPI's absorbance and fluorescence spectra. To block the absorbing wavelengths used in the excitation spectra we used a 400 nm longpass filter which allows most of the emitted light to reach the detector and none of the incident light.

## Detected Linear Dichroism

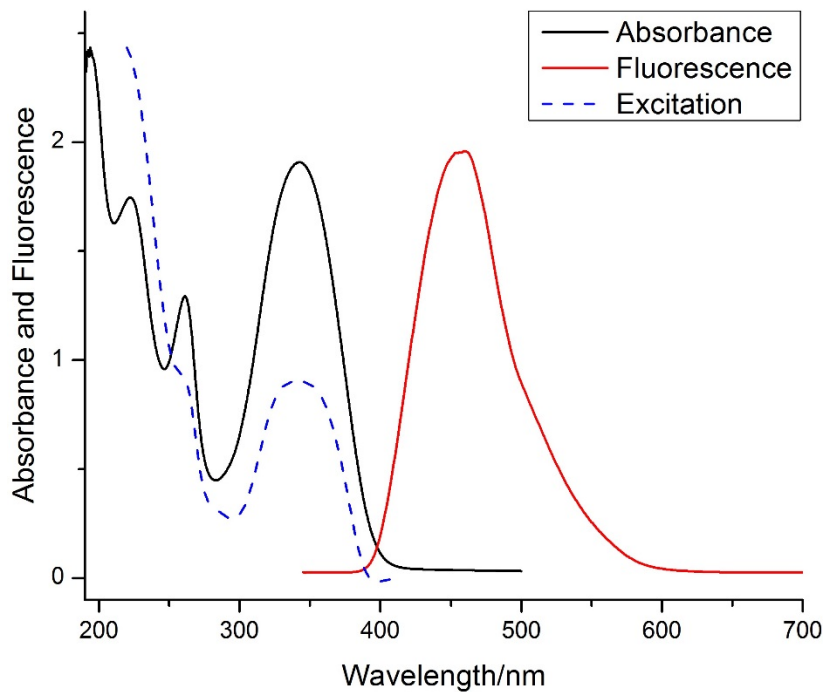


**Fig. 5.3** The absorbance, fluorescence emission (excitation wavelength: 342 nm) and excitation (emission wavelength: 455 nm) spectra of DAPI (0.1 mg/mL).

**Table 5.2** The absorption and emission wavelengths of DAPI from the literature<sup>84</sup> compared with the data we recorded in our laboratory. The error in peak wavelengths is less than 2 nm.

Absorbance / nm		Fluorescence / nm	
Recorded data	Literature	Recorded data	Literature
194		457	453
222			
261	258		
342	341		

As is reported in §2, using PE<sup>OX</sup> enabled us to study the alignment factor and transition moments of oriented DAPI molecules. The molecule's LD signals on PE<sup>OX</sup> show a slight red shift from their wavelengths in the solution absorbance spectrum which is due to major conformational order, resulting in different energy levels distribution (Fig. 5.3). The FDLD spectrum of DAPI on PE<sup>ox</sup> contains an intense negative band at 300 nm and some very weak bands below 258 nm (Fig. 5.4b and d). Adding more aliquots (40 µL) of DAPI did not lead to a change in the shape of DAPI's LD nor FDLD spectra. As shown in the Fig.

5.3 adding more sample only causes a slight fluctuation in the intensity of peaks in the LD and FDLD spectra of DAPI. This shows that there is no dimerisation occurring on PE<sup>OX</sup>.

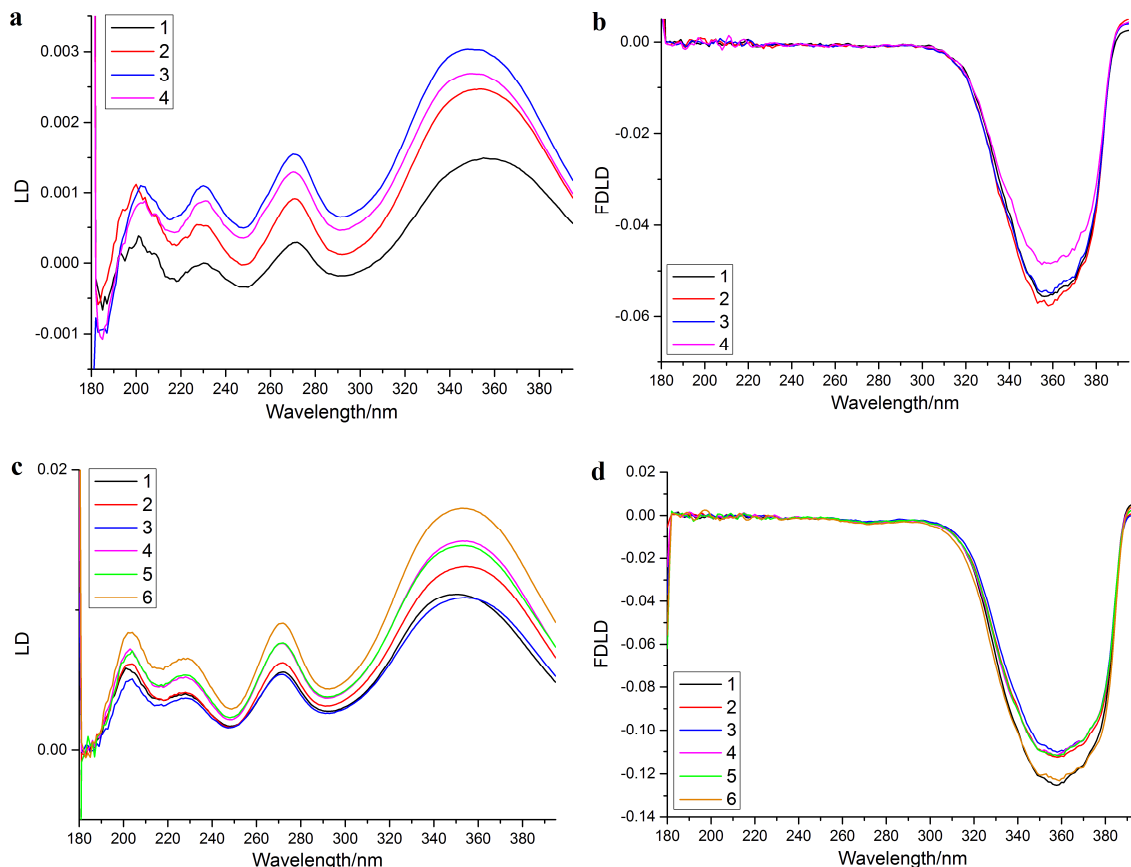


**Fig. 5.4** LD (left) and corresponding FDLD (right) spectra of DAPI deposited on 1.8 $\times$  stretched PE<sup>OX</sup> from (a and b) 0.01 and (c and d) 0.1 mg/mL methanolic solutions. The black line in each diagram (indicated as 1 in the legend) represents the first aliquot of sample (40  $\mu$ L) on the film. Each number in the legend represents the number of aliquots (40  $\mu$ L) added on the film.

As explained above and shown in Fig. 5.5, increasing the concentration (from 0.01 to 0.1 mg/mL) does not change the shape of the LD nor FDLD spectra of DAPI. The slight increase in the intensity of 0.1 mg/mL spectra is only due to the higher absorption caused by the increased amount of sample through which the light beam passes.

## Detected Linear Dichroism

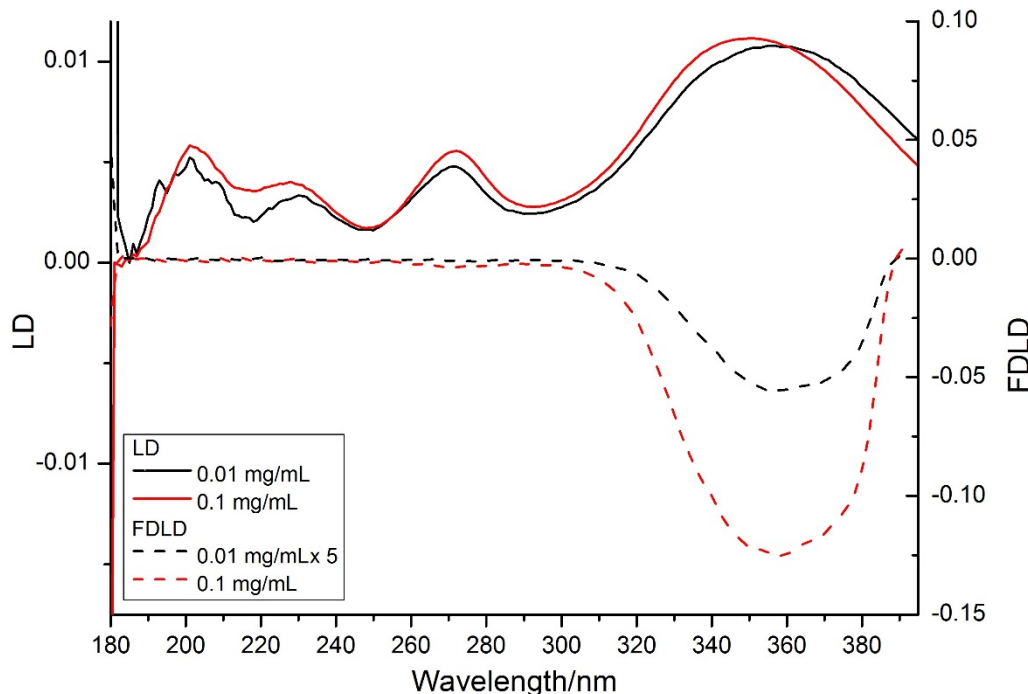


**Fig. 5.5** LD (solid) and FDLD (dashed) spectra of DAPI deposited on  $\text{PE}^{\text{OX}}$  ( $1.8\times$  stretched) from methanolic solutions with different concentrations: 0.01 (black) and 0.1 (red) mg/mL.

### 5.3.2 Naphthalene

In contrast to DAPI, polycyclic aromatic hydrocarbons such as anthracene (which was studied in §3) have the tendency to form dimers or other higher order structures. We started studying such phenomenon with the simplest polycyclic aromatic hydrocarbon, naphthalene.

Fig. 5.6 shows the absorbance and fluorescence spectra of naphthalene. Similar to anthracene, naphthalene's spectrum consists of two main bands: one with higher energy and intensity (220 nm) and another low intensity broad band with fine structure (vibronic

progression) at the lower energy side of the spectrum (240–295 nm). The more extended conjugation in anthracene leads to a significant wavelength red shift for the transition moments of the molecule in comparison to naphthalene.

The emission spectrum of naphthalene in the Fig. 5.6 (red line) shows that the molecule starts to fluoresce at around 312 nm (main peaks at 322, 331, 335 and 345 nm) with similar progression as for its absorption peaks in the 240–295 nm region (~10 nm). A 300 nm longpass filter was chosen to block all the excitation wavelengths and allow emission beams to reach the detector was used to record (Fig. 5.1). This allowed us to record FDLD spectra for naphthalene deposited on PE<sup>OX</sup> from methanolic solutions with 4 different concentrations (0.1, 1, 4 and 15 mg/mL).

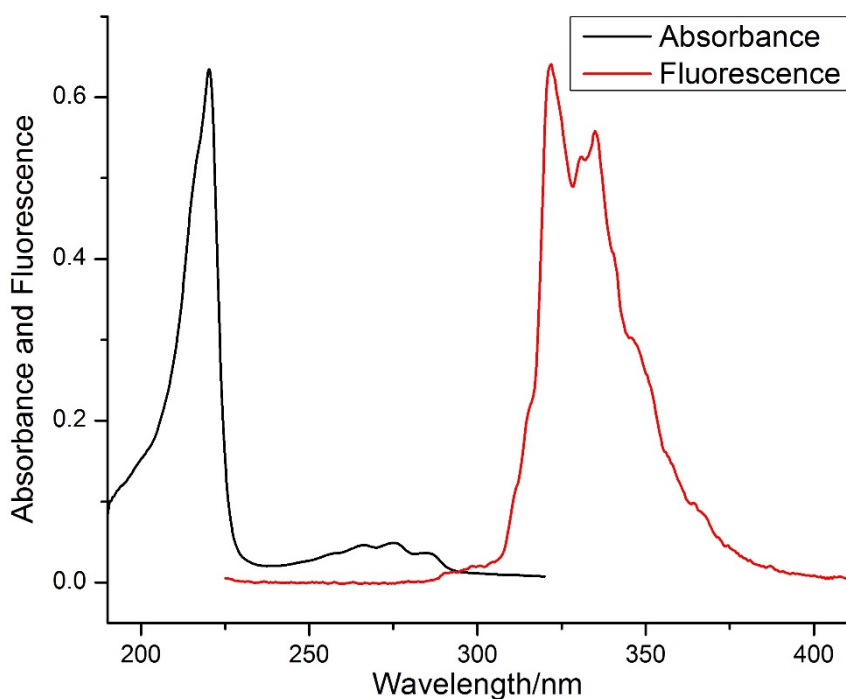


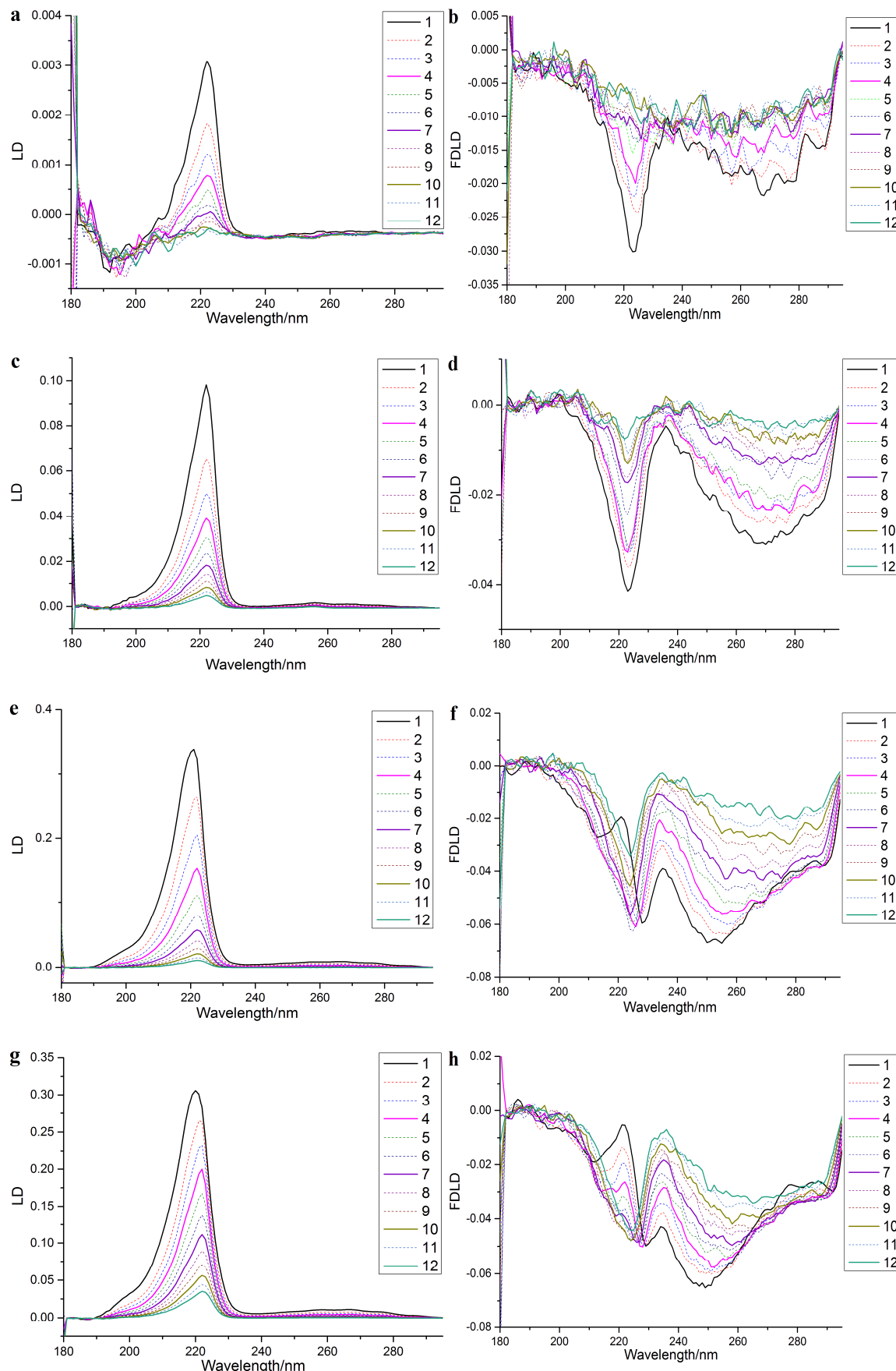
**Fig. 5.6** The absorbance and fluorescence emission spectra of naphthalene (0.01 mg/mL).

## Detected Linear Dichroism

The dried samples of naphthalene on PE<sup>OX</sup> underwent a photolysis during the course of the experiment. This prevented us from recording the LD and FDLD spectra for naphthalene with high numbers of accumulations. To investigate the formation of higher order structures for naphthalene we recorded LD and FDLD spectra for samples deposited on PE<sup>OX</sup> from solutions with different concentrations. Fig. 5.7 shows the spectra collected from 0.1, 1, 8 and 15 mg/mL methanolic solutions. Twelve sequential scans were recorded from each sample which show the decrease in the intensity of each spectrum upon the number of the scan.

The LD spectra of the sample deposited on PE<sup>OX</sup> from the 0.1 mg/mL solution are very similar to the absorbance spectrum of the solution sample in Fig. 5.5a (with a slight red shift of ~2 nm). There is about the same wavelength difference between the shoulder at ~216 nm and the band at 222 nm as for the long axis bands in anthracene spectrum (~8 nm). The FDLD spectra (Fig. 5.7b) show very similar intensity to their corresponding LD spectra (Fig. 5.7a) but with lower resolution especially in the longer wavelength region. In the case of samples deposited from higher concentrations, the FDLD spectra show much weaker intensities in comparison with their corresponding LD spectra, which could be due to the self-quenching effect of naphthalene molecules. The spectra of the sample deposited from the 1 mg/mL solution (Fig. 5.7c and d) are very similar in shape but higher in intensity compared with those of 0.1 mg/mL sample (showing monomeric characteristics, Fig. 5.8a).

Chapter Five - Molecular Dimerisation Investigation Using Stretched Polyethylene Linear Dichroism and Fluorescence Detected Linear Dichroism



## Detected Linear Dichroism

**Fig. 5.7** LD (left) and corresponding FDLD (right) spectra of naphthalene deposited on 1.8× stretched PE<sup>OX</sup> from (a and b) 0.1, (c and d) 1, (e and f) 8 and (g and h) 15 mg/mL methanolic solutions. The black line in each diagram (indicated as 1 in the legend) represents the first scan in the total of 12 scans. Each number in the legend represents the number of the scan recorded from each sample.

The LD spectra corresponding to the samples deposited from 8 and 15 mg/mL (Fig. 5.7e and g) show a slight blue shift for the intense peak in the short wavelength side of the spectrum. This could be due to the formation of H-aggregates and also a dimer with a geometry whose monomer units orient perpendicular to each other (in a crossed geometry, Fig. 5.8c). The latter is more obvious in their corresponding FDLD spectra (black line in the Fig. 5.7f and h) where there is an intense peak at ~222 nm pointing upwards (close to zero). This peak reduces intensity and turns to a more monomeric shape as time goes by (cyan line in the Fig. 5.7f and h). This might be illustrating that photolysis affects more on the dimer than the monomer molecules.

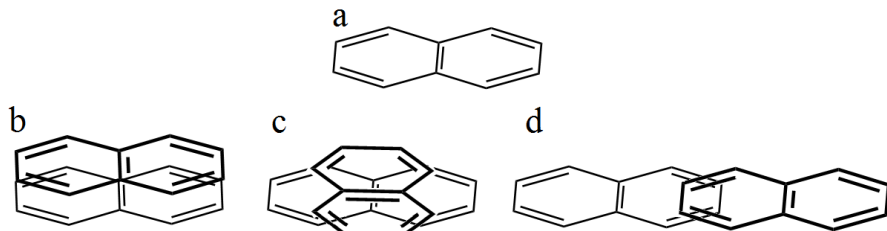


**Fig. 5.8** Schematic chemical structures for naphthalene's a) monomeric and three dimeric forms: b) eclipse, c) crossed and d) J-aggregate.

As shown in the Fig. 5.9 two negative peaks at 212 and 235 nm appear in the FDLD spectra of naphthalene upon increasing the concentration. The band at 212 nm could be due to formation of the dimer with its subunits' long axes parallel to each other (eclipse dimer, Fig. 5.8b), and the one at 235 nm could be corresponding to the formation of J-aggregates (Fig. 5.8d). This follows by appearance of a broad band at ~250 nm.

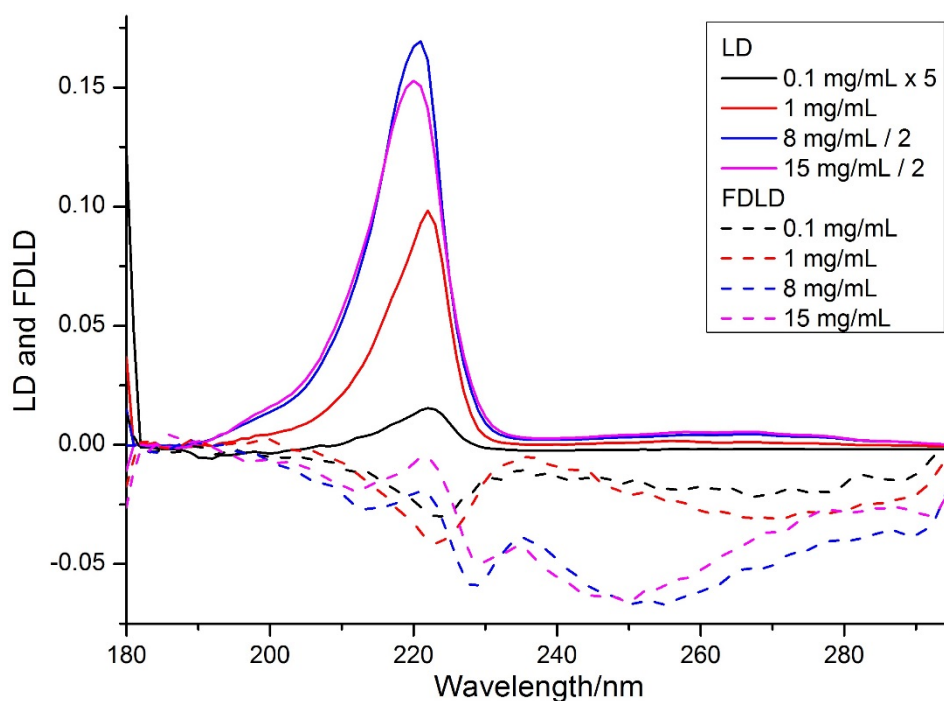


**Fig. 5.9** LD (solid) and FDLD (dashed) spectra of napthalene deposited on  $\text{PE}^{\text{OX}}$  ( $1.8\times$  stretched) from methanolic solutions with different concentrations: 0. 1 (black), 1 (red), 8 (blue) and 15 (magenta) mg/mL. The spectra shown in this figure are recorded by a single scan after depositing the sample on polyethylene film.

### 5.3.3 Pyrene

Pyrene's absorbance and emission fluorescence spectra are shown in the Fig. 5.10. The spectroscopic characteristics of pyrene carboxaldehyde, which is structurally similar to pyrene, is discussed previously in §2.

## Detected Linear Dichroism

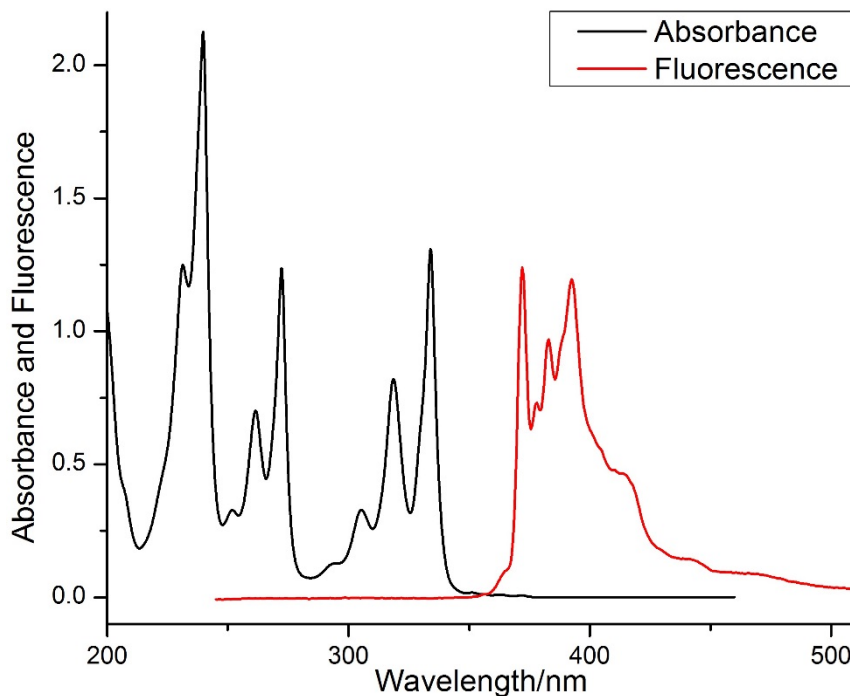


**Fig. 5.10** The absorbance and fluorescence emission spectra of pyrene (0.05 mg/mL).

The ~40 nm gap between the longest absorbance wavelength (334 nm) and the shortest emission wavelength (372 nm) allowed us to use a 341 nm longpass filter to record FDLD spectra of pyrene deposited on PE<sup>O<sub>X</sub></sup> from methanolic solutions with different concentrations (0.1, 1 and 4 mg/mL, Fig. 5.11). To compare the effect of blocking different wavelengths by using different longpass filters we repeated the experiment using a 400 nm longpass filter (Fig. 5.13).

Chapter Five - Molecular Dimerisation Investigation Using Stretched Polyethylene Linear Dichroism and Fluorescence Detected Linear Dichroism

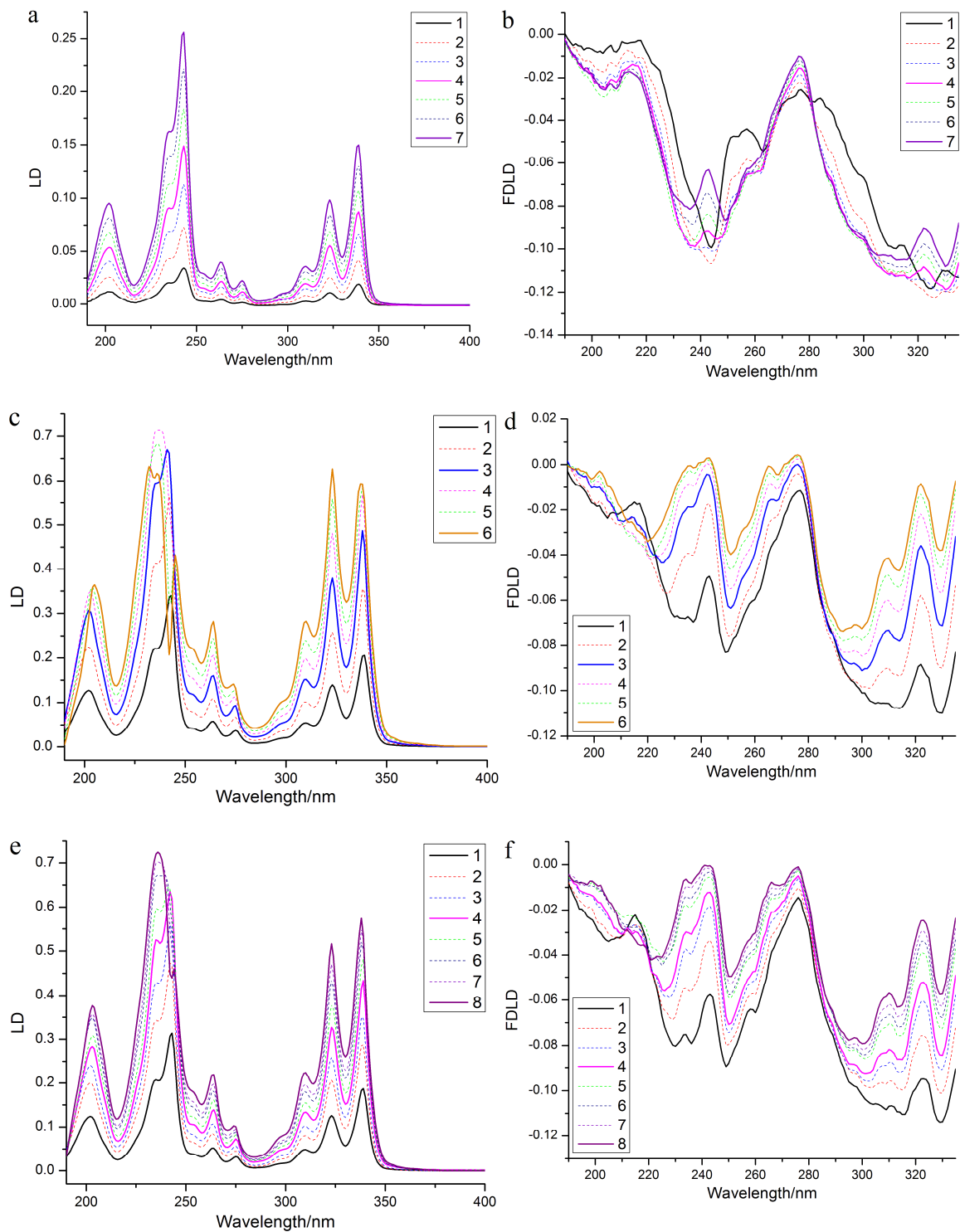


**Fig. 5.11** LD (left) and corresponding FDLD (right, a 341 nm longpass filter was used) spectra of pyrene deposited on 1.8 $\times$  stretched PE<sup>OX</sup> from (a and b) 0.1 and (c and d) 1 and (e and f) 4 mg/mL methanolic solutions. The black line in each diagram (indicated as 1 in the legend) represents the first aliquot of sample (40  $\mu$ L) on the film. Each number in the legend represents the number of aliquots (40  $\mu$ L) added on the film.

## Detected Linear Dichroism

The LD spectra of pyrene deposited on PE<sup>OX</sup> showed a ~4 nm red shift from the molecule's solution absorbance spectrum. When the solution's concentration was 0.1 mg/mL no change in the shape of LD spectrum was observed after we added more aliquots of sample on 1.8× stretched PE<sup>OX</sup>. However, their corresponding FDLD spectra in Fig. 5.11b show a sign change for the bands at 243 and 325 nm which, as Thulstrup et al.<sup>43</sup> reported, are related to the  $\pi \rightarrow \pi^*$  transitions of pyrene's long axis. When the sample was deposited from a 10 mg/mL solution, upon increasing the number of aliquots added on the PE<sup>OX</sup> the LD spectra changed shape from monomeric (Fig. 5.11c black line) to a dimeric spectrum with a downward band at 243 nm (Fig. 5.11c orange line). There is also a decrease in intensity for the band at 338 nm. The FDLD spectra in the Fig. 5.11d shows the presence of dimers or higher order structures from the first aliquot deposited on PE<sup>OX</sup> where all the peaks present in the monomeric spectrum (Fig. 5.11b black line) have upward peaks. Upon increasing the number of aliquots added, the intensity of FDLD peaks changes from more negative numbers towards positive numbers. The 4 mg/mL spectra showed similar trend to 1 mg/mL with higher intensity (Fig. 5.11e and f).

The LD and FDLD spectra of pyrene deposited on PE<sup>OX</sup> from solutions with different concentrations are compared in the Fig. 5.12. The FDLD of 4 mg/mL sample, with its peaks close to zero, could be illustrating a dimeric structure with its long axis perpendicular to the film's stretching direction.

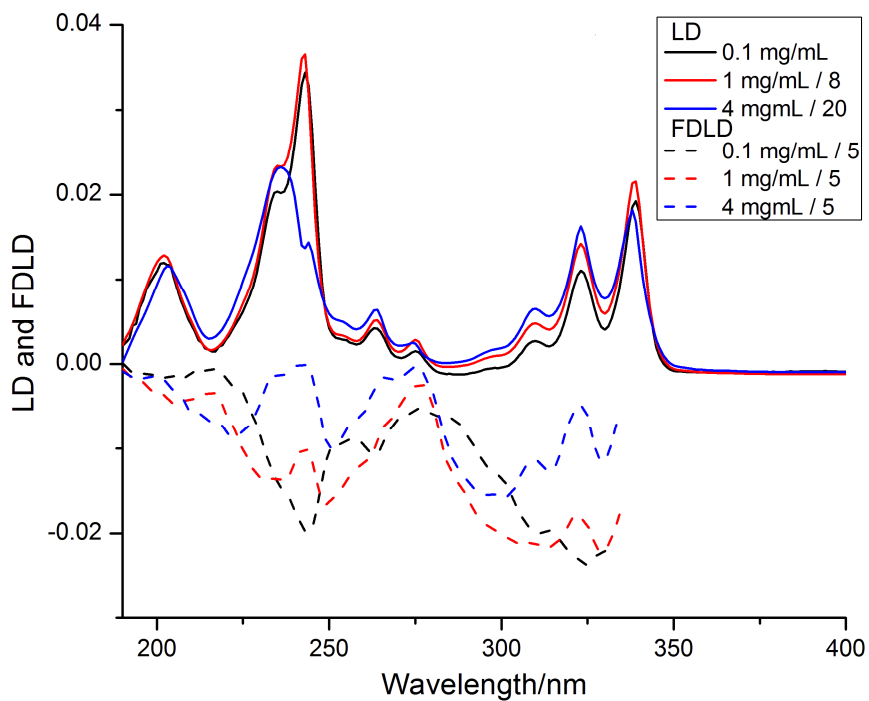


**Fig. 5.12** LD (solid) and FDLD (dashed, a 341 nm longpass filter was used) spectra of pyrene deposited on PE<sup>OX</sup> (1.8× stretched) from methanolic solutions with different concentrations: 0.1 (black), 1 (red) and 4 (blue) mg/mL. The 1 and 4 mg/mL LD spectra are respectively 8 and 20 times, and all FDLD spectra 5 times reduced in intensity.

Similar results achieved when a 400 nm longpass was used to record FDLD spectra of pyrene (Fig. 5.13 and 5.14). Again, a dimeric structure with its long axis perpendicular to the stretching direction was observed when higher concentrations of the sample solution was deposited on PE<sup>OX</sup>.

## Detected Linear Dichroism

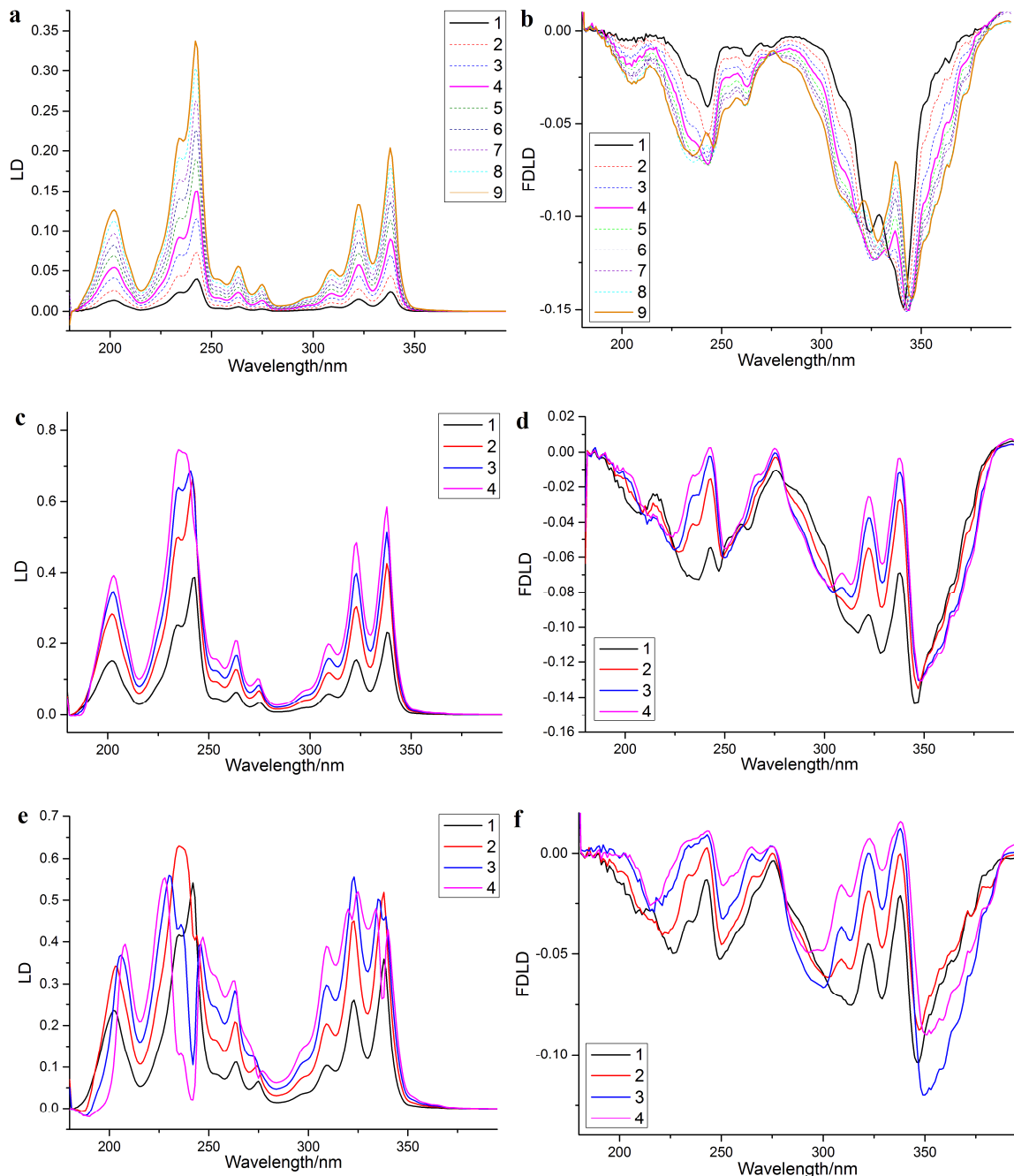


**Fig. 5.13** LD (left) and corresponding FDLD (right, a 400 nm longpass filter was used) spectra of pyrene deposited on 1.8× stretched PE<sup>OX</sup> from (a and b) 0.1 and (c and d) 1 and (e and f) 4 mg/mL methanolic solutions. The black line in each diagram (indicated as 1 in the legend) represents the first aliquot of sample (40 μmL) on the film. Each number in the legend represents the number of aliquots (40 μmL) added on the film.

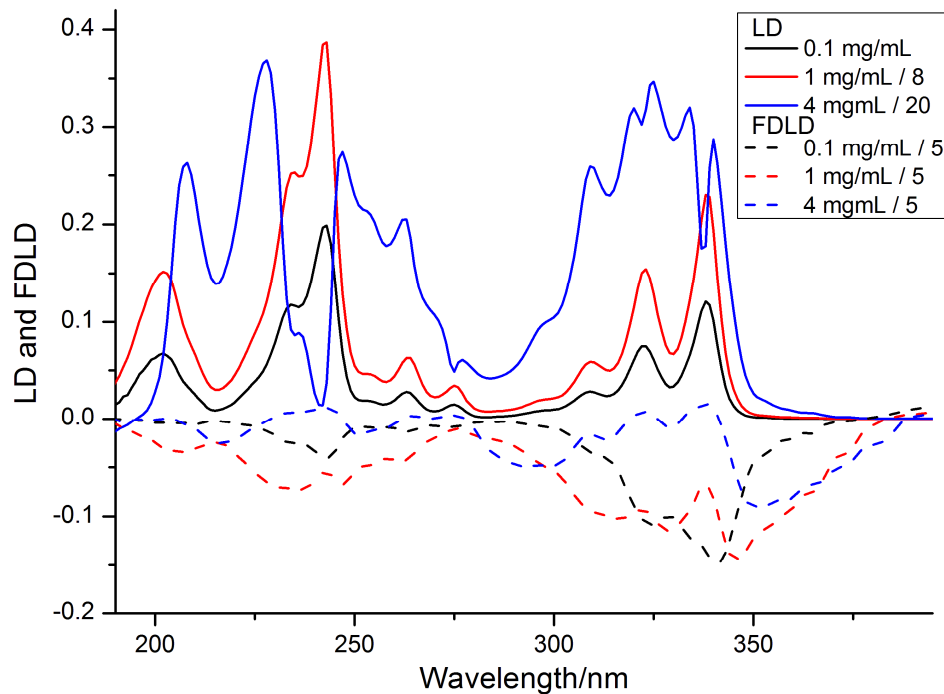
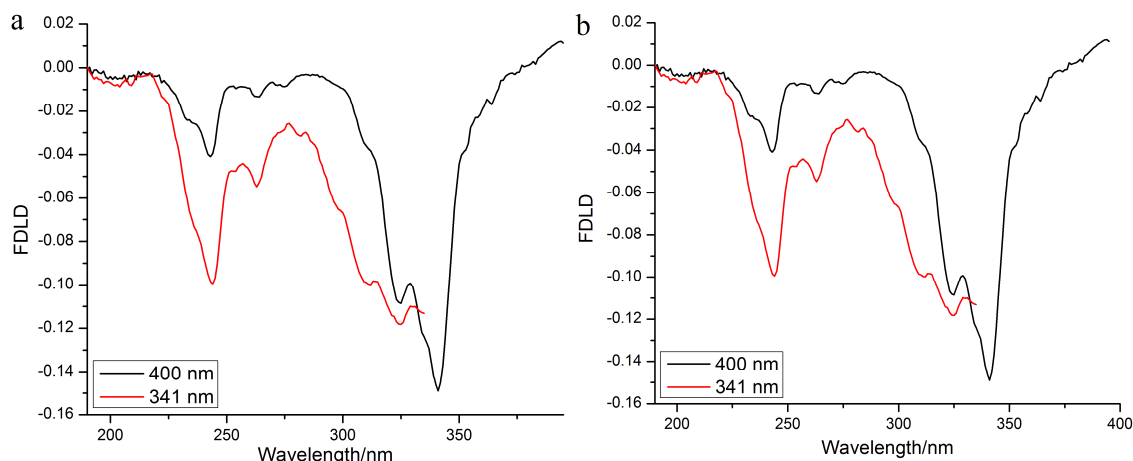


**Fig. 5.14** LD (solid) and FDLD (dashed, a 400 nm longpass filter was used) spectra of pyrene deposited on PE<sup>OX</sup> (1.8 $\times$  stretched) from methanolic solutions with different concentrations: 0.1 (black), 1 (red) and 4 (blue) mg/mL. The 0.1 mg/mL LD spectrum is 5 times magnified and that of 4 mg/mL is 1.5 times reduced in intensity.

As shown in Fig. 5.15 using a longer wavelength longpass filter allowed us to scan a bigger range of spectrum, however, blocking the main emission fluorescence wavelengths led to a decrease in the intensity of FDLD peaks.



## Detected Linear Dichroism

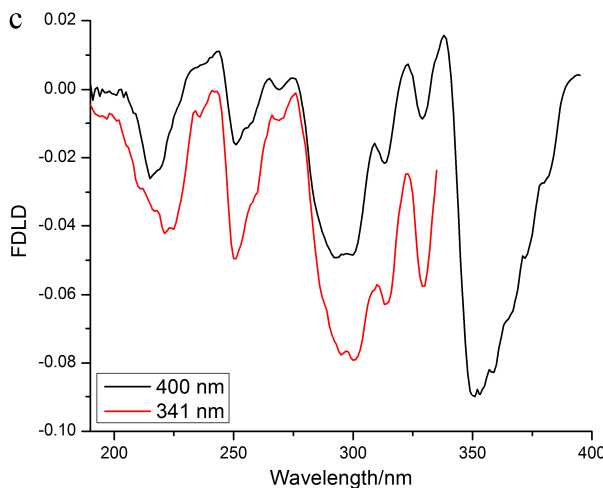


**Fig. 5.15** The FDLD spectra of pyrene using a 400 (black) and a 341 (red) nm longpass filters when the solution concentration is a) 0.1, b) 1 and c) 4 mg/mL. The spectra recorded using different longpass filters are obtained from different samples.

### 5.3.4 Perylene

The absorbance, LD and  $LD^r$  spectra of perylene are shown in Fig. 5.16. The bands at  $\sim 441$  and  $255$  nm are related to the transitions with perpendicular transition moment directions.<sup>85</sup> Also Halasinski et al.<sup>85</sup> experiments showed that these bands are long and short axis polarised respectively. The perylene's  $LD^r$  spectrum (Fig. 5.16) shows that the band at  $\sim 200$  nm has a polarisation parallel to the long axis of the molecule and the stretching direction. We calculated the alignment parameter of  $S = 0.3$  when the angle for the long axis polarised transition moments is close to zero, and close to  $90^\circ$  for the band at  $255$  nm. Thulstrup et al.<sup>43</sup> reported that the band at  $441$  nm is related to the  $0-0$  electronic transition and the fine structures with shorter wavelengths are vibronic transitions.

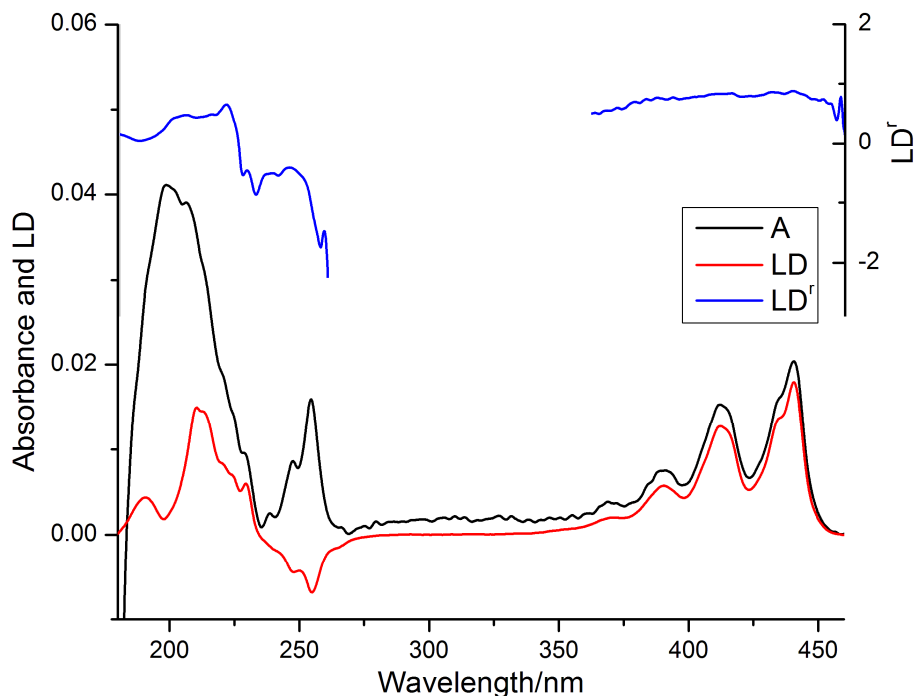


**Fig. 5.16** Absorbance (black), LD (red) and LD' (blue) spectra of perylene (from a 0.01 mg/mL methanolic solution) deposited on 1.8 $\times$  stretched PE<sup>OX</sup>.

Fig. 5.17 shows the absorbance and emission fluorescence spectra of pyrene (0.01 mg/mL, methanolic solution). A 400 nm longpass filter was used to block most of the absorbance wavelength and allow all emission bands (starting from 439 nm).

## Detected Linear Dichroism

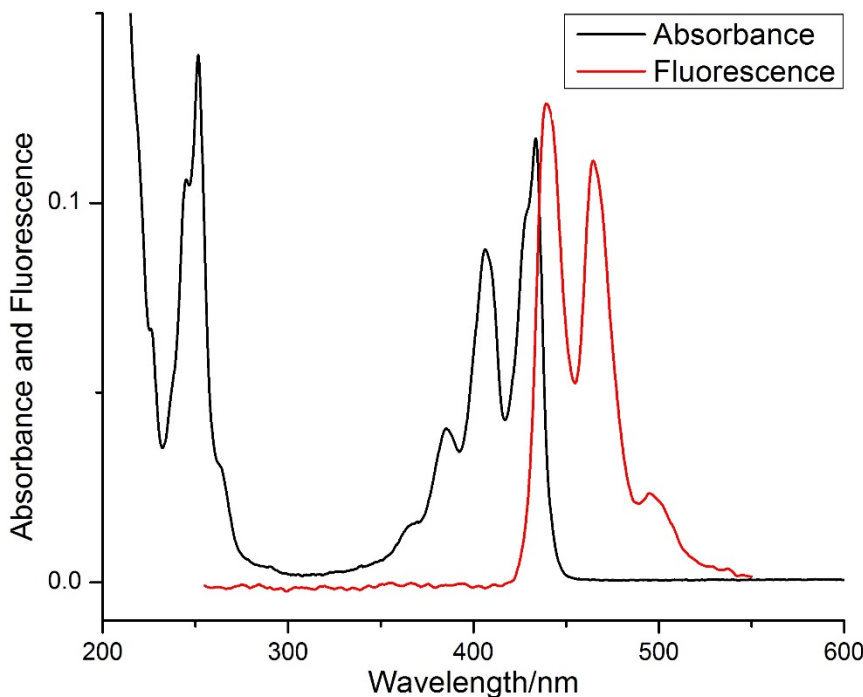


**Fig. 5.17** The absorbance and fluorescence emission spectra of perylene (0.01 mg/mL).

The LD and FDLD spectra of perylene (Fig. 5.18) were recorded when the sample deposited on 1.8 $\times$  stretched PE<sup>OX</sup> from methanolic solutions with three different concentrations (0.01, 0.1 and 1 mg/mL, perylene's solubility decreases in higher concentrations). As shown in the Fig. 5.18 LD and FDLD spectra of the sample change not in shape but in intensity when more aliquots are deposited on PE<sup>OX</sup>. This could be due to the increase in the thickness of the dried sample or the increase in the alignment of the molecules.

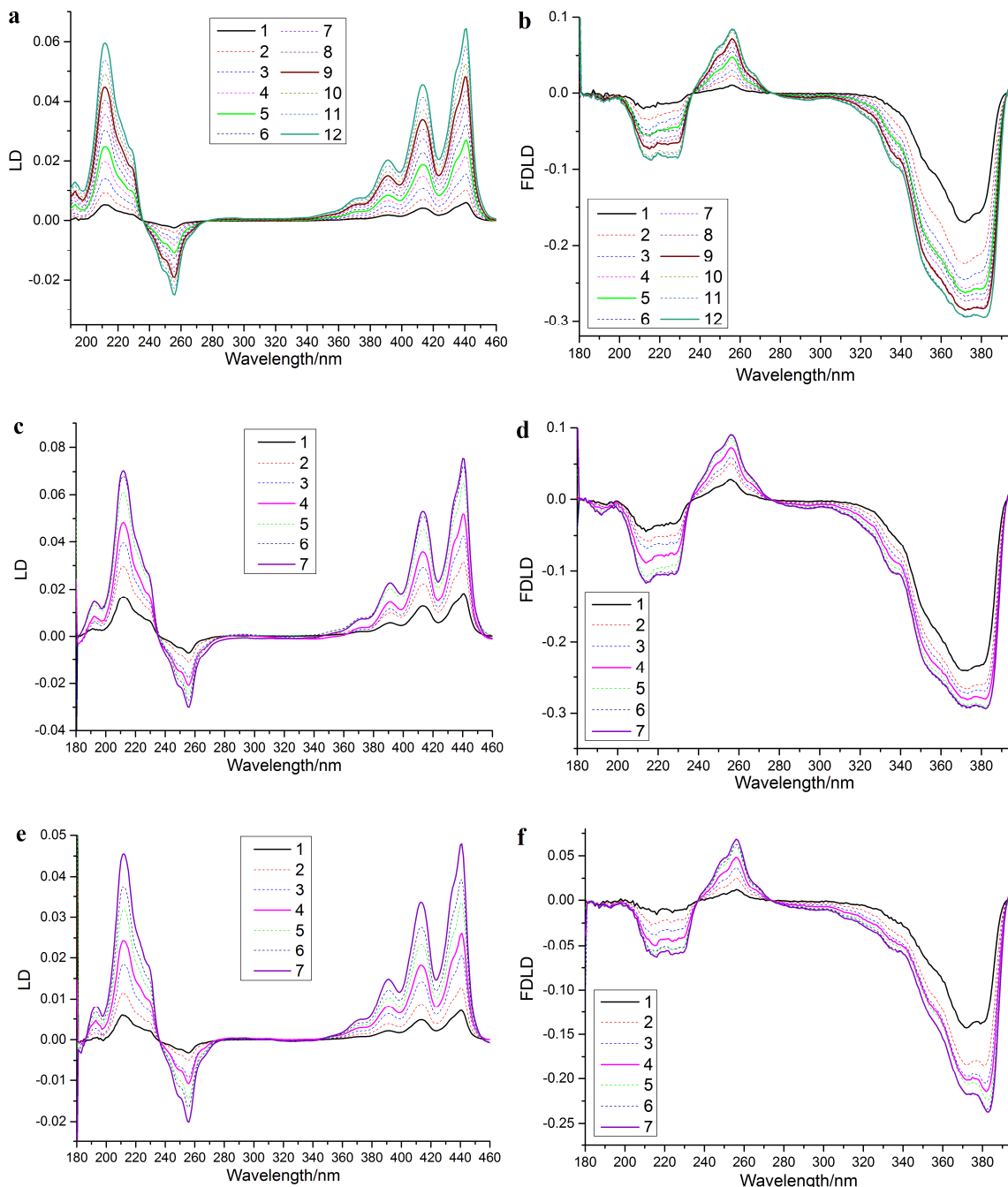


**Fig. 5.18** LD (left) and corresponding FDLD (right) spectra of perylene deposited on 1.8 $\times$  stretched PE<sup>OX</sup> from (a and b) 0.01, (c and d) 0.1 and (e and f) 1 mg/mL methanolic solutions. The black line in each diagram (indicated as 1 in the legend) represents the first aliquot of sample (40  $\mu$ L) on the film. Each number in the legend represents the number of aliquots (40  $\mu$ L) added on the film.

Besides the slight difference in the shape of the FDLD band at  $\sim$ 380 nm when the sample is deposited from a higher concentration solution, there is no significant change in the LD or FDLD spectra of the samples deposited from different solutions (Fig. 5.19). This could

## Detected Linear Dichroism

be interpreted as the absence of the higher order structures of perylene when the molecules are dried on PE<sup>OX</sup>. Nevertheless, we could find reports on perylene dimer formation in the literature. Oliveira et al.<sup>87</sup> reported the formation of perylene aggregations by appearing a band at ~458 nm whilst the bands at 441 and 414 nm decrease in intensity.

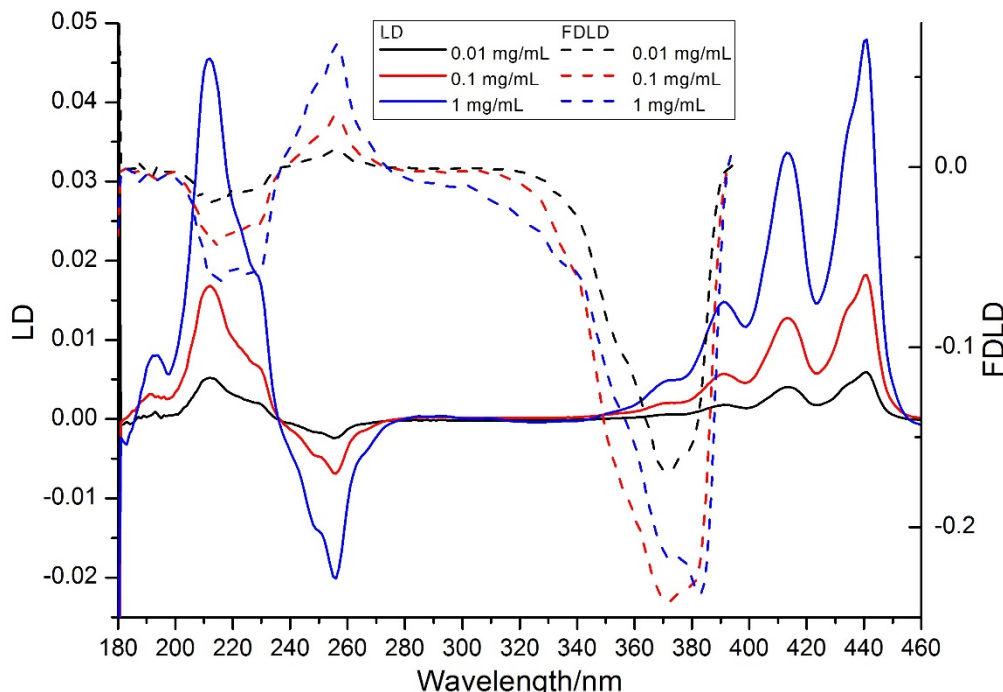


**Fig. 5.19** LD (solid) and FDLD (dashed) spectra of perylene deposited on PE<sup>OX</sup> (1.8× stretched) from methanolic solutions with different concentrations: 0.01 (black), 0.1 (red) and 1 (blue) mg/mL.

### 5.3.5 Olympicene

Benzo[cd]pyrene cation was first synthesised by Reid and Bonthrone<sup>88</sup> in 1965. In 2013 the neutral molecule was synthesised by David Fox and Anish Mistry in the University of Warwick and called olympicene.<sup>83</sup> The sample worked on in this chapter was kindly provided by A. Mistry. Fig. 5.21 shows the absorbance and emission fluorescence spectra of olympicene (0.1 mg/mL methanolic solution) and Fig. 5.20 shows the UV-visible LD

and LD<sup>r</sup> spectra of the molecule deposited on a 1.8× stretched PE<sup>OX</sup> from two different solution concentrations (0.01 and 0.1mg/mL). In order to check the effect of depositing more aliquots on the alignment of the molecules we calculated the LD<sup>r</sup> spectra of first and second aliquots of olympicene added on PE<sup>OX</sup> (Fig. 5.20 red and blue spectra). As it is shown in Fig. 5.20 LD<sup>r</sup> spectra of both conditions are the same meaning that adding more sample does not significantly change the orientation of the molecules adsorb onto polyethylene. Alignment parameter (S) of 0.3 was calculated when the sample was deposited form a lower concentration solution (0.01 mg/mL, black spectra). Having positive LD<sup>r</sup> intensity we figured that the band at 297, 224 and 198 nm are long axis polarised with their transition moments respectively 0°, 17° and 30° away from the stretching direction. The only short axis polarised band we were able to distinguish is the negative LD band at 241 nm with the transition moment angle of 64° away from the stretching direction.

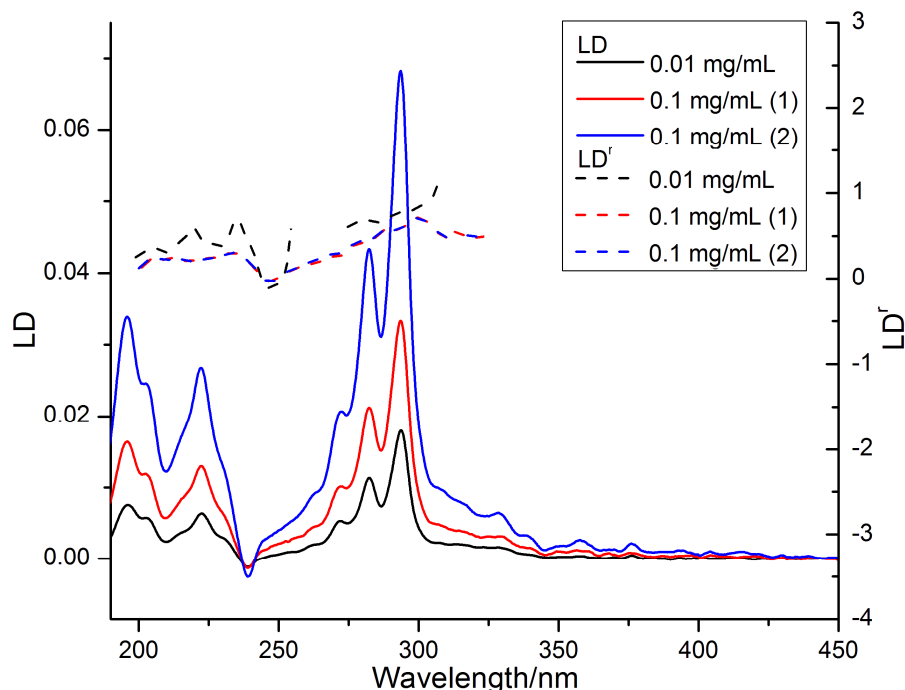


**Fig. 5.20** LD (solid line) and LD<sup>r</sup> (dashed) spectra of olympicene deposited from 0.01 (black), 0.1 (red and blue) mg/mL methanolic solutions on 1.8× stretched PE<sup>OX</sup>. The blue spectra are recorded when two aliquots (each aliquot is 40  $\mu$ L) of the sample (0.1 mg/mL) was deposited on the film.

## Detected Linear Dichroism

The FDLD spectra of olympicene (from three different concentrations of 0.01, 0.1 and 1 mg/mL) were recorded placing a 341 nm longpass filter in front of the PMT (Fig. 5.22).

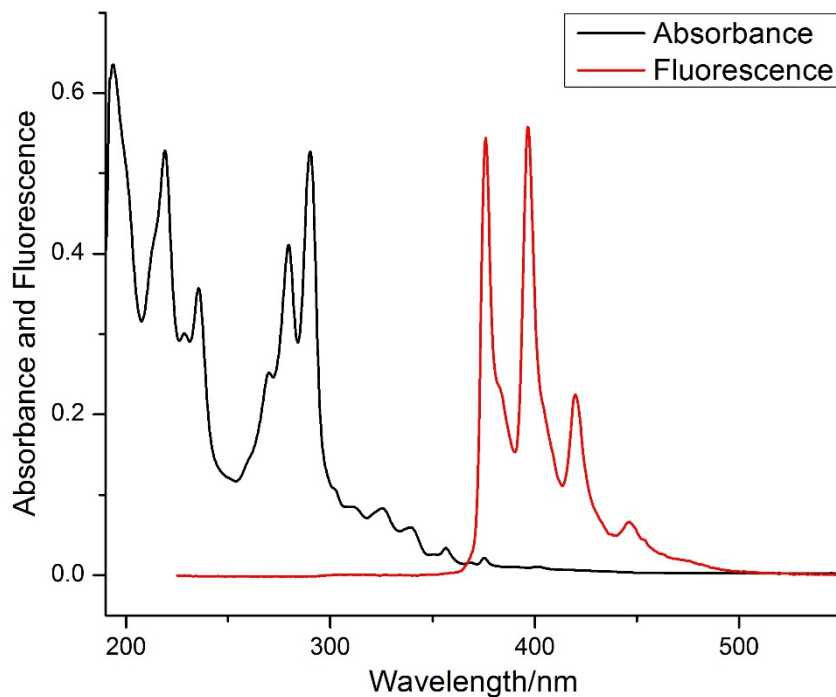


**Fig. 5.21** The absorbance and fluorescence emission spectra of olympicene (0.1 mg/mL).

Fig. 5.22a shows LD spectra of olympicene aliquots deposited from a 0.01 mg/mL methanolic solution on 1.8 $\times$  stretched PE<sup>OX</sup>. The shape of the spectra does not change upon adding aliquots and only the intensity of them increases which is due to the concentration change. Fig. 5.22b shows corresponding FDLD spectra; adding more aliquots increased the intensity of the FDLD peaks and slightly decreased the intensity ratio of the bands at 297 and 285 nm. The LD spectra of olympicene deposited from a 0.1 mg/mL solution (Fig. 5.22c) also does not show significant change in shape upon adding more aliquots. However, their FDLD spectra (Fig. 5.22d) show a change in direction of peaks at long wavelength following by decreasing in intensity and progressing towards the positive side

of the spectrum. This trend continues when the aliquots are deposited from 1 mg/mL solution until peaks intensity get close to zero (Fig. 5.22f). The LD peaks at 197 and 295 nm in Fig. 5.22e also show a gradual change in signal sign.

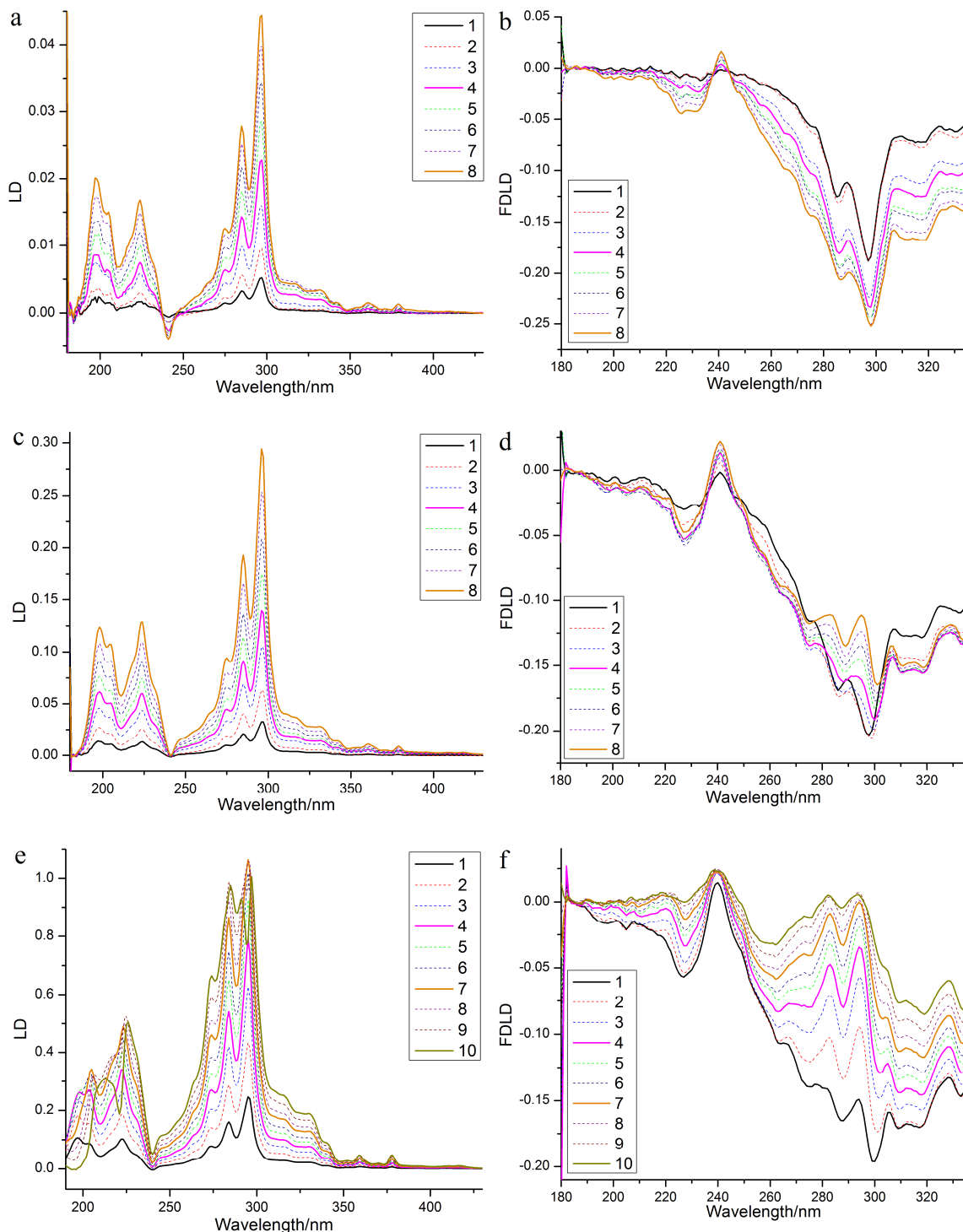


**Fig. 5.22** LD (left) and corresponding FDLD (right) spectra of olympicene deposited on 1.8 $\times$  stretched PE<sup>OX</sup> from (a and b) 0.01, (c and d) 0.1 and (e and f) 1 mg/mL methanolic solutions. The black line in each diagram (indicated as 1 in the legend) represents the first aliquot of sample (40

## Detected Linear Dichroism

$\mu\text{L}$ ) on the film. Each number in the legend represents the number of aliquots ( $40 \mu\text{L}$ ) added on the film.

Fig. 5.23 shows an overlay of LD (solid lines) and FDLD (dashed) spectra of olympicene deposited from different concentration on  $\text{PE}^{\text{OX}}$ . There is no significant shape difference between LD spectra of samples deposited from 0.01 and 0.1 mg/mL solutions. However, there is a change in sign of the long axis-polarised bands 197 and 295 nm. This could be due to the formation of dimer with its long axis perpendicular to the stretching direction. The FDLD spectra of different concentrations show more difference as all bands start changing sign in higher concentrations.

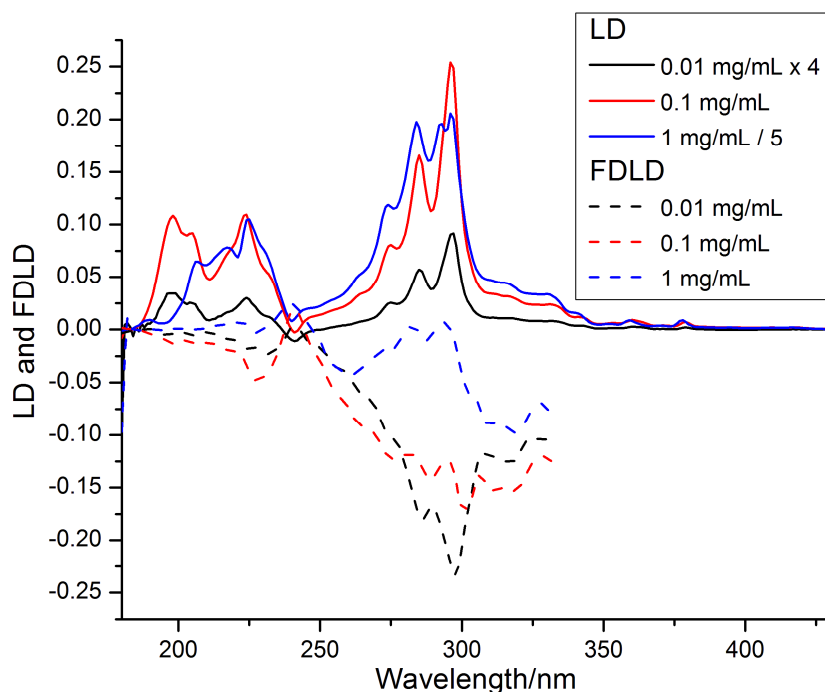


**Fig. 5.23** LD (solid) and FDLD (dashed) spectra of olympicene deposited on  $\text{PE}^{\text{OX}}$  ( $1.8\times$  stretched) from methanolic solutions with different concentrations: 0.01 (black), 0.1 (red) and 1 (blue) mg/mL. The LD spectrum of 0.01 mg/mL sample has been magnified 5 times and the intensity of the spectrum related to 1 mg/mL sample is reduced 8 times for presenting purposes.

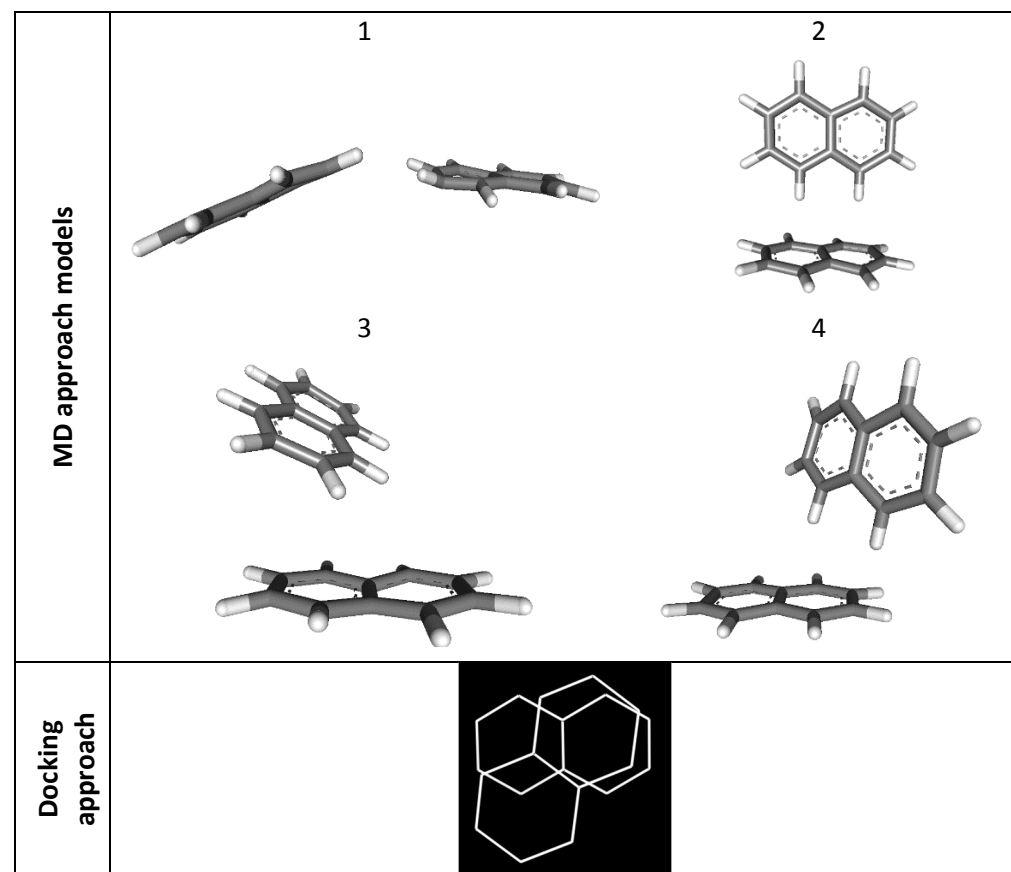
### 5.3.6 Computational modelling to study the possibility of dimerisation for polycyclic aromatic hydrocarbons

Computational simulations, done by Dr. Shirin Jamshidi, showed at least 5 possible dimers for each molecule studied in this chapter (Fig. 5.24–27). The modelling was performed as explained in §3. The angles between long axes and short axes of each dimer units were calculated using two different approaches of Molecular Dynamics and Docking (Table 5.3). Our experimental data showed the presence of dimeric structures for all the polycyclic aromatic hydrocarbons apart from perylene. This could be due to the way perylene interacts with stretched polyethylene. Previously in §3 we observed that in high stretching factors molecules tend to show monomeric behaviour. Other possible reason could be the weak attraction forces between dimeric units which undergo decomposition under light exposure.

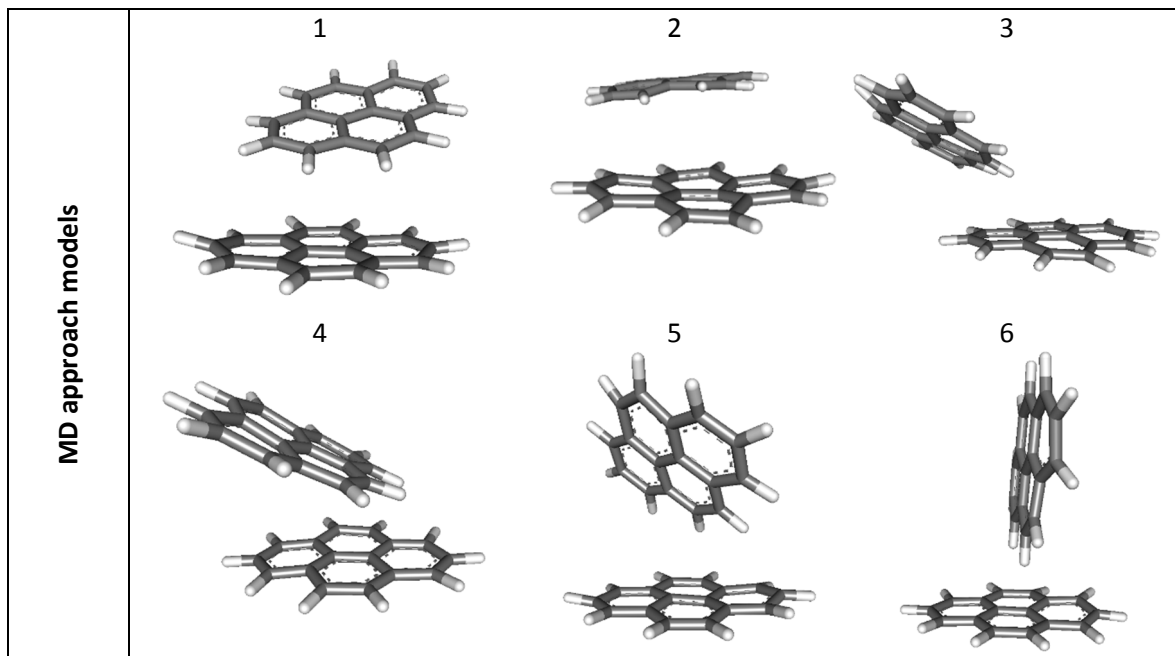
**Table 5.3** The angles between the long axes and the short axes of each dimer units. To estimate the angles we assumed the long axis horizontal and then calculated the angles between two dimer units. The numbers in front of each configuration in the table below refer to the models in the Fig. 5.24–27.

Dimer		Naphthalene		Pyrene		Perylene		Olympicene	
Angles between dimeric units		Long axes	Short axes	Long axes	Short axes	Long axes	Short axes	Long axes	Short axes
MD approach	1	3.37	54.90	8.64	74.29	2.26	36.6	2.28	26.12
	2	16.41	11.20	9.21	87.12	39.02	32.42	46.21	70.95
	3	50.02	48.57	56.46	31.16	82.64	59.21	49.79	19.14
	4	79.54	98.73	71.99	32.73	82.65	35.14	78.09	54.05
	5			73.59	76.41			83.65	53.92
	6			84.70	12.66				
Docking approach		11.11	46.11	87.11	46.51	20.48	39.22	9.7	4.01

## Detected Linear Dichroism



**Fig. 5.24** The schematic models of the possible dimers of naphthalene generated by Molecular Dynamics and docking approach.



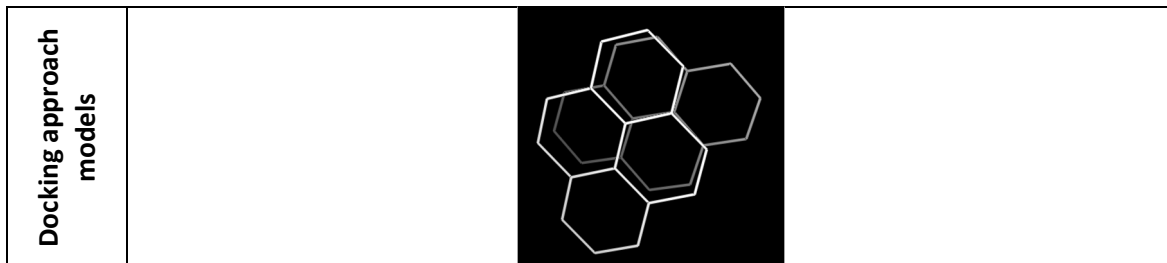


**Fig. 5.25** The schematic models of the possible dimers of pyrene generated by Molecular Dynamics and docking approach.

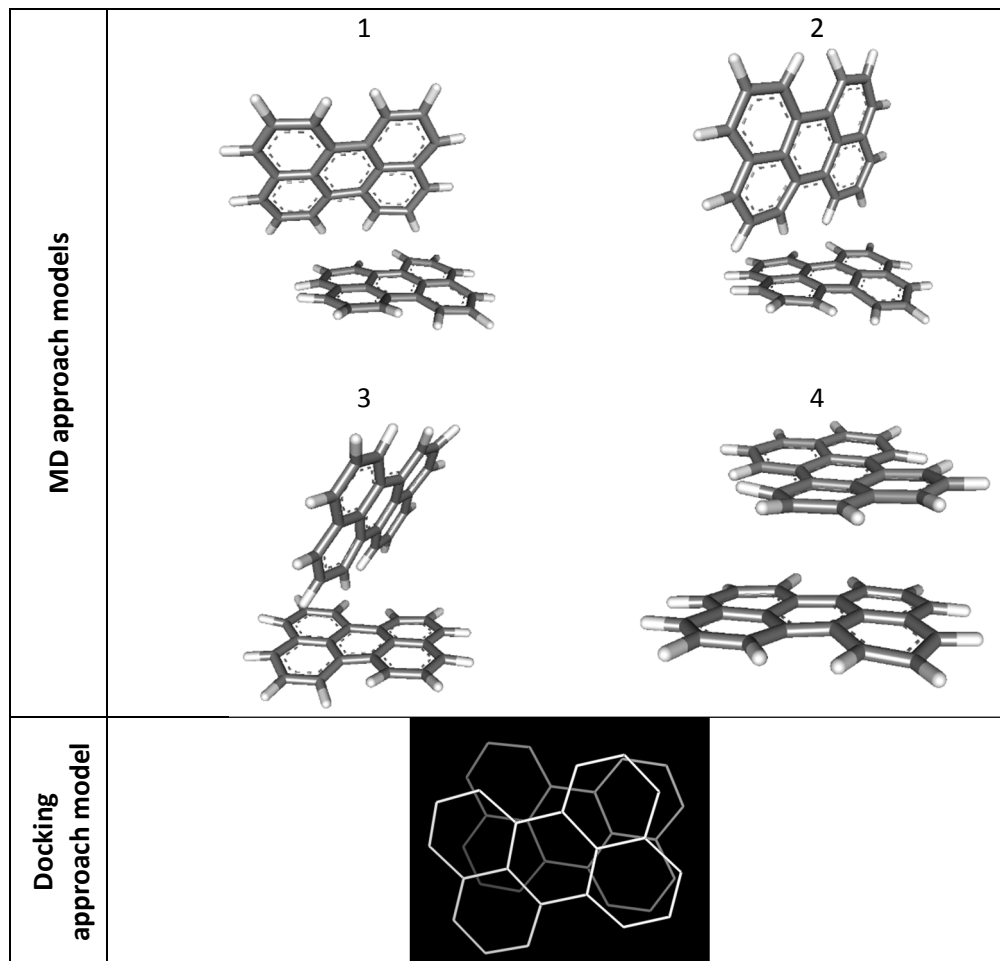


**Fig. 5.26** The schematic models of the possible dimers of perylene generated by Molecular Dynamics and docking approach.

## Detected Linear Dichroism

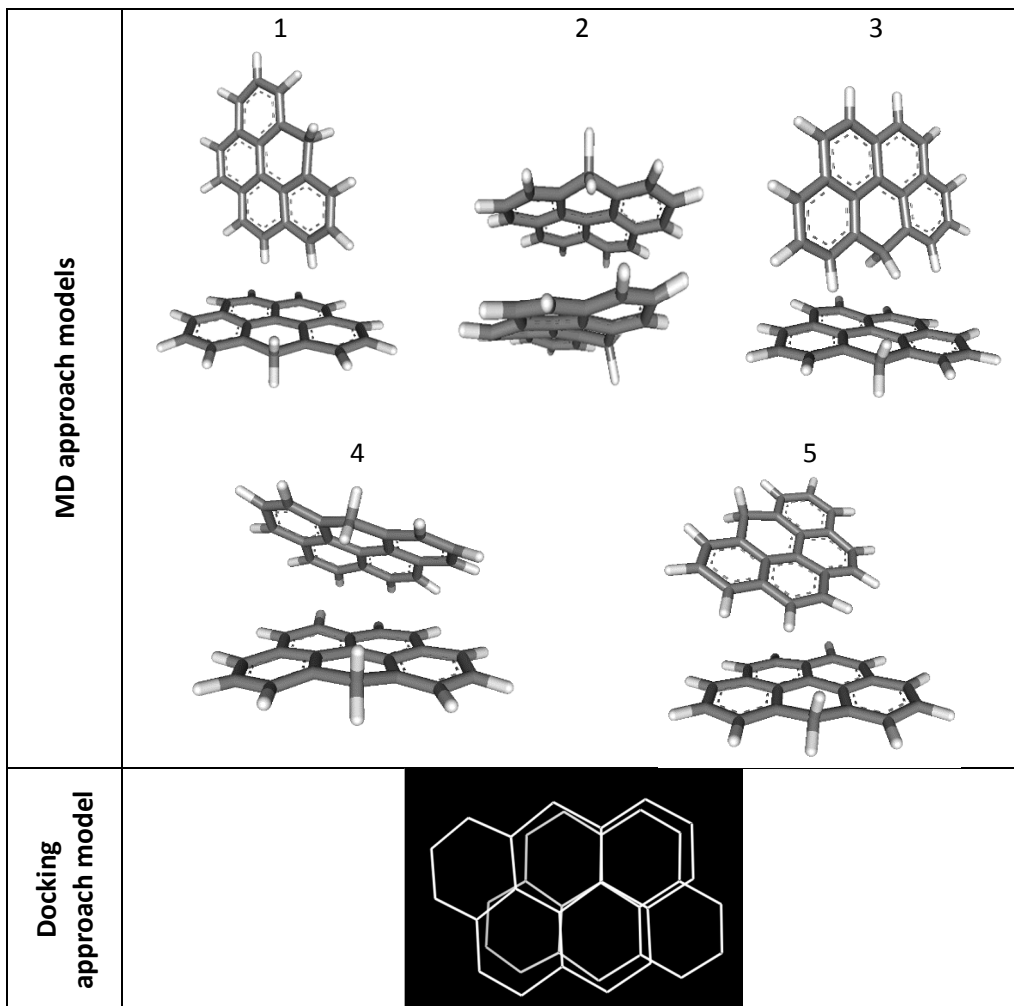


**Fig. 5.27** The schematic models of the possible dimers of olympicene generated by Molecular Dynamics and docking approach.

#### 5.4 Conclusions

The dimerisation of DAPI, naphthalene, pyrene, perylene and olympicene was investigated using stretched polyethylene LD and FDLD. DAPI and perylene's experimental data did not show any significant evidence on the formation of higher order structures, however, the computational simulations done by Dr. Shirin Jamshidi showed possible dimeric

configurations for perylene. Comparing LD and FDLD data, we noticed that FDLD is much more sensitive to the changes in the structure of molecules.

The electronic transition moments of olympicene, for the first time, were investigated and the alignment parameters of the molecule deposited on PE<sup>OX</sup> were calculated. The LD and FDLD results on the dimerisation of olympicene might help synthetic chemists to use the molecule in order to build bigger polycyclic aromatic hydrocarbonic structures.

# Chapter Six

Polarised Raman spectroscopy application for  
aligned small biomolecules  
(Introducing Raman linear sum and difference  
spectroscopy)

## Acknowledgement

I wish to thank Amie Roberts for helping me with the data collection for this chapter as a part of her MChem project. I am also thankful to Prof. Alison Rodger for helping me with the data analysis and also calculating the fibre's secondary structure percentages using Curtis Johnson's programme CDssstr.

Polarised Raman data was partially recorded using the Raman spectrometer machine in the EPR and Diamond Research group, University of Warwick.



## 6.1 Introduction

As explained §2, treating polyethylene films (PE) with oxygen in a plasma asher resulted in a more hydrophilic surface. Such treated films (denoted PE<sup>OX</sup>) assisted us with aligning polar or hydrophilic molecules which we had not been able to align with normal PE films. The degree of surface hydrophilicity was evaluated by contact angle measurement experiments and the newly added functional groups were investigated using X-ray photoelectron spectroscopy. The ability of PE<sup>OX</sup> in aligning different molecules with different polarities was examined using linear dichroism (LD) experiments. Depending on the sample preparation (depositing the aliquots of sample before or after stretching the film) the ideal stretching factor was determined. In this chapter we discuss polarised Raman spectroscopy of oriented small biomolecules on PE and PE<sup>OX</sup>.

## 6.2 Materials and methods

Progesterone, DAPI, 1-pyrenecarboxaldehyde, anthracene, thymine, thymidine, thymidine 5'-monophosphate (TMP), cytosine, cytidine, cytidine 5'-monophosphate (CMP), methyl 3alpha-acetoxy-delta 7,9(11)-choladienate, 1,10 – phenanthroline, fluorene and fmoc chloride were bought from Sigma Aldrich and 2,2':5',2"- terthiophene was obtained from Alfa Aesar. All chemicals were used without further purification. Methanol (Laboratory grade, Fisher Chemicals) and chloroform (spectrophotometric grade, Sigma-Aldrich) were used as the solvent for sample preparation.

Polyethylene pieces were treated in a plasma asher, as explained in §2, and used as a matrix for samples used in this chapter.

### 6.2.1 Polarised Raman spectroscopy

Samples from high concentrated solutions were deposited on  $1.8\times$  stretched PE or PE<sup>(OX)</sup> and left under a gentle stream of nitrogen gas to vaporise the solvent (mainly chloroform for PE and methanolic solvents for PE<sup>(OX)</sup>) and form a thin layer of sample on the film. Loading extra aliquots (40 µL) continued until the Raman spectrometer's CCD camera detected signals from the sample. If possible, the sample's alignment and the possibility of dimerisation were determined and checked by LD experiments after each aliquot was added. Polarised Raman spectra were recorded (Table 6.1) using either a Renishaw inVia Microscope equipped with a CCD camera or a custom-made BioTools Chiral Raman 2-X Spectrometer (Fig. 6.1). The former spectrometer records polarised Raman spectra in 0 and 90 degrees, then the average and difference spectra (Raman linear sum, RLS, and Raman linear difference, RLD, respectively) were calculated manually (Eq. 6.1).

**Eq. 6.1**

$$RLS = \frac{0^\circ \text{ polarised Raman spectrum} + 90^\circ \text{ polarised Raman spectrum}}{2}$$

$$RLD = 0^\circ \text{ polarised Raman spectrum} - 90^\circ \text{ polarised Raman spectrum}$$

Thus, if the PE films stretching direction (z) is parallel to the instruments Z axis, and the guest molecule behaves uniaxially and aligns by its long axis in the stretching direction, then the Raman-active transitions along the long axis of the molecule cause positive RLD signals and transitions along its short axis would result in negative RLD peaks.<sup>6</sup>

The BioTools spectrometer (Fig. 6.1), which was designed and built for this project, has the ability to record Raman (RLS) spectrum in one channel and Raman optical activity (ROA) or RLD spectrum in another. In both BioTools and Renishaw spectrometers the

stretcher is placed in the machine in such a way that the electric field of a) the incident light for the Renishaw and b) scattered light for Biotools instrument, when the polarisation is  $0^\circ$ , was parallel to the film's stretching direction. A 20 fold microscope objective lens used when the Renishaw instrument was utilised.

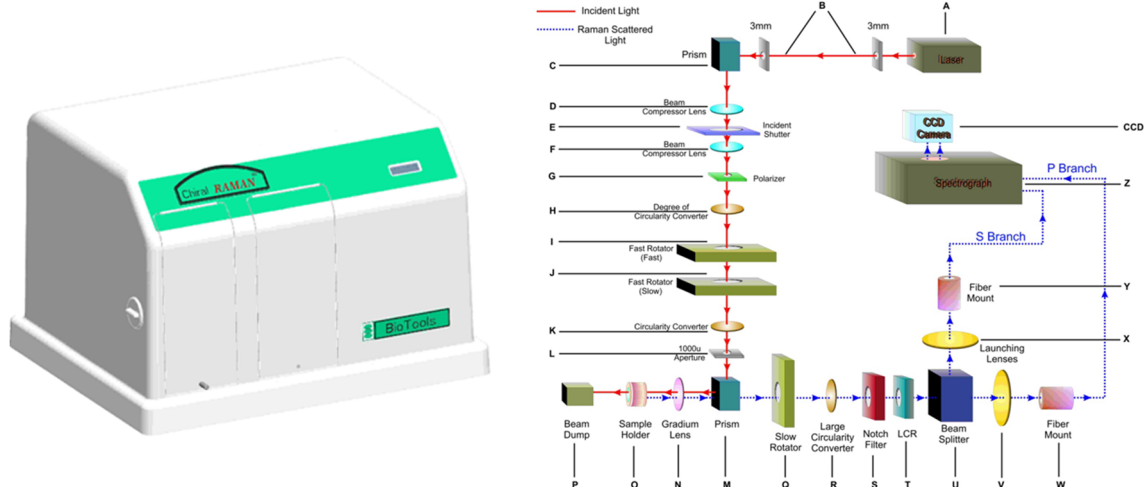


**Fig. 6.1** The custom-made BioTools Chiral Raman 2-X Spectrometer with its schematic instrumentation map.

**Table 6.1** List of samples and spectrometers used to produce the RLD spectra.

Sample	Spectrometer		Laser used / nm
	Renishaw inVia	BioTools	
Polyethylene		×	532
PTFE		×	532
Progesterone	×		633
DAPI	×		633
1-Pyrenecarboxaldehyde	×		633
Anthracene		×	532
Thymine		×	633
Thymidine		×	633
TMP		×	633
Cytosine		×	633
Cytidine		×	633
CTM		×	633
Methyl 3 $\alpha$ -acetoxy- $\delta$ -7,9(11)-choladienate		×	633
1,10 – phenanthroline		×	633
2,2':5',2"- terthiophene		×	633
Fluorene		×	633
Fmoc chloride		×	633

### 6.3 Results and discussion

The versatility of PE<sup>OX</sup> film, as a small molecule orienting substrate, means that we have been able to perform analogous experiments with a set of compounds (including ones of which we have investigated the alignment using UV-visible LD experiments in §2 and §3), using our new polarised Raman spectroscopy technique. Before recording polarised Raman spectra of molecules deposited on stretched PE<sup>OX</sup>, we investigated the vibrational structure of polyethylene and how it changes upon stretching. We repeated similar experiments for polytetrafluoroethylene films and compared the ability of it in orienting small molecules with that of PE<sup>OX</sup>.

#### 6.3.1 Polyethylene

Polyethylene played a significant role as sample substrate in our LD experiments as it is UV-invisible and gives fairly flat baseline with small raise of intensity in the short wavelength region of spectrum (~180 nm) due to light scattering. We used commercial PE plastic bags (Glad® Snap Lock® sandwich bags) as our PE source because they are cheap, very uniformly manufactured, thin and we were able to stretch them more than 3 times. The polyethylene film synthesis, also, is time consuming and the resulting film's thickness is not as even as plastic bags. In §2 we reported how PE induces alignment for guest molecules. Here we explain the change in the orientation of PE chains upon stretching using polarised Raman spectroscopy.

The vibrational spectrum of polyethylene consists of numerous peaks. Generally the spectrum's fingerprint is studied in three regions: 1) C–C stretching vibrations in 1000–1130 cm<sup>-1</sup> region, 2) CH<sub>2</sub> twisting vibrations around 1300 cm<sup>-1</sup> and 3) CH<sub>2</sub> bending and wagging vibrations in 1360–1500 cm<sup>-1</sup>. The peak numbers, their RLD direction and assignments<sup>89–92</sup> are summarised in the Table 6.2 and the CH<sub>2</sub> in-plane and out-of-plane vibrations are illustrated in the Fig. 6.2.

**Table 6.2** The Raman band frequency and RLD direction (Fig. 6.3) with the assignment of PE Raman peaks. Abbreviation: sym: symmetrical, asym: asymmetrical.

Band cm <sup>-1</sup>	RLD direction	Assignment
1461	–	CH <sub>2</sub> bending
1441	–	CH <sub>2</sub> scissoring
1417	+	CH <sub>2</sub> wagging
1371	+	CH <sub>2</sub> bending
1295	+	CH <sub>2</sub> twisting
1173	–	CH <sub>2</sub> rocking
1129	+	C–C sym stretching
1080	+	C–C stretching
1063	+	C–C asym stretching
888	+	

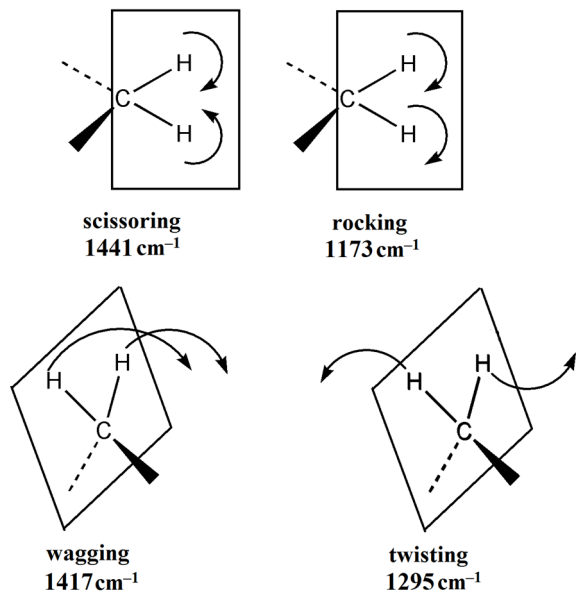


**Fig. 6.2** The schematic model for in and out of plane bending vibrations for  $\text{CH}_2$ .

The RLS and RLD spectra of unstretched  $\text{PE}^{\text{OX}}$  were recorded and compared to ones of stretched films (Fig. 6.3). Stretching the film causes a change in the relative intensity of RLS bands corresponding to the in-plane  $\text{CH}_2$  vibrations, whilst the relative intensities of the bands at  $1295$  and  $1417 \text{ cm}^{-1}$  remain unchanged (Fig. 6.3a). Strobl and Hagedorn<sup>93</sup> found that these two out-of-plane  $\text{CH}_2$  bands, along with the bands at  $1063$  and  $1129 \text{ cm}^{-1}$  (symmetrical and asymmetrical C–C stretching vibrations respectively), are related to the (orthorhombic) crystalline PE and the rest are observable in the Raman spectrum of melted PE (an amorphous phase). The decrease in the intensity of bands at  $1461$ ,  $1441$  and  $1080 \text{ cm}^{-1}$  upon stretching is thus further evidence for an increase in the amount of crystalline phase in comparison to the amorphous one during the stretching of polyethylene film (see §2).

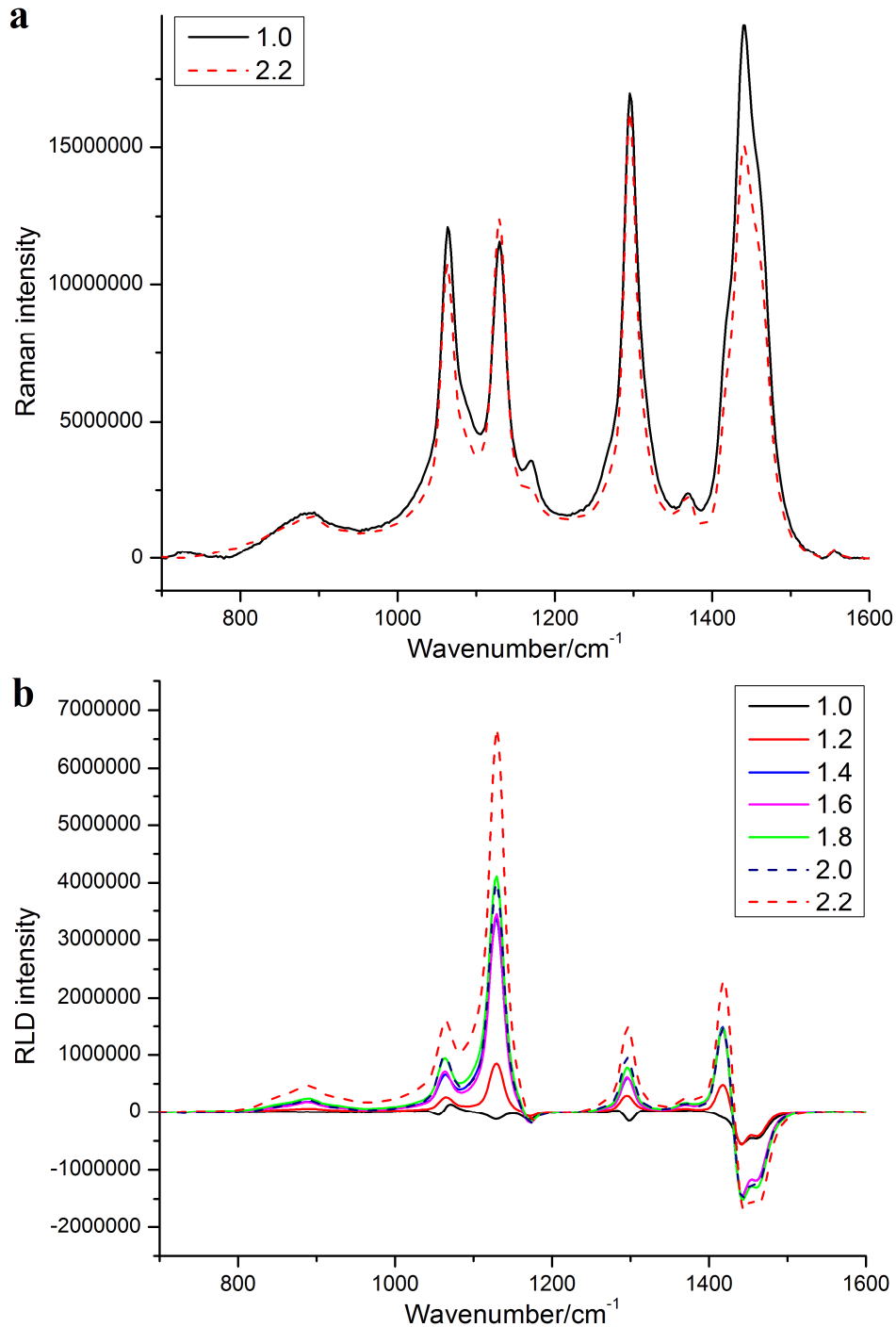


**Fig. 6.3** Spectra of PEO<sup>OX</sup>. a) RLS and b) RLD spectra recorded for different stretching factors, from unstretched (solid black) to 2.2× (dashed red). Each spectrum was recorded using the BioTools instrument with 60 mW laser power for 10 minutes.

The RLD spectra of Fig. 6.3 show an increase in the intensity of peaks upon stretching confirming our XRD results, discussed in the §2, meaning an enhancement in the

orientation of polyethylene chains. As discussed above, we assume that the stretching direction is along the C–C chains of polyethylene, thus their stretching vibrations in the 1000–1130 cm<sup>-1</sup> region and all CH<sub>2</sub> out-of-plane vibrations should result in positive RLD peaks. Vibrations perpendicular to the C–C chains (in-plane CH<sub>2</sub> bending and scissoring vibrations) should give negative RLD bands.

Polyethylene's RLS and RLD spectra confirmed that stretching causes an increase in the amount of crystalline phase, and the orientation of the PE chains. As we have concluded that the guest molecules orient on the crystalline phase, higher stretching factors not only provide more sites for guest molecules to attach to but also, by better orienting those sites, cause a better alignment for the attached molecules.

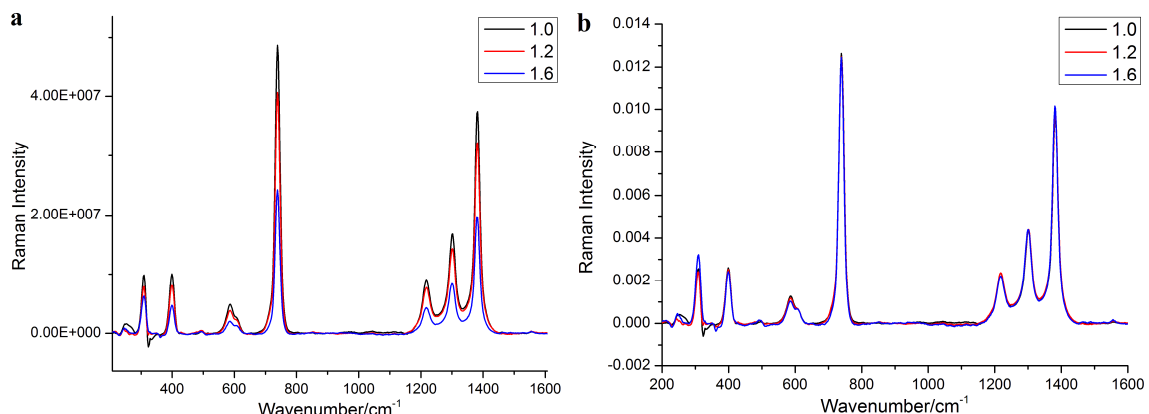
The high number of vibrational peaks of PE could be an obstacle when RLS and RLD of molecules deposited on film are studied. Conversely, it has the advantage of providing an internal standard to investigate the alignment of the guest molecule. Konwerska et al.<sup>94</sup> previously reported molecules preferentially absorbing on the film with the “zig-zag” pattern of their planar carbon structure, matching the similar pattern produced by the adjacent segments of the PE chain in the crystallite. Thus, knowing the vibrational structure and orientation of PE chains could help one to understand those of guest molecules adsorbed on PE films.

### 6.3.2 Polytetrafluoroethylene

We continued the study by recording polarised Raman spectra of polytetrafluoroethylene (PTFE) films with different stretching factors. The RLS peaks show a uniform decrease in intensity upon stretching (Fig. 6.4a). After normalising the spectra to have the area beneath them equal to 1, they became almost identical in all wavenumbers (Fig. 6.4b). The drop in Raman intensity is probably therefore simply due to the reduction in the thickness of the film during the stretching process.

**Table 6.3** The Raman band frequency and RLD direction (Fig. 6.4c), with the assignment, of PTFE Raman peaks. Abbreviation: sym: symmetrical, asym: asymmetrical<sup>96,97</sup>.

Band cm <sup>-1</sup>	RLD direction	Assignment
1380	+	C-C sym stretching
1302	+	C-C asym stretching
1217	-	CF <sub>2</sub> stretching
739	-	CF <sub>2</sub> sym stretching
602	-	CF <sub>3</sub> sym deformation
587	-	CF <sub>3</sub> umbrella
399	-	CF <sub>2</sub> twisting
309	?	CF <sub>2</sub> wagging



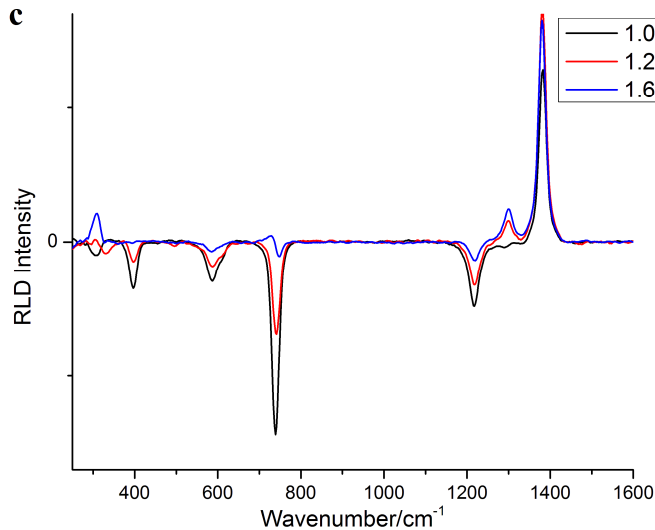


**Fig. 6.4** Raman spectra of PTFE film when it is unstretched (black), stretched with 1.2× (red) and 1.6× (blue) stretching factor. RLS spectra (a) before and (b) after normalising by the area beneath the spectra. (c) RLD spectra.

Carbon–carbon vibrations (1260–1480 cm<sup>-1</sup>) are the only positive bands in PTFE RLD spectrum (Fig. 6.4c) and the rest of the peaks (related to C–F vibrations) are negative (Table 6.3). Upon stretching, an increase in the intensity of C–C vibrations and a decrease in the intensity of C–F bands occurs. This indicates that the film stretching direction is along the PTFE chain axis. The former is simply because of the increase in orientation of chains and the latter could be due to a decrease in the distance between PTFE chains, or their distortion during stretching process.

To evaluate the ability of PE films in aligning molecules we compared the LD spectra of anthracene deposited on PE and polytetrafluoroethylene (PTFE). PTFE is another inert apolar polymer in this case with saturated CF<sub>2</sub> chains which is invisible in UV-Vis spectroscopy (Fig. 6.5).

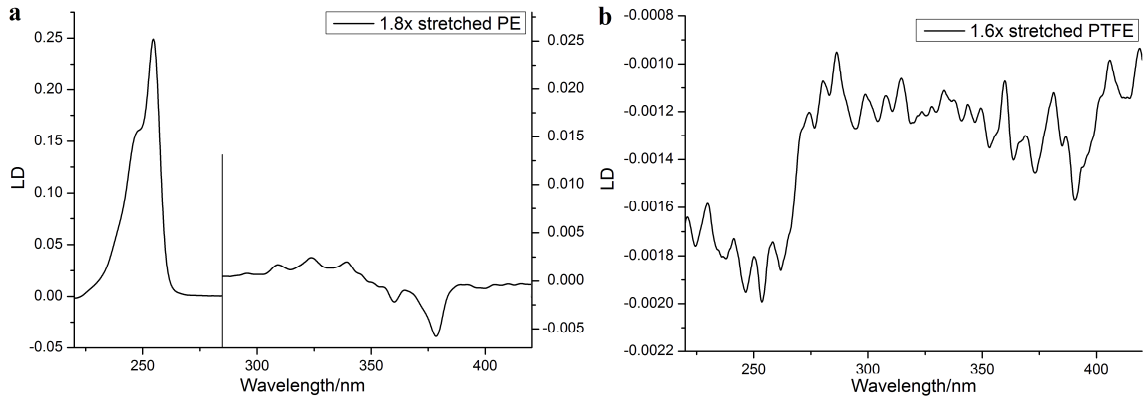


**Fig. 6.5** LD spectra of anthracene (40  $\mu\text{L}$ ) deposited on a) PE and b) PTFE (cut from thread seal tape) from a 0.1 mg/mL chloroform solution.

As shown in Fig. 6.5, the PTFE film failed to provide much orientation of anthracene compared to the effect of PE. The LD signal to noise ratio for anthracene molecules on PTFE film is very low which makes distinguishing of peaks from noise difficult. The short wavelength region includes a broad negative band and also a (presumably) oligomeric band at 390 nm (see §3) is observable, which is not found in anthracene spectrum when it is deposited on PE. This shows that anthracene molecules, even in low concentrations, do not orient well and tend to self-associate on the PTFE films.

### 6.3.3 Progesterone

Since studying polyethylene's vibrational structure and the way it behaves upon stretching could be measured using polarised Raman spectroscopy, also because the absorbance and LD data on PE and  $\text{PE}^{\text{OX}}$  were of high quality, we decided to investigate the behaviour of small molecules absorbed into polyethylene films using Raman spectroscopy to see if it provides complementary information. In §2 we reported the alignment of progesterone on PE and  $\text{PE}^{\text{OX}}$ . LD experiments showed that progesterone aligns approximately along its

long axis in a similar manner on both films. However, to get more orientation information we recorded RLS and RLD spectra of the molecule deposited on PE film (Fig. 6.6).

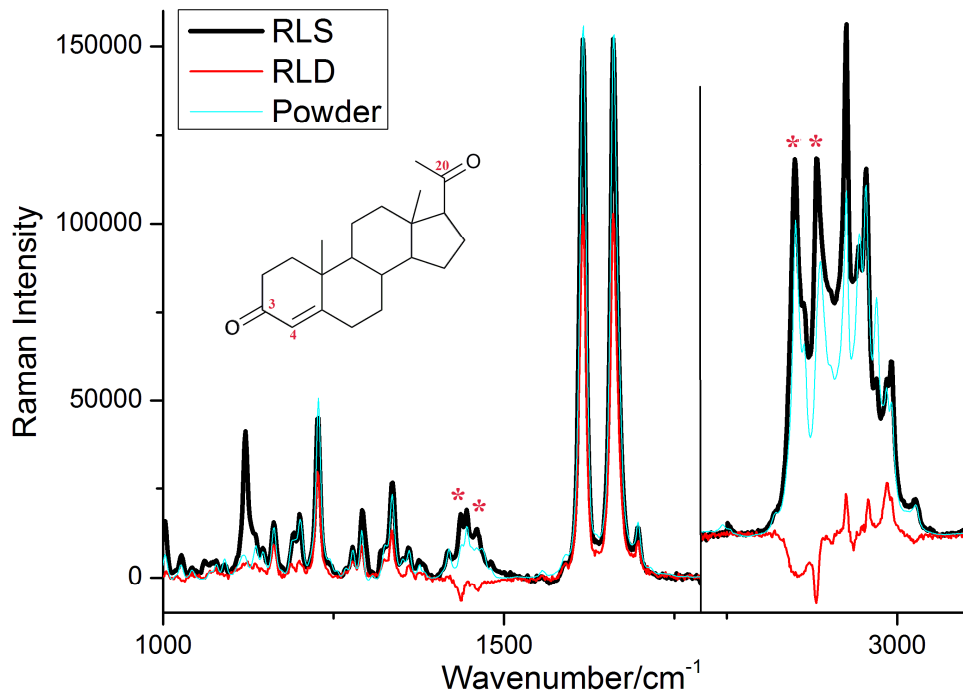


**Fig. 6.6** RLS (black) and RLD (red) spectra of progesterone deposited on PE film overlaid with the Raman spectrum of progesterone in powder phase (cyan, the spectrum intensity diminished 11 times). Peaks labelled by an asterisk are present in both the progesterone powder spectrum and PE. Progesterone's Raman spectrum below 1000 cm<sup>-1</sup> (not shown here), like other steroids, is full of C–H bending vibrations which makes the interpretation of each peak exceedingly difficult. The powder spectrum is recorded using the Renishaw inVia instrument and the spectra of the sample deposited on PE are recorded by the BioTools spectrometer.

Progesterone's long axis is parallel to its C<sub>3</sub> to C<sub>20</sub> axis (Fig. 6.6), thus vibrational transition moments along this axis should give positive RLD peaks (Table 6.4). Two carbonyl bands in the structure give peaks at 1697 and 1660 cm<sup>-1</sup>. The first peak corresponds to the stretching vibration of C<sub>20</sub>=O bond, as a free carbonyl bond, and the second one relates to the C<sub>3</sub>=O bond which is shifted to a lower frequency due to the conjugation of the band with C<sub>4</sub>=C leading to delocalisation of  $\pi$  electrons and reduce double bond characteristic

of the carbonyl band. All three unsaturated bonds have positive RLD bands (Fig. 6.6) confirming the alignment of progesterone along its long axis.

**Table 6.4** The band frequency, RLD direction (Fig. 6.6), and assignments of progesterone Raman peaks. The frequencies labelled in red are present in both progesterone (powder and sample deposited on PE film) and polyethylene. Abbreviation: str: stretching, bend: bending.<sup>97–99</sup>

Band cm <sup>-1</sup>	RLD direction	Assignment	Band cm <sup>-1</sup>	RLD direction	Assignment	Band cm <sup>-1</sup>	RLD direction	Assignment
3027	–	C–H str	2863	–	"	1419		"
2991	+	"	2850	–	"	1336	+	"
2984	+	"	1697	+	C <sub>20</sub> =O str	1291	+	C <sub>20</sub> =O bend
2969		"	1660	+	C <sub>3</sub> =O str	1277	+	C <sub>3</sub> =O bend
2954	+	"	1616	+	C <sub>4</sub> =C str	1227	+	Ring vibration
2943		"	1590	+	Ring vibration	1199	+	"
2925	+	"	1480	–	CH <sub>3</sub> and CH <sub>2</sub> scissoring	1192	+	"
2901	–	"	1460	–	"	1162	+	"
2887		"	1445	+	"			
2881	–	"	1436	–	"			

### 6.3.4 DAPI

DAPI is a polar molecule with a long semi-planar structure and the accessible (*i.e.* above 200 nm) electronic transition moments are along its long axis (see §2). The LD spectrum of the molecule deposited on PE<sup>OX</sup> and PVA<sup>57</sup> contains several positive bonds corresponding the conjugated C=N and C=C bands (in the long axis of the molecule).

The most important and studied peak in the Raman spectrum of DAPI is the peak at 1612 cm<sup>-1</sup> which corresponds to stretching vibrations of C=N bonds. The rest of the spectrum is

dominated by C–C and C–N peaks in 1139–1212 cm<sup>−1</sup> region and ring C=C peaks around 1460–1584 cm<sup>−1</sup><sup>100</sup> (Table 6.5). The RLD spectrum of DAPI consists of all positive Raman bands indicating that all Raman-active vibrational transition moments of the molecule are along its long axis (Fig. 6.7), except perhaps C–H vibrations overlaid on top of PE bands or other DAPI vibrations.

**Table 6.5** The Raman band frequency and RLD direction (Fig. 6.7) with the assignment of DAPI Raman peaks. The band at 2879 cm<sup>−1</sup> labelled with red is present in polyethylene. Abbreviation: str: stretching.

Band cm <sup>−1</sup>	RLD direction	Assignment	Band cm <sup>−1</sup>	RLD direction	Assignment
3065	+	Sp <sup>2</sup> C–H	1388	+	
2936		Sp <sup>2</sup> N–H	1317	+	
<b>2879</b>		Sp <sup>3</sup> N–H	1294	+	
1612	+	C=N str	1182	+	<b>C–C and C–N str</b>
1580	+	C=C str	1140		"
1519	+	"	1016	+	
1485	+	"	934	+	
1461	+	"	745	+	

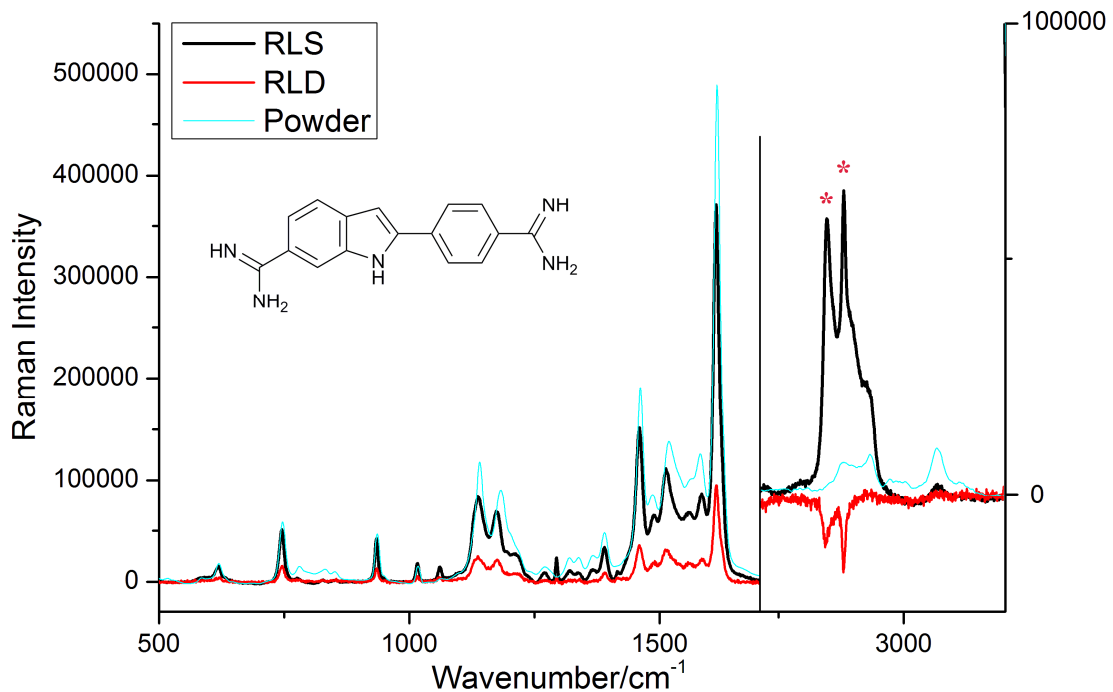


**Fig. 6.7** Raman spectrum of DAPI in powder phase (cyan) overlaid with RLS (black) and RLD (red) spectra of the molecule deposited on PE<sup>OX</sup>. The labelled peaks by asterisks are from the PE substrate. The polyethylene negative C–H band in the spectrum works like an internal standard to confirm the aligning orientation of DAPI on PE chains.

### 6.3.5 1-Pyrenecarboxaldehyde

1-PyCO, due to its aldehyde group ( $C_s$ ), does not align along its pyrene ( $D_{2h}$ ) motif on PE films.<sup>101</sup> As discussed in §2 the molecule orients such that all its electronic transition moments are below the magic angle. As Fig. 6.8 and Table 6.6 show the ring C–H stretching modes in 3070–2910 cm<sup>-1</sup> give positive RLD peaks while the aldehyde C–H vibration at 2904 cm<sup>-1</sup> gives a very weak negative band. The aldehyde band at 1598 cm<sup>-1</sup> has a red shift with respect to the free aldehyde bands (1725 cm<sup>-1</sup>) which is due to its conjugation with the pyrene motif of the molecule. Its RLD peak is split into a positive and a weaker negative band. This splitting could be due to free rotation (or distribution of

orientations) of the chromophore. Pyrene's ring C=C bands in 1350–1500 cm<sup>-1</sup> have positive RLD peaks. Polyethylene's negative C–H stretching bands at 2848 and 1880 cm<sup>-1</sup>, as an internal standard, confirms the orientation of 1-PyCO vibrations. Thus pyrene's C=C and C–H stretching vibrations are aligned along the PE film stretching direction and due to the free rotation of aldehyde bond, its vibrations give weak RLD peaks.

**Table 6.6** 1-PyCO Raman band frequencies with their RLD directions (Fig.6.8). The frequencies labelled with red are arise from PE film C–H stretching vibrations.

Band cm <sup>-1</sup>	RLD direction	Band cm <sup>-1</sup>	RLD direction	Band cm <sup>-1</sup>	RLD direction
3068	+	1401	+	701	+
3043	+	1359	+	586	+
3013	+	1295	-	563	+
2951	+	1252	+	510	+
2939	+	1195	+	465	+
2917	+	1163	+	510	+
2904	-	1128	-	465	+
2880	-	1059	-	410	+
2848	-	1038	+	367	-
1598	±	901	+	216	+
1441	+	874	+	169	+
1415	-	805	+		

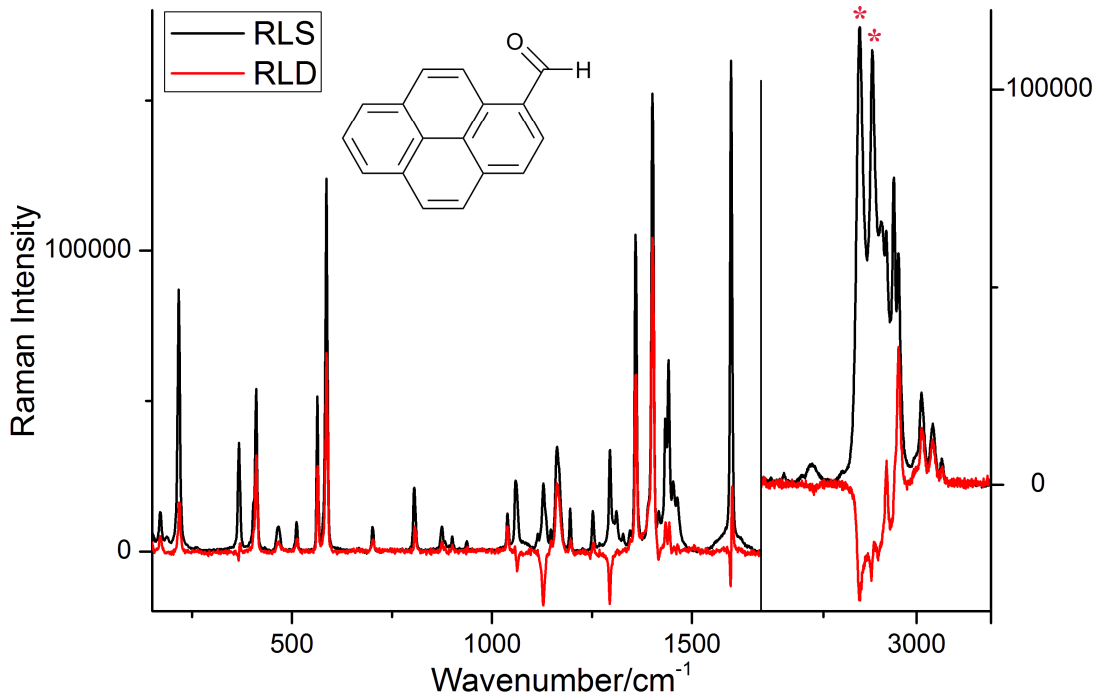


**Fig. 6.8** RLS (black) and RLD (red) spectra of 1PyCO on PE. The labelled peaks with asterisks correspond to polyethylene's C–H stretching vibrations. The spectra recorded by the Renishaw inVia spectrometer.

### 6.3.6 Anthracene

Anthracene belongs to the  $D_{2h}$  group point. It has 66 vibrations of symmetry ( $12 A_g + 11 B_{1g} + 6 B_{2g} + 4 B_{3g} + 5 A_u + 6 B_{1u} + 11 B_{2u} + 11 B_{3u}$ ) of which 28 (the  $B_{1g}$ ,  $B_{2g}$  and  $B_{3g}$  vibrations) are IR and 33 (the  $A_g$ ,  $B_{1g}$ ,  $B_{2g}$  and  $B_{3g}$  vibrations) are Raman active bands.

As LD results for anthracene deposited on PE and PE<sup>OX</sup> showed the  $1.8\times$  stretched film gives a decent orientation parameter (S) on both films. Previously, James Cheeseman<sup>6</sup> calculated the RLS and RLD spectra for anthracene when its long axis is oriented in  $0^\circ$ ,  $45^\circ$ , and  $90^\circ$  to the orientation direction (Fig. 6.9), which correspond to Fig. 3.4a, c and b

in §3 respectively. In our article in 2010, we compared the calculated spectra with anthracene's powder, dried-on-quartz and deposited-on-PE-film spectra measured using the Renishaw microscopy Raman spectrometer.<sup>6</sup>

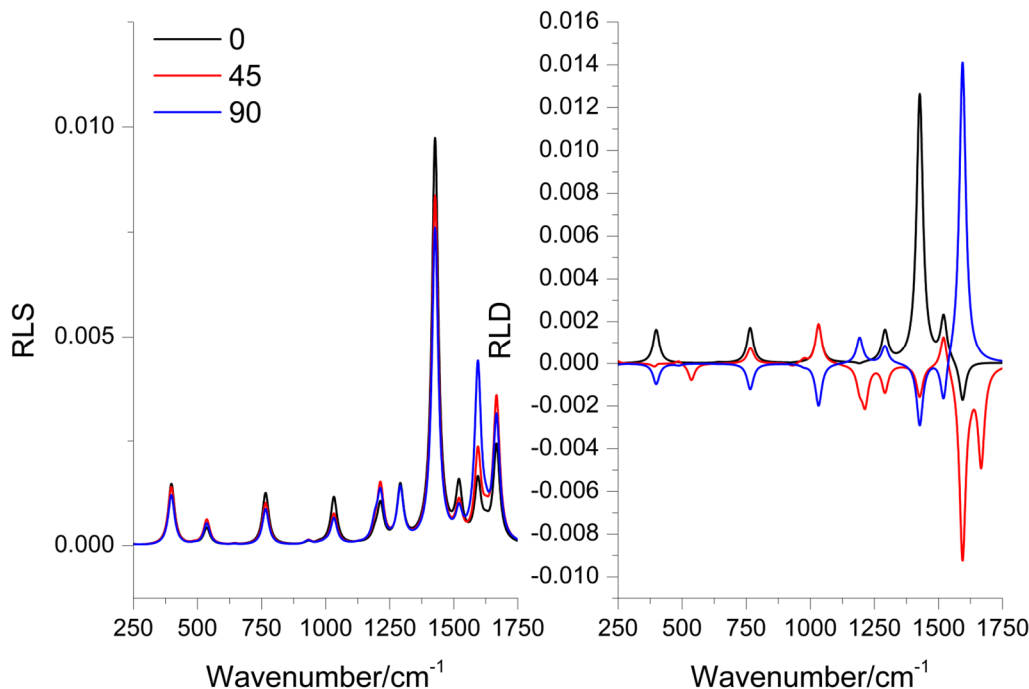


**Fig. 6.9** Calculated RLS spectra (with arbitrary, but consistent, intensity scale), and calculated RLD spectra (with arbitrary, but consistent, intensity scale) for anthracene oriented with the anthracene long axis at 0°, 45°, and 90° to the orientation direction.

The peaks previously reported for anthracene<sup>18,102–105</sup> between 244 and 1632 cm<sup>-1</sup> are all present and shown in the Table 6.7.

**Table 6.7** Anthracene Raman frequencies in powder phase and dried on PE film compared with literature along with the assignment for each vibration.

Anthracene Raman band wavenumbers / cm <sup>-1</sup>				Assignment
Calculated	Powder (Renishaw)	Dried on PE (BioTools)	Literature	
398	393.3 (w)	409.9 (w)	395	C–C out of plane bending
536	518 (vw)	534.8 (vw)	522	
766	750.8 (m)	756.6 (m)	753	C–C in plane bending
1033	1006.4 (vw)	1008.3 (w)	1010	Ring breathing

1213	1162.1 (m)	1164.6 (w)	1155	C–H out of plane bending
	1185.7 (w)	1185.5 (m)	1184	
1292	1257.6 (m)	1259 (m)	1257	C–H in plane bending
	1357.1 (vw)	1375.8 (vw)	1375	C=C stretching
1427	1401.2 (s)	1402.3 (s)	1400	C=C stretching
	1410.4 (m)		1414	C=C stretching
	1478.9 (vw)	1478.5 (w)	1481	C=C stretching
1521	1503.1 (w)	1504.3 (vw)	1505	C=C stretching
1594	1555.8 (s)	1555.3 (s)	1557	C=C stretching
1667	1632.1 (w)	1630.5 (m)	1630	C=C stretching

Due to the insensitivity of Raman spectra we had to load high volumes of anthracene solution on the PE film in order to observe anthracene's Raman peaks. This prevented us from collecting monomeric spectra. Instead, we could detect different dimeric or oligomeric species formed on the PE film. Fig. 6.10 shows a number of different RLD spectra recorded for anthracene and their corresponding RLD peak directions are summarised in the Table 6.8.

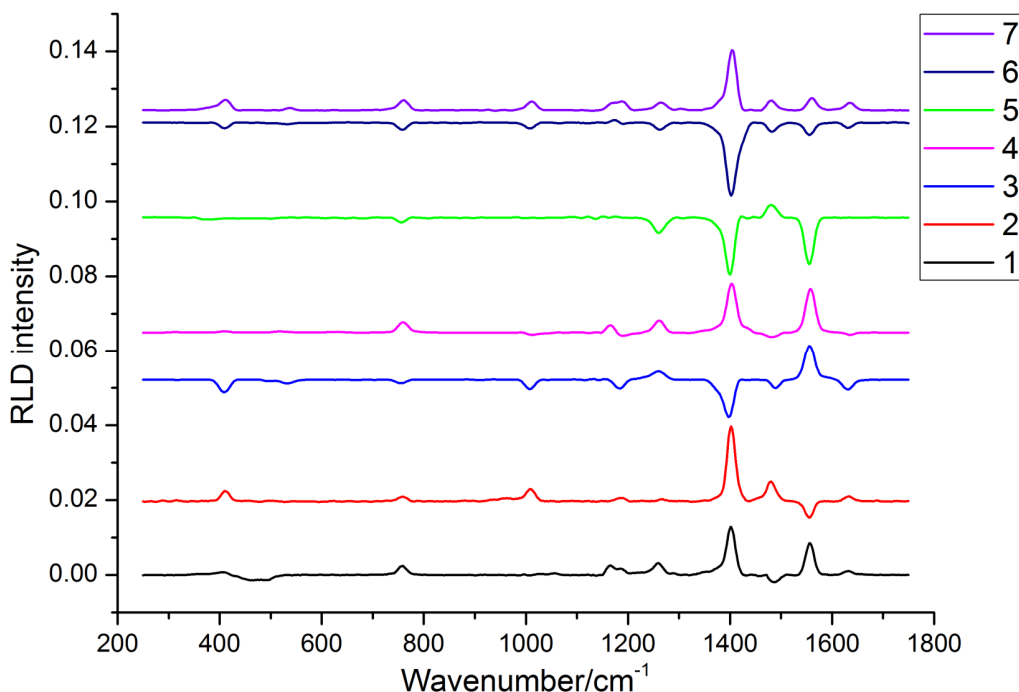


**Fig. 6.10** Different RLD spectra of anthracene deposited on PE film recorded using the BioTools spectrometer. The numbers in the legend are to label each spectrum. Each spectrum is recorded by either moving the film around or preparing a new sample by depositing the molecules on a new PE film. The PE spectrum has been subtracted from each anthracene spectrum. The spectra are displaced to present the change in the peak directions more clearly.

**Table 6.8** Anthracene's RLD peak directions for calculated and recorded spectra for each peak. The first three rows correspond the RLD peak directions of calculated anthracene spectra when the molecule is aligned 0 (bold black), 45 (bold red) and 90 (bold blue) degrees in respect to the orienting direction. The rest are related to the RLD spectra shown in Fig. 6.10. The bold spectra are the ones with similar RLD directions to the calculated spectra.

	RLD direction of peaks / $\text{cm}^{-1}$									
	409	495	756	1010	1164	1261	1402	1487	1555	1630
<b>Calc. 0°</b>	+		+	+	+	-	+	+	-	
<b>Calc. 45°</b>		-	+	+	-	-	-	+	-	-
<b>Calc. 90°</b>	-		-	-	+	+	-	-	+	
Spectrum number (Fig. 6.10)										
1	+	-	+		+	+	+	-	+	+
2	+		+	+	+	+	+	+	-	+
3	-	-	-	-	-	+	-	-	+	-
4	+	+	+	-	+	+	+	-	+	-
5	-		-			-	-	+	-	
6	-	-	-	-	+	-	-	-	-	-
7	+	+	+	+	+	+	+	+	+	+

Comparison between calculated and experimental data (shown in Table 6.8) we observed that the RLD spectrum number 2 has similar peak directions to anthracene monomers oriented with their long axis parallel to the orientation direction. The spectrum number 5 has similar RLD peak directions to the calculated spectra of anthracene when the molecule is oriented with its long axis at 45° to the orientation direction, whereas the spectrum number 3 corresponds to the 90° calculation. The rest of the spectra show different vibrational transition moment behaviour.

According to the peak assignments in the Table 6.7 the vibrations in the 1500–1640  $\text{cm}^{-1}$  region correspond to C=C vibrations. The band at 1630  $\text{cm}^{-1}$  shows no RLD signal when the molecule is oriented with either its long or short axis parallel to the PE film stretching direction (Table 6.8). Therefore, this signal could originate from two symmetrical C=C stretching vibrations of equal intensity but perpendicular polarizations, thus cancelling each other out when RLD spectrum is calculated (Fig. 6.11, when the red and blue

vibrations are equal). The bands at 1555 and 1261 cm<sup>-1</sup> give RLD signals with negative signs when the molecule is oriented with its long axis parallel to the stretch direction and positive when it is aligned with the short axis along the stretch direction. The first signal (1555 cm<sup>-1</sup>) could be due to the C=C vibrations perpendicular to the long axis of the molecule (Fig. 6.11, vibrations highlighted by blue). The band at 1261 cm<sup>-1</sup> corresponds to C–H in-plane bending vibrations which are short axis polarized. The out-of-plane C–H bending vibrations (1164 cm<sup>-1</sup>) and C–C stretching vibrations (1402 and 1487 cm<sup>-1</sup>) are along the long axis of the molecule (Fig. 6.11, red), thus they result in positive and negative RLD signals when the molecule is oriented along its long and short axis respectively.

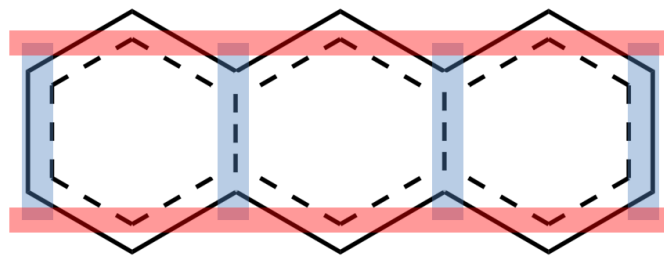


**Fig. 6.11** Schematic structure of anthracene with its vibration directions along its long (red) and short axis (blue).

### 6.3.7 Thymine, thymidine and thymidine 5'-monophosphate

The molecular structures of thymine, thymidine and thymidine 5'-monophosphate are shown in Fig. 6.12.

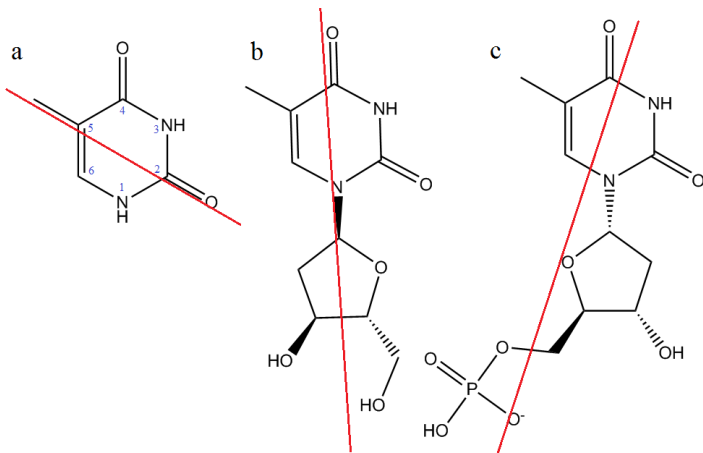


**Fig. 6.12** Molecular structures of a) thymine, b) thymidine and c) thymidine 5'-monophosphate with their longest axes shown in red.

RLS and RLD spectra of thymine, thymidine and thymidine 5'-monophosphate (Fig. 6.12) are shown in Fig. 6.13. The peak assignments for the molecules are presented in Table 6.9.<sup>106–113</sup> The bands in common between three molecules are due to the thymine moiety and the bands only appearing in the spectra of thymidine and thymidine 5'-monophosphate are due to the deoxyribose moiety. The band at  $1671\text{ cm}^{-1}$  corresponds to the stretching vibrations of  $\text{C}_{(4)}=\text{O}$  and  $\text{C}_{(5)}=\text{C}_{(6)}$  in thymine, this band red-shifts to  $1665\text{ cm}^{-1}$  in thymidine and TMP spectra. The  $\text{N}_{(3)}-\text{H}$  bending vibration gives a peak at  $\sim 1480$  and  $\sim 1230\text{ cm}^{-1}$  for thymine and thymidine. The  $\text{N}_{(1)}-\text{H}$  bond, only presenting in the structure of thymine, vibrates at  $1408\text{ cm}^{-1}$ . The in-plane bending vibrations of  $\text{C}_{(6)}-\text{H}$  and in-phase and out-of-phase rocking vibrations  $\text{CH}_3$  appear at  $\sim 1370$ ,  $1000$  and  $1060\text{ cm}^{-1}$ . The peak at  $746\text{ cm}^{-1}$  is related to the pyrimidine ring breathing vibrations and the bands at  $380\text{ cm}^{-1}$  in thymidine and TMP are corresponding to the deoxyribose vibrations.

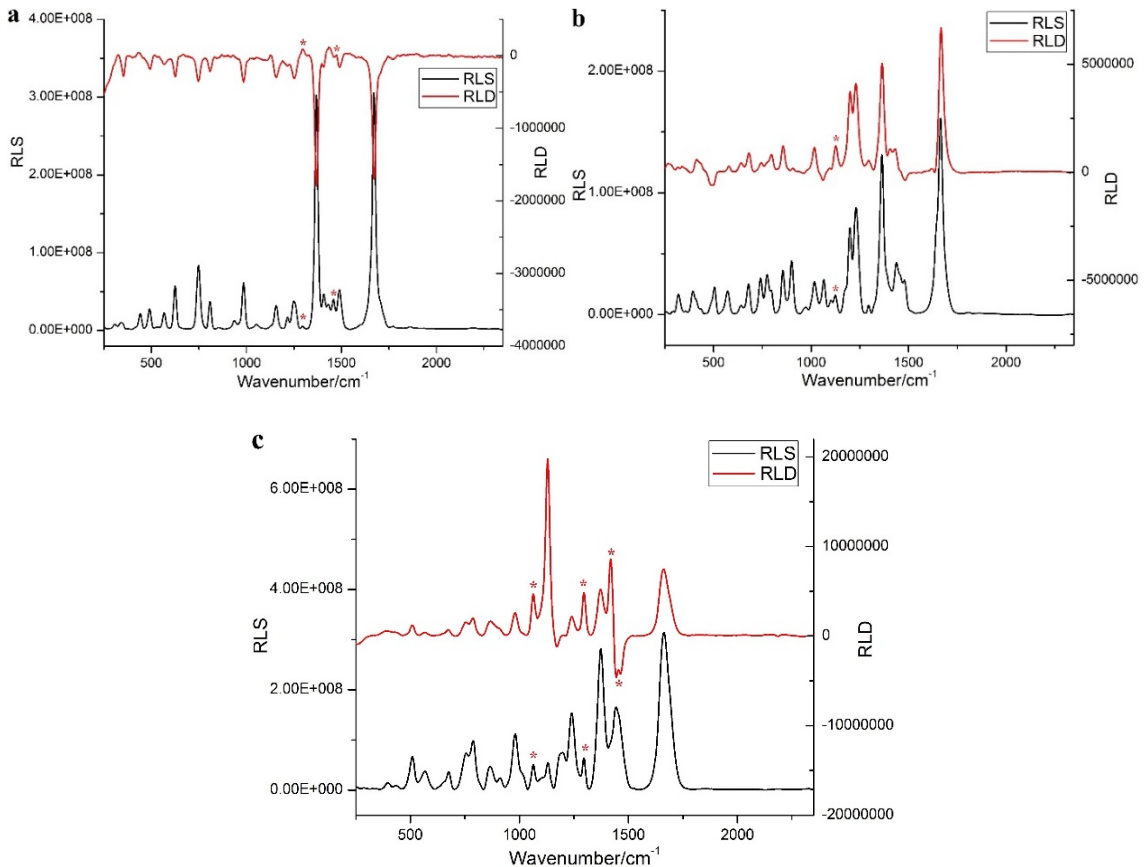


**Fig. 6.13** The RLS (black) and RLD (red) spectra of a) thymine, b) thymidine and c) thymidine 5'-monophosphate deposited on 1.8× stretched PE<sup>OX</sup>. The peaks labelled by asterisks are from polyethylene vibrations.

According to Ushizawa et al.<sup>113</sup> the bands at 1665, 1370, 1000, 680 and 630 cm<sup>-1</sup> (respectively corresponding to C<sub>(4)</sub>=O and C<sub>(5)</sub>=C<sub>(6)</sub> stretching, C<sub>(6)</sub>-H in-plane bending, CH<sub>3</sub> in-phase rocking, deoxyribose mode and C<sub>(2)</sub>=O/C<sub>(4)</sub>=O “windscreen wiper” vibrations) have the same polarisations. The RLD peaks corresponding to these vibrations are negative in the thymine spectrum and positive in the thymidine and TMP spectra. This is consistent with their orientation being along the longest axes of the molecules in thymidinr and TMP (Fig. 6.12) leading to a different (by almost 90°) orientation with respect to thymine on PE<sup>OX</sup>. Bonds with negative RLD signals in the thymine spectrum (Fig. 6.13a) have vibrational transition moments perpendicular to the molecules long axis

(stretching direction, Fig. 6.12a). The same vibrations in thymidine and TMP (Fig. 6.12b and c) have transition moments parallel to the molecules' long axis (Fig. 6.13b and c).

**Table 6.9** The RLS peak wavenumbers, their corresponding RLD signs (Fig. 6.13) and assignments for thymine, thymidine and thymine 5'-monophosphate. The frequencies labelled by red are related to vibrations from polyethylene. Abbreviations: str (stretching), bend (bending), def (deformation), sym (symmetrical) and asym (asymmetrical).

Band / cm <sup>-1</sup> with RLD directions			Assignment
Thymine	Thymidine	TMP	
1671 –	1665 +	1663 +	C <sub>(4)</sub> =O and C <sub>(5)</sub> =C <sub>(6)</sub> in-phase str
1489 –	1478 –		N <sub>(3)</sub> –H in-plane bend
1459 –			Polyethylene CH <sub>2</sub> bend
1430 +	1437	1441 –	C–N asymmetrical str / CH <sub>3</sub> asymmetrical bend / polyethylene CH <sub>2</sub> scissoring
		1419 +	polyethylene CH <sub>2</sub> wagging
1408 –			N <sub>(1)</sub> –H bend
1369 –	1362 +	1373 +	C <sub>(6)</sub> –H in-plane bend / C–N / CH <sub>3</sub> asymmetrical bend
1295 +		1295 +	Polyethylene CH <sub>2</sub> twisting
1252 –			Thymine ring str
1215 –	1229 +	1238 +	N <sub>(3)</sub> –H bend / C–N
1155 –	1199 +	1199 +	C–C / ribose C–O str
	1124 +		Polyethylene C–C sym str
	1103		
1053 +	1065 –	1063 +	CH <sub>3</sub> out-of-phase rocking / polyethylene C–C asym str
	1018 +		CH <sub>3</sub> in-phase rocking
986 –		981 +	CH <sub>3</sub> in-phase rocking
938 +			
	901 +	908 +	Sugar, 2'-CH <sub>2</sub> rocking
856 –	854 +	866 +	C–C str
809 –	794 +		N <sub>(1)</sub> –C <sub>(2)</sub>
		786 +	P–O str
746 –	746 +	754 +	Pyrimidine ring breathing / C=O def
	682 +	675 +	Coupling of deoxyribose mode with 641 cm <sup>-1</sup> band
626 –	641 +		C <sub>(2)</sub> =O/C <sub>(4)</sub> =O "windscreen wiper"
566 –	579 +	566 +	Base in-plane ring deformation
489 –	503 –	508 +	Base in-plane ring deformation
442 +			
	396 +	396 +	

### 6.3.8 Cytosine, cytidine and cytidine 5'-monophosphate

The molecular structures of cytosine, cytidine and cytidine 5'-monophosphate are shown in Fig. 6.14. The polarised Raman spectra of them are shown in Fig. 6.15.

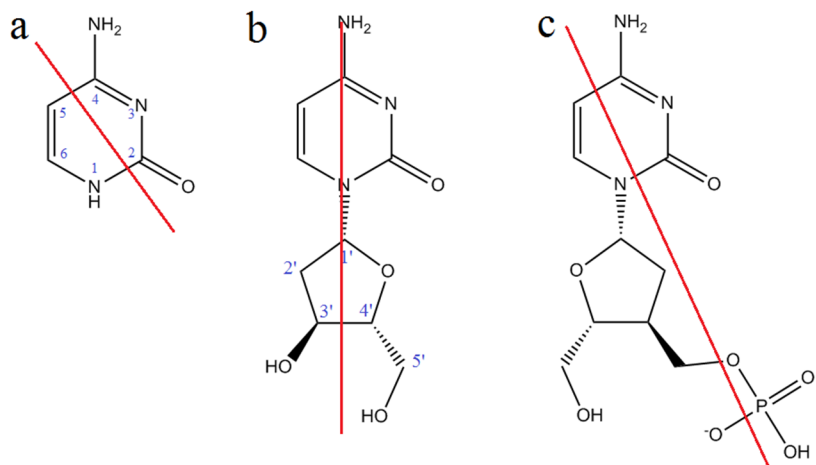


**Fig. 6.14** Molecular structures of a) cytosine, b) cytidine and c) cytidine 5'-monophosphate with their longest axes shown in red.

The RLS band assignments<sup>114–119</sup> and their corresponding RLD signal signs for cytosine, cytidine and CMP are summarised in Table 6.10. The broad band covering the 1560–1695 cm<sup>-1</sup> region corresponds to the cytosine moiety's C<sub>(2)</sub>=O and C<sub>(5)</sub>=C<sub>(6)</sub> stretching vibrations. This band continues to 1730 cm<sup>-1</sup> in cytosine's RLS spectrum due to overlap with the bending vibrations of N<sub>(1)</sub>–H bond which is absent in cytidine and CMP molecules. The peaks corresponding to cytidine ring stretching and C–H bending vibrations occupy the 1200–1500 cm<sup>-1</sup> region of the three molecules' spectra. The vibrations related to the sugar moiety of cytidine and CMP molecules happen in 600–1200 cm<sup>-1</sup> region.

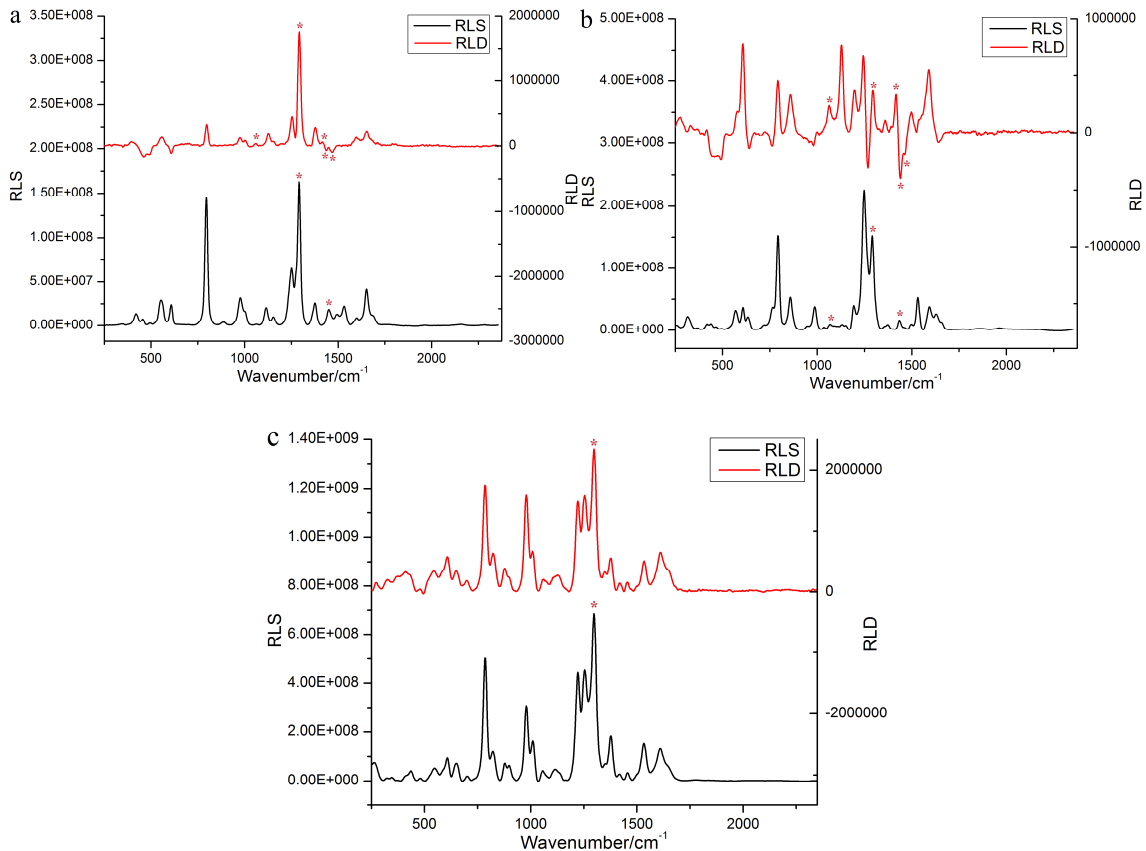


**Fig. 6.15** The RLS (black) and RLD (red) spectra of a) cytosine, b) cytidine and c) cytosine 5'-monophosphate deposited on 1.8× stretched PE<sup>OX</sup>. The peaks labelled by asterisks are from polyethylene vibrations.

Assuming that the molecules are aligned with their long axis parallel to the PE<sup>OX</sup> stretching direction, the RLD signal directions suggest that almost all Raman-active vibrations in cytosine and CMP molecules are long axis (within 54.7° from the long axis) polarised (Fig. 6.15a and c). The cytidine long axis, however, is located in the way that C<sub>(2)</sub>=O and C<sub>(5)</sub>=C<sub>(6)</sub> vibrations have different angles with respect to the PE<sup>OX</sup> stretching direction. As it is shown in the Fig. 6.15b and Table 6.10 the carbonyl polarisability changes more when the incident light's polarization is perpendicular to the long axis of the molecule. However, the polarisability of the C<sub>(5)</sub>=C<sub>(6)</sub> bond changes more with parallel polarised incident light. Thus their RLD signs are respectively negative and positive for cytidine molecule.

**Table 6.10** The RLS peak wavenumbers, their corresponding RLD signs (Fig. 6.15) and assignments for cytosine, cytidine and cytidine 5'-monophosphate. The frequencies labelled by red are related to vibrations from polyethylene. Abbreviations: str (stretching), bend (bending).

Band / cm <sup>-1</sup> with RLD directions			Assignment
Cytosine	Cytidine	CMP	
1683 +			N <sub>(1)</sub> -H bend / C <sub>(2)</sub> =O str
1651 +	1657 -	1649 +	C <sub>(2)</sub> =O str / C <sub>(5)</sub> =C <sub>(6)</sub> str
	1627 -		C <sub>(2)</sub> =O str
1597 +	1596 +	1608 +	C <sub>(5)</sub> =C <sub>(6)</sub> str
1532	1532 +	1532 +	NH in-plane bend / N <sub>(3)</sub> =C <sub>(4)</sub> / ring str
1493 +	1496 +		NH bend / ring str
1469 -	1463 -	1458 +	C-N str / CH bend / <b>Polyethylene CH<sub>2</sub> bending</b>
1450 +			N <sub>(1)</sub> -H bend / C-N str / CH bend???
1435 -	1434 -		<b>Polyethylene CH<sub>2</sub> scissoring</b>
1415 +	1416 +	1420 +	<b>Polyethylene CH<sub>2</sub> wagging</b>
1378 +	1374 +	1379 +	C-N str / CH bend
1293 +	1291 +	1298 +	<b>Polyethylene CH<sub>2</sub> twisting</b>
	1279 -		CH out-of-phase bend
1254 +	1247 +	1252 +	Ring str / CH bend
		1222 +	
	1193 +		Sugar vibrations / C <sub>(1')</sub> -N <sub>(1)</sub> str
1155 +	1155 +	1116 +	Ring bend and str / CO str
	1129 +		Sugar vibrations
1061 +	1067 +		<b>Polyethylene C-C asym stretching</b>
	1040 +	1053 +	Sugar vibrations
		1012 +	
1003 +			Ring bend / out-of-plane C-H bend
974 +	988 -	980 +	Ring bend / NH <sub>2</sub> rocking
	952 -		Sugar vibrations
		898 +	Sugar vibrations
	861 +	879 +	Sugar vibrations / C <sub>(1')</sub> -N <sub>(1)</sub> bend
		822 +	O-P str
794 +	795 +	787 +	Ring breathing / out-of-plane C-H bend
	763 -		Sugar vibrations
		700 +	
	637 -	651 +	Sugar vibrations
608 -	606 +	605 +	Ring bend / C=O bending
561 +	568 +	551 +	C-N in-phase bend
495 -		480 +	
463 -	465 -		

### 6.3.9 Methyl-3- $\alpha$ -acetoxy- $\delta$ -7,9(11)-choladienate

The chemical structure, RLS and RLD spectra for methyl-3- $\alpha$ -acetoxy- $\delta$ -7,9(11)-choladienate (donated as choladienate) are shown in the Fig. 6.16 and the RLS wavenumbers, their corresponding RLD signal directions and assignments<sup>120</sup> are presented in the Table 6.11.

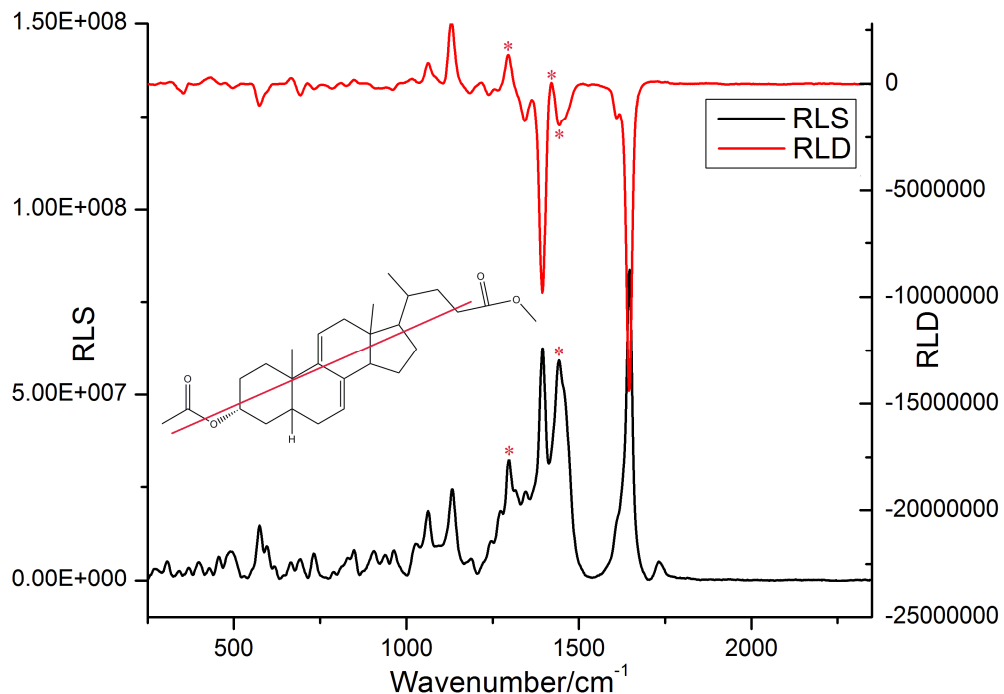


**Fig. 6.16** The schematic structure for methyl 3 $\alpha$ -acetoxy- $\delta$  7,9(11)-choladienate with the RLS (black) and RLD (black) spectra of the molecule deposited on a 1.8 $\times$  stretched PE<sup>OX</sup>. The peaks labelled with asterisks are from polyethylene vibrations. The red line on the structure presents the molecule's long axis. (However, there are free rotations along chain C-C bonds.)

As shown in the Fig. 6.16 the most intensive peak in the RLS spectrum of coladienate appearing at 1647  $\text{cm}^{-1}$ , belongs to the asymmetrical stretching vibrations of the conjugated C=C. The ester carbonyl bond of the molecule exhibits a weak RLS peak at 1732  $\text{cm}^{-1}$  which is not apparent in the RLD spectrum. The second most intense RLS band

at  $1393\text{ cm}^{-1}$  corresponds to the scissoring vibrations of the methyl group adjacent to the carbonyl bond. The ester C–O stretching vibrations occur in the  $1025\text{--}1245\text{ cm}^{-1}$  region of the spectrum. The spectrum region below  $1000\text{ cm}^{-1}$  is full of out-of-plane deformations of the molecule's C–H bonds.

**Table 6.11** The RLS wavenumber peaks with their corresponding RLD signal signs (Fig. 6.16) and assignments for methyl  $3\alpha$ -acetoxy- $\delta$  7,9(11)-choladienate. Abbreviations: str: stretching, def: deformation, sym: symmetrical, asymm: asymmetrical.

Band / $\text{cm}^{-1}$ with RLD directions	Assignment
1732	C=O str
1647 –	C=C asymm str
1605 –	C=C symm str
1441 –	Polyethylene $\text{CH}_2$ scissoring
1419 +	Polyethylene $\text{CH}_2$ wagging
1393 –	(OC)– $\text{CH}_3$ scissoring
1344 –	(OC–O)– $\text{CH}_3$ scissoring
1297 +	Polyethylene $\text{CH}_2$ twisting
1272 –	
1245 –	Ester C–O str
1185 –	Ester C–O str
1131 +	Ester C–O str
1065 +	Ester C–O str
1027 –	(OC)–O– $\text{CH}_3$ str
964 –	C–H out-of-plane def
938 –	"
906 –	"
849 +	"
731 –	
690 –	
664 +	
597 –	
574 –	
489 –	

As the RLD spectrum of choladienate in Fig. 6.16 shows the carbonyl band does not show any significant RLD intensity. This could be due to the free rotation existing between the carbonyl bands and their adjacent carbons leading to different orientations for them. By way of contrast, C=C vibrations exhibit a strong negative RLD band, showing that the orientation of these bonds are perpendicular to the long axis of the molecule. Different vibrations of the ester C–O gives positive and negative RLD peaks in the 1025–1245 cm<sup>-1</sup> region of the spectrum.

### 6.3.10 2,2':5',2''-terthiophene

According to the UV/visible absorbance spectroscopy studies of Potratz et al.<sup>121</sup> on terthiophene, the absorbance spectrum of this molecule (Fig. 6.17 black line) contains one long axis polarised band at ~355 nm and a short axis polarised band at ~256 nm. Our stretched PE<sup>OX</sup> LD experiments (Fig. 6.17) showed that terthiophene aligns with an alignment parameter of 0.52 with its long axis parallel to the stretching direction and its short axis is perpendicular to it. We also detected a third band at 204 nm with a mixed polarization ( $\langle\alpha\rangle = 62^\circ$ ). Knowing the alignment direction of terthiophene we recorded its RLS and RLD spectra (Fig. 6.18).

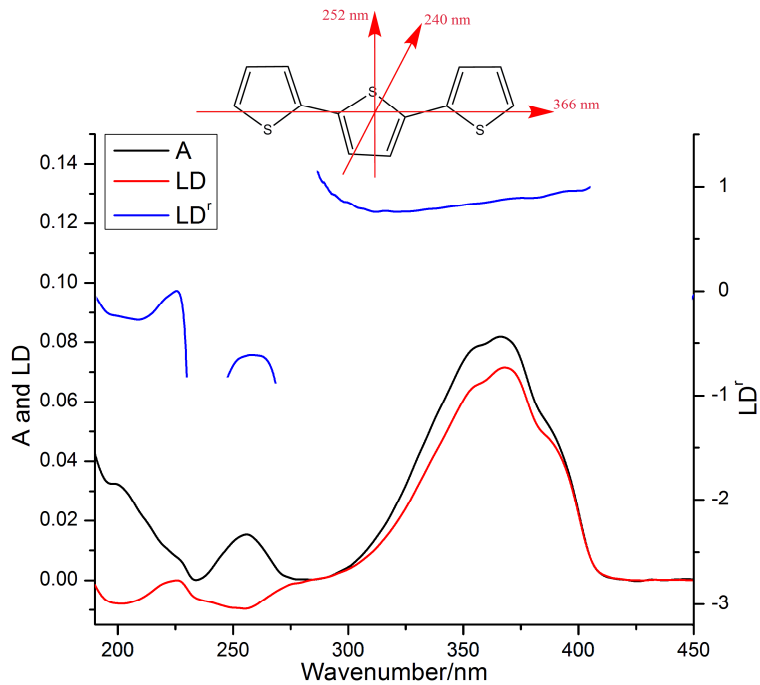


**Fig. 6.17** The absorbance, LD and  $\text{LD}'$  spectra of 2,2':5',2''-terthiophene deposited from a 0.3 mg/mL methanolic solution onto 1.8 $\times$  stretched  $\text{PE}^{\text{OX}}$  overlaid with the schematic chemical structure of the molecule with its transition moment directions labelled on it with red arrows.

The wavenumber, RLD sign and assignments<sup>17,122</sup> for the RLS peaks of terthiophene are summarised in the Table 6.12. The C=C bonds of terthiophene exhibit vibrations in the  $1430\text{--}1560\text{ cm}^{-1}$  region of the molecule's RLS spectrum. Another strong peak from the sample occurring at  $1063\text{ cm}^{-1}$  is related to the out-of phase bending vibrations of C-H bonds.

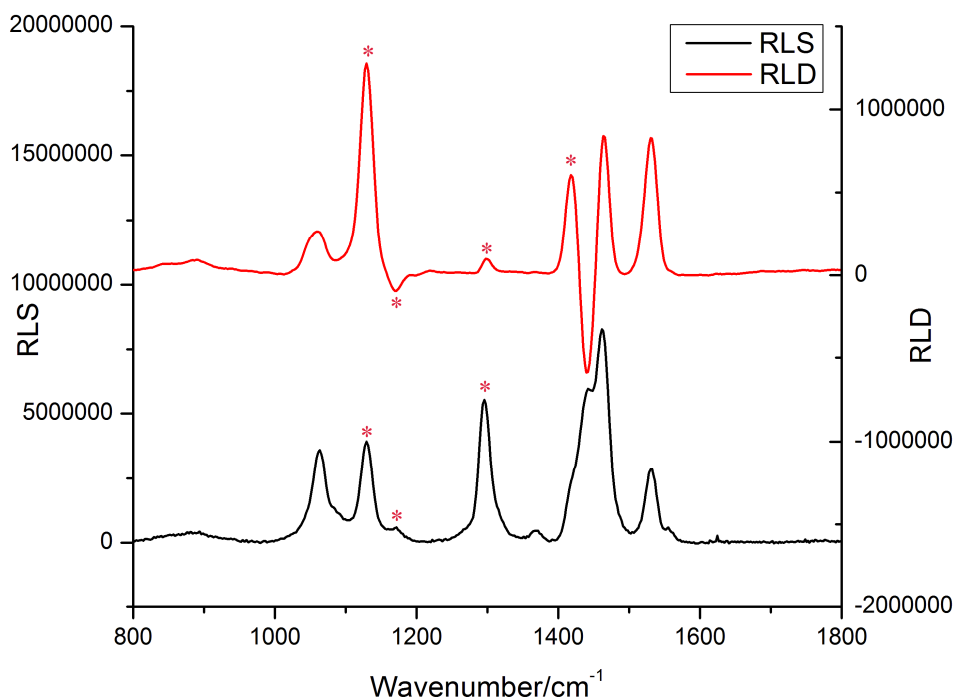


**Fig. 6.18** The RLS (black) and RLD (red) spectra of 2,2':5',2''- terthiophene deposited on 1.8× stretched PE<sup>OX</sup>. The peaks labelled by asterisks are from polyethylene vibrations.

The in-phase stretching vibrations of the molecule's C=C bonds show positive RLD peaks in Fig. 6.18 indicating their vibrations are parallel to the PE<sup>OX</sup> stretching direction. As expected, their out-of-phase stretching vibrations have negative RLD signals. The positive RLD signal for the band at 1063 cm<sup>-1</sup> confirms that the direction of the in-plane C-H bending vibrations is parallel to the in-plane stretching vibrations of C=C bonds.

**Table 6.12** The RLS wavenumber peaks with their corresponding RLD signal signs (Fig. 6.18) and assignments for 2,2':5',2"- terthiophene. Abbreviations: str: stretching, def: deformation, sym: symmetrical, asymm: asymmetrical.

Band / cm <sup>-1</sup> with RLD directions	Assignment
1550 +	C=C str
1532 +	C=C asym str
1461 +	C=C sym str
1439 -	Out-of-phase C=C str
1417 +	Polyethylene CH <sub>2</sub> wagging
1367	
1295 +	Polyethylene CH <sub>2</sub> twisting
1171 -	Polyethylene CH <sub>2</sub> rocking
1129 +	Polyethylene C-C sym str
1063 +	In-plane C-H bend / polyethylene C-C asym str

### 6.3.11 1,10-phenanthroline

As reported by Fergusen et al.<sup>123</sup> 1,10-phenanthroline's absorbance spectra (Fig. 6.19) contains two long axis polarised transition moments at 231 and 265 nm. Our UV-visible stretched PE<sup>OX</sup> LD experiment showed that the molecule aligns with its long axis parallel to the stretch direction on the PE<sup>OX</sup> surface ( $S = 0.09$ ).

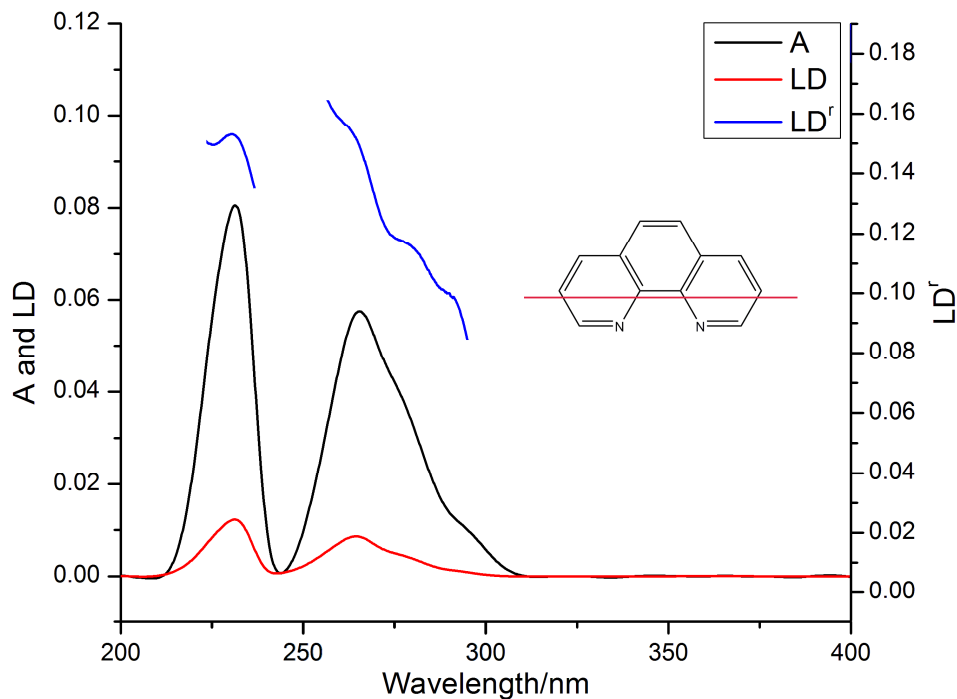


**Fig. 6.19** The absorbance, LD and  $\text{LD}^r$  spectra of 1,10-phenanthroline deposited on  $1.8\times$  stretched  $\text{PE}^{\text{OX}}$  overlaid with the schematic chemical structure of the molecule with its transition moment direction labelled on it with red arrow.

The unpolarised and polarised Raman spectra of phenanthroline are shown in the Fig. 6.20.

The C=C and C=N stretching and bending vibrations occur in the  $1340\text{--}1600\text{ cm}^{-1}$  region of spectrum. The CH<sub>2</sub> bending vibrations happen at  $1446$  and  $1096\text{ cm}^{-1}$ . The band at  $1037\text{ cm}^{-1}$  corresponds to symmetrical ring stretching vibrations.<sup>124,125</sup>

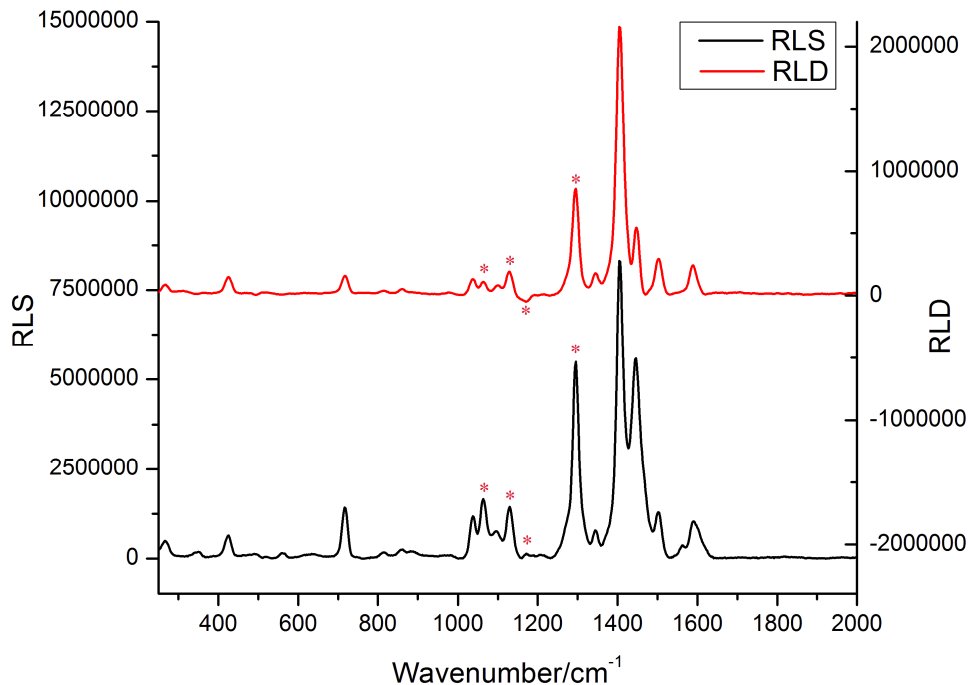


**Fig. 6.20** The RLS (black) and RLD (red) spectra of 1,10-phenanthroline deposited on 1.8× stretched PE<sup>OX</sup>. The peaks labelled by asterisks are from polyethylene vibrations.

The stretching vibrations of C=C and C=N bonds of phenanthroline have positive RLD signals (Table 6.13) showing that the polarisability of these bonds changes more when the electric field of the incident light is parallel to the stretching direction of PE<sup>OX</sup>. The RLD signal direction of the bending vibrations of CH<sub>2</sub> is also positive, showing that their vibrations are in the same direction as those of unsaturated bonds of the molecule.

**Table 6.13** The RLS wavenumber peaks with their corresponding RLD signal signs (Fig. 6.20) and assignments for 1,10-phenanthroline. Abbreviations: str: stretching, def: deformation, sym: symmetrical, asymm: asymmetrical.

Band / cm <sup>-1</sup> with RLD directions	Assignment
1591 +	C=C and C=N str
1567	C=N str
1504 +	C=C str
1446 +	CH <sub>2</sub> scissoring

1404 +	
1344 +	C=C and C=N str
1295 +	Polyethylene CH <sub>2</sub> twisting
1171 -	Polyethylene CH <sub>2</sub> rocking
1131 +	Polyethylene C-C sym str
1096 +	C-H bend
1063 +	Polyethylene C-C asym str
1037 +	Sym ring str
718 +	Out-of-plane ring def

### 6.3.12 Fluorene and Fmoc chloride

The unpolarised and polarised Raman spectra of fluorene (Fig. 6.21a) and fmoc chloride (Fig. 6.21b) are shown in the Fig. 6.22. The RLS wavenumbers, their corresponding RLD sign directions and assignments are summarised in the Table 7.6.

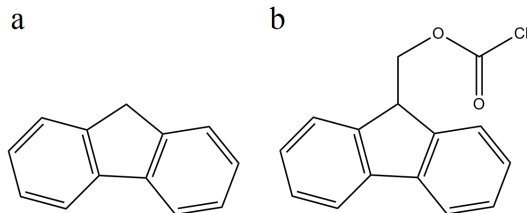


**Fig. 6.21** The schematic chemical structures of a) fluorene and b) fmoc chloride.

Fluorene and fmoc chloride have similar RLS and RLD spectra. The only differences are in the presence of the bands at 1402, 1325, 1090 and 849 cm<sup>-1</sup> only in the spectrum of fluorene and the bands at 1105 and 870 cm<sup>-1</sup> only in the spectrum of fmoc chloride.

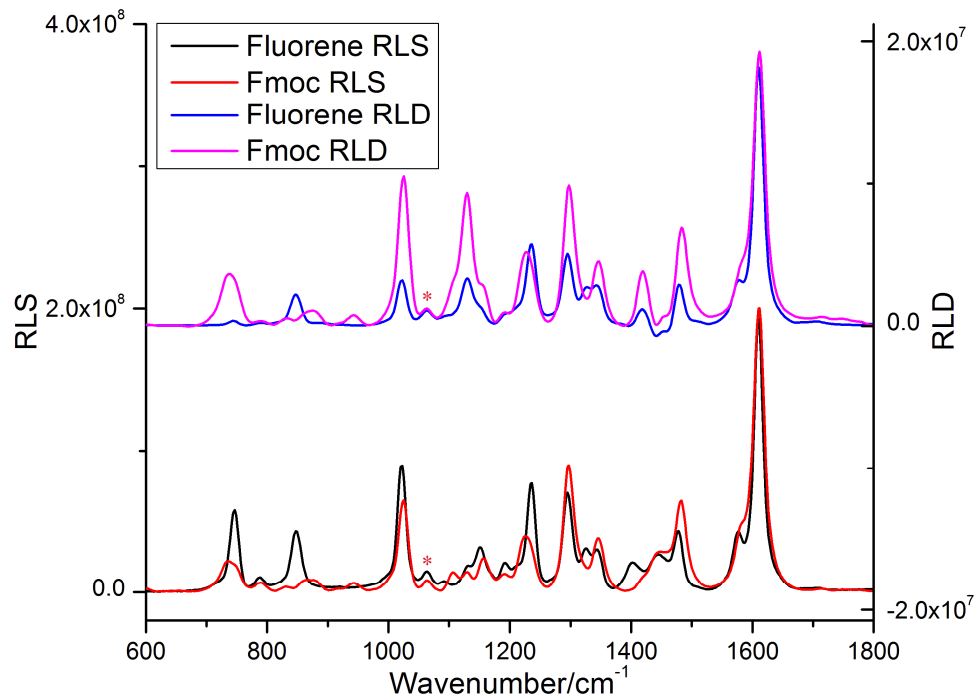


**Fig. 6.22** The RLS spectra of fluorene (black) and fmoc chloride (red) with their corresponding RLD spectra (blue and purple respectively). The peaks labelled by asterisks are from polyethylene vibrations.

The RLD peaks of the both molecules are positive (Table 6.14) confirming that the orientation of all Raman-active vibrations of them are parallel to the PE<sup>OX</sup> stretching directions.

**Table 6.14** The RLS wavenumber peaks with their corresponding RLD signal (Fig. 6.22) signs and assignments<sup>126–131</sup> for fluorene and Fmoc chloride. Abbreviations: str: stretching, bend: bending, def: deformation, asymm: asymmetrical.

Band / cm <sup>-1</sup> with RLD directions		Assignment
Fluorene	Fmoc chloride	
1611 +	1614 +	In-plane C=C str
1576 +	1585 +	
1478 –	1482 +	CH <sub>2</sub> bend
1442 +	1448 +	CH <sub>2</sub> bend
1402 +		
1343 +	1347 +	C–C str
1325 +		

1295 +	1299 +	C–C str
1191 +	1191 +	
1151 +	1157 +	
1133 +	1129 +	
	1105 +	Ester C–O str
1090 +		Aromatic CH def
1063 +	1063 +	Polyethylene C–C asym str
1022 +	1024 +	Ring breathing mode
	944 +	
	870 +	
849 +		C–C str
787 +	791 +	
745 +	737 +	Ring breathing

## 6.4 Conclusions

In this chapter we examined and evaluated our new polarised Raman spectroscopy technique by recording RLS and RLD spectra of polyethylene and polytetrafluoroethylene and aligned small biomolecules deposited on stretched PE<sup>OX</sup> films. The RLS and RLD spectra of polyethylene gave us more information on how the film structure and crystallinity changes upon stretching. Understanding the RLD spectrum of stretched polyethylene abled us to interpret the vibrational alignment of molecules deposited on the stretched film. The vibrational orientation of a set of compounds with different polarity from different types was investigated. The differences between the alignment of nucleic acid bases, nucleosides and nucleotides, and fluorene and fmoc chloride were studied. The addition of deoxyribose moiety to thymine changed the long axis direction of the molecule, thus the RLD spectra of thymidine and TMP are different from that of thymine. However, adding extra groups to cytosine and fluorene did not significantly change their vibrational transition moments. Recording the polarised Raman spectra of different anthracene

samples resulted in different RLD spectra, showing the difference in the alignment of different anthracene dimers or higher order structures.



# **Chapter Seven**

## **Studying the alignment of small biomolecules embedded in lipid vesicles**

### **Acknowledgement**

I wish to thank Miss Amie Roberts for helping me with the data collection for this chapter as a part of her MChem project. I would like to express my appreciation to the Materials and Analytical Sciences (MAS) Facility of the University of Warwick for giving me the permission to use their differential scanning calorimeter, and Mr. Dave Hammond for kindly helping me in running the experiments. I also want to thank Dr. Shirin Jamshidi for performing the computational modelling techniques for the experimental results of this chapter.



## 7.1 Introduction

Lipid vesicles play an important role in biological systems. They provide a semi-permeable bilayer membrane around cells and isolate the cytoplasm from the external environment. They also provide cellular compartments in eukaryotic cells. Many molecules such as proteins and steroids can bind to lipids and form channels, receptors and fluidity regulators. Embedding small biomolecules in lipid vesicles in order to investigate their influence on the fluidity of lipid bilayer systems<sup>132,133</sup> and also to transport them in biological systems<sup>134,135</sup> has been studied for decades. One important question is that of where and how does the guest molecule orient in a phospholipid bilayer? Depending on the size, polarity and charge of the molecule, it may align between the phospholipid molecules, lie on the surface of the vesicle or be captive inside it (Fig. 7.1). There are different techniques, including linear dichroism, that have been utilised to investigate the way a molecule interacts with lipid vesicles.<sup>136–138</sup> Our aim has been to develop methods to use Raman spectroscopy to study lipid bilayer systems and to probe how guest molecules orient inside them.

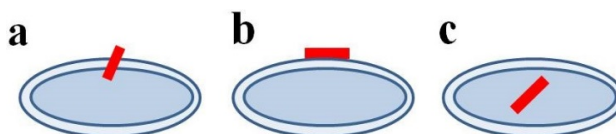


**Fig. 7.1** Three general ways a guest molecule interacts with lipid vesicles: a) inserting between the phospholipid molecules, b) lying on the surface of the vesicle and c) being captive inside the vesicle.

In this chapter we report the study of a range of molecules (listed in the Fig. 7.2) using: (1) UV-visible linear dichroism to investigate their orientation on polyethylene films (PE and

$\text{PE}^{\text{OX}}$ ), (2) polarised Raman spectroscopy to identify vibrational bands of molecules in known orientation, (3) polarised Raman spectroscopy to study their alignment in lipid vesicles dried on polyethylene, and finally (4) differential scanning calorimetry (DSC) to measure the effect of the probe molecule in lipid environment and also to determine their interaction sites.

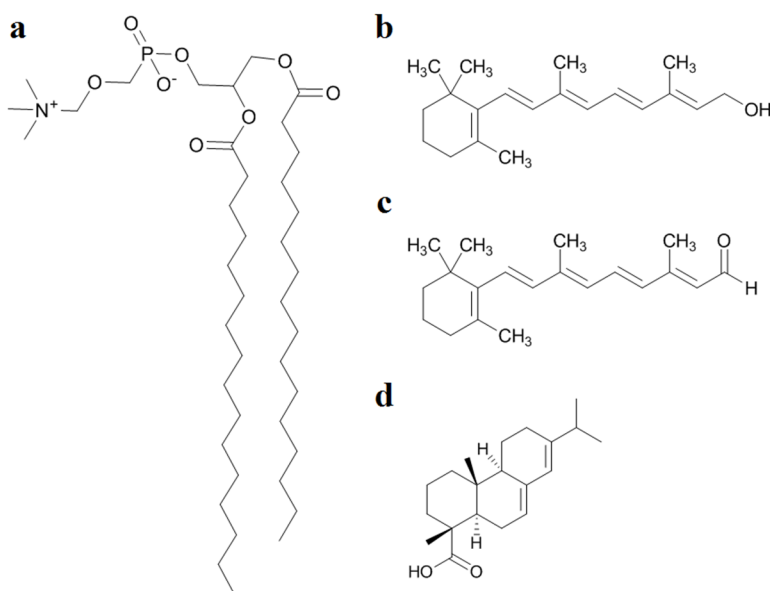


**Fig. 7.2** Chemical structures of a) DPPC, b) retinol, c) retinal and d) abietic acid.

Retinoids and abietic acid (Fig. 7.2) were chosen as the guest molecules for this study and DPPC (dipalmitoyl phosphatidyl choline) as the lipid. Vitamin A and its aldehyde form (retinol and retinal respectively) are naturally fat soluble vitamins effective in vision and growth.<sup>139</sup> NMR studies of Hilde De Boeck et al. in 1988 confirmed an interaction between DPPC fatty acid tails and retinol.<sup>140</sup> Four years later Antonio Ortiz et al. reported that the high hydrophobicity of retinoids leads to them interacting with the non-polar phases of lipid bilayer.<sup>141</sup> Their DSC experiments showed that retinol aligns with the acyl chains of DPPC in the way that its hydroxyl group be placed in lipid/water interface.

Abietic acid, usually used as an inhibitor of testosterone 5- $\alpha$  reductase<sup>142</sup>, is a tricyclic carboxylic acid with a isopropyl substituent considered as a toxic substance for the environment with potential health hazard for human.<sup>143</sup> Its amphiphilic behaviour makes it an interesting molecule to be studied inside membrane bilayers.

## 7.2 Materials and methods

Dipalmitoyl phosphatidyl choline (powder) was purchased from Avanti Polar Lipids. Retinol, retinal and abietic acid were purchased from Sigma. All chemicals were used without further purification. Solvents used in the measurements were 18.2 M $\Omega$ -cm water (Millipore Direct-QTM), chloroform (spectrophotometric grade, Sigma-Aldrich) and methanol (Laboratory grade, Fisher Chemicals).

### 7.2.1 UV-visible LD

UV-visible linear dichroism was used to investigate the alignment and uniaxial behaviour of the molecules on PE and PE<sup>OX</sup> as reported in §2.

### 7.2.2 Polarised Raman spectroscopy of molecules on polyethylene

Polarised Raman data of molecules deposited on polyethylene were recorded as reported in §6.

### 7.2.3 Lipid preparation

Firstly the solid lipid (10 mg) and the molecule of interest were co-dissolved in a 2:1 mixture of chloroform and methanol. The molar ratio of the small molecule to DPPC was taken to be 1:10 for DSC and 1:4 for Raman experiments. After evaporating the solvent under a stream of nitrogen gas to produce a ‘cake lipid’ layer, the dried sample was frozen in liquid nitrogen. Then the sample was placed in a rotary evaporator for at least 12 hours above its gel-to-liquid-crystalline transition temperature (around 50°C for DPPC) to make sure all the solvent had evaporated. The sample was then hydrated by adding purified water (1 mL) to make multilamellar vesicles (LMV) and sonicated for 15 minutes above 50°C to homogenize their size. To break the large multimellar vesicles into unilamellar vesicles, we froze and thawed them (at least three times) and then extrude them (using a 200 nm pore filter).<sup>144</sup>

#### **7.2.4 Polarised Raman spectroscopy of molecules embedded in lipid vesicles**

Aliquots (30 µl) of DPPC/guest molecule aqueous solutions (1:4 molar ratio of the guest molecule to DPPC) were dropped on polyethylene (1.8× stretching factor) until the sample signal was detected by the Raman spectrometer's CCD camera (Renishaw inVia microscope Raman spectrometer, the stretcher was placed in the instrument so that the stretching direction is parallel with the Z axis of the instrument). Polarised Raman spectra of the sample deposited on polyethylene was recorded in two polarisation of 0° and 90°, then RLS and RLD were calculated in the way reported in §6.

#### **7.2.5 Differential scanning calorimetry experiments of molecules embedded into lipid vesicles**

Differential scanning calorimetry (DSC), first was developed in 1962 by Emmet Watson and Michael O'Neil<sup>145</sup>, is a thermoanalytical technique to measure the difference in the amount of heat required to increase the temperature of sample and a reference in a heating-cooling process.<sup>146</sup> The sample and reference are kept at nearly the same temperature as each other throughout the experiment and the temperature of the reference (usually air) is set to increases or decreases during the programmed heating-cooling cycles. However, during the measurement, the sample goes through physical reactions (phase transition) which depending on whether they are exothermic or endothermic release or absorb energy. The machine records the released or absorbed heat and outputs it as enthalpy changes ( $\Delta H$ )

in a thermogram. DSC thermograms include a peak corresponding to the temperature at which the sample (here lipids) goes through a phase transition from ordered gel packing to fluid liquid/crystalline phase. In the case of lipids this temperature ( $T_c$ ) depends on the head group, the fatty acid chain length and the degree and type of unsaturations present in the chains. If the head groups are the same, lipids with shorter tails or higher number of unsaturated chains leads to lower  $T_c$ , also cis-unsaturated tails lower the  $T_c$  more than trans-unsaturated ones.<sup>147</sup>

Addition of a foreign molecule to a phospholipid system changes the transition temperature of the lipid if both molecules are miscible.<sup>143</sup> Ladbrook et al. in 1967 reported that transition temperature ( $T_c$ ) of dipalmitoyl-L-lecithin decreased after the addition of low concentrations of cholesterol.<sup>148</sup> Ortiz et al.<sup>141</sup> in 1992 discovered that the change in the enthalpy of DPPC and DPPE after introducing retinal and retinoic acid into vesicles is due to the interactions between the guest molecules and the lipid system. According to Mady et al.<sup>149</sup> the change in the gel→liquid/crystalline transition temperature of DPPC when doxorubicin (a frequently used chemotherapy drug) is added corresponds to the binding of the guest molecule to the heads or tails of phospholipids. They reported that the decrease in the  $T_c$  is because of the significant perturbing effect of doxorubicin present on the phospholipid tails.

DSC data of the system (50  $\mu$ L of 1:10 molar ratio) were recorded by a DSC 1 STAR<sup>e</sup> System Metler Toledo in three heating-cooling runs between temperature ranges of 30° to 60°, with the scanning speed of 0.2 °C/sec until identical thermograms were obtained.

### 7.3 Results and discussion

The alignment of retinoids (Fig. 7.1–4) and abietic acid (Fig. 7.5) deposited on PE and PE<sup>OX</sup> was studied using UV-visible LD and polarised Raman spectroscopy (Fig. 7.6–7). Then the result was compared with that of embedded sample in DPPC vesicles dried on polyethylene film. Differential scanning calorimetry was performed to measure the effect of guest molecules on the fluidity of DPPC and also to locate if the molecules interact with the polar head or fatty acids of DPPC.

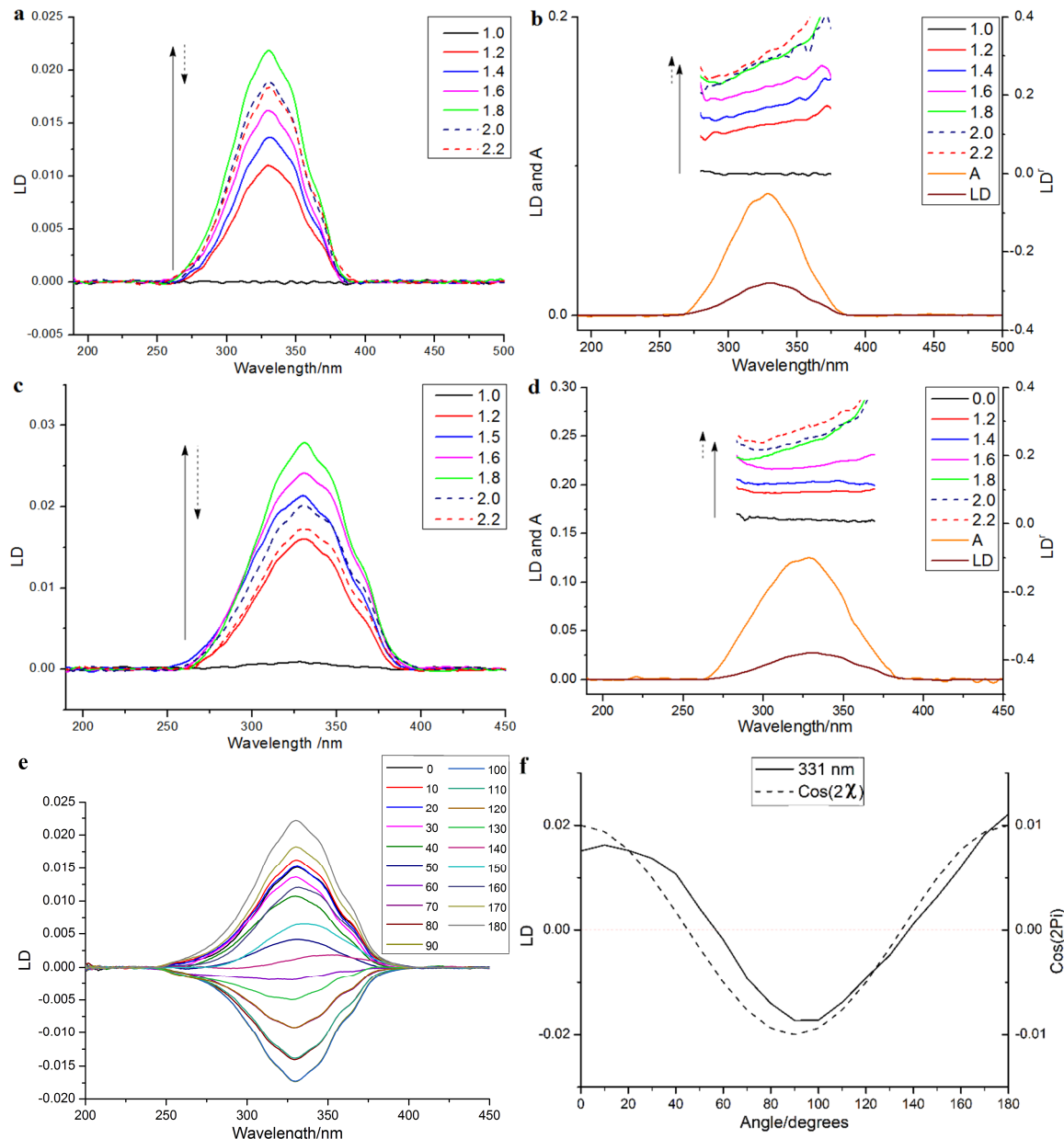
#### 7.3.1 UV-visible LD experiments of the molecules aligned on PE and PE<sup>OX</sup>

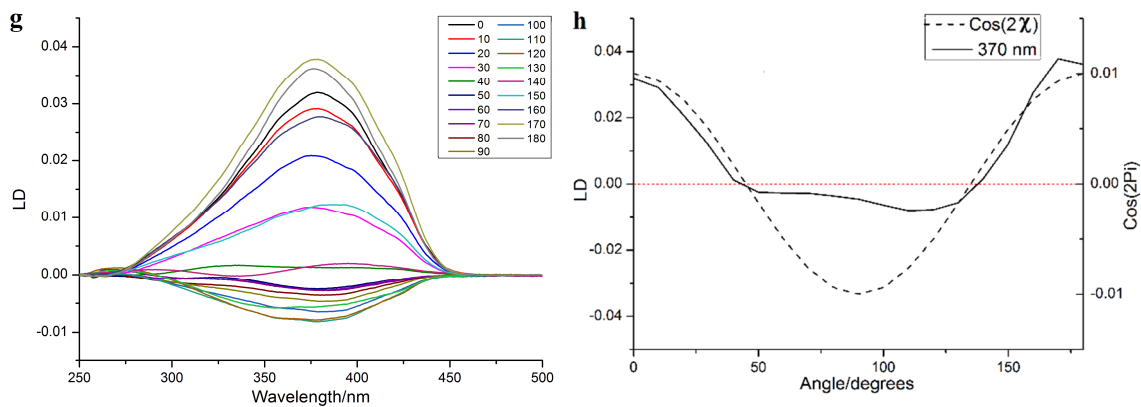
##### 7.3.1.1 Retinoids

Absorbance spectra of retinol and retinal, in the wavelength range 190–500 nm, contain only one peak due to the  $\pi-\pi^*$  transition of the long polyunsaturated chain. Due to the aldehyde's electron withdrawing effect this peak which occurs at 331 nm for retinol red shifts to 370 nm in retinal's UV absorbance spectrum. Our LD by the factor of rotation experiments show that both retinoids behave uniaxially on both PE and PE<sup>OX</sup> films (Fig. 7.3 and 7.4). As their LD spectra in Fig. 7.3 and 7.4 show, both molecules align with their long axis on PE and PE<sup>OX</sup> with their transition moment parallel to the film stretching direction. Retinal aligns slightly better than retinol on both films, whilst in both molecules, PE<sup>OX</sup> results in a higher *S* value (Table 7.1).

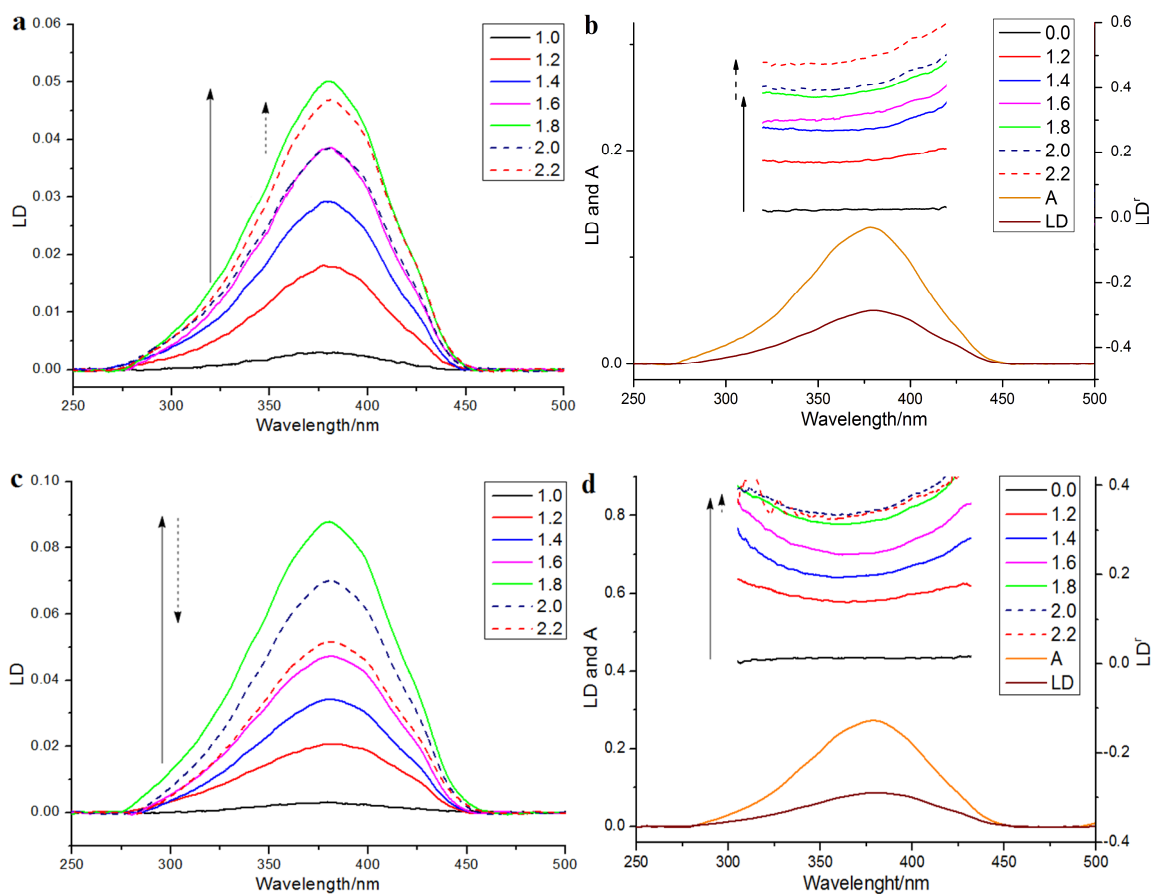
**Table 7.1** The  $S$  value of retinol and retinal deposited on PE and  $\text{PE}^{\text{OX}}$  (determined by assuming the transition moment of the molecule is parallel to the stretching direction ( $\alpha=0$ )).

Sample	Retinol		Retinal	
Film	PE	$\text{PE}^{\text{OX}}$	PE	$\text{PE}^{\text{OX}}$
S	0.08	0.1	0.11	0.14





**Fig. 7.3** LD spectra of retinol (0.4 mg/mL, 35–40  $\mu\text{L}$ ) deposited on a) PEOX and c) PE stretched to different lengths (from unstretched to the stretching factor of 2.2 $\times$ ). b) and d) LD' spectra respectively correspond to a) and c) overlaid with absorbance and LD spectra of the sample deposited on 1.8 $\times$  stretched films. e) and g) LD spectra by the factor of rotation when the film (PEOX and PE respectively) is stretched 1.8 $\times$ . f) and h) signals from e) and g) respectively at 370 nm as a function of rotation angle  $\chi$  overlaid on a plot of  $\text{cos}(2\chi)$ .



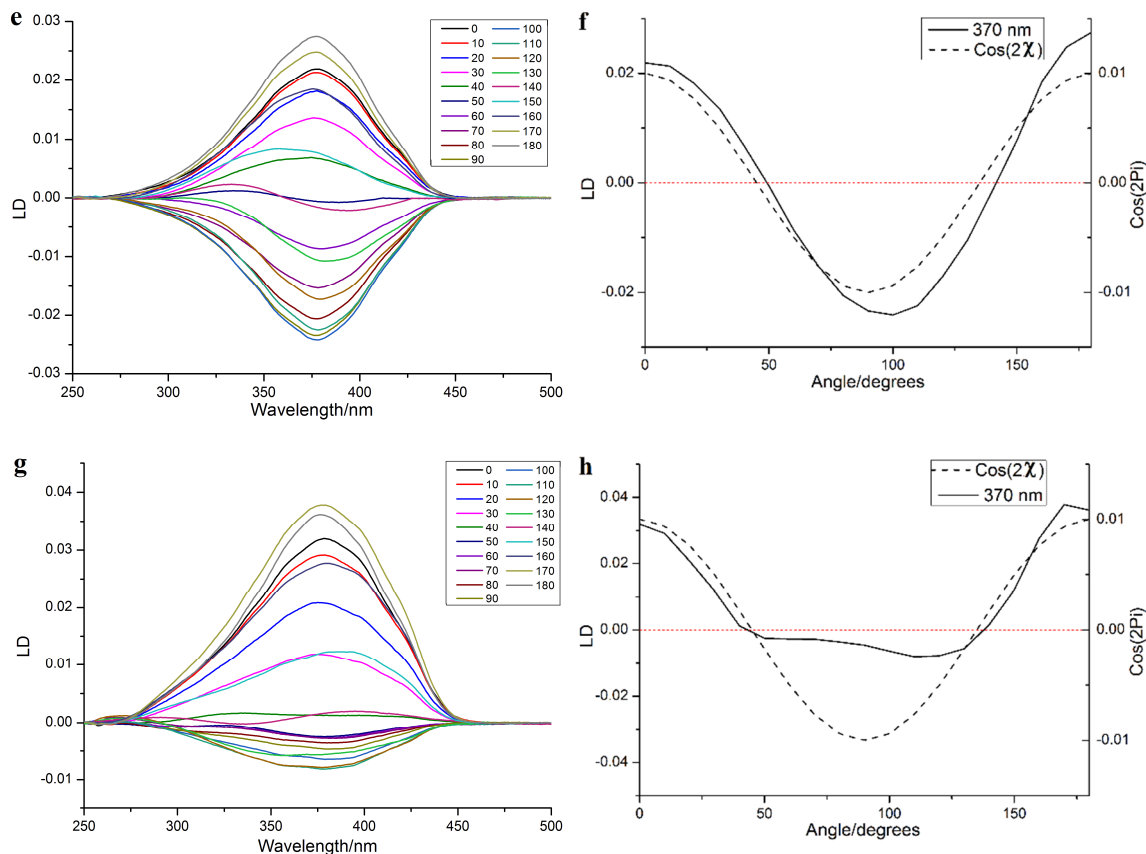


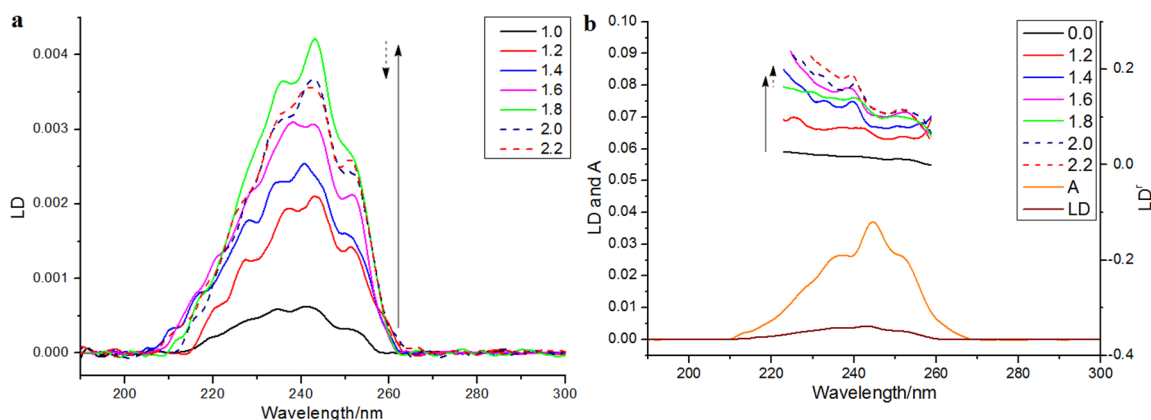
**Fig. 7.4** LD spectra of retinal (0.4 mg/mL, 35–40  $\mu\text{L}$ ) deposited on a)  $\text{PE}^{\text{OX}}$  and c) PE stretched to different lengths (from unstretched to the stretching factor of 2.2 $\times$ ). b) and d) LD' spectra respectively corresponding to a) and c) overlaid with absorbance and LD spectra of the sample deposited on 1.8 $\times$  stretched films. e) and g) LD spectra by the factor of rotation when the film ( $\text{PE}^{\text{OX}}$  and PE respectively) is stretched 1.8 $\times$ . f) and h) signals from e) and g) respectively at 370 nm as a function of rotation angle  $\chi$  overlaid on a plot of  $\cos(2\chi)$ .

### 7.3.1.2 Abietic acid

The conjugated C=C diene is the only UV-active chromophore existing in the structure of abietic acid and its UV absorbance spectrum consists only of one  $\pi-\pi^*$  transition centred at 242 nm, with  $\sim 1430$  and  $1278 \text{ cm}^{-1}$  vibronic progressions, in 190–300 nm region. The LD spectra of the molecule deposited on PE and  $\text{PE}^{\text{OX}}$  are shown in Fig. 7.5 (part (a) and (b))

respectively). Similar to the retinoids and other molecules studied in the previous chapters, stretching factors above  $1.8\times$  result in the higher LD and LD<sup>r</sup> intensities (for both PE and PE<sup>OX</sup>) than stretching factors below it (Fig. 7.5 a–d). As Fig. 7.5 e–h show, abietic acid behaves uniaxially on both films. Nevertheless, a better spreading pattern from methanolic solutions on PE<sup>OX</sup> than chloroform solutions on PE lead to more uniform thickness of sample on PE<sup>OX</sup>. Thus, rotating the PE<sup>OX</sup> film in order to examine uniaxial behaviour of the molecule did not lead to the light being incident on different thicknesses of the sample, unlike what happened in the case of sample deposited on PE film (Fig. 7.5 g and h).

The positive LD band at 242 nm, arising from the conjugated chain of the molecule, shows that the molecule aligns with its long axis parallel to the film stretching direction. The polarity of abietic acid makes it orient slightly better on PE<sup>OX</sup> than PE film. This is illustrated by the slightly higher *S* value calculated for PE<sup>OX</sup> (0.05) than PE (0.045).



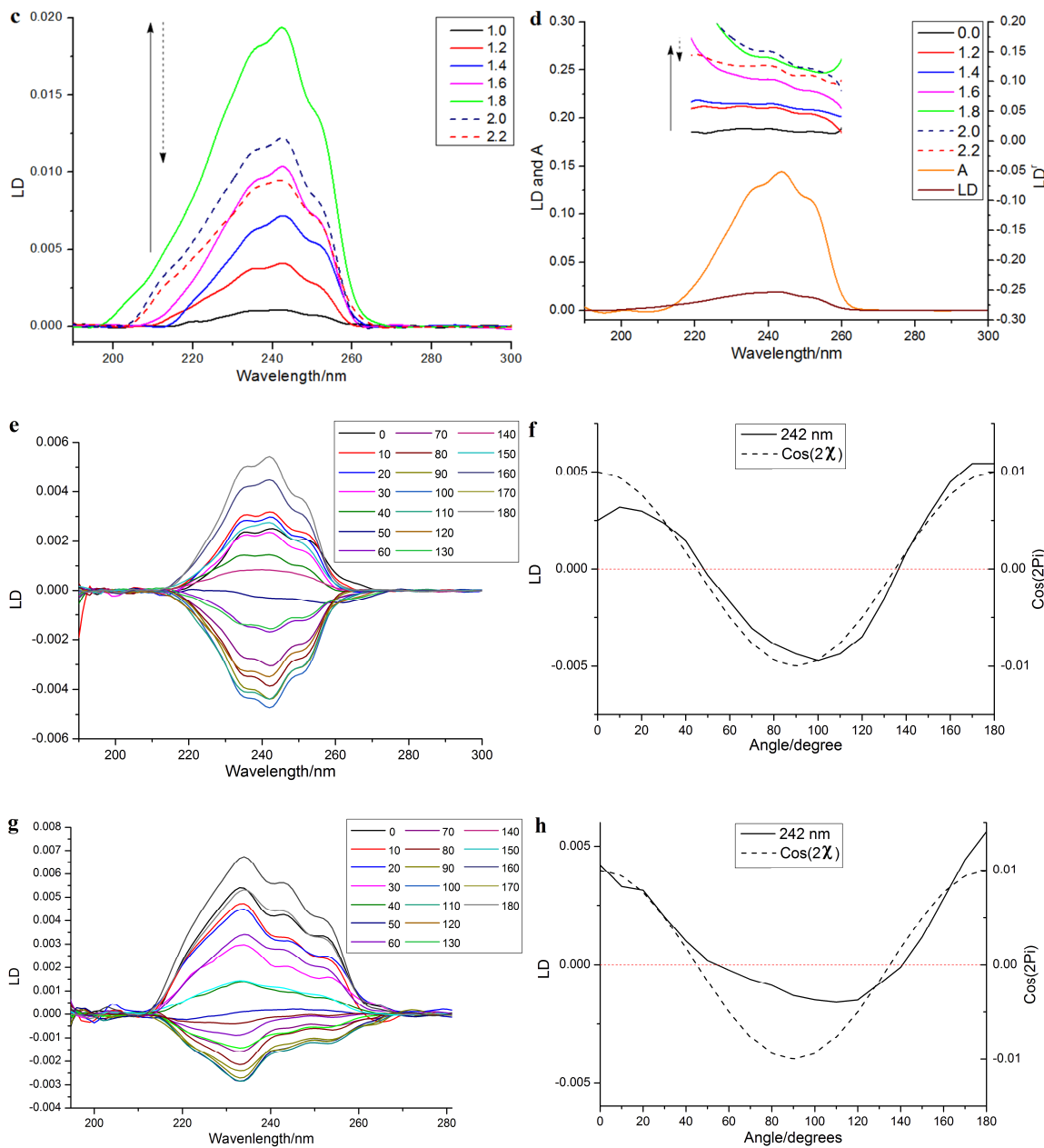


**Fig. 7.5** LD spectra of abietic acid (0.4 mg/mL, 35–40  $\mu\text{L}$ ) deposited on a)  $\text{PE}^{\text{OX}}$  and c) PE stretched to different lengths (from unstretched to the stretching factor of 2.2 $\times$ ). b) and d) LD' spectra respectively correspond to a) and c) overlaid with absorbance and LD spectra of the sample deposited on 1.8 $\times$  stretched films. e) and g) LD spectra by the factor of rotation when the film ( $\text{PE}^{\text{OX}}$  and PE respectively) is stretched 1.8 $\times$  (the polyethylene baseline of spectra in the figure g is not subtracted and only manually corrected using OriginLab software's baseline subtraction tool). f) and h) 370 nm signals from e) and g) respectively overlaid on a plot of  $\cos(2\chi)$ .

### 7.3.2 Polarised Raman spectroscopy of the molecules aligned on polyethylene

#### 7.3.2.1 Retinoids

Polarised Raman data of retinoids on treated polyethylene film ( $\text{PE}^{\text{OX}}$ ) are presented in the Fig. 7.6 and the peak frequencies and associated assignments are given in the Table 7.2. The peaks from the sample deposited on  $\text{PE}^{\text{OX}}$  are slightly shifted to higher frequencies comparing with those from powder. The  $\text{sp}^3$  stretching vibrations of C–H bonds occur in  $2790\text{--}2930\text{ cm}^{-1}$  while the peak at  $2992\text{ cm}^{-1}$  is related to the C–H  $\text{sp}^2$  stretching vibration. These peaks are only visible in the powder spectra and are covered by the C–H stretching vibrations of polyethylene in RLS and RLD spectra of retinoid deposited on polyethylene film. Due to the conjugation with carbonyl group, C=C bonds of retinal (1574 with a shoulder at  $1595\text{ cm}^{-1}$ ) vibrate in lower frequency than retinol ( $\sim 1595$  with a shoulder at  $1625\text{ cm}^{-1}$ ). Retinal's conjugated carbonyl group gives a weak peak at  $1657\text{ cm}^{-1}$ . All vibrations along the molecules' conjugated chain have positive RLD peaks and the peaks at  $1280$  and  $1295\text{ cm}^{-1}$  relating to  $\text{CH}_2$  unmethylated trans vibrations are negative, confirming the orientation of the molecules as having their long axis along the film stretch direction.

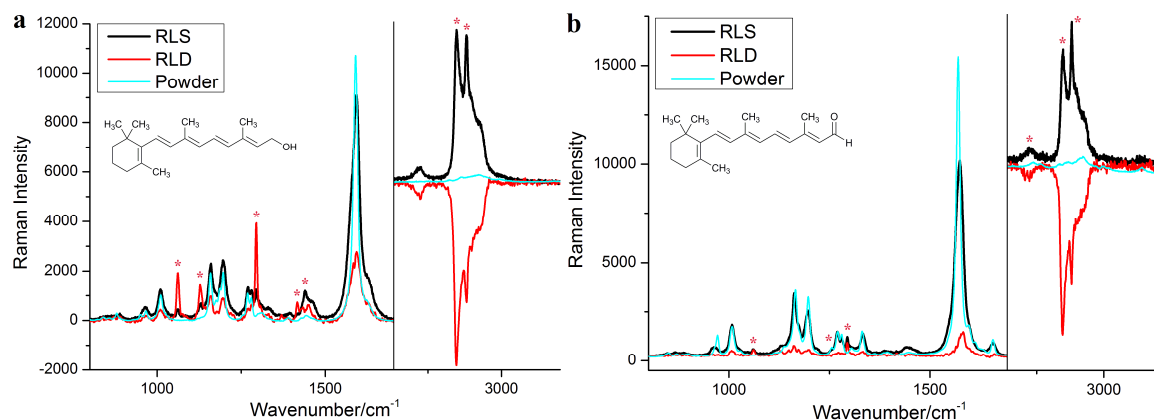


**Fig. 7.6** RLS (black) and RLD (red) spectra of a) retinol and b) retinal (on polyethylene film) overlaid with their powder spectra (cyan, the spectrum intensity diminished for presenting purposes). Peaks labelled by an asterisk are from polyethylene vibrations.

**Table 7.2** The band frequency, RLD direction, and assignments of retinol and retinal's Raman peaks.<sup>150,151</sup> The frequencies labelled in red are polyethylene vibrations. Abbreviation: str: stretching, bend: bending, UT: unmethylated trans mode.

Retinol		Retinal		Assignment
Band cm <sup>-1</sup>	RLD direction	Band cm <sup>-1</sup>	RLD direction	
2992		2992		sp <sup>2</sup> C-H str
2922		2922		sp <sup>3</sup> C-H str
2881	—	2880	—	
2848	—	2848	—	
		1657	+	C=O str
1625	+			C=C str
1595	+	1595	+	C=C str
		1574	+	C=C str
1440	—			
1418	+			
1330	+	1333	+	C-H bend
1294	+	1294	+	
1281	+	1280	—	CH=CH UT
1270	+	1269	+	CH <sub>2</sub> deformation
		1255	—	CH=CH UT
1196	+	1197	+	C-C str
		1177	+	
1160	+	1162	+	C-C str
		1148	+	
1128	+	1128	+	
1061	+	1061	+	
		1027	+	
1010	+	1007	+	Methyl in-plane rocking
965	+	966		C-H out-of-plane wagging

### 7.3.2.2 Abietic acid

The most intensive band in the fingerprint region of abietic acid Raman spectrum (Fig. 7.7) appears at  $1648\text{ cm}^{-1}$  which is related to the stretching vibrations of conjugated trans C=C bonds in the molecule. Bands at  $1468$  and  $1430\text{ cm}^{-1}$  correspond to the bending vibrations of CH<sub>2</sub> and CH<sub>3</sub>, and the band at  $1441\text{ cm}^{-1}$  is related to the scissoring vibrations of the same bonds. The bands in  $2880\text{--}3030\text{ cm}^{-1}$  correspond to the stretching vibrations of sp<sup>3</sup> and sp<sup>2</sup> C–H bonds.

As shown in the Table 7.3, bonds along the long axis of the molecule including the C=C stretching and CH<sub>2</sub> bendings have positive RLD peaks. One of a few bands with negative RLD peak is the scissoring vibration of CH<sub>2</sub>. Therefore, we conclude that the molecule aligns with its long axis parallel to the film stretching direction in accord with the UV LD.

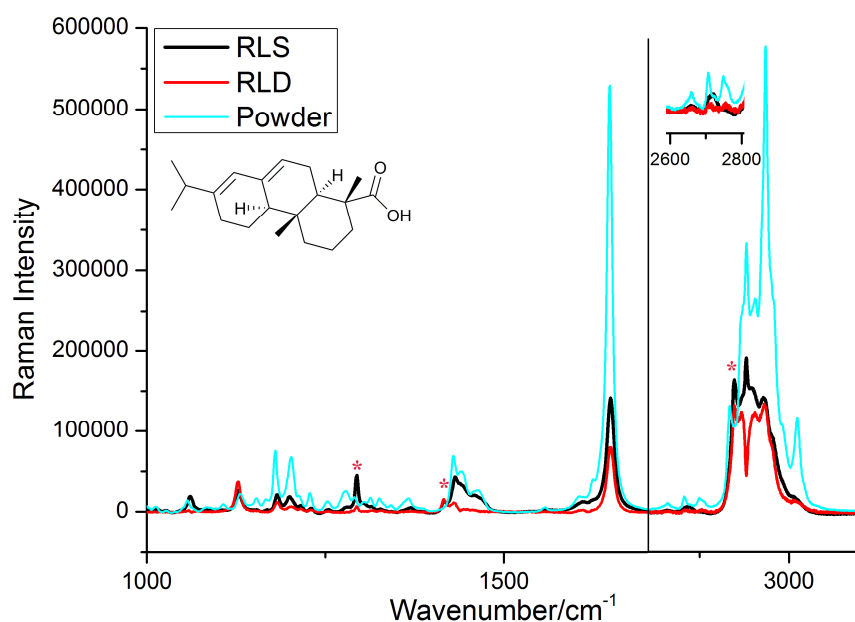


**Fig. 7.7** The RLS and RLD spectra (black and red solid lines respectively) of abietic acid deposited on polyethylene film overlaid with the unpolarised powder spectrum (cyan). The long frequency region of the spectrum is magnified 10 times.

**Table 7.3** The band frequency, RLD direction, and assignments of abietic acid's Raman peaks.<sup>152</sup> The frequencies labelled in red are polyethylene vibrations. Abbreviation: PE: polyethylene, str: stretching, bend: bending, scissors: scissoring vibrations.

Band cm <sup>-1</sup>	RLD direction	assignment	Band cm <sup>-1</sup>	RLD direction	assignment	Band cm <sup>-1</sup>	RLD direction	assignment
3023	+	SP <sup>2</sup> C–H str	2660	+	"	1365		CH <sub>2</sub> and CH <sub>3</sub> bend
2934	+	CH <sub>2</sub> , CH <sub>3</sub> and OH str	1648	+	C=C str	1295	+	PE CH <sub>2</sub> twisting
2904	+	"	1628	+	"	1278		
2881	–	"	1605	+	"	1227	+	
2847	+	PE C–H str	1558			1213	+	
2833	+	CH <sub>2</sub> , CH <sub>3</sub> and OH str	1468		CH <sub>2</sub> and CH <sub>3</sub> bend	1202	+	CCH str
2749	+	"	1441	–	CH <sub>2</sub> and CH <sub>3</sub> scissors	1180	+	C–C ring breathing
2707	+	"	1430	+	CH <sub>2</sub> and CH <sub>3</sub> bend	1166	–	PE CH <sub>2</sub> rocking
2660	+	"	1416	+	PE CH <sub>2</sub> wagging	1127	+	C–C ring breathing

### 7.3.3 Differential scanning calorimetry of the molecules embedded into lipid vesicles

Fig. 7.8 shows the thermograms of pure DPPC and DPPC with embedded molecules. The horizontal axis shows the transition temperature and the vertical axis presents the heat flow ( $\Delta H$ ). The effect of the guest molecules on the transition temperature of DPPC is listed in the Table 7.4.

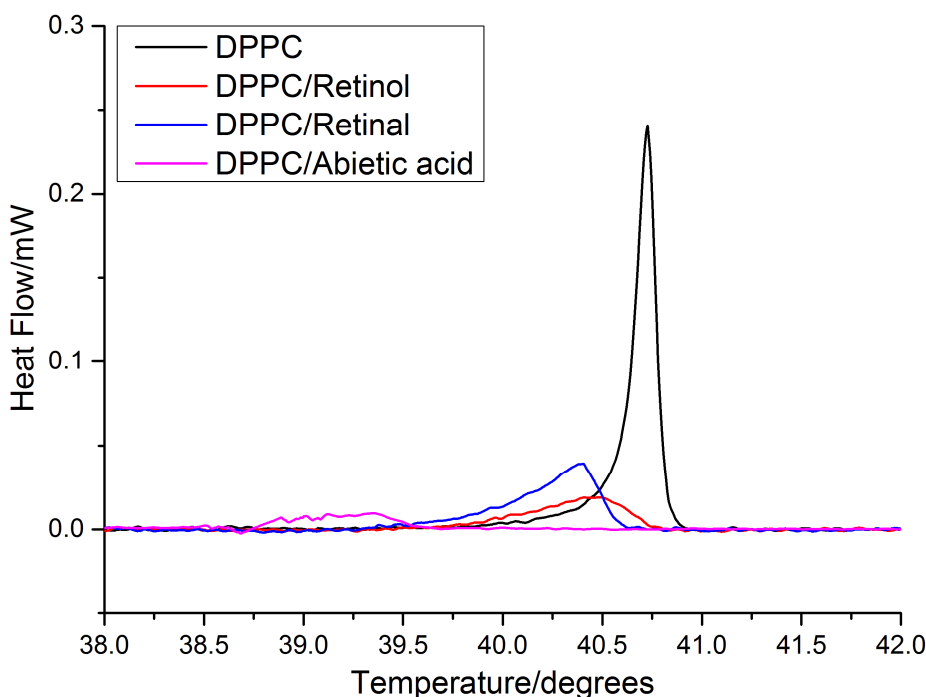


**Fig. 7.8** DSC thermograms illustrating the effect of retinoids and abietic acid on gel→liquid/crystalline transitions of DPPC.

**Table 7.4** Transition temperatures ( $T_c$ ) of pure DPPC and DPPC/retinoids and DPPC/abietic acid (0.1 molar fraction).

	DPPC	DPPC/retinol	DPPC/retinal	DPPC/abietic acid
$T_c$ (°C)	40.72	40.48	40.40	39

The thermograms of DPPC/retinoids systems in Fig. 7.8 show a decrease in both  $\Delta H$  and  $T_c$  of DPPC vesicles in the presence of retinoids, indicating that they both interact with the acyl chains of DPPC phospholipids and increase its fluidity. However, it appears that retinal decreases the transition temperature slightly more than retinol. This could be attributed to the different polarity strengths of the carbonyl and alcohol functional groups: the more polar alcohol group in retinol gives rise to interactions between it and carbons of the acyl chains closer to the polar head group in DPPC, whereas the less polar carbonyl group will interact with carbons further away from the head group. The increased

interactions between retinal and DPPC molecules results in a decrease in the transition temperature greater than that caused by interactions between retinol and DPPC. On the other hand, retinol decreases the enthalpy slightly more than retinal, which means a higher degree of fluidity and disorder is induced by retinol than retinal.

Aranda et al.<sup>143</sup> published DSC data for abietic acid in 1997 and concluded that the polar carboxyl group of abietic acid tends to locate near the polar head of DPPC phospholipids in order to interact with the water interface and probably form hydrogen bonds with water molecules. They reported that low concentrations of abietic acid do not affect  $\Delta H$  significantly. However, concentrations higher than 0.1 mol fraction (similar to the concentration ratio in our experiments) cause lateral separation between DPPC molecules and bulky abietic acid domains. This perturbs the lipid system highly and leads to a crucial reduction in DPPC's transition temperature and  $\Delta H$ . Fig. 7.8 shows the thermogram of DPPC with 0.1 mole fraction of abietic acid overlaid with the pure DPPC thermogram. The presence of abietic acid shifts the transition temperature of DPPC from 40.72 °C to a very broad band at 39°C. The significant reduction of  $\Delta H$  could be due to the significant disruption of the phospholipid molecules' structure caused by bulky non planar abietic acid molecules.

#### **7.3.4 Computational modelling studies on the docking position of guest molecules embedded in lipid bilayer**

The computational modelling performed by Dr. Shirin Jamshidi confirmed our DSC data. The simulation performed using the docking approach and the affinity energy between the

guest molecules and DPPC was calculated using Autodock Vina program package<sup>72</sup> (Table 7.5). Negative affinity energies confirmed the favourable interactions between molecules. As Fig. 7.9 shows, all three molecules align with their long axis parallel to the DPPC molecules while their polar groups located towards hydrophilic side of the lipid bilayer. As discussed above retinal locates closer to DPPC head groups than retinol. On the other hand, abietic acid interacts with phospholipid bilayer the way Aranda et al.<sup>143</sup> reported, showing that the concentration we used in our experiment was too high and caused formation of a cluster spacing between lipid molecules.

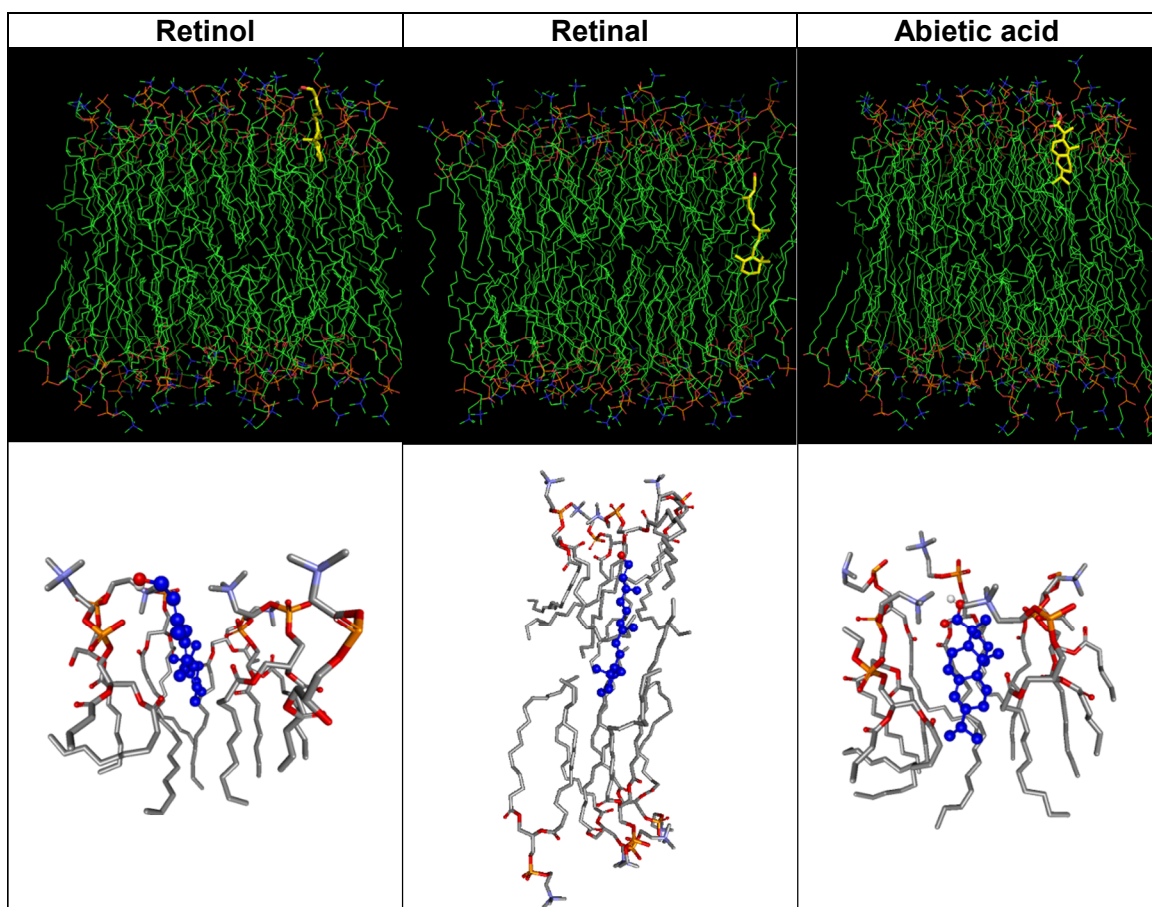


**Fig. 7.9** Simulated models for interactions between retinol, retinal and abietic acid with DPPC molecules in a bilayer system (top) with their corresponding zoomed in ball-and-stick models (bottom).

**Table 7.5** The calculated affinity energies of retinol, retinal and abietic acid with DPPC molecules obtained from Autodock Vina program package.

Guest molecule	Retinol	Retinal	Abietic acid
Calculated affinity energy (kcal/mol)	-5.4	-7.9	-5.7

### 7.3.5 UV-visible LD experiments of retinal embedded into lipid vesicles deposited on PE<sup>OX</sup> and quartz

LD experiments of retinal embedded into DPPC vesicles deposited on PE<sup>OX</sup> and quartz (Fig. 7.10) revealed important information about the alignment of vesicles on both surfaces.

When the incident light was perpendicular to the surface of lipid molecules deposited on quartz, any transition moment oriented perpendicular to the surface will not absorb light. In practice orientation is not perfect so some absorbance is observed. However, there will be no LD for such transitions as the sample is symmetric about the incidence direction. This is what we observed for DPPC/retinal samples on quartz (Fig. 7.10b black line). When the quartz was tilted to ~45°, an LD signal appeared (Fig. 7.10b red line). Somewhat to our surprise, the LD experiments with DPPC/retinal deposited on PE<sup>OX</sup> (Fig. 7.6a) showed different behaviour. A strong retinal LD signal, increasing in intensity upon stretching, convinced us that lipids align on PE<sup>OX</sup> differently from quartz and more similar to the way small molecules orient on polyethylene.

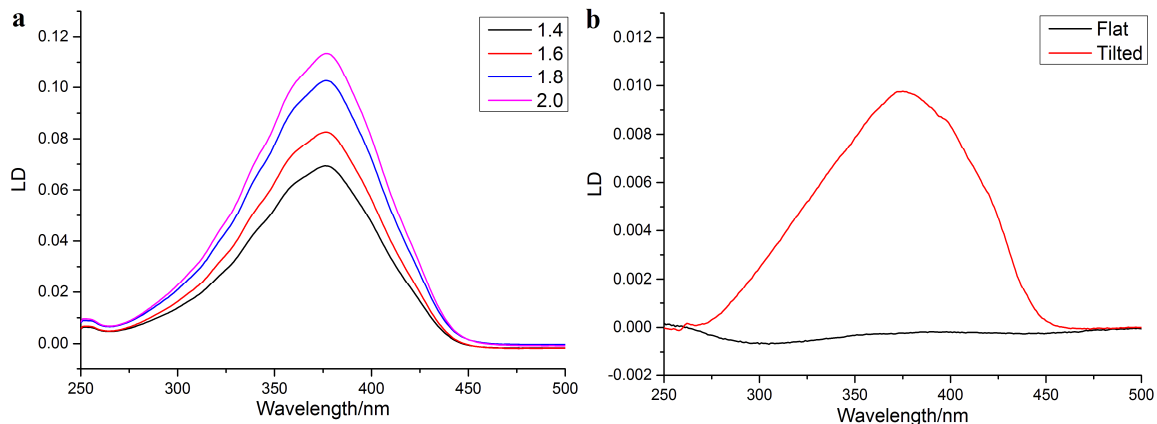


**Fig. 7.10** LD spectra of retinal deposited on a) PE<sup>OX</sup> (then stretched from 1.4× to 2.0× stretching factor) and b) quartz plate when the plate's surface was placed perpendicular to the direction of beam light (black line) and when it was tilted to 45° (red line).

### 7.3.6 Polarised Raman spectroscopy of the molecules embedded into lipid vesicles

The Raman spectra of DPPC deposited on PE<sup>OX</sup> are dominated by polyethylene peaks. However, the 1500–1850 cm<sup>-1</sup> region is dominated by stretching vibrations of DPPC carbonyl bonds. The DPPC carbonyl bonds give a peak at ~1736 cm<sup>-1</sup> with negative RLD signal (Fig. 7.11) suggesting that the carbonyl is preferentially perpendicular to the stretch direction, so the long chains are preferentially parallel to it. RLD spectra of retinoids and abietic acid embedded into lipid vesicles (Fig. 7.11) show negative bands at 1625 (corresponding to retinol's C=C bond), 1586 (with a shoulder at 1625 cm<sup>-1</sup> from retinal's C=C bond) and 1648 cm<sup>-1</sup> (related to abietic acid's double bonds stretching vibrations). The disappearance of retinal's carbonyl band and shifting its C=C band vibrations closer to that of retinol could be an evidence for the interactions between the carbonyl band of retinal and the phospholipid molecules. The change in the direction of RLD signals for the guest molecules when embedded in the vesicles shows the formation of a different

alignment compared to their orientation on PE (Fig. 7.5 and 7.6) where their long axis were aligned parallel to the stretching direction. However, the LD spectra of retinal embedded into DPPC deposited on PE<sup>OX</sup> (Fig. 7.10a) suggested that retinal is aligning by its long axis parallel to the polyethylene's stretching direction. Thus we conclude that retinoids and abietic acid, when embedded inside DPPC vesicles, have their long axis electronical and vibronical transition moments perpendicular to each other.

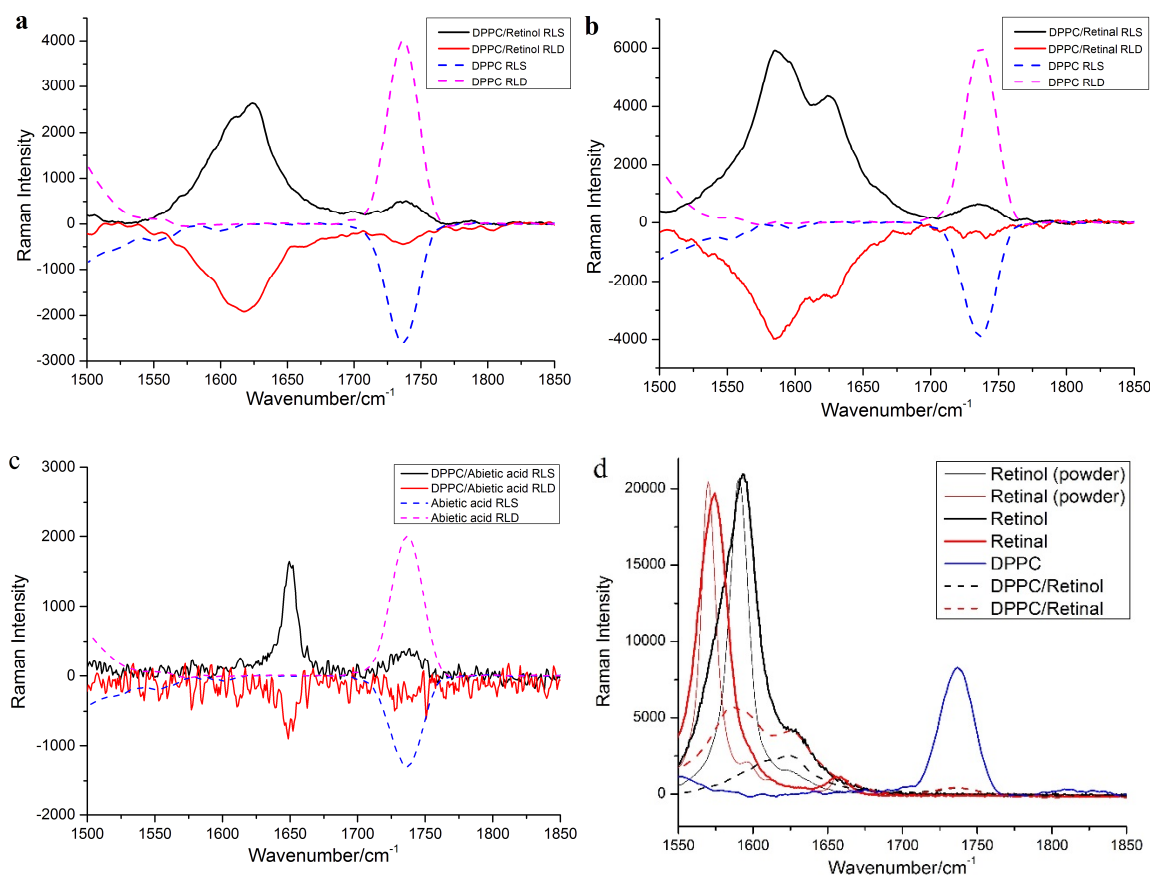


**Fig. 7.11** RLS and RLD spectra of DPPC vesicles (magenta and blue dashed lines respectively) and DPPC vesicles containing guest molecules: (a) retinol, (b) retinal and (c) abietic acid (with 1:4 lipid to retinoid molar ratio) dried on PE<sup>OX</sup> (black and red solid lines respectively). d) The RLS spectra of retinoids (powder: thin solid line, deposited on PE<sup>OX</sup>: thick solid line, and embedded into DPPC vesicles deposited on PE<sup>OX</sup>: dashed line). The 1500–1850 cm<sup>-1</sup> region of the spectra is selected to present as the rest is dominated by polyethylene peaks. The intensity for DPPC spectra (dashed magenta and blue) has been normalised in this diagram.

#### 7.4 Conclusions

Combining the results from UV-visible linear dichroism, differential scanning calorimetry and polarised Raman spectroscopy (RLD), we were able to study the interactions between three small biomolecule (retinol, retinal and abietic acid) and phospholipid (DPPC) molecules. This work could be a preliminary stage to investigate: 1) the interactions between more complex molecules such as membrane proteins with membrane lipids and 2) the respective orientation of such molecules embedded in lipid vesicles, which is very complicated and difficult using techniques such as NMR and x-ray crystallography.



# **Chapter Eight**

## **Spectroscopic signatures of an fmoc– tetrapeptide, fmoc and fluorine**

### **Acknowledgement**

I am grateful to Yi Zou for helping me with the data collection for this chapter as a part of her MChem project. I am also thankful to Prof. Alison Rodger for helping me with the data analysis and also calculating the fiber's secondary structure percentages using Curtis Johnson's programme CDssstr.



## 8.1 Introduction

The hydrophobic Fmoc [N-(fluorenyl)-9-methoxycarbonyl, Fig. 8.1b] unit is a protective group commonly used in solid state peptide synthesis.<sup>153</sup> Fmoc is also often conjugated to peptides to confer amphiphilicity on the molecules and introduce the potential for aromatic stacking interactions.<sup>154,155</sup> Some applications of Fmoc chemistry include self-assembling biomimetic scaffolds,<sup>156,157</sup> functionalised gold nanoparticles,<sup>158</sup> PNA synthesis and functionalization,<sup>159,160</sup> and amino acid analysis.<sup>161</sup> In each case, the Fmoc conjugates need to be characterised by a number of different techniques including the spectroscopic ones: absorbance, fluorescence, circular dichroism, linear dichroism, infrared absorbance and Raman spectroscopy. The work reported here was undertaken because extracting as much information as possible from spectroscopic data on complicated structures including Fmoc groups requires a clear idea of which spectral signatures are due to the Fmoc chromophore. Our group's recent work on Fmoc–GRDS (Fig. 8.1c) and Fmoc–RGDS peptides,<sup>155,162,163</sup> and the structures they form led us to realise that the spectroscopic features of Fmoc were not available in the literature. In 2011, Castelleto et al.<sup>155</sup> needed to know whether observed bands are due to the Fmoc or the peptide (glycine-arginine-aspartic acid-serine) or due to a combination of the two. This work has been undertaken to answer that question and to identify transition polarisation directions and energies of the Fmoc chromophore. The GRDS peptide used in this work was supposedly a random sequence control for the RGD sequence from fibronectin,<sup>164</sup> but it was found to form structured fibres that contain  $\beta$ -sheet structure.<sup>155</sup>

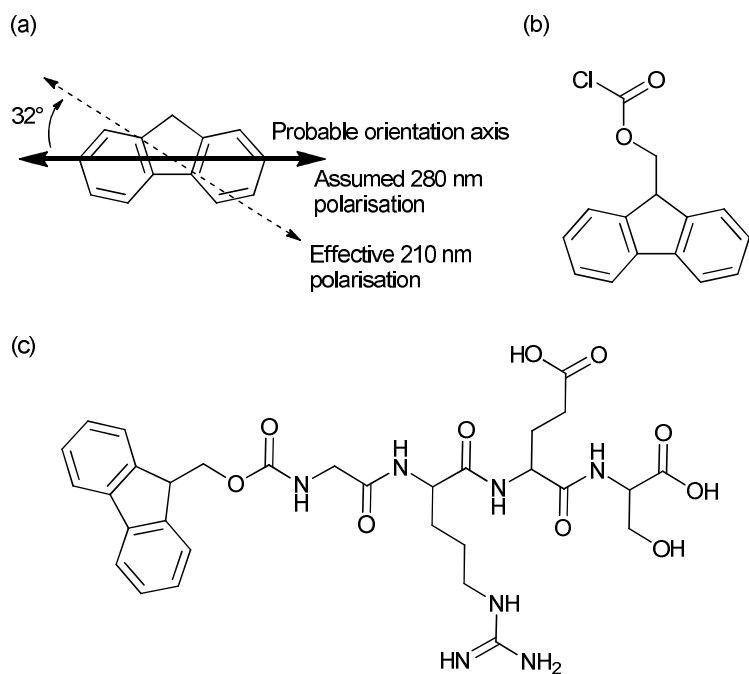


**Fig. 8.1** Molecular structures of a) fluorene, b) Fmoc-Cl, and c) Fmoc-GRDS with probable fluorene orientation axes in stretched polyethylene films as deduced from reduced linear dichroism spectra (see text)

## 8.2 Materials and methods

Fmoc-GRDS and GRDS were purchased from AltaBioSciences and used without further purification (preliminary experiments on extensively HPLC-purified samples gave the same results). Peptide samples for spectroscopy were made up in water (Millipore, 18.2 M $\Omega$ -cm) to the required concentrations and sonicated either for 5 minutes at room temperature (denoted RT) or for 10 minutes at 55–60°C (denoted FT). The notation FT refers to fibre-forming temperature as upon cooling to room temperature Fmoc-GRDS forms a gel that has previously been shown to contain fibres.<sup>155</sup>

### 8.2.1 Ultra-violet absorbance, circular and linear dichroism spectroscopy

UV absorption spectra were collected on a Jasco V-660 spectrometer in 1 mm path length quartz cells. Circular dichroism (*CD*) spectra were collected on a Jasco J-815 spectropolarimeter and data were analysed using Johnson's structure fitting programme CDssstr.<sup>165</sup> Linear dichroism (*LD*) data were also collected in a Jasco J-815 spectropolarimeter adapted for *LD* spectroscopy. Experiments were performed using either polyethylene (PE) stretched films to orient small molecules to determine transition polarisations or Couette flow to orient polymeric samples (in this case fibres).<sup>45,46,166</sup> The polyethylene films, used as sample holders in LD and Raman measurements, were cut from Glad® Snap Lock® bags, and stretched so that the direction of stretch is parallel to the faint lines observable in the film. The Couette flow cell<sup>45,46,166</sup> was custom built by Crystal Precision Optics, Rugby and is now available from Dioptica Scientific Ltd, Rugby.

All samples in this work can be treated as uniaxial rods so the reduced *LD* may be written<sup>10,46</sup>

$$LD^r = \frac{LD}{A} = \frac{3}{2} S (3\langle \cos^2 \alpha \rangle - 1) \quad \text{Eq. 8.1}$$

where *A* is the isotropic absorbance of the same sample, *S* is the orientation parameter (=1 for perfect orientation and 0 for no orientation) and  $\alpha$  is the angle between the polarisation of the transition and the sample orientation axis.  $\langle \rangle$  denotes average over the molecules in the sample. *LD* spectra of fibres often have a

significant contribution from light scattering. Miakti et al.<sup>167</sup> found that an empirical correction of the form

$$LD(\text{scattering}) = a\lambda^{-k} \quad \text{Eq. 8.2}$$

where  $a$  and  $k$  are constants and  $\lambda$  is the wavelength (nm) of light is often useful in LD spectroscopy. This is implemented here with  $a=92000$  and  $k=3$ .

### 8.2.2 Fourier transform infrared and Raman spectroscopy

Fourier transform infrared (FT/IR) spectra were collected on a Jasco FT/IR-470 plus Fourier transform infrared spectrometer, equipped with linear polarizers, an MCT detector, and germanium attenuated total reflectance (ATR) accessory (Pike Technologies). 1000 scans were performed for each spectrum, using a resolution of  $4 \text{ cm}^{-1}$ . Powder samples were placed on the germanium plate. Solution samples were dissolved in water (sonicated and heated if required) or methanol and air-dried.

Raman spectra were collected on Renishaw InVia Raman microscopes, equipped with 633 nm He–Ne or 785 nm solid state diode lasers together with Renishaw CCD (Visible → NIR) and InGaAs (Infrared) detectors. The 633 nm laser was used unless fluorescence dominated the spectrum. Samples were prepared as for IR, but deposited on quartz.

## 8.3 Results and discussion

### 8.3.1 UV-visible spectroscopic data

#### 8.3.1.1 Absorbance

Fig. 8.2a contains the absorbance spectra of fluorene, Fmoc-Cl, GRDS and Fmoc-GRDS. Peptide GRDS without conjugated Fmoc shows gradually increasing absorbance due to the peptide bonds from about 220 nm downwards. Fmoc-Cl and fluorene have similar spectra with Fmoc peaks in methanol at 299, 288, 264, 210 nm and clear shoulders at 275, 227 and 219 nm. Fmoc peaks on polyethylene are 1–2 nm red-shifted and Fmoc-GRDS on PE are further red-shifted. Conjugation of the Fmoc to the peptide removes some of its spectral structure and overlays the 210 nm band with peptide intensity.

#### 8.3.1.2 Circular dichroism

CD is the difference in absorption of left and right circularly polarized light. It is particularly useful for identifying the appearance of chiral structures in proteins.

Empirical estimates of *e.g.*  $\alpha$ -helical or  $\beta$ -sheet content can often be made from data.

Fig. 8.2b shows the circular dichroism spectra of the tetrapeptide GRDS and of Fmoc-GRDS prepared either with short sonication at room temperature (RT) or with incubation for 10 minutes at  $\sim 60^\circ\text{C}$  (FT) which usually produces fibres. There

is no induced *CD* apparent in the Fmoc transitions of any of the samples. The GRDS peptide (however samples are prepared) and Fmoc–GRDS( RT) have *CD* spectra with a single negative peak at 200 nm consistent with a random coil structure being adopted.<sup>168</sup> The Fmoc–GRDS(FT) is not purely random coil, nor does it look like a  $\beta$ -sheet/random coil mix. If one assumes that the concentration of 0.1 mg/mL is accurate (accurate concentrations are a challenge for fibrous samples) and also that a *CD* structure fitting programme not designed for peptides can be used, then we can estimate the secondary structure content of our Fmoc–GRDS(FT) fibre. Curtis Johnson's programme CDssstr<sup>165</sup> estimates ~10% helix, ~20%  $\beta$ -sheet, and ~10% polyproline II (which is spectroscopically indistinguishable from random coil), and ~45% other structures.

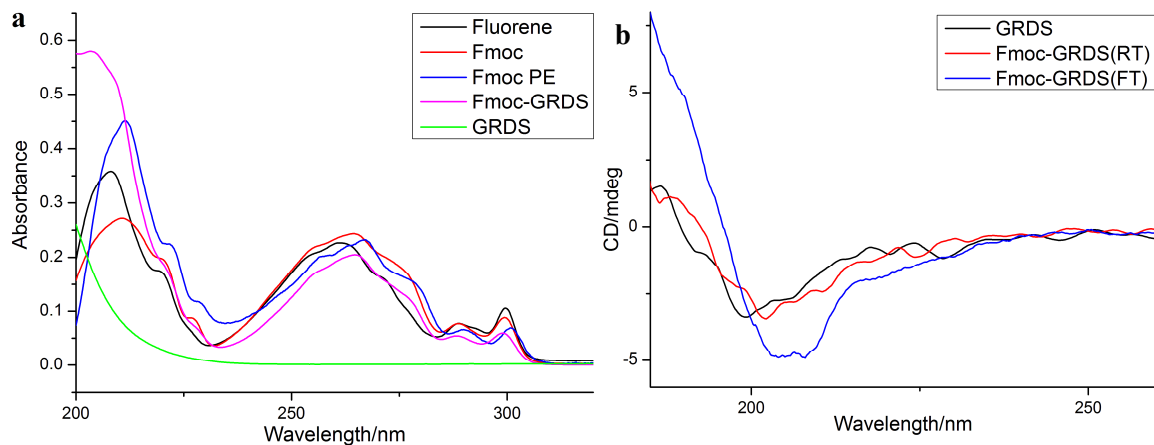


**Fig. 8.2** a) Absorbance spectra (0.1 mg/mL in 1 mm pathlength cuvettes) of fluorene and Fmoc-Cl in methanol, Fmoc-Cl on PE film (dried sample) GRDS and Fmoc-GRDS in water. b) CD spectra of GRDS, Fmoc-GRDS( RT) and Fmoc-GRDS(FT) (0.1 mg/mL, 1 mm path length), GRDS, Fmoc-GRDS( RT) spectra are smoothed (30 points with 3 polynomial order).

### 8.3.1.3 Linear dichroism

Fig. 8.3a and b show the film absorbance, LD and  $LD'$  spectra for fluorene and Fmoc-Cl and the LD for Fmoc-GRDS( RT). The observed bands are all positive indicating the molecules are all oriented so that the transition moments are preferentially along the stretch direction of the films. The GRDS samples were indistinguishable from the film baseline, and the Fmoc-GRDS(FT) (data not shown) spectrum is the same as the Fmoc-GRDS( RT) but with smaller intensity LD signal for the same absorbance suggesting less effective orientation. Overall the fluorene and Fmoc LD spectra are similar, the Fmoc peaks are slightly red-shifted. Fmoc has positive LD maxima at 301, 290, 277 (shoulder), 267, 259 (shoulder), 228 (shoulder), 221, and 211 nm.

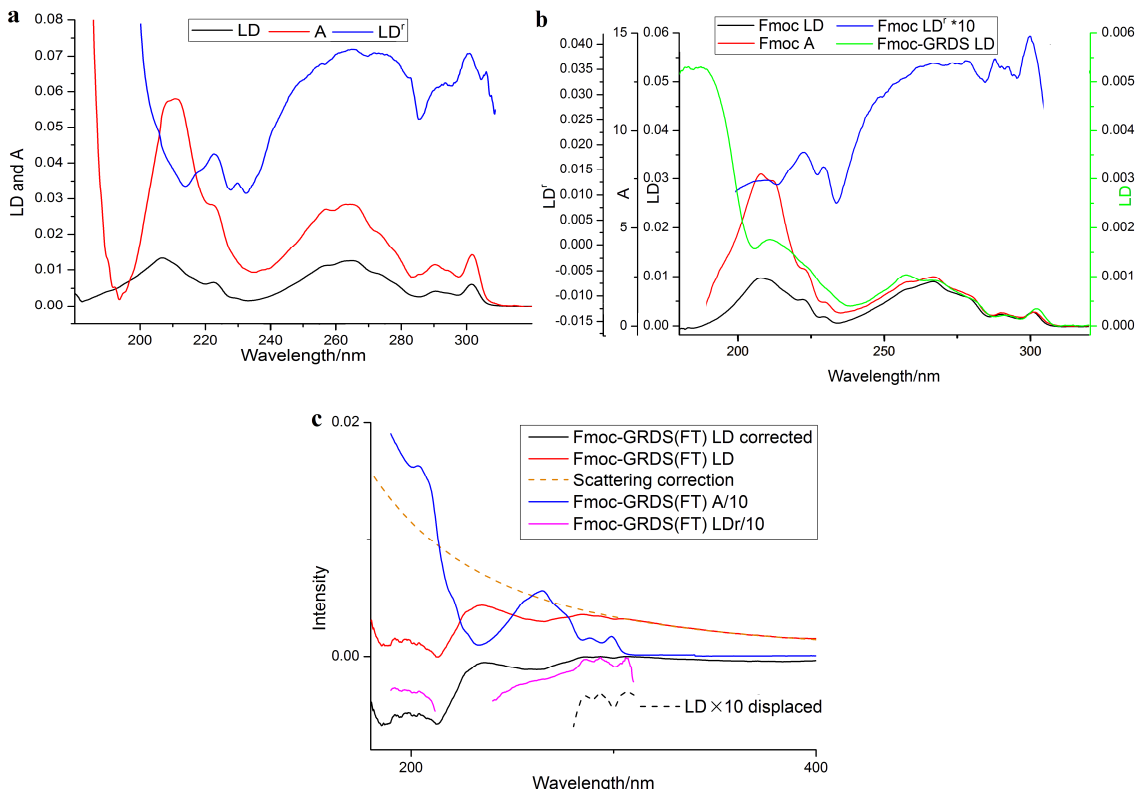


**Fig. 8.3** a) Polyethylene stretched film absorbance, LD, and  $LD'$  spectra of fluorene, b) polyethylene stretched film absorbance, LD, and  $LD'$  spectra of Fmoc-Cl and LD of Fmoc-GRDS, c) solution absorbance (0.5 mm pathlength), couette flow LD, scattering corrected LD ( $a = 92000$  and  $k = 3$ ) and  $LD'$  of Fmoc-GRDS(FT).

Fluorene has  $C_{2v}$  symmetry so all its  $\pi$ - $\pi$  transitions are polarized either along its long axis or its short axis. In order to extract more information from the spectra we need an estimate of the orientation parameter S. We proceed by assuming that the fluorene chromophore orients with its long axis along the stretch direction of the film and that 270 nm region of the spectrum for fluorene and Fmoc-Cl (which has close to maximum LD signal) is long axis polarized – *i.e.* along the probable orientation axis illustrated in Fig. 8.1 (with  $\alpha = 0$ ). The 270 nm fluorene  $LD^r \sim 0.47$ , so, from Eq. 8.1, the orientation parameter in this experiment is  $S \sim 0.16$ . It then follows that the polarisation of the transitions at  $\sim 210$  nm lies at  $32 \pm 3^\circ$  from the orientation axis (Fig. 8.1). This means that the 220 nm region of the spectrum is an overlay of long and short axis transitions. The Fmoc-Cl spectra in Fig. 8.3b are very similar to those of fluorene indicating the fluorene chromophore dominates the Fmoc orientation in PE films. The contribution of the peptide backbone to the low wavelength end of its spectra is apparent in the Fmoc-GRDS film LD spectrum in Fig. 8.3b.

Fmoc-GRDS(FT) samples were the only ones that gave a flow aligned LD spectrum and the details of what was observed varied from sample to sample. The spectrum of the sample in Fig. 8.3c is typical. The  $LD^r$  spectrum was estimated after correcting the LD spectrum for light scattering. Overall the main thing to note is that the Fmoc LD signals (down to  $\sim 210$  nm) are of opposite sign from the film experiment. Thus in the fibres formed by Fmoc-GRDS, the long axis of the fluorene chromophores (260 nm) is more perpendicular than parallel to the helix axis. This is expected if  $\beta$ -strand orientation occurs along the flow direction. The mixed polarisation 210 nm fluorene band is further from the helix axis than the long axis polarized 260 nm

band, suggesting that Fmoc groups are stacked tilted slightly from perpendicular to the fibre axis. The shape of the fibre LD spectrum at 200 nm and below (which is dominated by the GRDS spectrum) suggests there is positive signal at 200 nm overlaid on a negative one. It is not however the large positive signal at 200 nm expected of a classic cross- $\beta$  amyloid fibre.<sup>169,170</sup>

### 8.3.2 Vibrational data

#### 8.3.2.1 FTIR

Fig. 8.4 contains FTIR absorbance spectra of fluorene, Fmoc-Cl, GRDS and Fmoc-GRDS(FT). The fluorene chromophore contributes a lot of the structure to the Fmoc-Cl spectrum. Fmoc also shows evidence of C=O stretches at 1765 and 1756  $\text{cm}^{-1}$ . The GRDS spectrum is essentially a single broad spectrum with Amide I maximum at 1650  $\text{cm}^{-1}$  consistent with the peptide being unfolded.<sup>171</sup> The Fmoc-GRDS spectrum is not simply the sum of the Fmoc and the GRDS indicating that the fibres adopt a new structure. We previously concluded the IR spectrum was consistent with the presence of at least some  $\beta$ -sheet due to the peak at 1630  $\text{cm}^{-1}$ .<sup>155</sup>

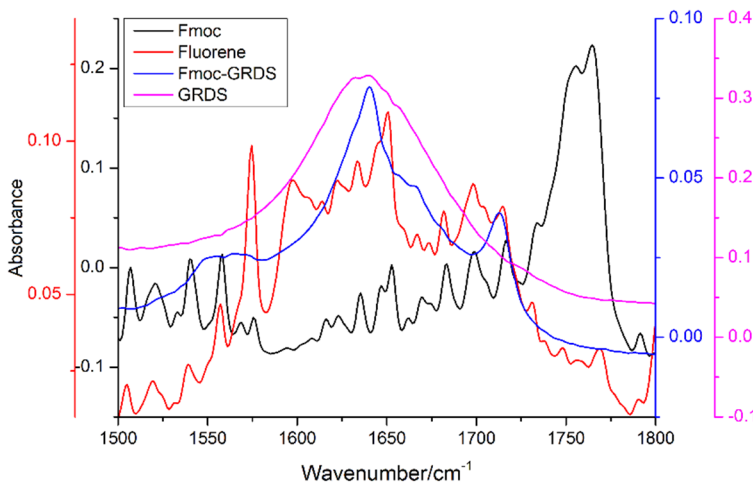


**Fig. 8.4** ATR FTIR spectra of fluorene and Fmoc (0.5 mg/mL) in methanol, GRDS (100 mg/mL) and Fmoc–GRDS (0.1 mg/mL respectively, sonicated or for 10 minutes at 55–60°C) in water.

### 8.3.2.2 Raman spectroscopy

The Raman spectra of fluorene and Fmoc-Cl powders from 500–1800 cm<sup>-1</sup> are shown in Fig. 8.5a. Most of the peaks present in fluorene are also present in Fmoc, the main exception being the 1400 cm<sup>-1</sup> region. An overlay of Fmoc, GRDS and Fmoc–GRDS in powder and fibre forms is given for the 1500–1800 cm<sup>-1</sup> region (Fig. 8.5b). Although both providing vibrational data, due to the high symmetry of the Fmoc group, the IR and Raman spectra look quite different. The GRDS Raman spectrum is dominated by arginine signals<sup>155,172,173</sup> in the 1700 cm<sup>-1</sup> region. Fluorene signals are prominent in samples containing it. The Fmoc-GRDS(FT) also has a large 1666 cm<sup>-1</sup> peak which is present but small in the powder. There is also an IR band at this point. Its most probable assignment is to  $\beta$ -turns or  $3_{10}$  helices.<sup>174</sup> Combining this with the IR signals suggests the fibre contains secondary structure elements but not the classic amyloid fibre cross- $\beta$  strand structure.<sup>175</sup>

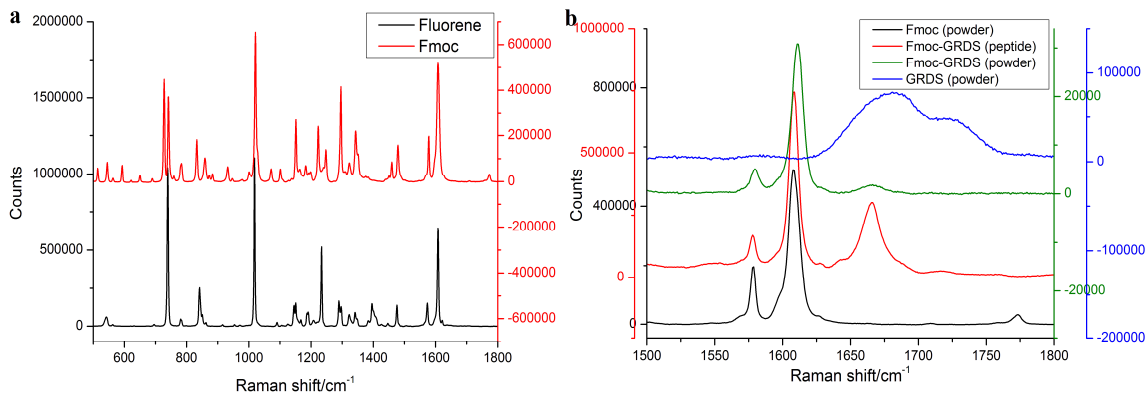


**Fig. 8.5** a) Raman spectra of fluorene and Fmoc powders (with 785 nm laser, 30 scans). b) Raman spectra (collected with samples placed on a quartz plate) of Fmoc powder (785 nm laser, 30 scans), Fmoc-GRDS(FT) (100 mg/mL, 785 nm laser, 100 scans), Fmoc-GRDS powder (633 nm laser, 100 scans) and GRDS powder (633 nm laser, 100 scans).

#### 8.4 Conclusions

A variety of spectroscopic techniques were used to characterise Fmoc and Fmoc-peptide conjugates. Fmoc has two UV-region bands, one centred at 265 nm and one centred at 210 nm. Fmoc itself is achiral and so has no solution phase CD signal. When conjugated to GRDS as a free monomer in solution, the CD spectrum corresponds to that of the unfolded peptide. When fibre structures are formed, induced CD signals are not observed in the Fmoc absorbance region suggesting that the Fmoc groups are not arranged in strongly chiral structures. By way of contrast the Fmoc-GRDS fibre LD is dominated by the Fmoc units. The 265 nm region of the Fmoc film LD spectrum is positive and so we deduce it is polarized along the

long axis of the fluorene group. In the fibres, this transition has a negative signal indicating that the long axis of the Fmoc units extends away from the fibre axis. The 210 nm region of the film spectrum is neither long axis nor short axis polarized, though by symmetry any one transition must be one or the other. Thus this region of the spectrum is an overlay of different transitions. In the fibre these transitions have a large negative signal. These two pieces of information together suggest the Fmoc units are approximately perpendicular to the helix axis with the long axis tilted somewhat more than the short axis. The IR and Raman spectra support that the fibres structures differ from those of free monomer systems—but do not correspond to the classic cross- $\beta$  strand structure.

These Fmoc spectroscopic data will be useful in characterising a wide range of biomaterial structures and delivery agents that are currently being developed with Fmoc.<sup>176</sup>

# **Chapter Nine**

Conclusions and the future work



## 9.1 Conclusions

One of the main aims of this work was to improve the molecular alignment techniques for polarised spectroscopic techniques such as UV-visible linear dichroism. One of the most widely used alignment techniques is to deposit the analyte on the surface of a stretched polymer film and stretch it more (or load the sample on an unstretched film, then stretch it) to orient the molecules in the direction of stretching. Previously, depending on the polarity of the molecule under the study, polyethylene, polyvinylalcohol or polyvinylchloride films (PE for non-polar, PVA and PVC for polar molecules) were used. However, using PVA and PVC requires long sample preparation procedures and results in brittle films. This would make the type of experiments we were interested in (such as recording spectra of the analyte deposited on films with different stretching factor), very time consuming and difficult. Thus, in order to record polarised spectroscopic data of polar molecules, we changed the PE surface to be more hydrophilic by treating it in an oxygen plasma asher. Our contact angle measurement data showed that treating the films for one minute when the power is set to 50 mW results in an ideal degree of hydrophilicity on the surface of the polyethylene film. Also the X-ray photoelectron spectroscopy experiments showed that treated samples exhibit a slight enhancement over time in carbonyls relative to OH, consistent with oxidation proceeding from alcohol, to aldehyde, to carboxylic acid. We examined the ability of the treated PE films (denoted as PE<sup>OX</sup>) in orienting molecules by comparing the LD spectra collected for a set of small molecules deposited on them with ones using PE and PTFE films. Using PE<sup>OX</sup> films, we were able to align polar molecules such as DAPI and xanthene based dyes which previously were had not been able to be studied using PE films. We realised that molecules, regardless of their polarity, align with a slightly bigger aligning factor (S) on PE<sup>OX</sup> than on PE films. Some molecules (such as

1-pyrene carboxaldehyde) aligned differently on PE<sup>OX</sup> and PE which resulted in more structural information about the alignment of the molecules. This enabled us to deduce spectroscopic information for low symmetry molecules. We also investigated the sample's orientation upon increasing the film's stretching factor. We have found out, depending on the sample preparation technique (depositing the analyte before or after stretching the film), what stretching factor would result in the highest alignment in the sample. We studied the reason using X-ray diffraction experiments (done by Dr. Nikola Chmel), LD, temperature dependent UV and LD and polarised Raman spectroscopy, and we realised that the molecule's alignment on PE's surface is very depending on the amount of crystalline phase in the polymer which increases upon stretching and also freezing.

During our studies we noticed a change in the shape of anthracene's LD spectra upon increasing the solution concentration. After collecting UV-visible absorbance, fluorescence emission, LD and fluorescence detected linear dichroism (FDLD) we detected the formation of different dimers when increasing the concentration of the analyte. Prof. Alison Rodger's calculations on the exciton couplings helped us identifying some of the possible dimers on the stretched polyethylene film. Also we could confirm the presence of dimers by comparing our experimental data with the molecular dynamics by Dr. Shirin Jamshidi. Performing different spectroscopic techniques, we realised how necessary and complementary is to collect fluorescent data along with absorbance data in order to investigate small changes in the structure of sample under the study. We repeated LD and FDLD experiments for a set of polycyclic aromatic hydrocarbons to study the dimerisation of them on the stretched PE<sup>OX</sup> film.

After optimising the orienting technique, examining and evaluating it with UV-visible techniques, we utilised it for our newly introduced polarised Raman spectroscopy (Raman linear difference - RLD). We recorded RLS (Raman linear sum) and RLD spectra of a set of molecules, with known and unknown electronic transition orientations, on stretched PE<sup>OX</sup> films. Obtaining satisfactory results about the orientation of vibrational transition moments of the samples, we designed a ROA/RLD spectrometer working with the theory we had developed. The newly made instrument's result validity was examined by comparing them with known vibrational transition moment orientation. We also were able to detect the presence of different anthracene dimers and oligomers using the RLD technique.

As an application for our new technique we studied the orientation of small biomolecules imbedded into phospholipid bilayer systems supporting by data obtained from UV-visible absorbance, LD, differential scanning calorimetry and computational modelling. We found out that the molecules we chose (retinol, retinal and abietic acid) align parallel to the phospholipid (DPPC) molecules such that their C=C vibrations are in the same plane as the carbonyl group vibrations in the DPPC molecules.

## **9.2 Future work**

### **9.2.1 Shear flow Raman linear difference**

As for LD spectroscopy, to record an RLD signal the molecules have to be intrinsically aligned or oriented by an aligning technique such as stretched polymer which we optimised in this work. However, this technique is helpful only if the size of the analyte is small. In the case of samples such as DNA, fibre proteins and vesicles it is recommended to use other aligning techniques such as shear flow. The next stage of this work will be to design a shear flow cell for ROA/RLD instrument and recording polarised Raman spectra upon increasing the sheer flow.

### **9.2.2 Linear dichroism and RLD of molecules imbedded inside lipid systems deposited on quartz**

Another ongoing project is to investigate the alignment of small molecules imbedded into lipid vesicles deposited on quartz plate. As we discussed in §7, due to the hydrophilic characteristic of quartz, lipid molecules tend to orient on it with their head groups close to the surface. If there is a molecule imbedded inside the lipid system, its transition moments would be parallel to the incident light beam direction when the sample is deposited on quartz and the quartz surface is placed in front of the light beam. In such situation there must not be any LD or RLD signal detected by the detector whilst absorbance spectrum could be recorded. By tilting the quartz surface the angle between the molecules transition

moment and the light beam increases so a weak LD or RLD signal should be detected. The LD or RLD signal should be increased upon increasing the angle. This experiment would give useful information about the orientation of molecules inside lipid bilayer systems.

### **9.2.3 Cryo-linear dichroism and cryo-polarised Raman spectroscopy**

As reported in §2 cryo studies could be very helpful to study linear dichroism of samples with high vibrational interference or weak electronic transition moments. This effect could also be studied with polarised Raman spectroscopy.

### **9.2.4 Calculating the reduced fluorescence detected linear dichroism**

As our FDLD results in §5 showed, this technique adds more sensitivity and selectivity to conventional LD experiments. Similar to the LD data, in order to eliminate the effects of concentration and path-length, it is possible to calculate reduced FDLD ( $FDLD^r$ ). This requires to divide the FDLD spectra by their corresponding excitation fluorescence data.

### **9.2.5 Polarised Raman mapping for stretched polyethylene films**

In §6.3.1 we studied the effect of stretching on the vibrational structure of PE<sup>OX</sup> films by recording polarised Raman spectra of a single film when it was stretched to different stretching factors. During the measurement we tried to keep the laser beam on the same spot on the PE<sup>OX</sup> film everytime we stretched it more. This experiment could be done with higher accuracy if it is done with an automated stretcher. Polarised Raman mapping also could help to investigate the uniformity of stretching effect along the film.

## Bibliography



## Bibliography

1. König, P. and T.J. Richmond, *The X-ray Structure of the GCN4-bZIP Bound to ATF/CREB Site DNA Shows the Complex Depends on DNA Flexibility*. Journal of Molecular Biology, 1993. **233**(1): p. 139-154.
2. Cross, T.A. and S.J. Opella, *Protein structure by solid-state NMR*. Journal of the American Chemical Society, 1983. **105**(2): p. 306-308.
3. Heller, W. and G. Quimfe, *On the Validity of the Langevin Theory of Orientation and the Possibility of Distinguishing Between Inherent and Photoelastic Anisotropy*. Physical Review, 1942. **61**(5-6): p. 382-382.
4. Yamada, S., A. Nakahara, and R. Tsuchida, *Dichroism of the Crystal of Dicyclopentadienyl-Iron*. The Journal of Chemical Physics, 1954. **22**(9): p. 1620-1621.
5. Pacheco-Gómez, R., et al., *Detection of Pathogenic Bacteria Using a Homogeneous Immunoassay Based on Shear Alignment of Virus Particles and Linear Dichroism*. Analytical Chemistry, 2011. **84**(1): p. 91-97.
6. Kowalska, P., et al., *Experimental and Theoretical Polarized Raman Linear Difference Spectroscopy of Small Molecules with a New Alignment Method Using Stretched Polyethylene Film*. Analytical Chemistry, 2011. **84**(3): p. 1394-1401.
7. Raman, C.V., *A new radiation*. Indian J. Phys., 1928. **2**: p. 287-398.
8. Natarajan, L.V., M. Robinson, and R.E. Blankenship, *Linear dichroism of cyanine dyes in stretched polyvinyl alcohol films: a physical chemistry laboratory experiment*. Journal of Chemical Education, 1983. **60**(3): p. 241.
9. Bulheller, B.M., et al., *Flow Linear Dichroism of Some Prototypical Proteins*. Journal of the American Chemical Society, 2009. **131**(37): p. 13305-13314.
10. Norden, B., M. Kubista, and T. Kurucsev, *Linear dichroism spectroscopy of nucleic acids*. Quarterly Reviews of Biophysics, 1992. **25**(01): p. 51-170.
11. Rittman, M., et al., *Probing the structure of long DNA molecules in solution using synchrotron radiation linear dichroism*. Physical Chemistry Chemical Physics, 2012. **14**(1): p. 353-366.

## Bibliography

12. Dafforn, T.R., et al., *Protein Fiber Linear Dichroism for Structure Determination and Kinetics in a Low-Volume, Low-Wavelength Couette Flow Cell*. Biophysical Journal, 2004. **86**(1): p. 404-410.
13. Yoge, A., et al., *Linear dichroism. I. Quantitative evaluation of linear dichroic properties of molecules in stretched polyethylene films*. Journal of the American Chemical Society, 1969. **91**(16): p. 4558-4559.
14. Thulstrup, E.W. and J. Michl, *Orientation and linear dichroism of symmetrical aromatic molecules imbedded in stretched polyethylene*. Journal of the American Chemical Society, 1982. **104**(21): p. 5594-5604.
15. Matsuoka, Y. and B. Nordén, *Linear dichroism studies of nucleic acids. III. Reduced dichroism curves of DNA in ethanol–water and in poly(vinyl alcohol) films*. Biopolymers, 1983. **22**(7): p. 1731-1746.
16. Vandenabeele, P., H.G.M. Edwards, and L. Moens, *A Decade of Raman Spectroscopy in Art and Archaeology*. Chemical Reviews, 2007. **107**(3): p. 675-686.
17. Svedberg, F., et al., *Raman Spectroscopic Studies of Terthiophenes for Molecular Electronics*. The Journal of Physical Chemistry B, 2006. **110**(51): p. 25671-25677.
18. Lefrant, S., M. Baibarac, and I. Baltog, *Raman and FTIR spectroscopy as valuable tools for the characterization of polymer and carbon nanotube based composites*. Journal of Materials Chemistry, 2009. **19**(32): p. 5690-5704.
19. Raman, C.V. *The Official Web Site of the Nobel Prize*. 1930 [cited 2014 2014/09/10]; Available from: [http://nobelprize.org/nobel\\_prizes/physics/laureates/1930/press.html](http://nobelprize.org/nobel_prizes/physics/laureates/1930/press.html).
20. Strutt, J.W., XV. *On the light from the sky, its polarization and colour*. Philosophical Magazine Series 4, 1871. **41**(271): p. 107-120.
21. Raman, C.V. and K.S. Krishnan, *A New Type of Secondary Radiation*. The Nature magazine, 1928.
22. Venkatesachar, B. and L. Sibaiya, *The fine structure of spectral lines in relation to selective absorption* Indian J. Phys., 1930. **5**(747).

## Bibliography

23. Zonen, P.J.K.e., *Quartz spectrograph and visual ultra-violet absorptiometer*. Journal of Scientific Instruments, 1938. **15**(4): p. 141.
24. Chalmers, J.M. and G.P. R., *Handbook of Vibrational Spectroscopy*. 2002, Chichester: John Wiley & Sons Ltd.
25. Hibben, J.H., *The Raman effect and its chemical application*. 1939, New York: Reinhold Publishing Corp.
26. Spedding, F.H. and R.F. Stamm, *The Raman Spectra of the Sugars in the Solid State and in Solution I. The Raman Spectra of α- and β-d-Glucose*. The Journal of Chemical Physics, 1942. **10**(3): p. 176-183.
27. Rank, D.H., J.S. McCartney, and G.J. Szasz, *Intensity and Polarization of Brillouin Spectra*. Journal of the Optical Society of America, 1948. **38**(3): p. 287-289.
28. Welsh, H.L., et al., *RAMAN SPECTROSCOPY OF LOW PRESSURE GASES AND VAPORS*. Canadian Journal of Physics, 1952. **30**(5): p. 577-596.
29. Ham, N.S. and A. Walsh, *Microwave-powered Raman sources*. Spectrochimica Acta, 1958. **12**(1): p. 88-93.
30. Gilson, T.R. and P.J. Hendra, *Laser Raman Spectroscopy*. 1970, London: Wiley-Interscience.
31. Demidovich, A.A., et al., *Sub-nanosecond microchip laser with intracavity Raman conversion*. Applied Physics B, 2003. **76**(5): p. 509-514.
32. Rank, D.H. and R.V. Wiegand, *A Photoelectric Raman Spectrograph for Quantitative Analysis*. Journal of the Optical Society of America, 1946. **36**(6): p. 325-330.
33. Heigl, J.J., et al., *Direct-Recording Raman Spectrometer*. Analytical Chemistry, 1950. **22**(1): p. 154-159.
34. Stamm, R.F. and J.C.F. Salzman, *Photoelectric Raman Spectrometer with Automatic Range Changing. II. Conversion of Perkin-Elmer Infrared Instrument to Grating Type*. Journal of the Optical Society of America, 1953. **43**(2): p. 126-137.
35. Ferraro, J., *Advances in Raman Instrumentation and Sampling Techniques*, in *Raman Spectroscopy*, H. Szymanski, Editor. 1967, Springer US. p. 44-81.

## Bibliography

36. Pelletier, M.J., *Analytical Applications of Raman Spectroscopy*. 1999: Wiley-Blackwell Science.
37. Smith, W.E. and G. Dent, *Modern Raman Spectroscopy – A Practical Approach*. 2005: Wiley.
38. Ferraro, J.R. and K. Nakamoto, *Introductory Raman Spectroscopy*. . 1994, London: Academic Press.
39. Anderson, A., *The Raman effect*. Vol. 1. 1971, New York: Marcel Dekker.
40. Campbell and White. *IR Spectroscopy and Raman Scattering*. . Bristol University [cited 2014 2014/09/10]; Available from:  
<http://www.eng.uc.edu/~gbeaucag/Classes/Analysis/Chapter5.pdf>
41. Michl, J., E.W. Thulstrup, and J.H. Eggers, *Polarization spectra in stretched polymer sheets. Physical significance of the orientation factors and determination of .pi.-.pi. \*transition moment directions in molecules of low symmetry*. The Journal of Physical Chemistry, 1970. **74**(22): p. 3878-3884.
42. Wirtz, A.C., C. Hofmann, and E.J.J. Groenen, *Stretched Polyethylene Films Probed by Single Molecules*. ChemPhysChem, 2011. **12**(8): p. 1519-1528.
43. Thulstrup, E.W., J. Michl, and J.H. Eggers, *Polarization spectra in stretched polymer sheets. II. Separation of .pi.-.pi. \* absorption of symmetrical molecules into components*. The Journal of Physical Chemistry, 1970. **74**(22): p. 3868-3878.
44. Matsuoka, Y. and B. Norden, *Linear dichroism studies of nucleic acid bases in stretched poly(vinyl alcohol) film. Molecular orientation and electronic transition moment directions*. The Journal of Physical Chemistry, 1982. **86**(8): p. 1378-1386.
45. Ismail, M.A., et al., *Spectroscopic studies of 9-hydroxyellipticine binding to DNA*. Biopolymers, 1998. **46**(3): p. 127-143.
46. Norden, B., A. Rodger, and T.R. Dafforn, *Linear dichroism and circular dichroism: a textbook on polarized spectroscopy*. 2010, Cambridge: Royal Society of Chemistry.
47. Juul, H. and S. Vrønning Hoffmann, *private communication*. 2009.

48. Briggs, D. and N. Fairley, *XPS of chemically modified low-density polyethylene surfaces: observations on curve-fitting the C 1s spectrum*. Surface and Interface Analysis, 2002. **33**(3): p. 283-290.
49. Tissington, B., G. Pollard, and I.M. Ward, *A study of the effects of oxygen plasma treatment on the adhesion behaviour of polyethylene fibres*. Composites Science and Technology, 1992. **44**(3): p. 185-195.
50. Lee, S.G., T.J. Kang, and T.H. Yoon, *Enhanced interfacial adhesion of ultra-high molecular weight polyethylene (UHMWPE) fibers by oxygen plasma treatment*. J. Adhes. Sci. Technol., 1998. **12**(7): p. 731-748.
51. Razmkhah, K., et al., *Oxidized polyethylene films for orienting polar molecules for linear dichroism spectroscopy*. Analyst, 2014. **139**(6): p. 1372-1382.
52. Bunn, C.W., *Trans. Faraday Soc.*, 1939. **35**: p. 482–491.
53. Natta, G. and P. Corradini, *Structure and properties of isotactic polypropylene*. Il Nuovo Cimento Series 10, 1960. **15**(1): p. 40-51.
54. Patterson, A.L., *The Scherrer Formula for X-Ray Particle Size Determination*. Physical Review, 1939. **56**(10): p. 978-982.
55. Cowie, J.M.G. and I.J. McEwen, *Molecular Relaxations in Partially Hydrogenated cis-1,4-Polybutadienes. A Guide to the Glass Transition Temperature of Amorphous Polyethylene*. Macromolecules, 1977. **10**(5): p. 1124-1128.
56. Gaur, U. and B. Wunderlich, *The Glass Transition Temperature of Polyethylene*. Macromolecules, 1980. **13**(2): p. 445-446.
57. Kubista, M., B. Aakerman, and B. Albinsson, *Characterization of the electronic structure of 4',6-diamidino-2-phenylindole*. Journal of the American Chemical Society, 1989. **111**(18): p. 7031-7035.
58. Ardhammar, M., N. Mikati, and B. Nordén, *Chromophore Orientation in Liposome Membranes Probed with Flow Dichroism*. Journal of the American Chemical Society, 1998. **120**(38): p. 9957-9958.

## Bibliography

59. Rodger, A., et al., *Flow oriented linear dichroism to probe protein orientation in membrane environments*. Physical Chemistry Chemical Physics, 2002. **4**(16): p. 4051-4057.
60. Norden, B. and F. Tjerneld, *Binding of inert metal complexes to deoxyribonucleic acid detected by linear dichroism*. FEBS Lett., 1976. **67**: p. 368–370.
61. Friedrich, D.M., R. Mathies, and A.C. Albrecht, *Studies of excited electronic states of anthracene and some of its derivatives by photoselection and PPP-SCF calculations*. Journal of Molecular Spectroscopy, 1974. **51**(1): p. 166-188.
62. Michl, J., E.W. Thulstrup, and J.H. Eggers, *Polarization Spectra in Stretched Polymer Sheets. V. Excited States of Anthracene and Transition Moment Directions in Aminoanthracenes*. Berichte der Bunsengesellschaft für physikalische Chemie, 1974. **78**(6): p. 575-586.
63. Chandross, E.A., J. Ferguson, and E.G. McRae, *Absorption and Emission Spectra of Anthracene Dimers*. The Journal of Chemical Physics, 1966. **45**(10): p. 3546-3553.
64. McL Mathieson, A., J.M. Robertson, and V.C. Sinclair, *The crystal and molecular structure of anthracene. I. X-ray measurements*. Acta Crystallographica, 1950. **3**(4): p. 245-250.
65. Kasha, M., H.R. Rawls, and M. Ashraf El-Bayoumi, *The exciton model in molecular spectroscopy*, in *Pure and Applied Chemistry*. 1965. p. 371.
66. Lacye, A.R. and L.E. Lyons, *1029. Luminescence from zone-refined anthracene at 4[degree]K, and the Davydov splitting*. Journal of the Chemical Society (Resumed), 1964(0): p. 5393-5400.
67. Ferguson, J., *Excited Dimer (Excimer) Luminescence from Aromatic Molecules in Crystalline Cyclohexane*. The Journal of Chemical Physics, 1965. **43**(1): p. 306-307.
68. Lacowicz, J.R., *Principles of Fluorescence Spectroscopy*. 1983, New York: Plenum Press.
69. Ware, W.R. and P.T. Cunningham, *Lifetime and Quenching of Anthracene Fluorescence in the Vapor Phase*. The Journal of Chemical Physics, 1965. **43**(11): p. 3826-3831.

## Bibliography

70. Alder, B.J. and T.E. Wainwright, *Studies in Molecular Dynamics. I. General Method*. The Journal of Chemical Physics, 1959. **31**(2): p. 459-466.
71. Rahman, A., *Correlations in the Motion of Atoms in Liquid Argon*. Physical Review, 1964. **136**(2A): p. A405-A411.
72. Trott, O. and A.J. Olson, *AutoDock Vina: Improving the speed and accuracy of docking with a new scoring function, efficient optimization, and multithreading*. Journal of Computational Chemistry, 2010. **31**(2): p. 455-461.
73. Jakobsen, P., H. Lyon, and S. Treppendahl, *Spectrophotometric characteristics and assay of pure pyronin Y*. Histochemistry, 1984. **81**(1): p. 99-101.
74. Arik, M., K. Meral, and Y. Organer, *Effect of surfactants on the aggregation of pyronin B and pyronin Y in aqueous solution*. Journal of Luminescence, 2009. **129**(6): p. 599-604.
75. Okubo, J., et al., *Polarized UV Absorption, X-Ray Photoelectron and  $^{13}C$  NMR Spectra of Pyronin Y*. J. Soc. Photographic Science and Technology of Japan, 1991. **54**(2): p. 150-154.
76. Arbeloa, I.L., *Dimeric and trimeric states of the fluorescein dianion. Part 1.-Molecular structures*. Journal of the Chemical Society, Faraday Transactions 2: Molecular and Chemical Physics, 1981. **77**(10): p. 1725-1733.
77. Sjöback, R., J. Nygren, and M. Kubista, *Absorption and fluorescence properties of fluorescein*. Spectrochimica Acta Part A: Molecular and Biomolecular Spectroscopy, 1995. **51**(6): p. L7-L21.
78. Lu, Y. and A. Penzkofer, *Absorption behaviour of methanolic rhodamine 6G solutions at high concentration*. Chemical Physics, 1986. **107**(2-3): p. 175-184.
79. Turner, D.H., I. Tinoco, and M. Maestre, *Fluorescence detected circular dichroism*. Journal of the American Chemical Society, 1974. **96**(13): p. 4340-4342.
80. Ettore, C., et al., *Chiroptical spectroscopic techniques based on fluorescence*. Methods and Applications in Fluorescence, 2014. **2**(2): p. 024006.

## Bibliography

81. Morimatsu, K. and M. Takahashi, *Structural analysis of RecA protein–DNA complexes by fluorescence-detected linear dichroism: Absence of structural change of filament for pairing of complementary DNA strands*. Analytical Biochemistry, 2006. **358**(2): p. 192-198.
82. Kapuscinski, J., *DAPI: a DNA-Specific Fluorescent Probe*. Biotechnic & Histochemistry, 1995. **70**(5): p. 220-233.
83. Schuler, B., et al., *Adsorption Geometry Determination of Single Molecules by Atomic Force Microscopy*. Physical Review Letters, 2013. **111**(10): p. 106103.
84. Kapuscinski, J., *Interactions of nucleic acids with fluorescent dyes: spectral properties of condensed complexes*. Journal of Histochemistry & Cytochemistry, 1990. **38**(9): p. 1323-9.
85. Williams, R., *Observation of the Relative Polarizations of Electronic Transitions*. The Journal of Chemical Physics, 1957. **26**(5): p. 1186-1188.
86. Halasinski, T.M., et al., *Electronic Absorption Spectra of Neutral Perylene (C<sub>20</sub>H<sub>12</sub>), Terrylene (C<sub>30</sub>H<sub>16</sub>), and Quaterrylene (C<sub>40</sub>H<sub>20</sub>) and Their Positive and Negative Ions: Ne Matrix-Isolation Spectroscopy and Time-Dependent Density Functional Theory Calculations*. The Journal of Physical Chemistry A, 2003. **107**(19): p. 3660-3669.
87. Oliveira, D., et al., *Stopped-Flow Studies of the Formation of Organic Nanocrystals in the Reprecipitation Method*. Nanocrystal. 2011.
88. Reid, D.H. and W. Bonthrone, *1109. Conjugated cyclic hydrocarbons. Part VIII. The benzo[cd]pyrene cation: synthesis and reactivity*. Journal of the Chemical Society (Resumed), 1965(0): p. 5920-5926.
89. Pigeon, M., R.E. Prud'homme, and M. Pezolet, *Characterization of molecular orientation in polyethylene by Raman spectroscopy*. Macromolecules, 1991. **24**(20): p. 5687-5694.
90. Lagaron, J.M., et al., *Morphological characterisation of the crystalline structure of cold-drawn HDPE used as a model material for the environmental stress cracking (ESC) phenomenon*. Polymer, 1999. **40**(10): p. 2569-2586.

## Bibliography

91. Naylor, C.C., et al., *Raman Spectroscopy Employed for the Determination of the Intermediate Phase in Polyethylene*. Macromolecules, 1995. **28**(8): p. 2969-2978.
92. Tashiro, K., S. Sasaki, and M. Kobayashi, *Structural Investigation of Orthorhombic-to-Hexagonal Phase Transition in Polyethylene Crystal: The Experimental Confirmation of the Conformationally Disordered Structure by X-ray Diffraction and Infrared/Raman Spectroscopic Measurements*. Macromolecules, 1996. **29**(23): p. 7460-7469.
93. Strobl, G.R. and W. Hagedorn, *Raman spectroscopic method for determining the crystallinity of polyethylene*. Journal of Polymer Science: Polymer Physics Edition, 1978. **16**(7): p. 1181-1193.
94. Konwerska-Hrabowska, J., G.W. Chantry, and E. Nicol, *Far infrared polarization spectra of anthracene and pyrene molecules dispersed in stretched polyethylene matrices*. International Journal of Infrared and Millimeter Waves, 1981. **2**(6): p. 1135-1149.
95. Wakabayashi, K., et al., *Time-resolved Raman spectroscopy of polytetrafluoroethylene under laser-driven shock compression*. Applied Physics Letters, 1999. **75**(7): p. 947-949.
96. Koenig, J.L. and F.J. Boerio, *Raman Scattering and Band Assignments in Polytetrafluoroethylene*. The Journal of Chemical Physics, 1969. **50**(7): p. 2823-2829.
97. Variankaval, N.E., K.I. Jacob, and S.M. Dinh, *Characterization of crystal forms of  $\beta$ -estradiol – thermal analysis, Raman microscopy, X-ray analysis and solid-state NMR*. Journal of Crystal Growth, 2000. **217**(3): p. 320-331.
98. Wang, F., et al., *An Investigation of Solvent-Mediated Polymorphic Transformation of Progesterone Using in Situ Raman Spectroscopy*. Organic Process Research & Development, 2000. **4**(5): p. 391-395.
99. Falcon, J.A. and K.A. Berglund, *In Situ Monitoring of Antisolvent Addition Crystallization with Principal Components Analysis of Raman Spectra*. Crystal Growth & Design, 2004. **4**(3): p. 457-463.

## Bibliography

100. Dou, X., et al., *Quantitative analysis of double-stranded DNA amplified by a polymerase chain reaction employing surface-enhanced Raman spectroscopy*. Applied Optics, 1998. **37**(4): p. 759-763.
101. Jones, C.M. and S.A. Asher, *Ultraviolet resonance Raman study of the pyrene S4, S3, and S2 excited electronic states*. The Journal of Chemical Physics, 1988. **89**(5): p. 2649-2661.
102. Bridge, N.J. and D. Vincent, *Fluorescence and Raman spectra of pure and doped anthracene crystals at 4 K*. Journal of the Chemical Society, Faraday Transactions 2: Molecular and Chemical Physics, 1972. **68**(0): p. 1522-1535.
103. Ting, C.-h., *Polarized Raman spectra—I. Selection rules*. Spectrochimica Acta Part A: Molecular Spectroscopy, 1968. **24**(8): p. 1177-1189.
104. Shinohara, H., Y. Yamakita, and K. Ohno, *Raman spectra of polycyclic aromatic hydrocarbons. Comparison of calculated Raman intensity distributions with observed spectra for naphthalene, anthracene, pyrene, and perylene*. Journal of Molecular Structure, 1998. **442**(1-3): p. 221-234.
105. Abasbegović, N., N. Vukotić, and L. Colombo, *Raman Spectrum of Anthracene*. The Journal of Chemical Physics, 1964. **41**(9): p. 2575-2577.
106. Otto, C., et al., *Surface-enhanced Raman spectroscopy of DNA bases*. Journal of Raman Spectroscopy, 1986. **17**(3): p. 289-298.
107. Szczepaniak, K., M.M. Szczesniak, and W.B. Person, *Raman and Infrared Spectra of Thymine. A Matrix Isolation and DFT Study†*. The Journal of Physical Chemistry A, 2000. **104**(16): p. 3852-3863.
108. Tsuboi, M., et al., *Raman and Infrared Spectra of (2'S)-[2'-2H]Thymidine: Vibrational Coupling between Deoxyribosyl and Thymine Moieties and Structural Implications*. Journal of the American Chemical Society, 1997. **119**(8): p. 2025-2032.
109. Singh, J.S., *FTIR and Raman spectra and fundamental frequencies of biomolecule: 5-Methyluracil (thymine)*. Journal of Molecular Structure, 2008. **876**(1-3): p. 127-133.

110. Rivas, L., S. Sanchez-Cortes, and J.V. Garcia-Ramos, *Raman structural study of thymine and its 2[prime or minute]-deoxy-ribosyl derivatives in solid state, aqueous solution and when adsorbed on silver nanoparticles*. Physical Chemistry Chemical Physics, 2002. **4**(10): p. 1943-1948.
111. Mathlouthi, M., A.M. Seuvre, and L.J. Koenig, *FT-IR and laser-Raman spectra of thymine and thymidine*. Carbohydrate Research, 1984. **134**(1): p. 23-38.
112. Nafisi, S., et al., *Interaction of Tl+3 with mononucleotides: metal ion binding and sugar conformation*. Journal of Molecular Structure, 2001. **562**(1-3): p. 35-43.
113. Ushizawa, K., T. Ueda, and M. Tsuboi, *Raman scattering tensors of thymidine*. Journal of Molecular Structure, 1997. **412**(3): p. 169-179.
114. Florián, J., V. Baumruk, and J. Leszczyński, *IR and Raman Spectra, Tautomeric Stabilities, and Scaled Quantum Mechanical Force Fields of Protonated Cytosine†*. The Journal of Physical Chemistry, 1996. **100**(13): p. 5578-5589.
115. Mathlouthi, M., A.M. Seuvre, and J.L. Koenig, *F.T.-I.R. and laser-raman spectra of cytosine and cytidine*. Carbohydrate Research, 1986. **146**(1): p. 1-13.
116. Nishimura, Y. and M. Tsuboi, *In-plane vibrational modes of cytosine from an ab initio MO calculation*. Chemical Physics, 1985. **98**(1): p. 71-80.
117. Susi, H., J.S. Ard, and J.M. Purcell, *Vibrational spectra of nucleic acid constituents—II: Planar vibrations of cytosine*. Spectrochimica Acta Part A: Molecular Spectroscopy, 1973. **29**(4): p. 725-733.
118. Lee, S.A., et al., *Temperature-dependent Raman and infrared spectra of nucleosides. II—Cytidine*. Journal of Raman Spectroscopy, 2001. **32**(9): p. 795-802.
119. Nishimura, Y., et al., *Conformation-sensitive Raman lines of mononucleotides and their use in a structure analysis of polynucleotides: guanine and cytosine nucleotides*. Journal of Molecular Structure, 1986. **146**(0): p. 123-153.
120. Kasal, A., M. Budesinsky, and W. Griffiths, *Spectroscopic Methods of Steroid Analysis*, in *Steroid Analysis*, H.L.J. Makin and D.B. Gower, Editors. 2010, Springer Netherlands. p. 27-161.

## Bibliography

121. Potratz, S., A. Mishra, and P. Bauerle *Thiophene-based donor–acceptor co-oligomers by copper-catalyzed 1,3-dipolar cycloaddition*. Beilstein-journals.org, 2012.
122. Moreno Castro, C., et al., *Efficiency of the π conjugation in a novel family of α,α'-bisphenyl end-capped oligothiophenes by means of Raman spectroscopy*. The Journal of Chemical Physics, 2002. **116**(23): p. 10419-10427.
123. Bray, R., J. Ferguson, and C. Hawkins, *Ultraviolet absorption spectra and circular dichroism of divalent metal complexes containing 1,10-phenanthroline and 2,2'-bipyridine*. Australian Journal of Chemistry, 1969. **22**(10): p. 2091-2103.
124. Diaz, G.F., et al., *Surface vibrational study of macrocycle complexes: Co(II), Ni(II), Cu(II) and Zn(II) bis(phenylhydrazine)-1,10-phenanthroline*. Vibrational Spectroscopy, 2002. **28**(2): p. 223-234.
125. Tsaryuk, V., et al., *Vibronic spectra and details of the structure of europium nitrates with derivatives of 1,10-phenanthroline*. Journal of Alloys and Compounds, 2000. **300–301**(0): p. 184-192.
126. Larsen, B.D., et al., *The Merrifield peptide synthesis studied by near-infrared Fourier-transform Raman spectroscopy*. Journal of the American Chemical Society, 1993. **115**(14): p. 6247-6253.
127. Houlne, M.P., et al., *Confocal Raman Microscopy for Monitoring Chemical Reactions on Single Optically Trapped, Solid-Phase Support Particles*. Analytical Chemistry, 2002. **74**(17): p. 4311-4319.
128. Ryttersgaard, J., et al., *Monitoring of a solid phase peptide synthesis by NIR-FT-Raman spectroscopy*. Spectrochimica Acta Part A: Molecular and Biomolecular Spectroscopy, 1997. **53**(1): p. 91-98.
129. Maher, R.C., et al., *Exploiting SERS Hot Spots for Disease-Specific Enzyme Detection†*. The Journal of Physical Chemistry C, 2009. **114**(16): p. 7231-7235.
130. Rahman, S.S., D.J. Busby, and D.C. Lee, *Infrared and Raman Spectra of a Single Resin Bead for Analysis of Solid-Phase Reactions and Use in Encoding Combinatorial Libraries*. The Journal of Organic Chemistry, 1998. **63**(18): p. 6196-6199.

## Bibliography

131. Tsoi, W.C. and D.G. Lidzey, *Raman spectroscopy of fluorene oligomers in the  $\alpha$ -,  $\beta$ - and  $\gamma$ -phases*. Journal of Physics: Condensed Matter, 2008. **20**(12): p. 125213.
132. O'Leary, T.J., P.D. Ross, and I.W. Levin, *Effects of anesthetic and nonanesthetic steroids on dipalmitoylphosphatidylcholine liposomes: a calorimetric and Raman spectroscopic investigation*. Biochemistry, 1984. **23**(20): p. 4636-4641.
133. Gardikis, K., et al., *A DSC and Raman spectroscopy study on the effect of PAMAM dendrimer on DPPC model lipid membranes*. International Journal of Pharmaceutics, 2006. **318**(1-2): p. 118-123.
134. Papahadjopoulos, D., et al., *Use of lipid vesicles as carriers to introduce actinomycin D into resistant tumor cells*. Cancer research, 1976.
135. Sharma, A. and U.S. Sharma, *Liposomes in drug delivery: Progress and limitations*. International Journal of Pharmaceutics, 1997. **154**(2): p. 123-140.
136. Damianoglou, A., et al., *The Synergistic Action of Melittin and Phospholipase A2 with Lipid Membranes: Development of Linear Dichroism for Membrane-Insertion Kinetics*. Protein and Peptide Letters, 2010. **17**(11): p. 1351-1362.
137. Rajendra, J., et al., *Quantitation of protein orientation in flow-oriented unilamellar liposomes by linear dichroism*. Chemical Physics, 2006. **326**(1): p. 210-220.
138. Dafforn, T.R. and A. Rodger, *Linear dichroism of biomolecules: which way is up?* Current Opinion in Structural Biology, 2004. **14**(5): p. 541-546.
139. Vogel, S., et al., *Retinol-Binding Protein-Deficient Mice: Biochemical Basis for Impaired Vision†*. Biochemistry, 2002. **41**(51): p. 15360-15368.
140. De Boeck, H. and R. Zidovetzki, *NMR study of the interaction of retinoids with phospholipid bilayers*. Biochimica et Biophysica Acta (BBA) - Biomembranes, 1988. **946**(2): p. 244-252.
141. Ortiz, A., F.J. Aranda, and J.C. Gómez-Fernández, *Interaction of retinol and retinoic acid with phospholipid membranes. A differential scanning calorimetry study*. Biochimica et Biophysica Acta (BBA) - Biomembranes, 1992. **1106**(2): p. 282-290.

## Bibliography

142. Roh, S.-S., M.-K. Park, and Y.-u. Kim, *Abietic Acid from Resina Pini of < i>Pinus</i> Species as a Testosterone 5&alpha;-Reductase Inhibitor*. Journal of Health Science, 2010. **56**(4): p. 451-455.
143. Aranda, F.J. and J. Villalaín, *The interaction of abietic acid with phospholipid membranes*. Biochimica et Biophysica Acta (BBA) - Biomembranes, 1997. **1327**(2): p. 171-180.
144. Webpage., A.P.L. *Preparation of Liposomes*. [cited 2014 2014/09/14].
145. O'Neill, M.J. and E.S. Watson, *Differential microcalorimeter*. 1966, Google Patents.
146. Gill, P. and T.R. Tohidi Moghadam, B., *Differential Scanning Calorimetry Techniques: Applications in Biology and Nanoscience*. J Biomol Tech, 2010. **21**(4): p. 167-193.
147. Oldfield, E. and D. Chapman, *Dynamics of lipids in membranes: Heterogeneity and the role of cholesterol*. FEBS Letters, 1972. **23**(3): p. 285-297.
148. Ladbrooke, B.D., R.M. Williams, and D. Chapman, *Studies on lecithin-cholesterol-water interactions by differential scanning calorimetry and X-ray diffraction*. Biochimica et Biophysica Acta (BBA) - Biomembranes, 1968. **150**(3): p. 333-340.
149. Mady, M., et al., *Interaction of Doxorubicin and Dipalmitoylphosphatidylcholine Liposomes*. Cell Biochemistry and Biophysics, 2012. **62**(3): p. 481-486.
150. Mukai, Y., et al., *Structure of all-trans-Retinal in the T1 State As Determined by Raman Spectroscopy: A Set of Carbon-Carbon and Carbon-Oxygen Stretching Force Constants Determined by the Normal Coordinate Analysis of the T1 Raman Lines of the Undeuterated and Variously Deuterated Retinals*. The Journal of Physical Chemistry, 1995. **99**(18): p. 7160-7171.
151. Qu, G.N., et al., *Difference in effect of temperature on absorption and Raman spectra between all-trans-b-carotene and all-trans-retinol*. Chin. Phys. B., 2012. **21**(21): p. 7830-7840.
152. Brody, R.H., H.G.M. Edwards, and A.M. Pollard, *Fourier transform-Raman spectroscopic study of natural resins of archaeological interest*. Biopolymers, 2002. **67**(2): p. 129-141.

## Bibliography

153. Fields, G.B. and R.L. Noble, *Solid phase peptide synthesis utilizing 9-fluorenylmethoxycarbonyl amino acids*. International Journal of Peptide and Protein Research, 1990. **35**(3): p. 161-214.
154. Smith, A.M., et al., *Fmoc-Diphenylalanine Self Assembles to a Hydrogel via a Novel Architecture Based on π–π Interlocked β-Sheets*. Adv. Mater., 2008. **20**: p. 37-41.
155. Castelletto, V., et al., *Self-assembly of Fmoc-tetrapeptides based on the RGDS cell adhesion motif*. Soft Matter, 2011. **7**(24): p. 11405-11415.
156. Zhou, M., et al., *Self-assembled peptide-based hydrogels as scaffolds for anchorage-dependent cells*. Biomaterials, 2009. **30**(13): p. 2523-2530.
157. Jayawarna, V., et al., *Introducing chemical functionality in Fmoc-peptide gels for cell culture*. Acta Biomaterialia, 2009. **5**(3): p. 934-943.
158. Sung, K.-M., et al., *Synthesis of Monofunctionalized Gold Nanoparticles by Fmoc Solid-Phase Reactions*. Journal of the American Chemical Society, 2004. **126**(16): p. 5064-5065.
159. Gildea, B.D., et al., *PNA solubility enhancers*. Tetrahedron Letters, 1998. **39**(40): p. 7255-7258.
160. Thomson, S.A., et al., *Fmoc mediated synthesis of Peptide Nucleic Acids*. Tetrahedron, 1995. **51**(22): p. 6179-6194.
161. Bank, R.A., et al., *Amino Acid Analysis by Reverse-Phase High-Performance Liquid Chromatography: Improved Derivatization and Detection Conditions with 9-Fluorenylmethyl Chloroformate*. Analytical Biochemistry, 1996. **240**(2): p. 167-176.
162. Adams, D.J., et al., *A new method for maintaining homogeneity during liquid-hydrogel transitions using low molecular weight hydrogelators*. Soft Matter, 2009. **5**(9): p. 1856-1862.
163. Yang, Z., et al., *Small molecule hydrogels based on a class of antiinflammatory agents*. Chemical Communications, 2004(2): p. 208-209.
164. Ruoslahti, E. and M.D. Pierschbacher, *New perspectives in cell adhesion: RGD and integrins*. Science, 1987. **238**(4826): p. 491-497.

## Bibliography

165. Johnson, W.C., *Analyzing protein circular dichroism spectra for accurate secondary structures*. Proteins: Structure, Function, and Bioinformatics, 1999. **35**(3): p. 307-312.
166. Marrington, R., et al., *Validation of new microvolume Couette flow linear dichroism cells*. Analyst, 2005. **130**(12): p. 1608-1616.
167. Mikati, N., J. Nordh, and B. Norden, *Scattering anisotropy of partially oriented samples: turbidity flow linear dichroism (conservative dichroism) of rod-shaped macromolecules*. The Journal of Physical Chemistry, 1987. **91**(23): p. 6048-6055.
168. Gokce, I., et al., *Single Peptide Bonds Exhibit Poly(Pro)II ("Random Coil") Circular Dichroism Spectra*. Journal of the American Chemical Society, 2005. **127**(27): p. 9700-9701.
169. Mazza, M., et al., *Nanofiber-Based Delivery of Therapeutic Peptides to the Brain*. ACS Nano, 2013. **7**(2): p. 1016-1026.
170. Marshall, K.E., et al., *Characterizing the Assembly of the Sup35 Yeast Prion Fragment, GNNQQNY: Structural Changes Accompany a Fiber-to-Crystal Switch*. Biophysical Journal, 2010. **98**(2): p. 330-338.
171. Barth, A., *Infrared spectroscopy of proteins*. Biochimica et Biophysica Acta (BBA) - Bioenergetics, 2007. **1767**(9): p. 1073-1101.
172. Kumar, S. and S.B. Rai, *Spectroscopic studies of L-arginine molecule*. Indian J. Pure Appl. Phys., 2010. **38**: p. 251-255.
173. Krimm, S. and J. Bandekar, *Vibrational Spectroscopy and Conformation of Peptides, Polypeptides, and Proteins*, in *Advances in Protein Chemistry*, J.T.E. C.B. Anfinsen and M.R. Frederic, Editors. 1986, Academic Press. p. 181-364.
174. Kong, J. and S. Yu, *Fourier Transform Infrared Spectroscopic Analysis of Protein Secondary Structures*. Acta Biochimica et Biophysica Sinica, 2007. **39**(8): p. 549-559.
175. Huang, C.Y. and G. Balakrishnan, *Protein secondary structure from deep-UV resonance Raman spectroscopy*. J. Raman Spectrosc., 2006. **37**: p. 277-282.
176. Pignatello, R., *Biomaterials Scence and Engineering*. 2011, New York: InTech.